



TECHNISCHE
UNIVERSITÄT
DARMSTADT

Process optimization for Si(Hf,Ta)(B)(C,N) polymer-derived ceramics via microstructural analysis

Prozessoptimierung für Si(Hf,Ta)(B)(C,N) polymer-abgeleitete Keramiken durch mikrostrukturelle Analyse

Genehmigte Dissertation zur Erlangung des Grades eines Doktors der Naturwissenschaften
(Dr. rer. nat.)

von Nathalie Thor

Fachbereich Material- und Geowissenschaften
Technische Universität Darmstadt

Erstgutachterin: Prof. Dr. Ute Kolb

Zweitgutachterin: Prof. Dr. Astrid Pundt

Darmstadt 2024

Process optimization for Si(Hf,Ta)(B)(C,N) polymer-derived ceramics via microstructural analysis
Prozessoptimierung für Si(Hf,Ta)(B)(C,N) polymer-abgeleitete Keramiken durch mikrostrukturelle
Analyse

Genehmigte Dissertation von Nathalie Thor geboren in Kreuztal

Tag der Einreichung: 31.10.2023

Tag der Prüfung: 24.01.2024

Darmstadt, Technische Universität Darmstadt

Bitte zitieren Sie dieses Dokument als:

URN: urn:nbn:de:tuda-tuprints-266251

URL: <http://tuprints.ulb.tu-darmstadt.de/26625>

Jahr der Veröffentlichung auf TUprints: 2024

Dieses Dokument wird bereitgestellt von tuprints,
E-Publishing-Service der TU Darmstadt

<http://tuprints.ulb.tu-darmstadt.de>

tuprints@ulb.tu-darmstadt.de

Die Veröffentlichung steht unter folgender Creative Commons Lizenz:

Namensnennung-Weitergabe unter gleichen Bedingungen 4.0 International

<https://creativecommons.org/licenses/by-sa/4.0/>

This work is licensed under a Creative Commons License:

Attribution-ShareAlike 4.0 International

<https://creativecommons.org/licenses/by-sa/4.0/>

Erklärung laut Promotionsordnung

§ 8 Abs. 1 lit. c PromO

Ich versichere hiermit, dass die elektronische Version meiner Dissertation mit der schriftlichen Version übereinstimmt.

§ 8 Abs. 1 lit. d PromO

Ich versichere hiermit, dass zu einem vorherigen Zeitpunkt noch keine Promotion versucht wurde. In diesem Fall sind nähere Angaben über Zeitpunkt, Hochschule, Dissertationsthema und Ergebnis dieses Versuchs mitzuteilen.

§ 9 Abs. 1 PromO

Ich versichere hiermit, dass die vorliegende Dissertation selbstständig und nur unter Verwendung der angegebenen Quellen verfasst wurde.

§ 9 Abs. 2 PromO

Die Arbeit hat bisher noch nicht zu Prüfungszwecken gedient.

Darmstadt, 31. Oktober 2023

Nathalie Thor

Table of Contents

Erklärung laut Promotionsordnung	I
Table of Contents	III
Abbreviations	V
Symbols	VIII
Abstract	X
Zusammenfassung	XI
1 Introduction	1
1.1 Background and Motivation	1
1.2 Scope of the Present Work	6
2 Literature Review & State of the Art	8
2.1 Ultra-High Temperature Ceramics (UHTCs)	8
2.2 Group IV and V Transition Metal Carbides, Nitrides and Carbonitrides	9
2.3 Polymer-Derived Ceramics (PDCs)	12
2.4 Preceramic Polymers	12
2.5 The Polymer-Derived Ceramic Route	16
2.6 Metal-Modification of Organosilicon Polymers - from Precursors into Ceramics	18
2.7 Ceramic Products Made by Precursor Processing	18
2.8 Processing of Bulk Ceramics via Sintering	19
2.9 Field-Assisted Sintering Technique (FAST/SPS)	22
2.10 Details on Preliminary Investigations	24
3 Applied Methods	27
3.1 Aspects of Optical Light Microscopy (OLM)	27
3.2 Scanning Electron Microscopy (SEM) for Microstructure Analysis	27
3.3 Electron Microprobe Analysis (EPMA) for Element Maps	33
3.4 Aspects of Transmission Electron Microscopy (TEM)	34
3.5 Analytical Electron Microscopy - Interaction of Electrons with Materials	42
3.6 X-ray (Powder) Diffraction (XRD) of PDCs	44
3.7 Chemical Composition of PDCs	45
3.8 Mechanical Properties via Nanoindentation Tests: Material Hardness	45
4 Materials Synthesis and Sample Preparation	47
4.1 Synthesis and Consolidation of SiHfCN	47
4.2 Synthesis and Annealing of Si(Hf _x Ta _{1-x})(C)N	48
4.3 Synthesis and Consolidation of Si(Hf _x Ta _{1-x})C(N,O)	51
4.4 Nomenclature of PDCs	52
4.5 Sample Preparation for OLM, SEM and EPMA	54
4.6 Specimen Preparation for TEM Analysis	55
5 Basic Ceramics: SiHfCN and SiC/Si₃N₄/HfC	60

5.1	Microstructure Analysis by SEM and TEM for SiHfCN_01	60
5.2	Elemental Distribution Maps Using EPMA Analysis for SiHfCN_01	65
5.3	Microstructure Analysis by SEM and TEM for SiHfCN_02	66
5.4	Discussion	66
6	The Influence of Tantalum: Si(Hf_xTa_{1-x})(C)N and Si₃N₄/SiC/(Hf_xTa_{1-x})C(N)	68
6.1	Phase Assemblage Determined via XRD Analysis	68
6.2	Microstructure of As-pyrolyzed Si(Hf _x Ta _{1-x})(C)N PDCs, (x=0.7 and x=0.3)	70
6.3	Microstructure of Annealed SiC/Si ₃ N ₄ /(Hf _x Ta _{1-x})(C)N PDCs, (x=0.7 and x=0.3)	75
6.4	Discussion	89
6.5	Conclusion	93
7	The Influence of Polysilan: Si(Hf_xTa_{1-x})C(N,O) and SiC/(Hf_xTa_{1-x})C	94
7.1	Chemical Composition and Phase Assemblage	94
7.2	Microstructure of As-pyrolyzed Si(Hf _{0.7} Ta _{0.3})C(N,O) Powders at 1000 °C in Ar	95
7.3	Microstructure of Sintered SiC/(Hf _{0.7} Ta _{0.3})C at 2200 °C in Vacuum	99
7.4	Discussion	111
7.5	Summary	120
8	The Influence of Boron Additive – Si(B)C/(Hf_{0.75}Ta_{0.25})C	122
8.1	Synthesis and Consolidation of Si(Hf _{0.75} Ta _{0.25})(B)C	122
8.2	Chemical Composition and Phase Assemblage	123
8.3	Microstructure of SiC/(Hf _{0.75} Ta _{0.25})C and SiBC/(Hf _{0.75} Ta _{0.25})C	125
8.4	Image Analysis for Determination of Porosity in SiBC/(Hf _{0.75} Ta _{0.25})C	127
8.5	Discussion	131
9	Conclusion	133
10	Outlook	138
	References	140
	Appendix	158
	List of Figures	166
	List of Tables	175
	Acknowledgements	176
	Curriculum Vitae	177
	Publications & Conference Contributions	178

Abbreviations

APT	Atom probe tomography
a.u.	Arbitrary units
BF	Bright-field
BFP	Back focal plane
BMS	Borane dimethylsulfide
BSE	Backscattered electrons
CAS-no	Chemical Abstracts Service Registry Number
CBED	Convergent beam electron diffraction
CCD	Charge-coupled device
cf	Cumulative frequency plots
CLEM	Correlative light and electron microscopy
CMC	Ceramic matrix composite
CT	Computer tomography
CTE	Coefficient of thermal expansion
CTEM	Conventional transmission electron microscopy
CVD	Chemical vapor deposition
DC	Direct current
DP	Diffraction pattern
EBC	Environmental barrier coating
EB-PVD	Electron beam physical vapor deposition
ECAS	Electric current activated/assisted sintering techniques
EDS	Energy dispersive X-ray spectroscopy
EELS	Electron energy-loss spectroscopy
EPMA	Electron probe microanalysis
eV	Electron volt
FAST	Field-assisted sintering technique
fcc	Face centered cubic
FEG	Field emission gun
FFT	Fast Fourier transform
FIB	Focused ion beam
FIB-SEM	Focused ion beam scanning electron microscopy
GIS	Gas inlet system
GB	Grain boundary
HIP	Hot isostatic pressing

HP	Hot pressing
HR-TEM	High-resolution transmission electron microscopy
ICDD	International Center for Diffraction Data
ICE	Internal combustion engine
ICP-AES	Inductively coupled plasma atomic emission spectroscopy
IFFT	Inverse Fast Fourier Transformation
keV	Kilo electron volt
LM	Light microscopy
MV	Mega volt
OLM	Optical light microscopy
OPSZ	Organopolysilazane
PHPS	Perhydropolysilazane
PDC	Polymer derived ceramic
PDC-NCs	Polymer derived ceramic nanocomposites
PDF	Powder diffraction file (nomenclature ICDD)
PDMAT	Pentakis(dimethylamino)tantalum(V), Formula: $C_{10}H_{30}N_5Ta$
PM	Powder metallurgical
PMS	Polymethylsilsesquioxane
PS	Pressureless sintering
PSZ	Polysilazane
PVD	Physical vapor deposition
ROI	Region of interest
rpm	Rounds per minute
RT	Room temperature
SADP	Selected area diffraction pattern
SAED	Selected area electron diffraction
SEM	Scanning electron microscopy
SE	Secondary electrons
SF	Stacking fault
SMP-10	Silicon carbide matrix precursor, formula: $[SiH(CH_2CH=CH_2)CH_2]_{0.1n} [SiH_2CH_2]_{0.9n}$
SPS	Spark plasma sintering
STEM	Scanning transmission electron microscopy
TBC	Thermal barrier coating
TEM	Transmission electron microscopy
TDEAH	Tetrakisdiethylamido(hafnium)(IV), Formula: $C_{16}H_{40}HfN_4$

TDMAH	Tetrakisdimethylamido(hafnium), Formula: $C_8H_{24}HfN_4$
TGO	Thermally grown oxide
TM	Transition metals
TMC	Transition metal carbides
TMN	Transition metal nitrides
TMCN	Transition metal carbonitrides
UHT	Ultra-high temperature
UHTCs	Ultra-high temperature ceramics
UHTC-NCs	Ultra-high temperature ceramic nanocomposites
WC	Wolfram carbide
WD	Working distance
WDS	Wavelength-dispersive X-ray spectroscopy
XRD	X-ray diffraction
YSZ	Yttria stabilized zirconia

Symbols

a, b, c	Lattice parameters along the crystallographic [100], [010], [001] axes
at-%	Atomic percent
α_{OA}	Aperture angle of the objective lens
A	Indentation area
Å	Ångstrom
β	Semi-angle of collection of the magnifying lens
C_c	Chromatic-aberration coefficient
C_s	Spherical-aberration coefficient
d_{hkl}	Lattice spacing
d_c	Diameter disk of least confusion (chromatic aberration)
d_s	Diameter disk of least confusion (spherical aberration)
δ	Smallest resolvable distance between two objects
E	Elastic modulus (Young's modulus)
E	Total energy in electron volts (eV)
E_0	Primary electron beam
ΔE	Energy spread
g	Reciprocal lattice vector
H	Hardness
h	Planckian quantum
hkl	Miller indices
[hkl]	Specific crystallographic direction
(hkl)	Specific crystallographic plane
I_i	Incident beam
I_d	Diffracted beam
K	Scattering vector
k	Coverage factor
k_d	Diffracted wave vector
k_i	Incident wave vector
κ	Thermal conductivity
N_A	Avogadro constant
P	Load/Force
p	Momentum of the particle
R_p	Yield strength
s	Excitation error

t	Thickness of specimen
t	(Service) time
T	Temperature
η	Backscattering coefficient
θ	Diffraction (Bragg) angle
ω	Fluorescence yield
λ	Wavelength of radiation
μ	Refractive index of the viewing medium
wt-%	Weight percent
ν	Poisson ratio
Z	Atomic number
z	Distance (thickness)
σ	Standard deviation

Abstract

Polymer-derived ceramics (PDCs) gained significant importance because of the unique combination of their commercial availability, molecular tailorability, reduced processing costs, high-temperature stability, chemical resistance and adherence. Thus, they can serve as potential thermal barrier coating (TBC) protecting an underlying alloy from high thermo-mechanical loads and degradation in extreme environments. The main focus in the development of novel PDCs lies in the modification of the polymeric precursors on a molecular level and in the subsequent treatment tailoring the nano- and microstructure to achieve attractive structural and functional properties. However, detailed information of the emerging microstructures upon different heat treatments is lacking.

In this work, the microstructure development of novel PDC nanocomposites (PDC-NCs) upon different heat treatments is investigated, primarily using scanning and transmission electron microscopy (SEM, TEM).

Polysilazane-based SiHfCN , $\text{Si}(\text{Hf}_x\text{Ta}_{1-x})(\text{C})\text{N}$ and polysilane-based $\text{Si}(\text{B})(\text{Hf}_x\text{Ta}_{1-x})\text{C}$ ultra-high temperature ceramic nanocomposites (UHTC-NCs) were analyzed in the as-pyrolyzed, annealed and sintered state.

In a first step, particular emphasis was placed onto the microstructure development of novel $\text{Si}(\text{Hf}_x\text{Ta}_{1-x})(\text{C})\text{N}$ UHTC-NCs upon pyrolysis and subsequent annealing. A microstructure evolution model shows the conversion from a single-source precursor into a mostly amorphous single-phase ceramic after pyrolysis. Annealing resulted in crystalline UHTC-NC, presenting two distinct microstructure regions, namely the bulk and surface of the powder particles with inherently different microstructures and phase compositions. Initiated by high-temperature annealing, the residual “free” carbon present in the system initiated the formation of SiC and thus, the thermal decomposition of Si_3N_4 , along with the release of gaseous nitrogen in the outer region of the powder particles. A detailed study of the crystallization behaviour and phase composition found local chemical variations and a gradual average increase of transition metal carbide (TMC) grain sizes in the proximity to surface-near regions. Grain sizes effects correlate with an outward zoning of increased carbon- and oxygen compositions accompanied by depleted nitrogen compositions in the matrix.

The experimental data clearly showed that polysilazane-based UHTC-NCs are prone to phase separation, accompanied by thermal decomposition and diffusion-controlled coarsening. This is disadvantageous when considering these materials as TBC materials, as the coarsening phenomena could induce thermal stresses and therefore lead to spallation.

By changing the precursor from polysilazane to polysilane, a reduced coarsening of TMCs was achieved. However, the polysilane-based UHTC-NC showed very similar microstructures upon sintering. Increased TMC grain sizes were attributed to a combination of the pulsed direct current (DC), the accompanying Joule heating and the presence of oxygen impurities promoting particle coarsening during evaporation, condensation and diffusion processes. A further modification of the polysilane-based UHTC-NC with small amounts of boron resulted finally in a homogeneous distribution of the constituting phases, a reduction of TMC grain sizes and a reduced porosity.

The findings demonstrate that SEM and TEM are useful for unravelling complex microstructures of multi-phase PDC-NCs and guiding their development. The results show that the correlation of different parameters such as the precursor selection as well as the process parameters of the sintering procedure have an enormous impact on the microstructural development. Therefore, microstructure characterization and continuous feedback is essential when designing and synthesizing novel PDC NCs for potential TBC materials.

Zusammenfassung

Polymer-abgeleitete Keramiken (PDC) haben aufgrund ihrer einzigartigen Kombination aus kommerzieller Verfügbarkeit, molekularer Anpassungsfähigkeit, geringeren Verarbeitungskosten, Hochtemperaturstabilität, chemischer Beständigkeit und Haftvermögen erheblich an Bedeutung gewonnen und werden unter anderem als potenzielle Wärmedämmschicht (TBC), die die darunter liegende Legierung vor hohen thermomechanischen Belastungen und Zersetzung in extremen Umgebungen schützt, genutzt. Das Hauptaugenmerk bei der Entwicklung neuartiger PDCs liegt auf der Modifizierung der polymeren Ausgangsstoffe auf molekularer Ebene, um die Nano- und Mikrostruktur so anzupassen, dass attraktive strukturelle und funktionelle Eigenschaften erzielt werden. Es fehlt jedoch an detaillierten Informationen über die bei verschiedenen Wärmebehandlungen entstehenden Mikrostrukturen.

In dieser Arbeit wird die Entwicklung der Mikrostruktur neuartiger PDC-Nanokomposite (PDC-NCs) bei verschiedenen Wärmebehandlungen untersucht, wobei in erster Linie Raster- und Transmissionselektronenmikroskopie (SEM, TEM) eingesetzt werden.

Polysilazan-basierte SiHfCN , $\text{Si}(\text{Hf}_x\text{Ta}_{1-x})(\text{C})\text{N}$ und Polysilan-basierte $\text{Si}(\text{B})(\text{Hf}_x\text{Ta}_{1-x})\text{C}$ Ultrahochtemperatur-Keramik-Nanokomposite (UHTC-NCs) wurden im pyrolysierten, wärmebehandelten und gesinterten Zustand analysiert.

Zunächst lag das Augenmerk auf der Entwicklung der Mikrostruktur von neuartigen $\text{Si}(\text{Hf}_x\text{Ta}_{1-x})(\text{C})\text{N}$ UHTC-NCs nach der Pyrolyse und einer anschließenden Wärmebehandlung. Ein Modell der Mikrostrukturevolution zeigt die Umwandlung von einem einphasigen Prekursor in eine überwiegend amorphe einphasige Keramik nach der Pyrolyse. Die Wärmebehandlung führte zu einem kristallinen UHTC-NC, das zwei unterschiedliche Mikrostrukturbereiche aufweist; nämlich die Masse und die Oberfläche der Pulverpartikel mit inhärent unterschiedlichen Mikrostrukturen und Phasenzusammensetzungen. Ausgelöst durch die Wärmebehandlung initiierte der im System vorhandene "freie" Restkohlenstoff die Bildung von SiC und damit die thermische Zersetzung von Si_3N_4 unter Freisetzung von gasförmigem Stickstoff im äußeren Bereich der Pulverpartikel. Die Untersuchung des Kristallisationsverhaltens und der Phasenzusammensetzung ergab lokale chemische Variationen und eine allmähliche Zunahme der Übergangsmetallcarbide (TMC) Korngrößen vom Inneren hin zu oberflächennahen Bereichen. Die Auswirkungen der Korngrößen korrelieren mit einer nach außen gerichteten Zonierung mit erhöhter Kohlenstoff- und Sauerstoffzusammensetzung bei gleichzeitig verringerter Stickstoffzusammensetzung in der Matrix.

Die experimentellen Daten zeigen deutlich, dass UHTC-NCs auf Polysilazanbasis zur Phasentrennung neigen, begleitet von thermischer Zersetzung und diffusionskontrollierter Vergrößerung. Dies ist von Nachteil, wenn diese Materialien als TBC-Materialien in Betracht gezogen werden, da die Vergrößerungsphänomene thermische Spannungen induzieren und somit zu Abplatzungen führen könnten. Durch den Wechsel des Prekursors von einem Polysilazan zu einem Polysilan konnte eine geringere Vergrößerung der TMCs erreicht werden. Doch entstanden nach dem Sintern sehr ähnliche Gefüge. Das Auftreten größerer TMC-Korngrößen wird auf eine Kombination aus gepulstem Gleichstrom, der begleitenden Joule-Erwärmung und dem Vorhandensein von Sauerstoffverunreinigungen zurückgeführt, die die Partikelvergrößerung während der Verdampfungs-, Kondensations- und Diffusionsprozesse begünstigten. Erst eine weitere Modifikation des auf Polysilan basierenden UHTC-NCs zeigte, dass geringe Mengen an Bor zu einer homogenen Verteilung der konstituierenden Phasen, einer Verringerung der TMC-Korngrößen und einer geringeren Porosität führte.

Für die strukturelle Charakterisierung dieser komplexen Mikrostrukturen mehrphasiger PDC-NCs waren elektronenmikroskopische Methoden unverzichtbar. Die Ergebnisse zeigen, dass die Korrelation

verschiedener Parameter wie die Auswahl des Prekursors sowie die Prozessparameter des Sinterverfahrens einen enormen Einfluss auf die Entwicklung der Mikrostruktur haben. Daher ist die Charakterisierung der Mikrostruktur und eine kontinuierliche Rückmeldung bei der Entwicklung und Synthese neuartiger PDC-NCs für potenzielle TBC-Materialien unerlässlich.

1 Introduction

1.1 Background and Motivation

The Paris Agreement on climate change negotiated at the 2015 United Nations Climate Change Conference aims to strengthen the global response to limit the temperature increase of global warming to no more than 1.5 °C above pre-industrial levels [1]. Since combustion is referred as the main source of energy for industrial activities worldwide an extensive reduction in greenhouse gas emissions is required [2–4]. Hence, the reduction of greenhouse gas emissions must be introduced by an improved efficiency of combustion equipment [2].

The urgency of the climate crisis has heightened the demand for innovative material developments in gas turbines in aircraft engines or modern power generation units to achieve higher efficiency, reduced greenhouse gas emissions and enhanced sustainability. These novel materials play a critical role in enabling higher operating temperatures, improved durability and enhanced performance, contributing to a more efficient and environmentally sustainable power generation process. Although the energy sectors are going through rapid changes due to the COVID-19 pandemic and recent geopolitical risks, the technological innovation led to an increased deployment of renewable energies in recent years, but also brings record-high levels of the fossil fuel industry, which is expected to continue in the future (cf. Figure 1) [5,6].

The efficiency of combustion engines and thermochemical processes such as pyrolysis, gasification, or reforming largely depends on the operating temperatures. Therefore, the development of advanced materials with improved high-temperature capabilities is crucial for enhancing the efficiency of both internal combustion engines (ICEs) and chemical plants (CPs) [4,7].

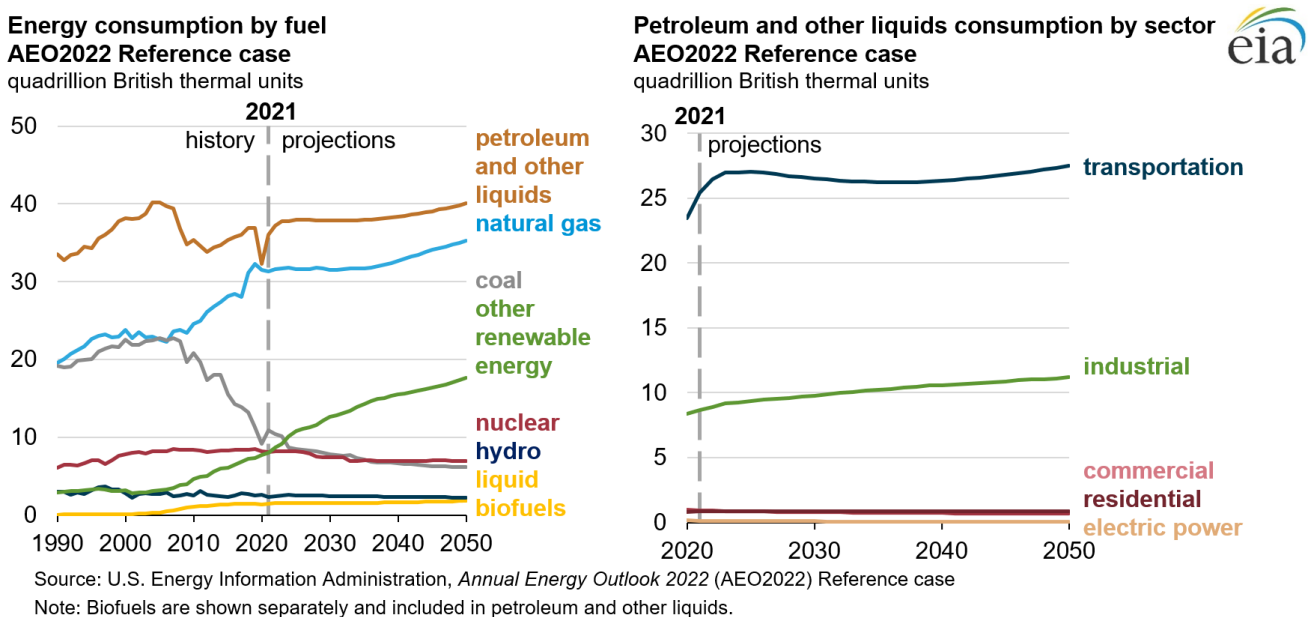


Figure 1 Long-term projections showing the energy consumption by fuel. Figure taken from Ref. [8].

In the last two decades a revival of high-temperature materials has taken place, where the recent interest is dedicated to applications in internal combustion engines or gas turbine engines where extreme oxidative, corrosive and/or erosive environments prevail [9–13]. Gas turbine engines are in general widely utilized in aircraft engines and land-based chemical plants for power generation [11]. Driven by the constantly increasing energy consumption worldwide (cf. Figure 1) higher power ratings and efficiency levels for those application fields are mandatory [6,11]. Further, the transportation sector,

specifically the airline traffic is expected to growth in the next ten years, while at the same time there is a urgent need to reduce the CO₂ and NO_x emissions [8,14]. Efforts to increase the efficiency of combustors are mainly dependent on the firing temperatures; the higher the temperature capability of the materials within the engines the more efficient they are [11,15]. A further development trend of these materials can be best described by the relationship between the core power output versus the turbine rotor inlet temperature as depicted in Figure 2 [15]. The green curve represents the ideal performance, it surpasses the trend of the actual engines shown in blue bullets, which in general highlights the existence of ineffectiveness [15].

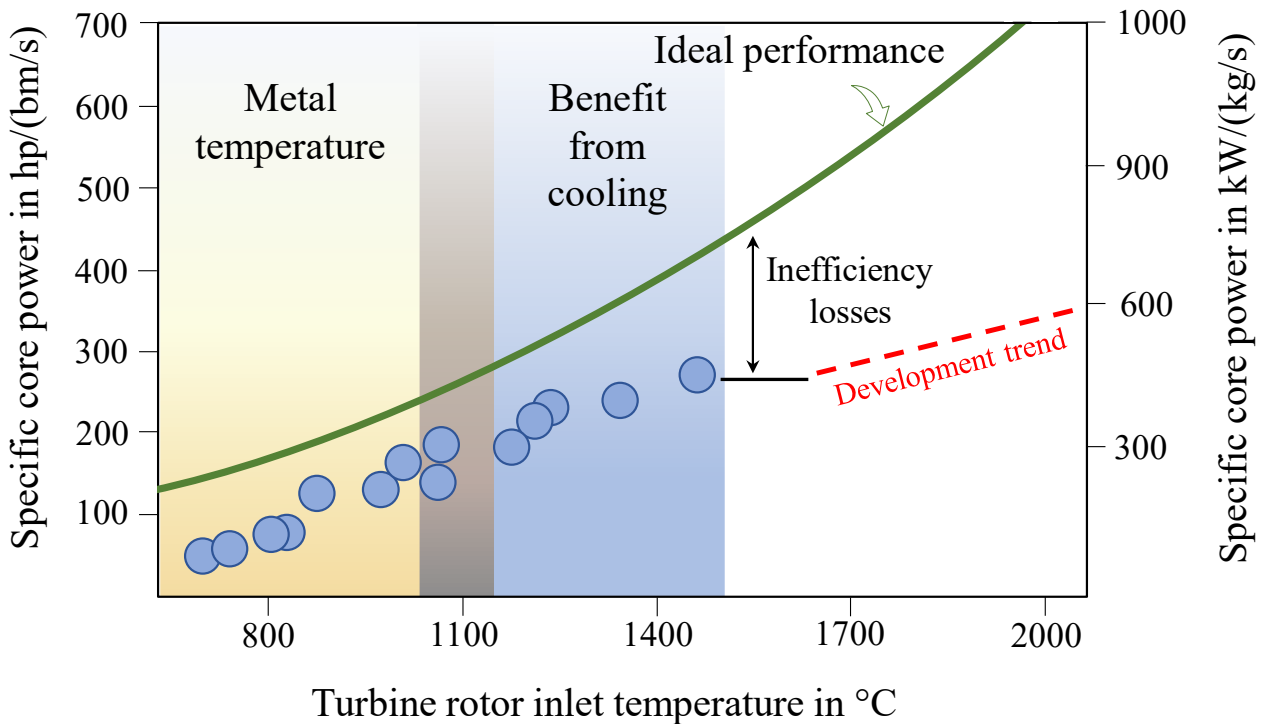


Figure 2 The specific core powder as function of the turbine rotor inlet temperature. Figure adapted from Ref. [15].

High-performance materials such as special steels, titanium alloys or superalloys are among the materials used for the construction of gas turbines [11]. In the last decades the mainly used high-performance materials for components in the hot section of gas turbine engines, which allowed a steady increase in the operation temperature and thus have contributed to a fuel efficiency were Ni-base superalloys [11,15–18]. However, the operating temperature of those Ni-based superalloys reaches limits; components in jet engines for example should reach maximum temperatures around 1000 °C, which is around ~300 °C below their melting point [15–18]. Figure 3 displays the yield strength values of various Ni-based superalloys, utilized in the hot-sections of gas turbine engines as a function of temperature. The yield strength (R_p) of metallic materials usually decreases with increasing temperature [19]. It can be seen that Ni-alloys display severely decreased Yield strengths at temperatures of ~1000 °C, which might lead to catastrophic failure [20]. Regarding this behaviour, a general “safety limit” of 1000 °C is considered to be the maximum temperature of Ni-base superalloys used in components operating in the hot-sections of gas turbine engines as substrate materials [20].

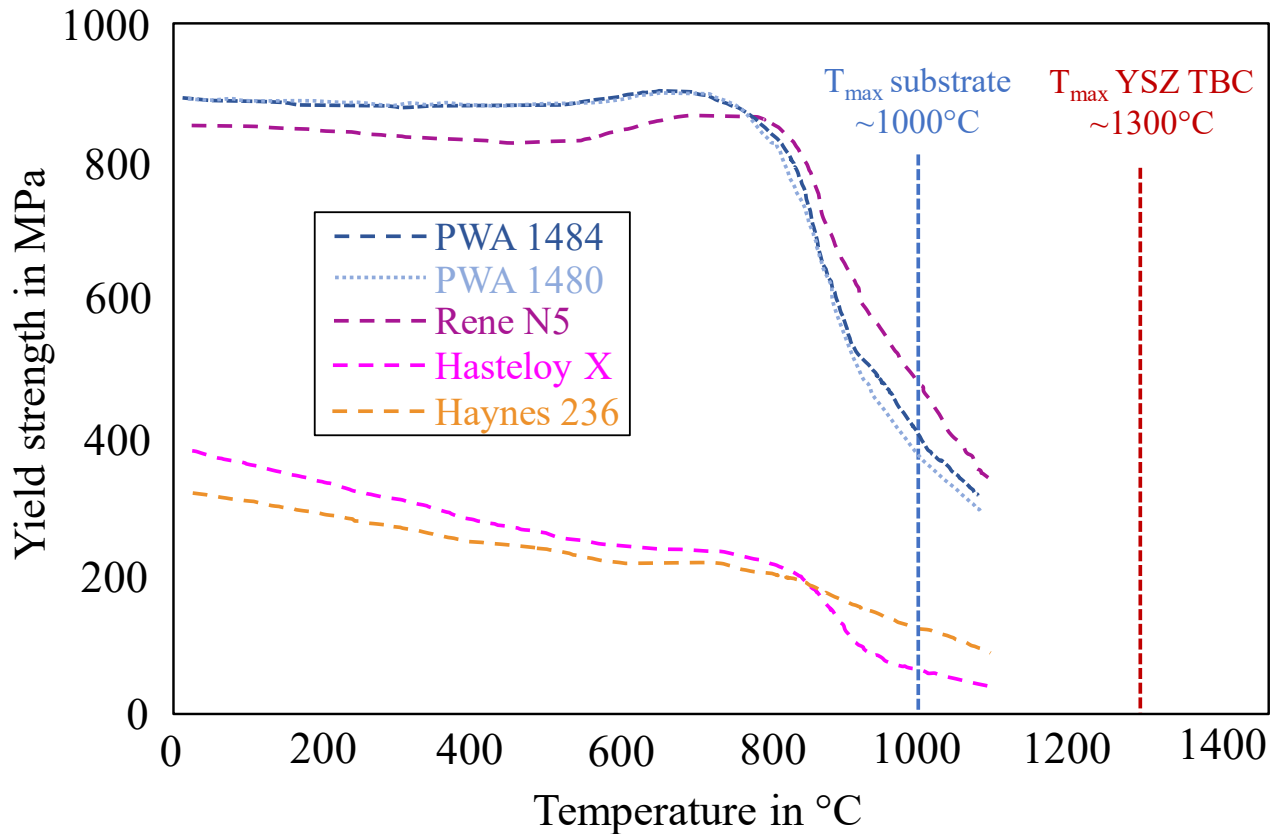


Figure 3 Yield strength versus temperature for different Ni-base superalloys for turbine engines employed in the hot-sections of gas turbine engines. Figure adapted from Ref. [20].

The engine's operating temperature is defined by the gas temperatures within the turbine, whereas the gas temperature in the turbine is actually much higher than the operating temperature [15]. Thus, additional effort in form of cooling air systems is mandatory to cool down the gas temperature in the turbine, so that the Ni-base superalloy parts do not start to melt [15]. Effective internal cooling structures (such as channels or passages) are incorporated into the turbine blade itself [21]. This process is highly inefficient and explains the urgent need for the design of new materials, possessing a significant higher melting point than the currently used Ni-based superalloys [15].

Significant research and development efforts were directed towards intermetallics, with the objective to exploit their exceptional features for improving the performance of gas turbine engines [11]. Metallic/intermetallic alloys based on refractory metal silicide systems such as Mo-Si-B-X (X= Nb, Fe, Cr, Ti, Hf, Zr...) are recently considered as alternative material systems for structural components in ultra-high temperature applications [11,15,22]. For example Mo-Si-based alloys macro alloyed with Ti meet several of the requirements for high temperature structural applications [23]. In addition to its high solidus temperature of approximately 1900 °C, resulting in excellent creep resistance, the eutectic Mo-Si-Ti alloy Mo-20Si-52.8Ti (at-%) shows a considerable reduction in density towards 6.2–7 g/cm³, which is significantly lower than the 8–8.5 g/cm³ of state-of-the-art Ni-based superalloys [11,23–26]. In contrast to various Mo-Si-based alloys it also possesses remarkable oxidation resistance [23,24,27]. Figure 4 shows that many engineering design factors contribute to the overall efficiency of gas-turbine engines [14]. The diagram depicts the progression of temperature capabilities on the example of Ni-base superalloys, the introduction of thermal barrier coatings (TBCs), additional cooling mechanisms and the frequently used deposition methods over the last 60 years [14,16,28].

A major step in the efficiency of gas-turbine engines was made by the introduction of a complex multilayer-system (100 – 500 μm in thickness), a TBC [14,15,28–30]. With the introduction of TBCs the maximum temperature in the hottest part of the engine was boosted to temperatures around $\sim 1500\text{ }^\circ\text{C}$, bringing extraordinary efficiency and performances for highly demanding thermal cycling conditions [17,18,28,30,31].

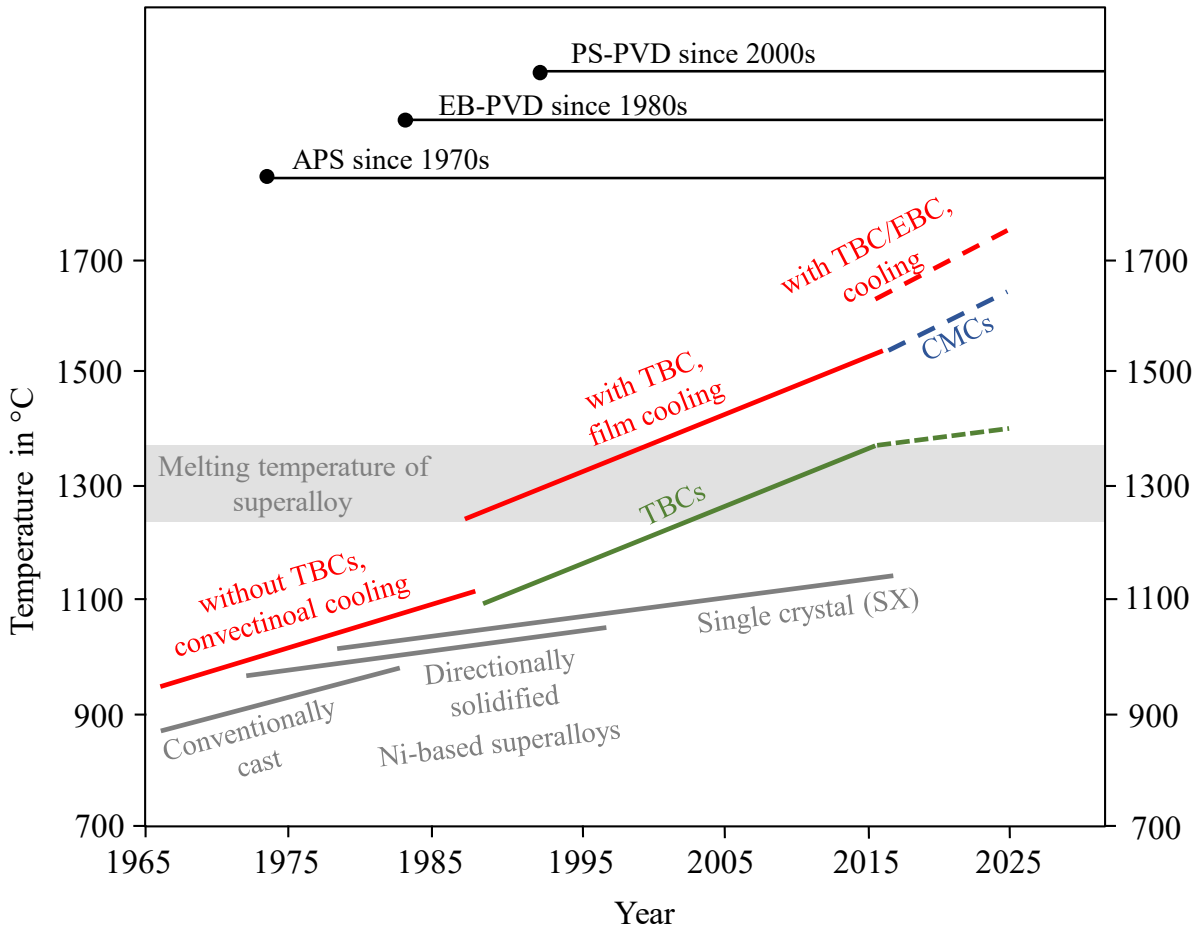


Figure 4 Temperature limit of superalloys for the aircraft turbine and recent developments of thermal barrier coatings and the deposition methods in the last 60 years. Figure adapted from Refs. [16,28].

TBCs are multifunctional: they protect high-temperature components, such as turbine blades from extreme heat and wear in corrosive and oxidative atmospheres for prolonged service times of 10,000 hours and thermal cycles between room temperature and $\sim 1300\text{ }^\circ\text{C}$ (between take-off and landing in case of an aircraft) [14,16,31]. The aim of a TBC system is to generate a thermal gradient between the coating surface and the substrate surface so that the substrate material can withstand elevated temperatures beyond $1600\text{ }^\circ\text{C}$ and harsh atmospheres (corrosive and oxidative) [17]. To achieve that, the applied TBCs must have strain compliance to minimize thermal-expansion-mismatch stresses with the underlying alloy parts on heating and cooling cycles [14,18]. Hence, the performance of the TBC system plays a vital role in improving the life time of the underlying metal substrate [17]. Functionally graded TBCs usually comprise a metallic substrate, actually a Ni-based superalloy (MCrAlY, M= Ni), which is then coated with an intermediate metallic bond layer (such as NiCoCrAlY, NiCrAlY or aluminides of Pt and Ni) and a ceramic top coat (yttria stabilized zirconia (YSZ), alumina or another advanced ceramic) [17,30,32]. Since its introduction in the 1970s, TBCs made of $\sim 7\text{ wt-}\%$ of Y_2O_3 -stabilized ZrO_2 (7YSZ) in its metastable tetragonal-prime structure is still the material of choice for top

coats [28,30,33,34]. In addition, a thermally grown oxide (TGO) layer forms due to oxidation of the intermetallic bond coat resulting from the oxygen diffusion through the top coat at operating temperature [30,32]. The bond coat serves to minimize the coefficient of thermal expansion (CTE) gradient between the top coat and the metallic substrate [17]. Thus, the aluminium-rich bond coat, forming the TGO primarily protects the metallic substrate from further oxidation and improves the scale adhesion [30,32]. Ideally, top coats exhibit a low thermal conductivity ($\kappa \sim 2.6 \text{ W}\cdot\text{m}^{-1}\cdot\text{K}^{-1}$ for 5.3 wt-% YSZ, 600 °C [35], $\kappa \sim 0.7\text{-}1.4 \text{ W}\cdot\text{m}^{-1}\cdot\text{K}^{-1}$ for 7.25 wt-% YSZ [36]), providing thermal insulation against high temperature degradation of the metallic substrate [17,30]. For comparison, the thermal conductivity of Al is $\kappa \sim 105 \text{ W}\cdot\text{m}^{-1}\cdot\text{K}^{-1}$ [33].

However, this widely applied TBC system needs further development, when considering service times of $t > 10,000$ hours and continuously increasing hot gas temperature demands in the gas turbine engine [29,32,34]. Its temperature limitation at about 1200 °C due to a phase transformation, its rapid creep at temperatures above 900 °C in combination with the great mismatch between the coefficient of thermal expansion (CTE) with the underlying alloy causes the formation of thermal stresses during thermal cycling and therefore, increasing the risk of spallation and limiting the life-time of metal-based components [29–31,33,37–39].

The most important criterion which needs to be considered during the development of new coating materials operating at harsh environments is related to the melting point of the material, as the maximum operation temperature is (with some exceptions) about half of its melting point [9]. There are a more than 300 materials possessing melting temperatures higher than 2000 °C, but only 15 elements or compounds possess melting temperatures above 3000 °C [9,13]. Among these few materials are elements like W, Re or C, as well as binary compounds with a high covalent bonding character, such as BN, ThO₂, TiC, ZrC, ZrB₂, HfC, HfN, HfB₂, NbC, TaC, TaN, TaB₂ [9,13]. This means that the development of completely new high-temperature materials is already severely limited by the melting temperature. TMCs like HfC, and its solid solutions with TaC, such as (Hf_{0.2}Ta_{0.8})C possess the highest ever known melting point of a solid material ($T_m \sim 4000$ °C) [13,40–45]. These compounds are so-called ultra-high temperature ceramics (UHTCs) with potential use as protective coatings on hard metal substrates in extreme conditions [10,12,46–48]. Because of their unique combination of their improved structural properties such as extreme high melting point, high hardness, excellent chemical stability, high stiffness modulus, high refractoriness, excellent thermal and electrical conductivity, UHTCs are considered as suitable candidates for thermal protection, which can withstand application temperatures exceeding ~ 1600 °C [9,12,13,42,45,49–51]. However, single-phase UHTCs exhibit a rather poor oxidation resistance and damage tolerance, which limit their practical application [9,13]. To improve the performance of UHTCs in harsh oxidative environments, oxidation resistant phases (silica formers) such as SiC or silicides were added as they form a passivating silica layer, which is protective at least to ~ 1700 °C [9,12,45,52,53].

The polymer-derived ceramic (PDC) route is an advanced ceramic manufacturing approach allowing the design and synthesis of multielement silicon-based ceramics, which can be tailored at the molecular level [54–56]. In particular, single-source polymeric precursors modified with organo-metallic precursors provide a facile and inexpensive access to obtain polymer-derived ceramic nanocomposites (PDC-NCs) with tailored phase compositions, microstructures and property profiles [9,54]. In order to prepare PDC-NCs, commercially available organosilicon polymers are chemically modified with metal alkoxides, acetates, amino complexes etc. [9,41,57,58]. Upon thermolysis at temperatures between 300 °C and 1000 °C the synthesized single-source precursors are subsequently converted into amorphous single-phase ceramics [59]. Further heat treatment at higher temperatures induce phase separation and crystallization reactions [60].

Several studies have indicated that PDC-NCs, specifically those composed of highly refractory secondary phases such as group IV and V transition metal carbides, nitrides, and borides uniformly dispersed within a silicon-based ceramic matrix phase (SiCN, SiOC, SiBCN) demonstrate enhanced thermal stability as well as an improved resistance to oxidation and corrosion when compared to their PDC counterparts [9,47,60–63]. In the last two decades the incorporation of Zr, Hf, Ta and Ti into PDC-based matrices became popular: SiHfN [61], SiHfCN [64], SiHf(B)CN [65,66], SiHfCNO [67], SiHfOC [63], SiZr(B)CN [60], SiHfTaCN [41,47], SiHfTiC [47] etc. The PDC route is in particular beneficial, because it allows the preparation of protective coatings from the solvent utilizing liquid silicon-based polymeric precursors [10,12,68,69]. With this a simpler preparation of ceramic coatings via inexpensive deposition techniques such as dip, spray or spin coating is possible [10,69]. Recently, several studies reported on the preparation of protective PDC coatings on dense substrates, such as metal alloys providing a potential approach of TBCs and EBCs [69–73].

1.2 Scope of the Present Work

The research training program 2561 “MatCom-ComMat: Materials Compounds from Composite Materials for Applications in Extreme Conditions” intends to combine refractory metal-based metallic/intermetallic materials (e.g., Mo-Si-B-X, with X = Nb, Fe, Ti, Hf etc.) as substrate material and polymer-derived ceramic nanocomposites (PDC-NCs) based on Si(M)CY (M = B, Zr, Hf and Y = O, N) systems as the preferred materials for protective coatings. Heat resistance, chemical stability, thermal, mechanical and electrical properties of PDC-NCs depend on the microstructure that develops during thermal treatments. As the low thermal conductivity of the coating is one of the vital parameters, a ceramic nanocomposite where the mean free path of phonons leads to a decreased thermal conductivity is beneficial [74]. The scope of this work is to identify each phase, its phase conversation upon high temperatures in detail and the microstructure of the newly developed PDC materials under different conditions. This allows for predicting the materials properties as well as determining the required material compositions and process parameters for a controlled synthesis. It is expected that a detailed understanding of the microstructure will allow various microstructure parameters to be individually tailored by processing.

This thesis focuses on the understanding of the high-temperature behaviour and microstructural changes in non-oxide Si-based PDC-NCs containing transition metal carbides (TMCs) and nitrides (TMNs). The aim of this work is to gain a detailed understanding of the potential design of novel material compounds from composite materials. It is particularly essential to characterize the distribution of the starting powder materials, the microstructural evolution and phase assemblage, as well as the anticipated nanocomposites in detail. The ultimate goal is to gain a comprehensive understanding of the microstructural changes of the different phases induced by thermal treatments and non-conventional sintering (the field-assisted sintering technique, FAST) and how these microstructural changes affect the materials properties at elevated temperatures.

The experimental and theoretical findings of the international research activities indicate that the tailoring of the microstructure in PDCs can be precisely controlled via numerous routes [9,54,57,68,75,76]. By tailoring the chemistry of the molecular preceramic polymers and the different processing parameters during the polymer-to-ceramic conversion, the microstructure can be adjusted [9,57,77]. Many previous studies have examined the effects of sintering temperature and dwell time on sinterability of UHTCs powder compacts [50,78–83]. However, only a limited number of studies investigated the high-temperature microstructure development of Hf/Ta-modified polymer-derived ceramic powders consolidated into bulk ceramics upon FAST [41,65].

The present work provides a comprehensive characterization of the microstructure of dense SiHfCN bulk ceramics, novel Si(Hf_xTa_{1-x})(C)N polymer-derived ceramic nanocomposites (PDC-NCs) and monolithic SiC/(Hf_{0.7}Ta_{0.3})C and Si(B)C/(Hf_{0.75}Ta_{0.25})C bulk ceramics. These four systems have been chosen to be used as top coat materials in the later stages of the research training group 2561 “MatCom-ComMat”. The results presented here contribute to the understanding of the microstructural evolution in these systems and provide valuable insights for further research and development in the field of high-temperature composite materials.

The thesis is divided into ten chapters. Following this introductory chapter, chapter 2 gives the theoretical background of UHTCs, PDCs, their synthesis route and the consolidation via sintering. Chapter 3 provides information of the applied methods including the theory of electron microscopy and the utilized microscopes/instruments.

In chapter 4 the materials synthesis and the sample preparation techniques are described.

Chapter 5 anticipates a detailed microstructural characterization of two SiHfCN bulk ceramics. It was decided that SiHfCN ceramics should be sintered at higher temperatures (~1950 °C) upon FAST. Two SiHfCN ceramics with different dwell times were consolidated by FAST and subsequently examined by numerous microscopic methods.

Chapter 6 focuses on the characterization of novel as-pyrolyzed (1000 °C) and annealed (1600 °C) ceramic powder samples in the Si(M)(C)N (M = transition metals) system. A series of novel Si(Hf_xTa_{1-x})(C)N polymer-derived ceramic powders, where x represents the molar ratio of Hf and Ta (x = 0.2 and 0.7) were characterized via electron microscopy and a detailed microstructural evolution upon different heat treatments was described. Different thermal treatments are crucial in order to understand how the material's microstructure changes under distinct possible application temperature conditions. By combining the data from analytical techniques, valuable insights into the microstructural evolution of Si(Hf_xTa_{1-x})(C)N PDC-NCs were gained. The results of this system were published in Ref. [84].

Chapter 7 characterizes the as-pyrolyzed Si(Hf_{0.7}Ta_{0.3})C(N,O) amorphous ceramic powders and thereof sintered SiC/(Hf_{0.7}Ta_{0.3})C bulk ceramics. Numerous mechanisms influencing the evolving microstructure during the sintering of the initial amorphous PDCs are not well understood yet. This is mainly due to the complex structure in combination with the numerous processes including phase separation reactions, crystallization and decomposition reactions upon sintering. A detailed analysis of the as-pyrolyzed ceramic powders and the thereof emerging microstructure of the system including the characterization of mechanical properties enables for a better understanding of the high-temperature behaviour of the anticipated SiC/(Hf_{0.7}Ta_{0.3})C ceramics. The results shown will be submitted for publication in Ref. [85]. In Chapter 8 a perspective on alternative materials is given. The single-source precursor was tailored on the molecular level, achieving a slight modification in the Hf:Ta ratio. Furthermore, one single-source precursor was tailored by the addition of small amounts of boron.

The conclusion and an outlook on possible studies in the future follow in chapter 9 and 10, respectively. Overall, the microstructural characterizations of these four systems are vital to advance the understanding of PDCs upon different heat treatments and to unlock their full potential in various high-temperature applications, contributing to the development of more efficient and durable materials in the future.

2 Literature Review & State of the Art

In the following subchapters a general literature review and state of the art regarding ultra-high temperature ceramics (UHTCs) in chapter 2.1, transition metal carbides, nitrides and carbonitrides (TMCs, TMNs and TMCNs) in chapter 2.2, polymer-derived ceramics (PDCs) in chapter 2.3, the preceramic polymers in chapter 2.4, a general introduction of the PDC route and the modification of polymers with metal-complexes are given in the chapters 2.5 and 2.6. Moreover, details on precursor processing in chapter 2.7, the principles of sintering and the concept of the non-conventional sintering method (FAST) as well as details on preliminary investigation are described in chapters 2.8 - 2.10.

2.1 Ultra-High Temperature Ceramics (UHTCs)

Ultra-high temperature ceramics (UHTCs) are a class of materials with potential use as structural components for extreme environmental conditions. There are mainly two scientifically representative definitions of UHTCs [9,86]. The first one relates to their ultra-high melting points, being greater than 3000 °C [9,12,13]. An alternative definition is that UHTCs are ceramic materials, which can withstand long-term exposure to environmental loading at temperatures exceeding 1600 °C [9,12,87]. Nearly all UHTCs are, chemically spoken, binary compounds of boron, carbon or nitrogen in combination with one of the early transition metals (TMs) such as Zr, Hf, Ti, Nb or Ta [9,12,51]. The bonding character of those binary compounds are described as a mixture of metallic and covalent bond character [12]. The strong covalent bonds between the TMs and B, C or N result in unique properties, including high refractoriness, extremely high melting temperatures, high hardness, high elastic moduli and an excellent chemical stability [12,13,42,45,50,51]. In addition, these compounds show higher thermal and electrical conductivity compared to oxide ceramics due to the metallic bond character [12].

The combination of these ceramic-like and metal-like properties makes UHTCs for consideration as potential candidates to withstand extreme high-temperature conditions including structural applications like engine components, furnace elements, high temperature shielding, cutting tools and plasma arc electrodes [51]. Components in those applications are exposed to extreme heat fluxes, chemical reactive plasma conditions in combination with load-bearing and mechanical loadings.

Research interest on this class of materials is not entirely new; fundamental technological interest has already taken place during the space race which started in the late 1950s extending through the 1960s in the Soviet Union and the U.S. [12,13]. At that time UHTCs were originally thought as materials for potential applications in the aerospace engineering used for propulsion system components and hypersonic concepts [13]. During this time the fundamental understanding of the bonding, the electronic structure, thermodynamic properties, mechanical behaviour, phase equilibria and oxidation response was documented [12]. After the initial research, the interest for those ultra-high temperature applications waned for several decades [12]. In the late 1980s, the material class of UHTCs received renewed attention [9]. This is because the materials could be used for structural applications including engines, hypersonic aerospace vehicles, leading-edge parts, plasma arc electrodes, cutting tools, furnace elements and high temperature shielding [9,12,51,88]. Diboride-based UHTCs (such as ZrB₂/SiC, HfB₂/SiC) were considered for hypersonic speed applications where the bow shock at the sharp features produces temperatures in excess of 2000 °C, heat fluxes of hundreds of Watts per cm² and highly reactive gas species occur [12,51,88–92].

However, pure UHTCs show a rather poor oxidation resistance and damage tolerance under extreme environments, limiting their practical applications [9,13]. Improvement in terms of performance in harsh oxidative environments led to the development of composite materials [9]. Therefore, oxidation-resistant silica-formers like SiC [53,89,93], Si₃N₄ [94] or silicides (TaSi₂, MoSi₂) [45,52,95] were added to the UHTCs [9,13]. The in-situ formation of a silica-rich scale on the surface of the material hinders

the oxidation diffusion into the parent material and thus improves the oxidation resistance up to temperatures of ~ 1700 °C [12,13].

Research on UHTCs has generated enormous scientific know-how in the fields of synthesis, processing, densification, thermomechanical properties and oxidation over the last decades [12]. Most commonly UHTCs are synthesized via the carbothermal reduction of the corresponding oxide [12]. However, this method has certain limitations, such as the production of relatively large particle sizes and the presence of impurities, including oxygen, nitrogen and/or carbon [12]. Despite these drawbacks, many investigations on UHTCs have employed the powder metallurgical (PM) route with commercially available powders for systems such as: $\text{ZrB}_2/\text{ZrC}/\text{SiC}$ [88], $\text{HfB}_2\text{-MoSi}_2$ [96], $\text{ZrB}_2\text{-MoSi}_2$ [83], $\text{HfB}_2\text{-SiC}$ [80], $\text{ZrB}_2\text{-TaSi}_2$, $\text{HfB}_2\text{-TaSi}_2$ [97], ZrB_2 [98], TaC-MoSi_2 , TaC-TaSi_2 , HfC-MoSi_2 , HfC-MoSi_2 [52], TaC-SiC [99], $\text{TiC}_{1-x}\text{N}_x$ and $\text{TaC}_{1-x}\text{N}_x$ [46].

2.2 Group IV and V Transition Metal Carbides, Nitrides and Carbonitrides

Transition metal carbides (TMCs), nitrides (TMNs) and carbonitrides (TMCNs) are characterized as a distinct class of non-oxidic ceramics exhibiting an unusual combination of exceptional structural properties [9,100,101]. These materials show extraordinary hardness and extreme high melting points [100]. The solid solution based on hafnium and tantalum carbides have the highest melting points of the known refractory materials with $T_m(\text{Hf}_{0.2}\text{Ta}_{0.8}\text{C}) = 4000$ °C, whereas the melting temperature of HfC is $T_m(\text{HfC}) = 3928$ °C and the melting temperature of TaC is $T_m(\text{TaC}) = 3985$ °C [9,43,45]. Since these intermetallic compounds are formed by the incorporation of carbon and nitrogen into the lattices of early transition metals, they produce a class of compounds with metallic character [42,101]. Thus, they also exhibit high electrical and thermal conductivities [9,42,100]. Many of the advantageous properties are due to their interatomic bonding being a mixture of metallic, covalent and ionic, whereas the strongest component in the monocarbides has been determined to be covalent [9,13,42,102]. Properties like the melting temperature and the high elastic modulus are affected by these highly covalent bonds [13]. Although they possess physical properties of ceramics, they exhibit electronic and magnetic properties of metals [101]. The solid-state chemistry of these intermetallic compounds is similar to that of pure metals [101]. They often adopt simple crystal structures with the metal atoms forming lattices of face-centered cubic (fcc) structure as for example HfC and TaC [9,101] (cf. the crystal structure of pure HfC in Figure 5). Hf and Ta carbides and nitrides are found in NaCl (rocksalt structure) [9,42,101]. In this structure, the carbon atom is coordinated octahedrally with the six Hf atoms surrounding it and thus achieves the highest possible coordination number [42].

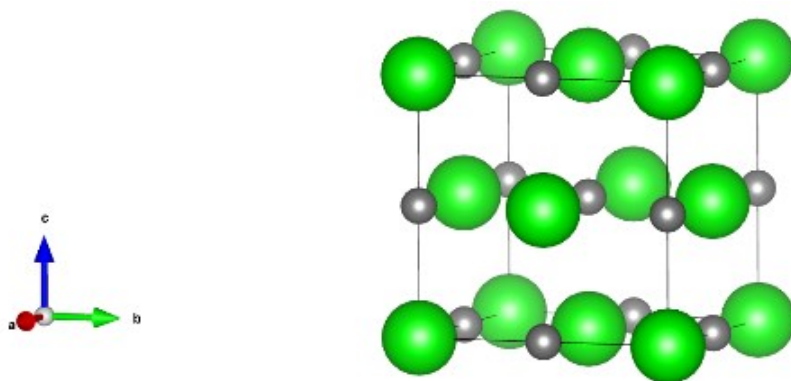


Figure 5 Common crystal structure of the TMC of HfC (NaCl type, $Fm\bar{3}m$, space group no. 225). Large atoms refer to the metal atom (Hf), the small atom depict carbon atom. Structure created with VESTA [103].

Figure 6 depicts the phase diagrams of hafnium - carbon (left) and tantalum - carbon (right). The composition range of HfC at temperatures between 2100 °C up to 2400 °C is from 37 to 48 at-% carbon [104]. The maximum melting temperature of HfC is 3950 ± 40 °C at 49 to 50 at-% carbon. No phase transformations of HfC up to temperatures of 3950 °C occur. Many binary TMCs (and TMNs) exist over a broad range of composition with an upper limit of the nonmetal/metal ratio (C:M or N:M) near 1 [9,13,100].

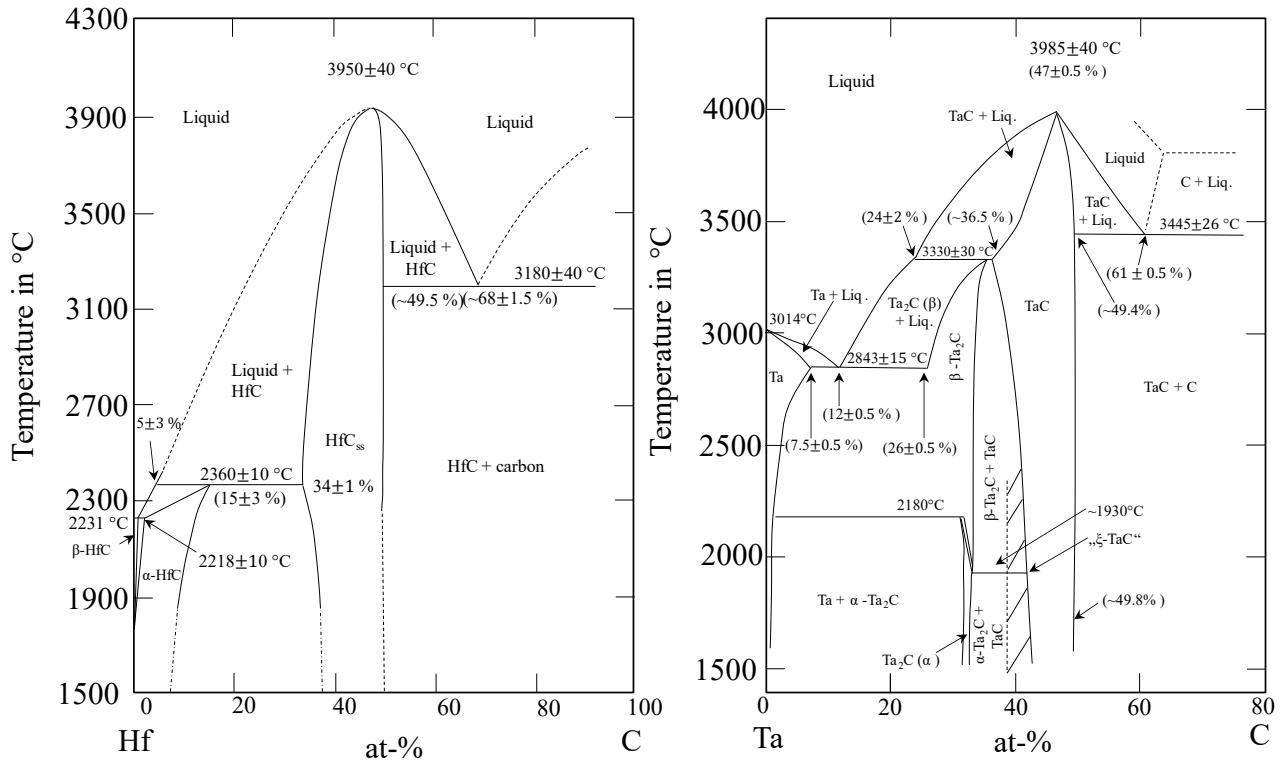


Figure 6 The phase equilibrium diagrams for the Hf-C and Ta-C systems. Figure adapted from Refs. [13,104].

Figure 7 depicts the ternary phase diagram of HfC-TaC with a miscibility gap below temperatures of 887 °C. Complete miscibility is found among HfC and TaC at high temperatures, whereas the stability of these solid solutions and the exact temperatures and shapes of miscibility gaps depend on vacancy concentrations [9,105].

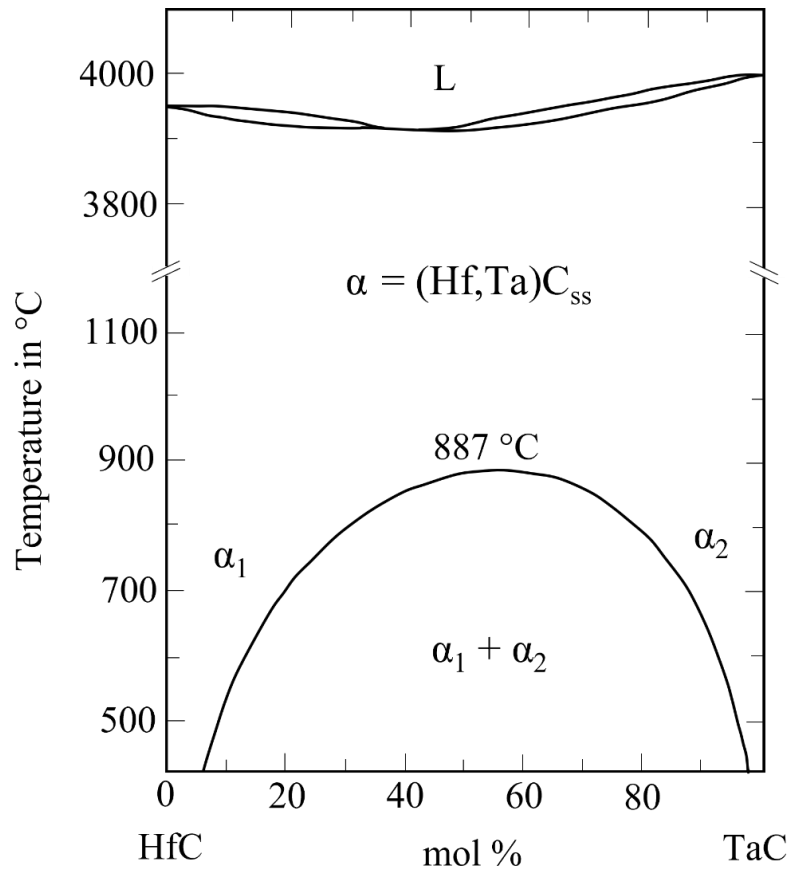


Figure 7 Phase diagram of HfC and TaC showing a complete solid solution at temperatures exceeding 887 °C and a miscibility gap below 887 °C. Figure redrawn after Ref. [106].

Combinations of group IV TMCs and TMNs form solid solutions resulting in carbonitrides, in which the solid-state properties change with the $[C]/([C]+[N])$ ratio, which offers a large field for tailoring carbonitrides [100]. Further, TMCs, TMCs and TMCNs show a very high chemical stability; these compounds are not attacked by dilute acids (except by oxidizing acids and hydrofluoric acid) or alkaline solutions [100]. Their thermal stability is closely related to their free energy of formation, with stability diminishing as the group number increases [100]. Among the group IV transition metal nitride HfN, and along with the carbonitride Hf(C,N) can be melted without decomposition [100]. However, the nitrides and carbonitrides belonging to other groups (e.g. TaN) decompose before reaching their melting points, leading to the release of nitrogen gas [100] (cf. Table 1). Table 1 gives an overview of the properties for technical applications.

Table 1 Selected physical and structural properties at room temperature of stoichiometric group IV and V TMCs and TMNs. Data taken from Ref. [9,43,45,100].

	HfC	TaC	HfN	TaN
Density [g cm ⁻³]	12.3	14.48	13.83	15.9
Lattice parameter [nm]	0.4638	0.4455	0.4516	0.4238
Melting point [°C]	3928	3985	3330	decomposes
CTE [$\times 10^{-6}$ K ⁻¹]	6.1	6.3	8.5	8.0
Th. Conductivity [W/(m*K)]	25.1	22.1	11	-
Hardness [GPa]	20	16	18	32
Young's Modulus [GPa]	420	290	380	-
Electrical resistivity [$\mu\Omega\cdot\text{cm}$]	67	15	27	-

2.3 Polymer-Derived Ceramics (PDCs)

The traditional fabrication method to prepare silicon-based ceramics is the solid state reaction or the sol-gel method which are either high-energy consumption or difficult in processing and shaping [57,107]. Often, this method involves conventional powder processing of green bodies, which requires the presence of sintering additives [54].

Alternatively, synthesis routes utilizing liquid or polymer precursors have been developed. The polymer-to-ceramic route enables the deposition of protective coatings, polymer infiltration and pyrolysis processing of UHTC-matrix composites [12,57,86]. Due to this fabrication method a renewed interest on the potential use of UHTCs as protective coating on metal substrates arose during the last decades [10,12,46–48]. Polymer-derived ceramics (PDCs) are additive-free ceramic materials, which cannot be obtained by using the powder technology [54]. Within the PDC route, ceramic fibres, composites or coatings are obtained directly by the pyrolysis of molecular precursors [54,68]. Starting from inorganic/organometallic polymeric precursors, ceramics with tailored chemical compositions are prepared by thermal treatment processes under a controlled atmosphere [54,57]. The PDC route is a chemical process to develop preceramic polymers into near-net shaped ceramics in a way not known from other techniques [54,108]. In general, precursors-derived ceramics demonstrate improved thermo-mechanical characteristics concerning creep, oxidation, crystallization or phase separation up to 1500 °C and beyond [54]. The most prominent classes of PDCs are binaries like Si_3N_4 , SiC, BN and AlN, the ternary systems of SiCN, SiCO and BCN as well as the quaternary systems of SiCNO, SiBCN, SiAlCN and SiAlCO [57,108]. Furthermore, in recent studies, metal-modified ceramic precursors are used to prepare multinary systems (pentanary and higher-order), which will be introduced later in chapter 2.6 [54,108].

2.4 Preceramic Polymers

The synthesis of preceramic polymers is a key issue in the fabrication of silicon-based ceramics, as it significantly influences the composition and properties of the final ceramics [54,107]. The molecular structure of the preceramic polymer has a significant impact not only on the composition, but also on the number of phases, phase distribution, and microstructure of the resultant ceramic material [54,77]. For a successful fabrication of silicon-based ceramics there are some requirements in order to achieve an effective thermal decomposition process [54,107]. Thus, the organosilicon polymers must have a high molecular weight to avoid volatilization of low-molecular components during the crosslinking process and conversion into a ceramic [10,54,107]. Precursors must be liquid or have an appropriate solubility in common solvents to enable shaping or coating deposition, and they should possess a latent reactivity and therefore an ability to cross-link upon thermal, radiative or chemical treatment [10,54,107]. A general oversimplified formula of the molecular structure of an organosilicon polymer suitable as a precursor for the synthesis of Si-based ceramics is shown in Figure 8.

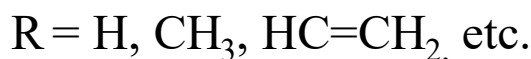
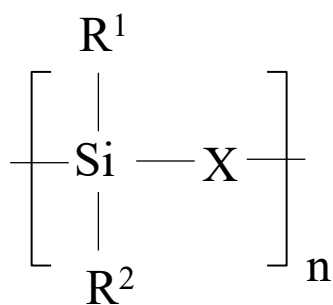


Figure 8 Oversimplified formula of the molecular structure of an organosilicon polymer. R¹ and R² corresponds to the mainly organic side groups, which are connected to the backbone. Redrawn after [54].

In general, there are two parameters to tailor the precursor on the molecular level: first, the group (X) of the polymer backbone and secondly, the substituents R¹ and R² attached to the silicon [54,107]. Figure 9 provides an overview of the different types of organosilicon polymers, which can be used to prepare Si-based ceramics. The polymers used and modified for this work are poly(carbo)silanes with X = CH₂ and polysilazane with X = NH, which are highlighted in green in Figure 9. The side chain groups attached to the silicon atoms and the molecular structure of the organosilicon polymers play important roles in determining the properties of the final ceramics, particularly their decomposition properties [107]. By modifying the functional groups R¹ and R², attached to the silicon, it is possible to alter and regulate the chemical and thermal stability, solubility, electronic properties, optical properties and rheological properties of the polymer [10,54]. Typically, silicon atoms are linked to hydrogen, aliphatic or aromatic organic side groups, such as alkyl (CH₃), vinyl (HC=CH₂), etc., as shown in Figure 8 [10,54,68]. In addition, the presence of organic substituents as side groups R governs the carbon content in the resulting ceramics [54].

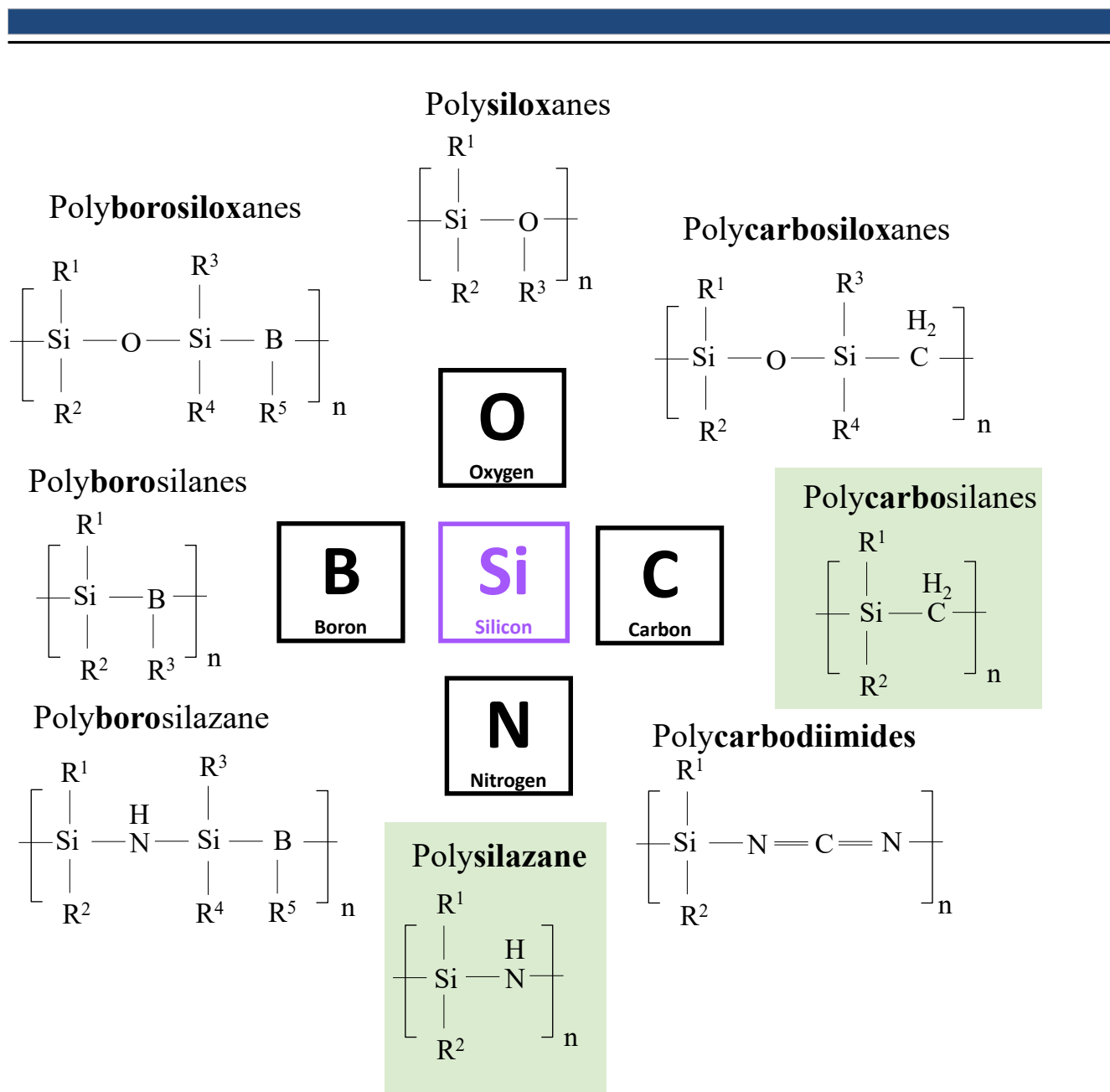


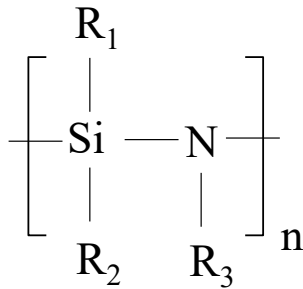
Figure 9 Silicon-based polymers and their fundamental chemical units. Figure redrawn after Ref. [54].

2.4.1 Polysilazane

Polysilazanes (PSZ) are polymers that consist of repeating units of silazane monomers. Silazanes consist of alternating silicon nitrogen backbone [57,109]. In addition, various reactive and/or inert side groups are attached to the basic Si-N-Si backbone. PSZs are classified into inorganic and organic PSZs depending on the type of side groups present.

The general formula of the organopolysilazane (OPSZ) is $[\text{R}^1\text{R}^2\text{Si-NR}^3]_n$ as shown in Figure 10, where R stands for hydrogen or a carbon-containing organic side group, such as CH_3 , $\text{HC}=\text{CH}_2$, etc. [107]. When only hydrogen atoms are present as substituents, the polymer is referred to an inorganic polysilazane, more precisely it is named as perhydropolysilazane (PHPS) with its formula $[\text{H}_2\text{Si-NH}]_n$, as shown in Figure 10.

Organopolysilazane
(OPSZ)



Perhydropolysilazane
(PHPS)

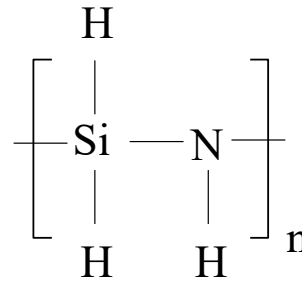
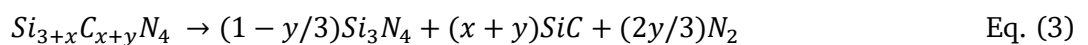
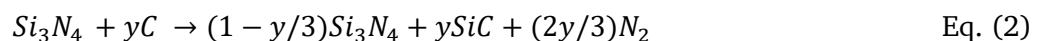


Figure 10 Simplified chemical formulas of organopolysilazanes (OPSZ) (left) and perhydropolysilazane (PHPS) (right). For this work PHPS was used (right formula) (cf. section 4.1, 4.2).

The bond energy between silicon and nitrogen is comparatively lower than that between silicon and oxygen or between silicon and carbon [107]. This lower bond energy facilitates the transformation of the silicon-nitrogen bond into other bonds during specific chemical reactions, promoting the formation of novel compounds under suitable conditions [107]. In general the synthesis of polysilazane can be divided into three categories: i) the polycondensation of halide substituted silanes and amines, ii) the ring-opening polymerization of cyclosilazanes and iii) the copolymerization of cyclosilazanes [107,110]. Typically, polysilazane are synthesized by the reaction of chlorosilanes by means of ammonolysis with ammonia or by aminolysis with amines [54,57,68,107].

In terms of ceramic materials, polyorganosilazane are well known for their utilization as precursor to fabricate Si_3N_4 and SiCN ceramics with tailored molecular structures by the polymer-to-ceramic route [54,57,68,107,111]. Among the polyorganosilazane-based precursors PHPS is in particular utilized for the synthesis of carbon-free silicon oxides or nitrides [109]. Pyrolysis involves a thermal treatment of the polysilazane in an inert atmosphere, such as argon or nitrogen, including temperatures of several hundred degrees Celsius. During this pyrolysis the organic substituents are removed, leaving behind a hydrogen-free silicon carbonitride ceramic [57]. Silazane-derived Si/C/N ceramics were studied in detail regarding the crystallization behaviour at temperatures below 1200 °C, the phase transformation and the thermal stability in different atmospheres [57]. The $\text{Si}_{3+x}\text{C}_{x+y}\text{N}_4$ ceramic remain meta-stable at temperatures <1440 °C and release nitrogen at temperatures of $T > 1440$ °C, when the system reaches the tie line composition $\text{Si}_{3+x}\text{C}_x\text{N}_4$, and crystallizes into Si_3N_4 and SiC , as described in Equation 1-3 [57].



Hence, the thermal stability of polysilane-derived SiCN ceramics can be enhanced by avoiding nitrogen evolution in the high-temperature regime [57]. This can be achieved by a direct formation of $\text{Si}_{3+x}\text{C}_x\text{N}_4$ ceramics via the thermal treatment of the preceramic polysilazane in mixed NH_3/Argon atmospheres

[57]. In this work a commercially available polysilazane was used to synthesize and characterize SiHfCN bulk PDCs and novel Si(Hf_xTa_{1-x})(C)N ceramic powder PDCs (cf. section 4.1, 4.2, chapter 5 and 6).

2.4.2 Polysilane and Polycarbosilane

Polysilanes are a class of materials of polymers possessing a one-dimensional Si backbone and organic substituted side chains. Polysilanes are prepared either by the dehalogenation of chlorosilanes with Na or via the electrochemical polymerization of organohalosilanes [55]. Organosilicon polymers like polysilane or polycarbosilane gained huge interest in chemistry due to their use as functional materials, e.g., as photoresists, semiconductors, hole-transporting materials etc. [68]. The general formula of the polycarbosilane is [R¹R²Si-R³R⁴C]_n as shown in Figure 11. In addition, polycarbosilane are valuable precursors, which transform into SiC, when thermally treated under inert conditions [10,68,112,113]. Prior to the conversion into SiC, polysilane undergo chemical rearrangements, the so-called Kumada rearrangement, transforming the precursors into polycarbosilane by heat treatment [55]. Especially interesting is the potential use of polycarbosilanes as source to produce continuous ceramic fibres [68].

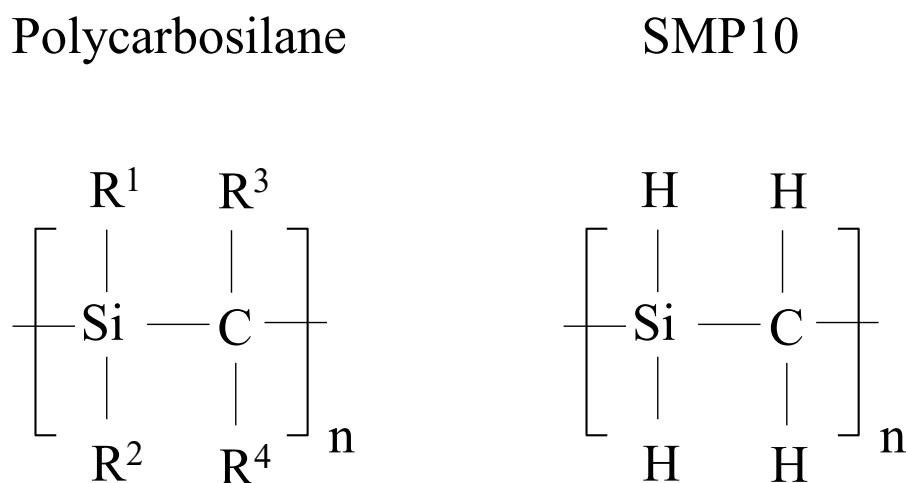


Figure 11 Simplified chemical formula of polycarbosilane. For this work SMP-10 was used (right diagram) (cf. section 4.3, 8.1).

In this work a commercially available polysilane was used to synthesize and characterize Si(Hf_{0.7}Ta_{0.3})C(N,O) ceramic powder PDCs, SiC/(Hf_{0.7}Ta_{0.3})C and Si(B)C/(Hf_{0.75}Ta_{0.25})C bulk PDCs (cf. section 4.3, 8.1).

2.5 The Polymer-Derived Ceramic Route

The transformation of organosilicon-based polymers into preceramic and ceramic Si-based materials involves a series of reactions, resulting in changes of the composition and properties [10,68]. Figure 12 summarizes the PDC processes for different temperatures and gives the related mass changes. As shown in Figure 12 thermal treatment of preceramic polymers usually leads to an amorphous ceramic [9]. Upon further heat treatment the amorphous material subsequently undergoes crystallization reactions and phase separation, ending up in multi-phase polymer-derived ceramic nanocomposites (PDC-NCs) [9]. The PDC processes are the cross-linking, pyrolysis and ceramization [55,68,107].

Soluble polymers and oligomers possess the ability to undergo cross-linking normally performed at temperatures lower than 200 °C, forming highly cross-linked preceramic and ceramic materials due to a

certain latent reactivity [10,54,107]. This transformation is possible due to the possibility of easy volatilization and depolymerization, resulting in low mass yields during the conversion process [10]. In order to reduce volatilization, cross-linking is essential, resulting in an increase of the mass yield during the polymer-to-ceramic-transformation [10]. Cross-linking is carried out by thermal treatment [114–116], moisture curing [117,118], vacuum ultraviolet radiation [119,120], oxidative curing [121,122] or plasma polymerization [123]. These techniques lead to the formation of three-dimensional infusible polymeric networks comprising organic and inorganic components [9,10,55,124]. Thus, mixtures of liquid or soluble polymers, oligomers and low molecular weight polymers are converted into unmeltable and insoluble thermoset materials via condensation and/or via the addition reactions of functional groups, such as Si-H, Si-OH and Si-vinyl groups [10,54,125,126].

Subsequent thermal treatment processes at temperatures greater than 300 °C are carried out after cross-linking, see Figure 12. These so-called pyrolysis step induces an organic-to-inorganic transformation, from a thermoset polymer into an amorphous single-phase ceramic [9,10,60,75,127]. Rearrangements, condensation and radical reactions therefore result in the cleavage of chemical bonds, the formation of new bonds and the decomposition and elimination of organic moieties such as CH₄, C₆H₆, CH₃NH₂, NH₃, H₂ and CO and CO₂ in oxidizing environment [10,54,128]. Most often, furnace pyrolysis is applied utilizing a flow gas to remove the decomposition gases from the system [54,125]. The polymer-to-ceramic conversion of most polymers is completed at temperatures between 1000 °C and 1400 °C [9,10,54]. It is always accompanied by the formation of gaseous species [10]. With this, a mass loss of around 10-30 % occurs, enabling the formation of microporosity [10,68,107,128,129]. The release of gaseous species in an early stage of the ceramization can lead to the formation of open transient pores [10,107]. Some of these transient pores will disappear (by closure or collapse) due to the shrinkage during the ceramization [10,129]. Often, residual porosity remains in the microstructure of the final ceramic [10,107]. Consequently, dense polymer-derived bulk ceramics without pores are difficult to prepare [10,128]. In addition to mass loss, shrinkage due to densification leads to significant stresses during the polymer-to-ceramic conversion [10,68,107]. The accompanying volume shrinkage then causes the formation of cracks, leading to a deterioration of the mechanical properties and in worst cases could also destroy ceramic bulk parts [68,107]. Therefore, the significant volume shrinkages accompanied in the polymer-to-ceramic conversion hinders the fabrication of bulk ceramics [130]. In order to reduce shrinkage and fabricate relatively dense and crack-free bulk ceramics fillers are added to the preceramic polymers [107,131].

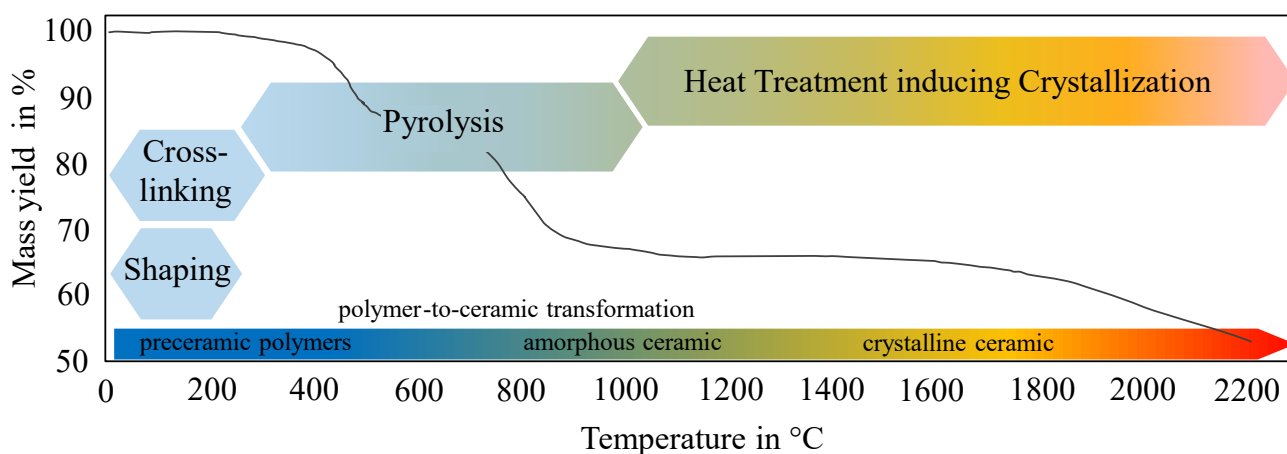


Figure 12 Graphical illustration of the PDC processing, correlating the temperature with the processing phases and mass changes of a polycarbosilane under inert gas atmosphere. Figure adapted from Ref. [10].

2.6 Metal-Modification of Organosilicon Polymers - from Precursors into Ceramics

After the pioneering work of Yajima and co-workers [132], various organosilicon polymers were developed and processed to generate ternary SiCN PDCs [57,108]. Among the quaternary PDC systems, such as in the Si-B-C-N the incorporation of boron in polyorganosilazanes results in an increase in the temperature resistance, suppressing crystallization at about 1800 °C [57,68,133]. Thus, the amorphous Si(B)CN phase encapsulates the formed Si₃N₄ and therefore hinders the thermal decomposition even at higher temperatures [68,133]. Quaternary SiBCN has gained a significant importance due to the high thermal stability up to 2000 °C [108]. Since the beginning of the 1990s, several studies focused on the preparation of metal-modified precursor derived ceramics as shown in the appendix in Table A 1. In general, the synthesis of metal-modified PDCs can be divided into three categories: i) blending of the precursor with metal or metal oxides, ii) synthesis from metallopolymers, iii) chemical modification of precursor polymers using coordination compounds [75]. Further information regarding these approaches can be found elsewhere in detail [75]. In particular modified versions of Si-based precursors containing boron [133,134], aluminium [135–137] as well as several transition metals (such as Ti [138,139], Zr [140,141], Pd [142], Fe [75,143], Hf [66] etc.) and fluorine [144] have been investigated. Through the incorporation of those additional elements several multinary ceramics were developed enabling an increase in high temperature stability, creep and the oxidation resistance [57,68]. The incorporation of additional elements strongly influences (i) the crystallization behaviour, (ii) the thermal stability, (iii) the thermomechanical properties and (iv) the ceramic microstructure of the resulting ceramics [57,68,145]. The focus in this work, lies in the microstructural characterization of PDCs prepared via the PDC route utilizing polymeric precursor modified with Hafnium and Tantalum complexes, as will be explained later in chapter 4.2 and 4.3.

2.7 Ceramic Products Made by Precursor Processing

As shown in Figure 13 ceramic fibres, porous ceramics, polymeric and ceramic coatings, as well as ceramic matrix composites can be produced by precursor processing. They provide a broad variety of specific properties, compositions or microstructures [55]. Monolithic bulk ceramics or powders can be produced from highly cross-linked infusible polymers [55]. For the preparation of ceramic coatings as well as for the infiltration of porous materials, soluble and fusible polymers are utilized [55,57,75]. Volatile precursors are used for the preparation of ceramic thin films coated via the chemical vapor deposition (CVD) technology [55]. PDC powders can be densified into monolithic bulk ceramics via several consolidation methods, such as hot pressing (HP), pressure-less sintering (PS), hot isostatic pressing (HIP), reactive hot-pressing and spark plasma sintering (SPS) also known as field-assisted sintering (FAST) [86,146,147]. Relevant processes for this work are shown in green in Figure 13. Additionally, in light green the process for the preparation of the ceramic coatings is shown.

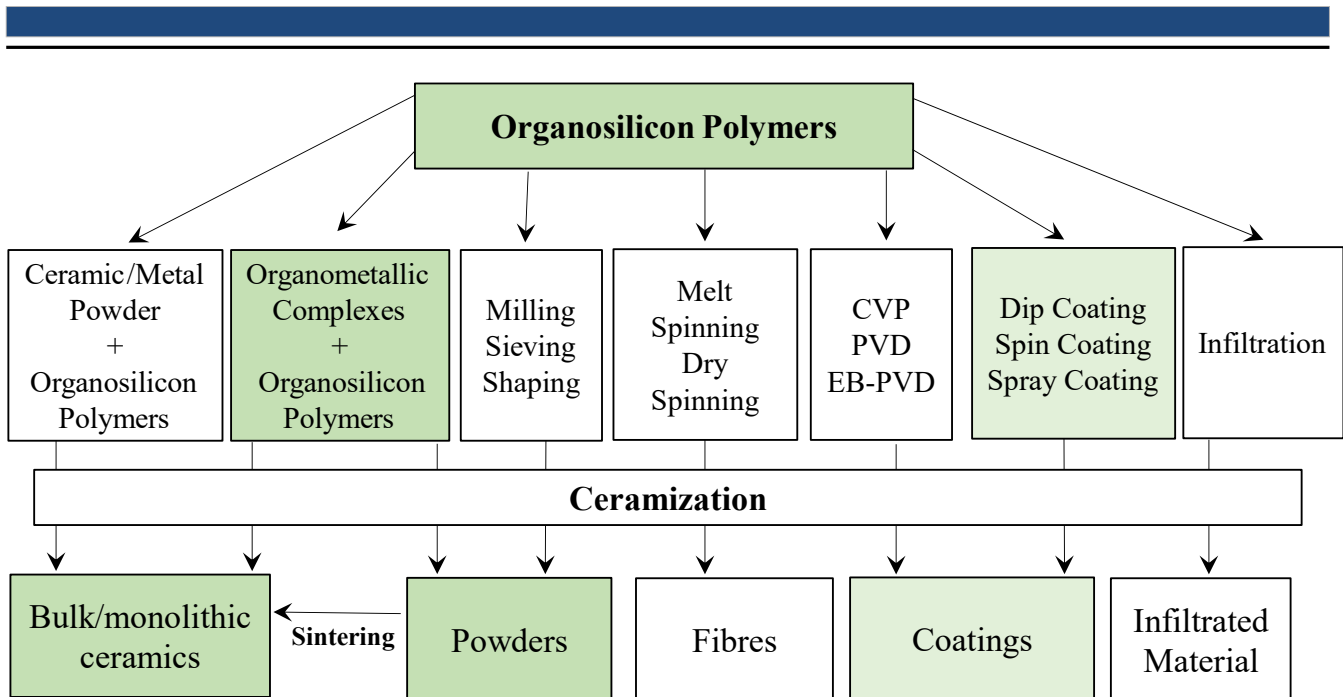


Figure 13 Various preparation methods of PDCs via precursor processing. Figure adapted from Ref. [55].

2.8 Processing of Bulk Ceramics via Sintering

The necessity of sintering in this work lies in the fact that mechanical characteristic values and oxidation tests can only be derived insufficiently on powder material and therefore dense bulk ceramics must be produced in the first step with the aid of sintering. Sintering is a materials processing technique, which is used to prepare density-controlled materials and components from either metal or/and ceramic powders by applying thermal energy [148]. Often, advanced ceramics are consolidated from fine raw particles into bulk ceramic components via liquid or solid state sintering [148–150]. According to Herring, sintering is defined as “morphological changes of particle and pore during heating of fine powder and agglomerate at high temperature below its melting point” [149]. This process is crucial for producing ceramics from compacted powders [149]. Sintering is an irreversible process, driven by the reduction of the total interfacial energy [148,150,151]. In particular, a reduction of the particle surface, grain boundary and pore surface energies based on thermodynamic principles is anticipated [149]. Due to the transfer (diffusion processes) of atoms and ions during the sintering process, particle and pore morphologies undergo changes [149]. During the sintering process grain growth reduces the excess grain boundary energies, resulting in a decrease of the number of particle surfaces and pores, leading to an overall densification of the material [149,150]. Thus, the two basic phenomena of sintering are densification (by transport matter from the grains into the pores) and grain growth or coarsening (by rearrangement of matter between different parts of the pore surfaces without actually leading to a decrease in pore volume and therefore to densification) [148,151]. Following the principle of minimization of the total energy, an atomic mass transfer builds up sinter necks [150]. Sintering of ceramic components include various processing steps and is influenced by several sintering variables, which needs to be considered for the production of those components [148]. The sinterability of a material depends on the material variables as well as the process variables [148]. Material variables influencing the powder compressibility and sinterability relate to the raw materials including the chemical composition, the powder particle size, the powder shape, the particle size distribution, the degree of agglomeration etc. [148]. For compacts, consisting of two kinds of raw powders, the homogeneity of the powder mixture also plays a significant role [148]. Process variables such as temperature, time, atmosphere, pressure, heating and cooling rate also influence the sintering process

[148]. In addition, sintering aims to produce sintered components with reproducible and designed microstructures through the control of various sintering variables [148]. A reproducible microstructure enables for a control in grain size, in sintered density and in the size and distribution of other phases including pores [148]. Details about sintering and fundamental research to understand the phenomena of consolidation by mass transport mechanisms were subsequently made by Frenkel [152], Kuczynski [153,154], Lenel [155], Coble [156,157], Kingery [158,159], German [160] and others [161]. Some aspects are regarded in the following.

2.8.1 Mechanisms of Sintering in the Two-Particle Model

The sintering of powder particles with complex shapes and different sizes is not straightforward [148]. Nevertheless, a simplified approach can be taken by considering spherical particles of uniform dimensions [148]. In this context, the sintering process within powder compacts can be conceptualized as the interaction between two such spherical particles A and B, in which diffusion is the most important sintering mechanism as illustrated in Figure 14. Figure 14 depicts the path of material transport for six different materials transport mechanisms, namely: surface diffusion from the particle surface (1), volume diffusion from the particle surface (2), gas phase transport, evaporation/condensation and gas diffusion (3), grain boundary diffusion from the grain boundary (4), volume diffusion from grain boundary (5) and volume diffusion from dislocations (6). In general, matter is transported from regions with higher chemical potential (the materials source) to regions with lower chemical potential (the materials sink). During sintering the material transport leads to bonding and neck formation. The dominant driving force in sintering is primarily determined upon neck geometry and size [148]. The dominant mechanisms vary depending on particle size, neck radius, temperature and dwell time for a given system [148].

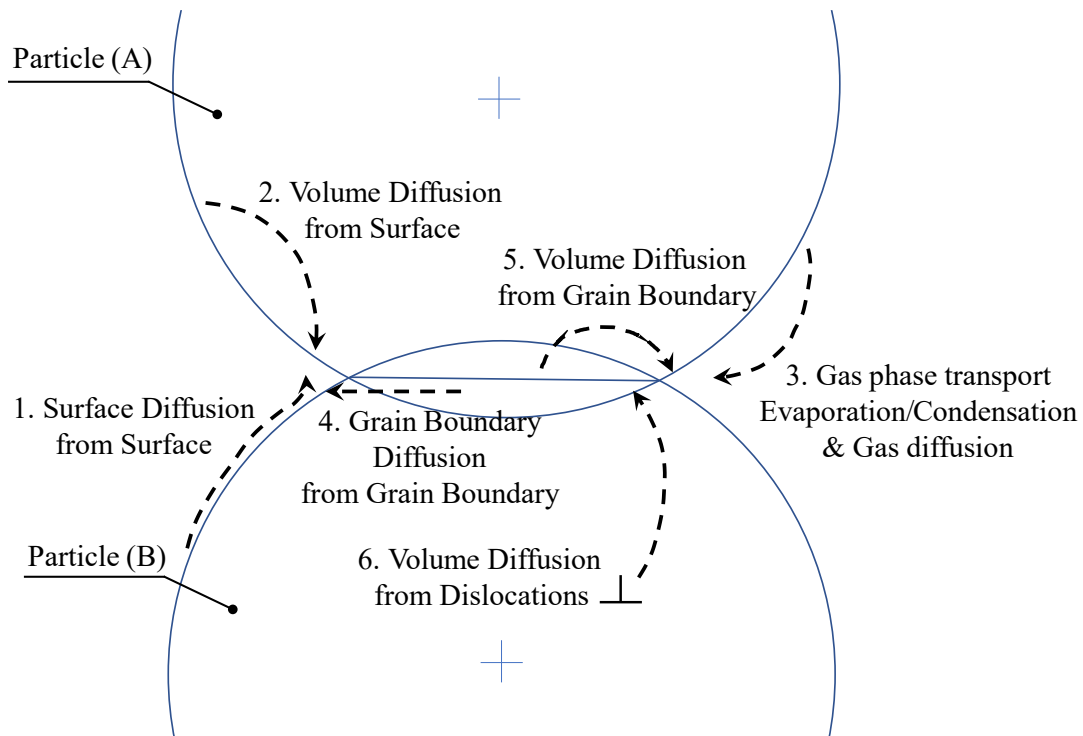


Figure 14 Different material transport mechanisms happening during the sintering of crystalline particles: (1) Surface diffusion from the surface, (2) volume diffusion from the surface, (3) Gas phase transport including evaporation/condensation, (4) grain boundary diffusion from the grain boundary, (5) volume diffusion from the grain boundary, and (6) plastic flow by dislocation motion. Figure adapted from. Ref. [151].

Table 2 lists the six typical material transport mechanisms and their related parameters. Some transport mechanisms, contribute to densification, while others do not. Consequently, these transport mechanisms are categorized into (i) nondensifying and (ii) densifying mechanisms:

(i) Nondensifying mechanisms like surface diffusion (mechanism 1), volume (lattice) diffusion from the surface (2. mechanism) and gas phase transport (mechanism 3) lead to neck coarsening without densification, meaning that the interparticle distance will not reduce through these mechanisms [148]. In general, nondensifying mechanisms have a huge influence on the sinter progress. As these processes reduce the curvature of the neck surface the driving force for sintering is reduced [148].

(ii) The interparticle distance is reduced only by bulk material flow via viscous flow or by material transport from the grain boundary via atom movement [148,157]. Densifying mechanisms are therefore grain boundary diffusion or volume diffusion/viscous flow.

Table 2 Six material transport mechanisms during sintering. Table taken from Ref. [148].

Material transport mechanism	Material source	Material sink	Related parameter
1. Surface Diffusion from Surface	Grain surface	Neck	Surface diffusivity
2. Volume (lattice) Diffusion	Grain surface	Neck	Lattice diffusivity
3. Gas phase transport			
3.1 Evaporation/Condensation	Grain surface	Neck	Vapour pressure difference
3.2 Gas diffusion	Grain surface	Neck	Gas diffusivity
4. Grain boundary diffusion	Grain boundary	Neck	Grain boundary diffusivity
5. Volume (lattice) diffusion	Grain boundary	Neck	Lattice diffusivity
6. Volume diffusion from Dislocations/Viscous flow	Bulk grain	Neck	Viscosity

2.8.2 Sintering Stages

Coble explained solid-state sintering in 1961 with three stages, whereas “a stage of sintering is an interval of geometric change in which the pore shape change is totally defined, or an interval of time during which the pore remains constant in shape while decreasing in size” [157]. Figure 15 shows the three stages of sintering, whereas the relative density in percentage is plotted against the sintering time. As shown in Figure 15 the initial stage contains neck formation, which increases the interparticle contact area. Densification is dominant at the initial stages, increasing the relative density to 50-60 %, while the first grain growth occurs at the end of this stage (cf. Figure 15). The intermediate stage during sintering begins after grain growth. The change in the pore shape leads into a configuration where pores and grain boundaries constitute a matrix. The end of the intermediate stage is indicated by the shrinkage of open pores and the density can reach approx. 90 % (cf. Figure 15).

The final stage is marked by the isolation of closed pores, where pores with an almost spherical shape are formed in the four grain corners because it is energetically favoured. The pores in this stage can shrink to zero continuously under stable conditions. The sintering process is complete, when all isolated pores have been eliminated. When discontinuous growth occurs, the sintering stage is called alternate stage including exaggerated grain growth or secondary recrystallization. [157]

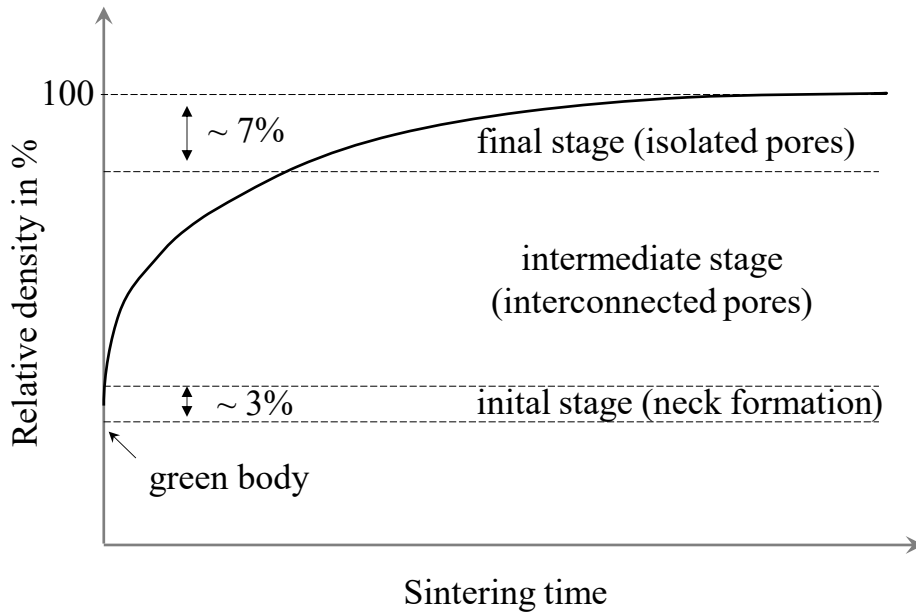


Figure 15 Relative density as a function of the sintering time. Schematic showing the three sintering stages (initial, intermediate and final stage) and the densification curve. Figure adapted from Ref. [148].

Figure 16 depicts a schematic drawing illustrating the three stages during the sintering among three individual powder particles. Before sintering, three individual spherical powder particles are present. In an early sintering stage (stage I) neck formation occurs between the adjacent particles. Subsequently in the intermediate stage (stage II), open pores experience gradual reduction through the establishment of grain boundaries. During the final stage (stage III) the interfacial contact area increases, thereby leading to a notable enhancement in the overall densification process.

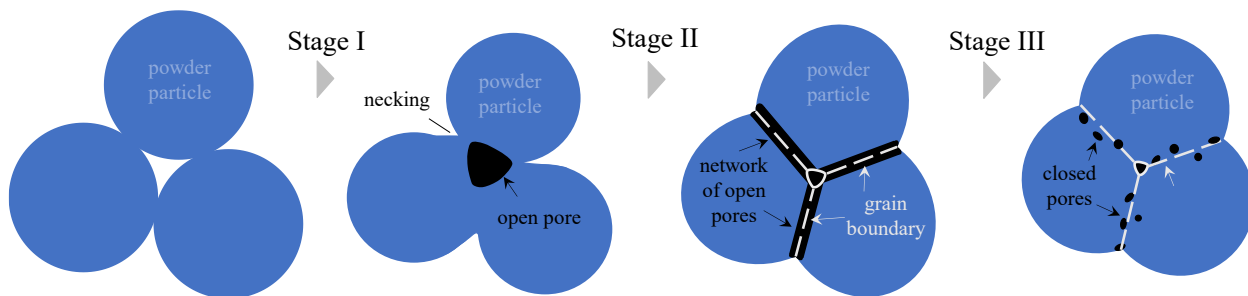


Figure 16 The three stages during sintering, starting with the initial stage, where powder particles are in tangential contact. At the end of the initial stage, the particles begin to coalesce, initiating neck growth. The intermediate stage consists of a metastable continuous pore phase and in the final stage isolated pores are present.

2.9 Field-Assisted Sintering Technique (FAST/SPS)

In general, pure UHTCs and in particular HfC and TaC are difficult to sinter due to their strong covalent bonds, low intrinsic self-diffusion coefficient, low volume and grain boundary diffusion rates [13,45,79,86,162]. Indeed, for a wider utilization of these UHTC materials efficient techniques enabling the fabrication of dense bodies is required [79]. To sinter these materials very high sinter temperatures assisted with pressure and additional electrical current is needed [50,88,163]. The field-assisted

sintering technique (FAST) more commonly known as Spark Plasma sintering (SPS)¹ or pulsed electric current sintering (PECS) is applied [79,86,147,165,166]. An effective approach to address the challenges associated with UHTC sintering involves the optimization of various sinter parameters. This is managed by the employment of high sinter temperatures (up to 2400 °C), utilizing high heating rates (up to 1000 °K min⁻¹), applying moderate pressures (ranging from 40 up to 100 MPa), and the incorporating of appropriate sintering aids such as silica-formers like SiC [53,93,99], Si₃N₄ [94], or silicides (MoSi₂, TaSi₂) [45,52,95,167]. FAST is an ultra-fast consolidation technique, allowing for the sintering of countless microscaled powder particles to become a macroscaled nearly fully dense bulk material with a fine-grained micro- and nanostructure [146,164,165,167,168]. The FAST process belongs to the group of “electric current activated/assisted sintering techniques” (ECAS), enabling an enhanced densification due to the superposition of external mechanical pressure and direct heating by an electrical field [147,169]. With respect to conventional Hot Pressing (HP), FAST is considered to be highly beneficial due to the application of the pulsed current [79,166]. HP requires relatively long sintering times in the order of several hours, where in contrast the powder samples during FAST are consolidated within a few minutes [166]. During FAST a pulsed direct current is passed through a conducting pressure die and through the containing powder (if the powders are electrically conductive) enabling a significant increase in the heating rates through the Joule effect [79,168,170]. Thus, the powder sample is heated from the inside (self-heating) and the outside [170]. Still, lattice diffusion and grain boundary diffusion are the dominating sintering processes [167,171].

In general, the FAST is carried out in four main steps: the first one is to remove gases and create a vacuum, the second stage includes the application of pressure followed by the third stage, which is the resistance heating, finally within the fourth step the cooling is addressed [170]. Figure 17 shows a schematic setup of a standard FAST apparatus containing a mechanical loading system, which acts at the same time as high-power electrical circuit [168]. The tooling materials possess high electrical conductivity, allowing for the application of low voltages (typically below 10 V) to generate high currents (usually ranging from 1 to 10 kA) [166,168]. This results in efficient Joule heating, even when sintering non-conductive powders, as the heat is rapidly and effectively transferred to the sample [168]. The system offers defining pulse and pause durations or use more specialized pulse patterns with typical pulse durations lasting a few milliseconds [165,166,168]. The compact geometry of the die and punches enables sintering cycles with heating rates as high as 1000 °C min⁻¹, reducing the process duration and energy costs [147,165,169]. Standard cooling rates of up to 150 °C min⁻¹ are achievable, and active cooling under gas flow allows for quenching rates of 400 °C min⁻¹ [168]. Simultaneously, applying uniaxial mechanical pressure (typically between 50 and 250 kN) enhances densification [168]. The process can be carried out under vacuum or protective gas [168,169]. The samples studied in this thesis were sintered under vacuum. Temperature control during the process is typically achieved through temperature measurements using thermocouples or axial/radial pyrometers [168,169]. Alternative methods such as power-, current-, or displacement control can also be employed [168]. Using standard graphite tools as heating element, shaping matrix and mechanical loading transmitting medium, the maximum achievable temperature is up to 2400 °C in nonoxidizing atmospheres and maximum stresses of up to 100 MPa [168,169]. When higher pressures are required, alternative materials such as refractory metals or ceramics should be chosen [169].

¹ The name Spark Plasma sintering originates from the idea of the high-energy pulse direct current inducing a spark discharge between the particles [164]. However, the experimental evidence for a spark discharge and/or plasma are still lacking and the exact nature of the SPS mechanisms is still under debate [164]. Instead of the in literature most commonly used abbreviation SPS the abbreviation FAST is used in this work.

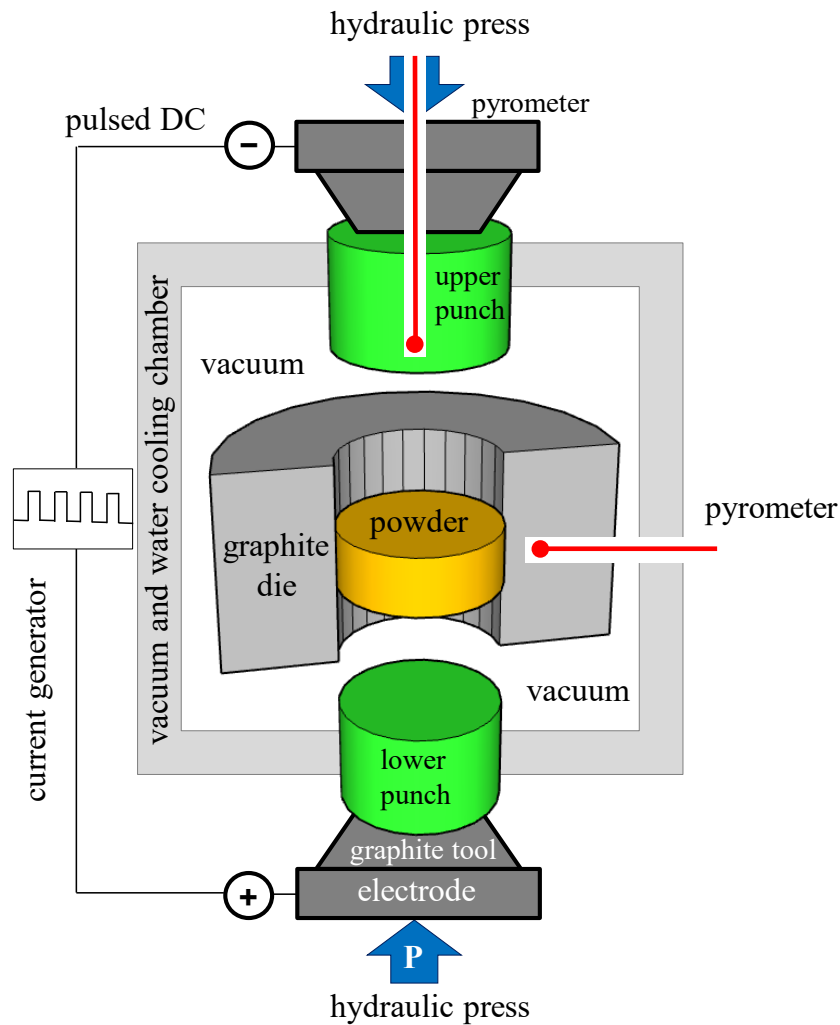


Figure 17 Schematic of a FAST apparatus. Figure adapted from Refs. [165,166,172].

The main goal of the consolidation of oxygen-free organosilicon precursors modified with transition metal complexes via FAST in this project is to prepare dense bulk ceramics with a homogenous micro-/ nanostructure, enabling for a general characterization of several properties, such as the determination of thermal and mechanical properties (this is not possible with ceramic powders). Furthermore the impact of the thermal and electrical fields on the evolving microstructure upon FAST is complex and the mechanisms behind these processes still not well understood [147,164,167,173]. In particular the microstructural evolution of PDCs upon FAST is not described in literature. Despite practical knowledge of the densification published by various authors [147,165,169,170,174], only a few publications give insights on the fundamental transport mechanisms of densification or the kinetics of the sintering processes of UHTCs [46,52,80,88,96–99], leaving plenty room for basic research on microstructural evolution of PDCs prepared via FAST [12,175].

2.10 Details on Preliminary Investigations

The following chapter deals with preliminary investigations of Prof. R. Riedel and Prof. H.-J. Kleebe and their teams in the period of 2010 to 2018, closely related to the topic examined here. E. Ionescu focused on the preparation of novel Hf-modified SiOC PDCs. In addition, Prof. H.-J. Kleebe and Dr. K. Nonnenmacher investigated the carbothermal decomposition, and the carbon mobility of the prepared

SiOC/HfO₂, respectively. The studies of Dr. J. Yuan and Dr. Q. Wen on the synthesis of novel SiHf(B)CN and Si(M)C(N), (with M = Hf and Ta) are summarized briefly.

2.10.1 Microstructure, Carbon Mobility and Thermal Decomposition Coarsening in SiOC/HfO₂

In 2010, Ionescu and co-workers prepared novel silicon oxycarbide/hafnia SiOC/HfO₂ nanocomposites via the PDC route [176]. Commercially available polymethylsilsesquioxane (PMS) was modified with hafnium tetra(n-butoxide) in order to prepare the precursors for the synthesis of the SiOC/HfO₂ PDCs [176]. The prepared mixture was cross-linked via warmpressing at 180 °C for 30 mins and subsequently pyrolyzed at 800 °C, 1100 °C, 1200 °C and 1300 °C in argon atmosphere for 3 hours [176]. The microstructure of the prepared bulk SiHfOC ceramic was assessed by means of TEM. Samples pyrolyzed at 1100 °C showed the presence of poorly crystallized spherical particles of HfO₂, embedded in an amorphous Si-O-C matrix [176]. Upon annealing at 1300 °C, well-crystallized spherical particles are clearly observed [176]. The authors stated that the ceramics obtained via pyrolysis are considered as amorphous single-phase SiOCHf materials up to temperatures around 800 °C [176]. Phase separation of HfO₂ begins at temperatures above 800 °C. Moreover, the formation of a-HfO₂/a-SiOC ceramic were observed via TEM. At higher temperatures, HfO₂ precipitates undergo a phase transition from a-HfO₂ into t-HfO₂ and the silicon oxycarbide matrix phase separates into an amorphous silica and amorphous SiC [176].

At this time, several studies highlighted that the solid-state microstructure and phase composition of the polymeric precursors significantly influence the high-temperature properties of PDCs [63,77,177–179]. Investigations regarding SiHfCO-based PDCs revealed microstructural variations in surface-near regions (100–200 nm) and internal surfaces (local cracks) as compared to the bulk when annealed at higher temperatures (<1300 °C) [180,181]. These microstructural variations were attributed to local changes in the chemical composition, which in turn influenced diffusional processes resulting in pronounced growth of HfO₂ precipitates near the sample surface [180,181]. In particular the local carbon content in close proximity to internal surfaces were assessed via TEM in combination with EDS analysis and seems to influence the hafnium diffusion in SiOC/HfO₂ nanocomposites [180].

2.10.2 Modification of Polysilazane with Early Transition Metals Hf and Ta

Extensive research has been directed towards developing oxidation-resistant Si-based matrix phases with dispersed nano-sized secondary phases containing Hf, Ta, and their solid solutions [13,41,45,47,58,61,64–66,182–184]. In particular (Hf_{0.2}Ta_{0.8})C is a promising compound possessing the highest ever known melting point among all materials [40,41] (cf. chapter 1.1). Zhou et al. successfully incorporated Hf into a Si-N matrix at the molecular level to obtain a novel ternary SiHfN nanocomposite ceramic [61]. By reacting a commercially available perhydropolysilazane (PHPS) with different amounts of tetrakis(dimethylamido)hafnium(IV) (TDMAH) a novel metal-modified polymer-derived SiHfN ceramic was prepared via the single-source precursor route [61]. Hf-based UHTC-NCs with small additions of boron were developed by J. Yuan et al. [66]. The authors prepared the SiHfCN UHTC-NC from a commercially available polysilazane (cf. section 2.4.1) (HTT 1800) by reaction with tetrakis(diethylamido)hafnium [65]. For the preparation of the B-containing SiHfBCN UHTC-NC the mentioned precursors were additionally modified with a borane dimethyl sulfide complex [65,66]. In addition, the authors used FAST (cf. chapter 2.9) to obtain consolidated polymer-derived UHTC bulk materials with good mechanical strength, hardness, thermal stability and short-term oxidation resistance [65]. The oxidation behaviour of these novel SiHf(B)CN materials at temperatures from 1200 °C –

1400 °C were studied and yielded promising results [62,66]. In 2018, Q. Wen et al. reported on the incorporation of Hf and Ta into a Si-based matrix phase to prepare a novel polymer-derived SiHfTaCN UHTC-NC [41]. SiC/Hf_yTa_{1-y}CN/C ceramics with y = 0.2 and y = 0.7 were synthesized upon reaction of a commercially available polysilane (cf. section 2.4.2) (SMP-10) with Hafnium- and Tantalum complexes (tetrakis(diethylamino)hafnium(IV), shortly known as TDMAH as Hf source and pentakis(dimethylamino)tantalum(V), shortly known as PDMAT for Ta) [41]. In this study, the pyrolyzed powders were also consolidated via FAST to obtain dense bulk ceramics. Moreover, it was shown, that the synthesis of a metal-modified precursor containing solid solution metal carbide (Hf_xTa_{1-x})C remarkably enhanced the short-term oxidation resistance [47]. This is achieved by a surface passivation prior to oxidation, generating the formation of a protective silica surface layer [47]. The studies described above show that TM-modified PDCs with their good mechanical strengths, hardness, thermal stability and good short-time oxidation could be used as potential TBC coatings. In continuation of the preliminary investigations, this work continues by investigating further novel PDCs and their microstructural changes upon different thermal treatments.

3 Applied Methods

Microscopic methods to characterize the microstructure are based on the interaction of either electromagnetic waves such as light or X-rays or corpuscular beams such as electrons or neutrons [185,186]. The application of microscopes in ceramic studies has been reported in detail in several books: e.g., by Insley and Frechette [187], Freund [188], Hornbogen and Skrotzki [189], Telle and Petzow [190] etc. In the following chapters, an introduction to each method used for materials characterization in this work is given, followed by a more detailed description of the used equipment.

3.1 Aspects of Optical Light Microscopy (OLM)

Light microscopes are the most common microscopes in the world because they are relatively cheap, robust and typically non-invasive [191]. The resolving power in optical light microscopy (OLM) is determined by the wavelength λ of visible light ranging from 400 nm (blue) to 700 nm (red) and is down to 0.3 - 0.5 μm [185,186,192]. For ceramic materials that are not too fine-grained, transmitted light microscopy is advantageous [186]. Observation in polarized light provides information on microstructural stresses, orientations and textures, grain boundary phases, and also some crystal defects (grain boundaries, twin boundaries) can be detected [185,186,190,193]. In order to utilize transmitted light microscopy, the incident light should not be weakened too much as it passes through the sample [185]. In metals and semiconductors, the interaction with the free electrons causes the light beams to have only a very small penetration depth [185]. Therefore, for metals, semiconductors and also ceramics, one has to rely on reflected light microscopy. In principle, reflected light microscopy of ground cross-sections is not very favourable for ceramics, since the reflectivity of silicates and oxides is only about 5 - 10 % and the differences between the individual phases and their anisotropy effects are not particularly pronounced [186]. However, better contrasts can be achieved by post-treatment of the ground surface, so that reflected light microscopy is now a standard method for imaging technical ceramics [186]. One of the post-treatment processes to increase the contrast is chemical or electrolytical etching [186,192]. Etching results in different reflection conditions for the individual microstructural components or even a relief structure that leads to shadow formation [192]. The etching processes are divided into grain boundary etching and grain surface etching [192]. This method is further improved by subsequent vapor deposition with a very thin layer of metal, usually gold or platinum [186]. A comprehensive description of the effects and etching recipes was published by Petzow [194].

In this work, a polarization microscope AX10 Lab A1 (Carl Zeiss Microscopy GmbH, Germany) equipped with a AxioCam ERc 5s camera (also from Carl Zeiss Microscopy GmbH) was used for checking the quality of individual steps during SEM and TEM sample/specimen preparation. The polarization microscope was in particular used to constantly check whether perforation occurred due to the Ar^+ -ion milling. The optical Microscope AXIO Zoom V16 Zeiss with the ZEISS ZEN core v3.2 software was obtained for optical light micrographs. Reflective light microscopy was used in terms of correlative light and electron microscopy (CLEM), when comparing the microstructure of bulk ceramics.

3.2 Scanning Electron Microscopy (SEM) for Microstructure Analysis

Scanning electron microscopy (SEM) is another microscopic method, in which magnified images are generated via an electron beam and electromagnetic lenses rather than by light and optic lenses [185]. Using electrons rather than light give a major advantage, since electrons have negative charge they interact very strongly with atoms [191]. Thus, the interaction of electrons with the sample leads to a wide range of phenomena, generating emission of several signals from the sample [191]. Therefore, SEM images contain microscopic-scale information on the size, shape composition, crystallography and other physical and chemical properties of the studied material [195].

Figure 18 shows schematically a typical setup of a SEM. In principle, a finely focused electron beam is scanned across the sample in a grid pattern by deflection coils [185,191,192,195]. The energy of the electron beam, E_0 , is typically in the range from $E_0 = 0.1$ up to 30 keV [191,195]. Electrons are emitted from an electron gun (i.e., a tungsten filament, LaB₆ cathode or a field-emission gun (FEG)), accelerated to high energy and modified by apertures, magnetic and electrostatic lenses and electromagnetic coils into an reduced beam diameter [186,195]. The beam is then focused and scanned in a x-y raster pattern on the sample surface [195]. The interaction of the beam with the material itself generates two outgoing electron signals: secondary electrons (SE) and backscattered electrons (BSE) [185,195].

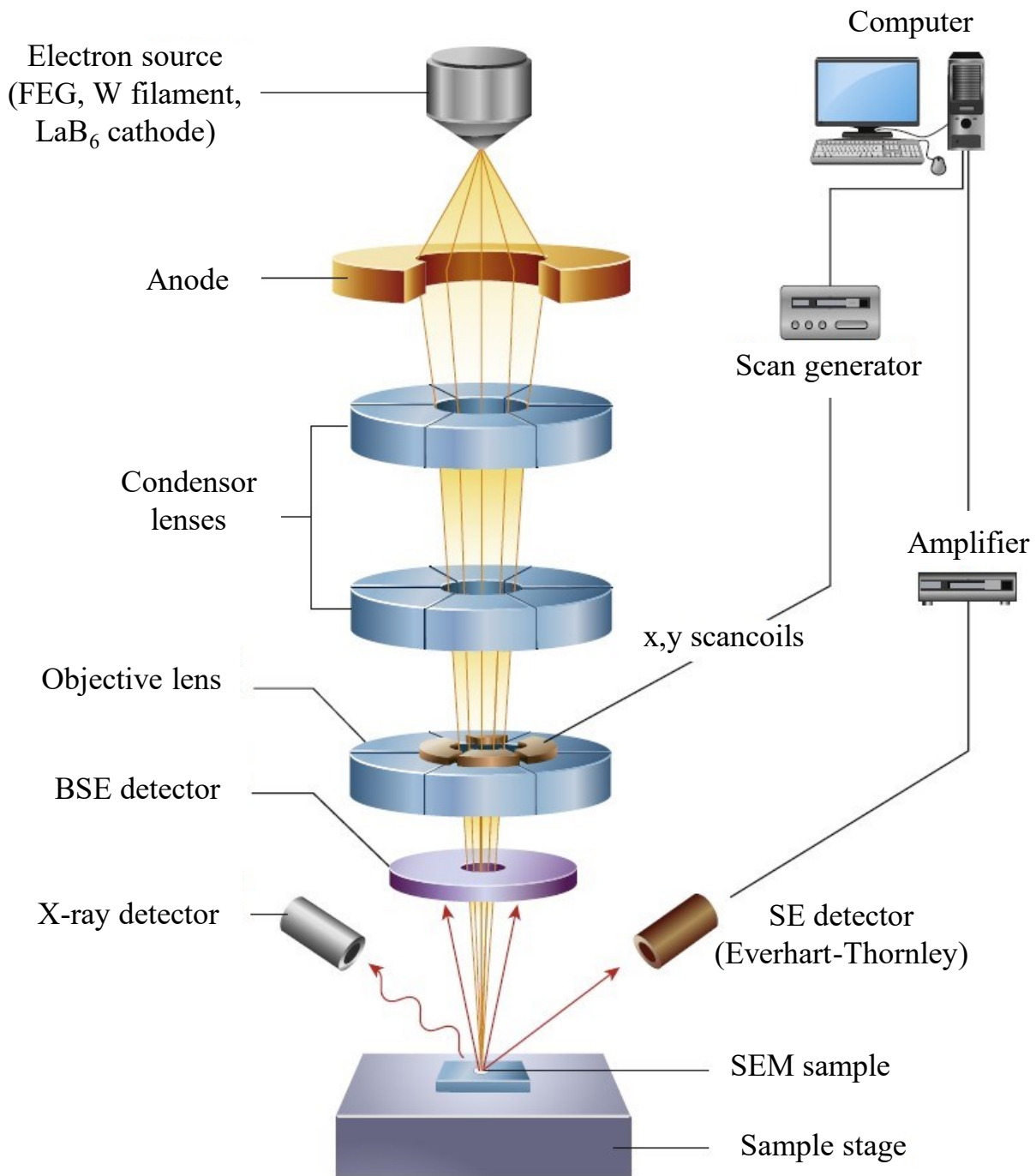


Figure 18 Schematic illustration of the set-up of a typical SEM microscope, encompassing the electron gun, electromagnetic lenses to focus the electrons into an electron beam, a vacuum chamber including the specimen stage and several different electron detectors to collect the emitted signals from the sample. Figure adapted from Ref. [191].

Secondary electrons escape the specimen surface after the primary beam electrons have ejected them from atoms in the sample [191,195]. The secondary electrons experience low kinetic energy transfer and subsequently exit the sample surface with low kinetic energies (in the range from 0 up to 50 eV), with most electrons having energies below 5 eV [195]. When these low-energetic secondary electrons leave the sample, they are collected by electron detectors, usually Everhart-Thornley “secondary electron” detectors are used [195]. Secondary electrons create a topographical contrast of the sample surface [185,192]. Combined with shadowing caused by the oblique incidence of the electron beam, SEM imaging by SE produces a plastic image of the surface [186,192].

Backscattered electrons emerge from the specimen with a large fraction of their incident energy remaining after experiencing scattering and deflection by the electric fields of the atoms in the sample [195]. The intensity of the backscattered electrons increases with the atomic number of the scattering atoms, because the repulsive power of atomic nuclei is proportional to their positive charge, determined by the number of protons (element Z-number) [185,191]. In this way, heavier elements (high Z) generate more BSEs than light elements (low Z) so that different phases can be distinguished by their brightness [185,191]. In particular in polished cross-sections, the backscattered electrons result in an atomic number contrast (Z contrast) due to the lack of topographical influences, which in the case of multiphase materials lead to material-specific greyscales [186]. Thus, regions with higher average Z numbers will emit more BSEs and therefore be brighter, than regions of lower average Z numbers [191]. This indeed can be used for a rapid qualitative phase identification, when two or more phases have a sufficiently different average Z-numbers to cause chemical contrast modulation in the BSE image, for example in the here studied multiphase PDCs [186,191]. Figure 19 shows the dependence of the backscattered electron intensity (fluorescence yield ω or “backscattering coefficient η ”) as function of the atomic number (Z) [186,196,197]. At low atomic number the fluorescence yield decreases rapidly and X-rays from elements below B are not detectable [198].

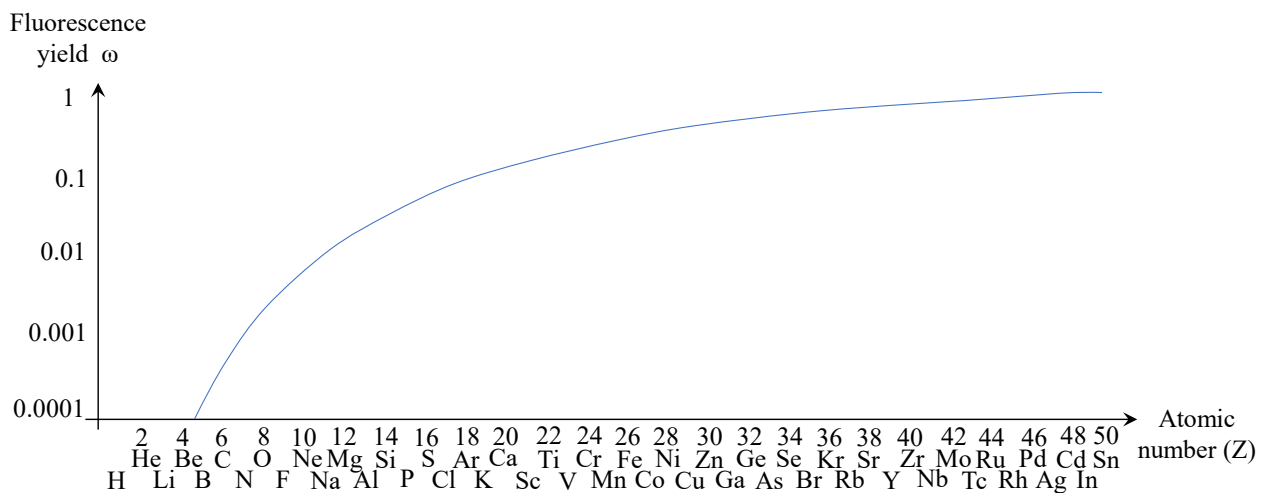


Figure 19 Fluorescence yield ω (also named backscattering coefficient η) for the K-shell X-rays as function of the atomic number (Z). Figure adapted from Refs. [186,196,198].

SE and BSE electrons enter a detector [186]. Within the detector, each electron triggers a light signal in a scintillator crystal, which is then amplified in a photomultiplier and converted into an electrical signal [186,195]. The resolving power in SEM is about ten times greater than that of the optical microscope because of shorter wavelengths of the accelerated electrons [186]. The resolution is better than <10 nm in topographic (SE) mode and 100 nm in compositional (BSE) mode for accelerating voltages of

10 - 50 keV [185,186]. The depth of focus allows the investigation of surface morphologies, i.e. especially fracture structures, sinter structures, etch pits and powder particles [185,192]. The SEM column and chamber operates under vacuum conditions ($< 10^{-4}$ Pa) to prevent scattering events with atmospheric molecules [191]. Different sizes of SEM samples can be installed in the sample chamber, depending on the sample stage utilized in the SEM. In addition to SEM it is also a spectroscopy tool. Further information regarding electron-matter information is given later in chapter 3.5. For further in-detail information regarding the techniques of SEM, please refer to the numerous textbooks and scientific papers available [191,195,196,199,200].

The Scanning electron microscopy (SEM) analyses were conducted using a JSM-76000F instrument (JEOL Ltd., Tokyo, Japan), equipped with an X-Max energy-dispersive X-ray spectroscope (EDS) from Oxford Instruments (Abingdon, United Kingdom) (cf. Figure 20 a)). BSE and SE images were captured with an acceleration voltage of 15 kV. EDS point measurements were obtained at the same acceleration voltage and a working distance (WD) of 8 mm. The beam size diameter was maintained below 2 nm. Each EDS point measurement was acquired for a duration of 30 seconds, with an estimated relative error of approximately 5 %. SEM analyses were used to gain surface structure information via secondary electron imaging (SEM-SE) and chemical information via backscatter electron imaging (SEM-BSE). SEM analysis of the as-pyrolyzed ceramic powder samples were conducted on ground powder particles, placed on an adhesive carbon pad (Plano GmbH, Wetzlar, Germany), coated with a thin carbon layer to avoid sample charging and mounted on an aluminium stub. Plan-parallel and polished cross-sections of sintered ceramic bulk samples were also mounted on the adhesive carbon pad, as shown in Figure 20 b), c).

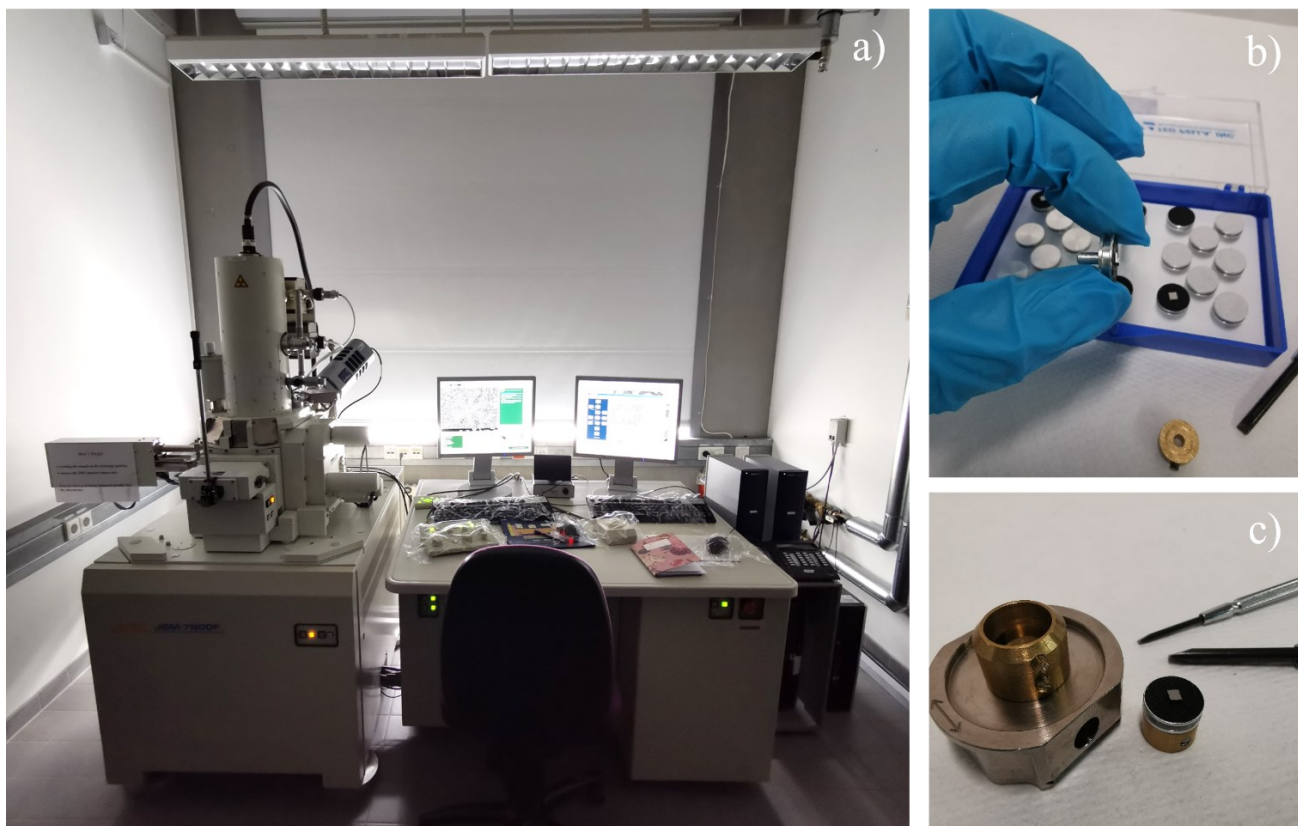


Figure 20 a) High resolution SEM microscope JSM-76000F from JEOL Ltd., Tokyo, Japan situated at the Materials Science Institute of the Technical University of Darmstadt, b) Sample box and aluminium Stub with sticky carbon pad and mounted cross-sectioned bulk ceramic sample for inspection under the SEM. c) The base part of the 12.5 mm sample holder (left) and the adapter part with a mounted aluminium stub ready to insert into the base part of sample holder (right).

3.2.1 Aspects of Quantitative Image Analysis for Pore Detection

The evaluation of documented microstructural images regarding porosity usually is very time-consuming [186]. Various methods have been employed for quantitative porosity measurements, enabling an important and integral part of microstructural characterization of sintered bulk ceramics. In particular, semi-automated quantitative image analysis has been a reliable, straightforward, versatile and inexpensive method for characterizing the porosity in metals as well as in ceramics [201–203]. The image taken from the SEM contains information in form of pixels with a specific grey value, which can be used for differentiation or thresholding. A prerequisite for this is a high-quality sample preparation (final polishing and less scratches) enabling the presence of clearly recognizable, high-contrast containing images. Here, however it must be noted that when grinding, pores get smeared with abrasion and thus appear smaller [204]. Another misinterpretation can occur due to preparation-related grain breakouts or so-called chips [186].

The determination of the closed porosity in dense $\text{SiC}/(\text{Hf}_x\text{Ta}_{1-x})\text{C}$ (cf, section 7.3.2) and $\text{SiBC}/(\text{Hf}_x\text{Ta}_{1-x})\text{C}$ (chapter 8.4) relies on semiquantitative image analysis of SEM-BSE images obtained from polished surfaces. These images were subjected to quantitative image analysis using the software package of ImageJ developed by the National Institute of Health, USA [205]. SEM-BSE images were chosen instead of SEM-SE images due to the charging effects of pores in SE imaging. The closed porosity was evaluated by calculating the percentage of the total surface area occupied by the pores (in area %) in the SEM-BSE images at two different magnifications. The average two-dimensional (2D) porosity was employed using the thresholding tool. A semi-automated image analysis requires an image segmentation step based on their pixel intensities [202]. Thus, the SEM-BSE images were converted into an 8-bit format (grayscale image), representing 256 different grayscale intensities. Each image has grayscale intensities ranging from 0 (black) to 255 (white). Due to the sensitivity of backscattered electrons to the atomic number of the materials pores in SEM-BSE images appear as grayscale intensity with low values. Pores are identified (minimum value in histogram) and quantified by the strong image contrast between the pores and the other constituting phases within the microstructure of the bulk ceramic [186,203]. An alternative method used in the RTG to determine the density and (open) porosity of sintered bulk ceramics is the Archimedes principle.

3.2.2 Focused Ion Beam Scanning Electron Microscopy (FIB-SEM): TEM Sample Preparation

The focused ion beam and the combined focused ion beam with the scanning electron microscope system (FIB-SEM) are specialized tools for various applications. The FIB-SEM technique was mainly developed during the 1970s and 1980s, while during the 1990s a widespread increase in FIB-SEMs and their applications occurred [206,207]. A FIB-SEM is essentially also a SEM with a built-in ion mill [198]. These dual-beam systems are characterized by their high resolution and integration of a Ga^+ -ion beam and electron beam microscopy functionalities within a single device. The ion column is positioned at an angle of 52° relative to the electron column. Consequently, the system allows for several processes, such as observation, imaging, and real-time analysis of nano-scale mask-less modifications induced by the ion beam, such as ion implantation, localized etching, ablation, and other related processes, using electron and ion beam microscopy [206,207].

The operation principle of a FIB-SEM is based on the following physical concepts. As energetic ions collide with the surface of a solid material, they lose energy to the electrons of the solid and to its own atoms [206,208]. There are three mainly important physical effects when it comes to the interaction of incident ions with the sample substrate:

-
- i) the sputtering of neutral and ionized atoms facilitates substrate milling,
 - ii) the release of electrons enables imaging, but could also lead to sample charging,
 - iii) the displacement of atoms within the solid results in induced damage as well as the emission of phonons leads to heating [206,208].

A very important application of the FIB micromachining is the preparation of TEM specimens [208]. With this method almost all kinds of materials can be milled locally, obtaining a site-specific and uniform TEM specimen [208,209]. Milling is the removal of sample material, which is achieved by using a high ion current beam [208]. Milling is achieved by scanning the Ga⁺ beam over the surface. In this way arbitrary shapes can be milled, but redeposition of milled material also needs to be considered [208]. Before the milling starts, most often a metal, either platinum (Pt) or tungsten (W) is deposited to protect the underlying material from the following preparation steps. The principle of the deposition is the CVD technique [208]. For material removal both sides of the desired section is milled and monitored in real time [208]. FIB preparation will also polish the sample to make it electron transparent [208]. In general, there are two commonly employed approaches for the FIB sample preparation: the lift out technique and the H-bar technique [207,208].

However, a third technique known as the microsampling technique emerged during the 1990s and gained popularity since then [207]. This technique is a hybrid approach combining the advantageous aspects of both, the lift-out and the H-bar technique [207].

The FIB-SEM method offers various advantages over other sample preparation techniques:

- 1) Targeted preparation with submicron Precision (50 nm) allowing the analysis of defects or interfaces with a high accuracy [207].
- 2) Minimal Preferential Milling enabling the preparation of lamellae from various materials including polymers on glass, silicon or patterned photoresists [207]. Additionally, it allows the creation of lamellae with nearly parallel sidewalls for accurate chemical analysis [207].
- 3) Small Volume Specimen Preparation: specimens as small as 20 x 15 μm² and 20 x 10 μm², respectively [207].
- 4) Rapid Cross-section Preparation in less than 30 minutes and TEM cross-sections in approx. 2 hours [207].
- 5) Handling Irregular Sample geometries without the need for embedding or mechanical polishing [207]. This capability has been utilized in the analysis of nanostructured films [210], heterogeneous catalysts [211], powders [212,213], and even fragments of meteorite samples [207].

In this work, the Strata 400 STEM Dual beam FIB-SEM system (FEI Company, Hillsboro, Oregon, US) equipped with a FEG Schottky gun, a Pt, C and W gas inlet system (GIS), a liquid Ga⁺ ion source and an omniprobe 200 micromanipulator with independent x, y, z motion was used. The instrument setup used for the preparation of the FIB lamella is shown in Figure 21 and is located at the Institute for Nanotechnology (INT) at the Karlsruhe Institute for Technology (KIT), Karlsruhe.

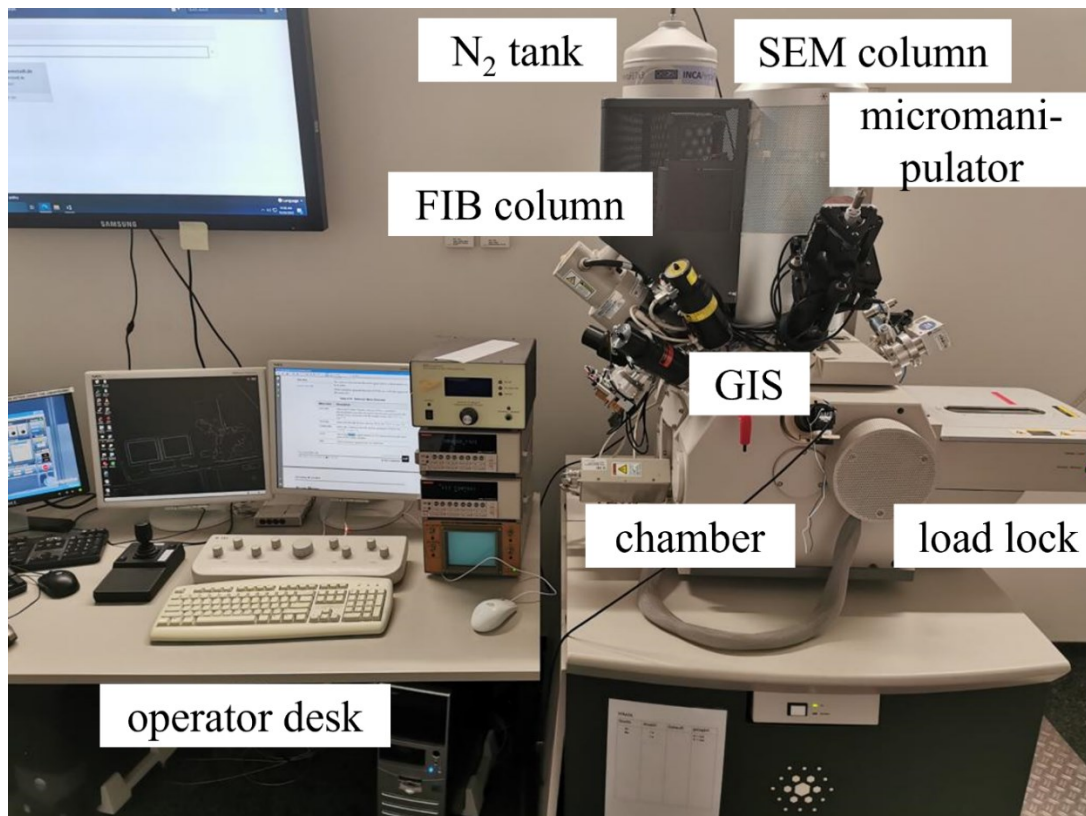


Figure 21 The dual beam FEI Strata 400 STEM system with a FEG (Schottky) at the Institute of Nanotechnology (INT) at the Karlsruhe Institute of Technology (KIT), Germany.

3.3 Electron Microprobe Analysis (EPMA) for Element Maps

The electron microprobe analysis is a technique used for chemical analysis of microstructural areas of solid samples by the excitation of X-rays through a focused electron beam [185,196]. Wavelength-dispersive X-ray spectroscopy (WDS) is based on the Bragg diffraction at an analyzer crystal of defined lattice constant [185,204]. The X-ray spectrum exhibits distinct lines indicating the constituent elements [196]. Consequently, a facile qualitative analysis can be conducted by identifying these lines based on their corresponding wavelengths [196]. By comparing their intensities with those emitted from standard samples (either pure elements or compounds of known compositions), it becomes viable to quantitatively ascertain the element concentrations [196]. Accuracy approaches approximately $\pm 1\%$ of relative deviation, while the detection limit can reach magnitudes on the order of parts per million in terms of weight fraction [196]. Typically, the spatial resolution is about 1 micron due to the diameter of the electron beam [196]. The spatial distribution of specific elements is documented by line profiles or two-dimensional maps [196]. These maps are frequently portrayed using a false-color spectrum to depict variations in elemental concentrations [196,204]. For a detailed description of the EPMA technique, please refer to Refs. [196] and [214].

In this work, electron probe microanalysis (EPMA) on polished cross-sections of sintered bulk samples were carried out by Dr. Gerald Schmidt (DECHEMA Forschungsinstitut, Frankfurt, Germany) using a JXA-8100 microprobe (JEOL Ltd, Akishima, Japan) equipped with five wavelength-dispersive X-ray spectrometer (WDS) to gain chemical information via semiquantitative element maps. The measurements were performed using an accelerating voltage of 15 keV, a dwell time of 30 ms per pixel, a probe current of 30 nA with a maximum beam diameter of $< 1 \mu\text{m}$. The following standards were used for calibration: Fe_4N (as standard for N), Cr_3C_2 (standard for C), Al_2O_3 (as standard for O), Si, Hf and Ta.

3.4 Aspects of Transmission Electron Microscopy (TEM)

The transmission electron microscope (TEM) offers a broad range of versatile characterization techniques with high spatial and analytical resolution enabling for comprehensive analysis of solid materials [198]. Since the structure and function of TEM are described in great detail in literature [198,215,216] and as this study predominantly relies on investigations conducted using conventional TEM (CTEM), the following paragraphs summarize the key aspects and techniques of a TEM.

3.4.1 TEM Resolution: The Abbé criterion

The resolving power of our eyes is defined as the smallest distance between two points and is about 0.1-0.2 mm [198]. The resolution of an optical light microscope is given by the Abbe-criterion or Rayleigh criterion, which states that the smallest resolvable distance between two objects, δ , is proportional to the wavelength and is given by:

$$\delta = \frac{0.61\lambda}{\mu \sin \beta} \quad \text{Eq. (4)}$$

In equation (4), λ is the wavelength of the radiation, μ the refractive index of the viewing medium and β the semi-angle of collection of the magnifying lens [198]. In order to simplify, $\mu \sin \beta$, which is also referred to the numerical aperture, is approximately equal to unity, resulting in a resolution that is equally half the wavelength of light. For example, the resolution for green light with a wavelength of $\lambda = 550$ nm is therefore about 300 nm [198].

In order to obtain higher resolutions, the wavelength of the imaging medium is reduced [198]. Because of the wave-particle duality, electrons can also be seen as waves with a wavelength $\lambda = h/p$. Here h is the Planckian Quantum of action and p the momentum of the particle [198]. By neglecting relativistic effects, which only become more significant at higher acceleration voltages, the wavelength of an electron can be approximated as follows:

$$\lambda = \frac{1.22}{E^{1/2}} \quad \text{Eq. (5)}$$

In equation (5), E is the energy in electron volts (eV) and λ the wavelength in nm [198]. An electron with an energy of 200 keV has a wavelength of about 2.7 pm, which is much smaller than the diameter of an atom [198]. However, it is not possible to build a “perfect” TEM approaching the wavelength-limited limit of resolution due to the imperfection of electromagnetic lenses (details will be rationalized later in section 3.4.3) [198,217]. Since the introduction of C_s - and C_c -corrected machines, a resolution of up to 0.5 Å can be reached [218,219].

3.4.2 The TEM Instrument

A typical TEM column configuration is depicted in Figure 22. It is divided into three main components: the illumination system, the objective lens with the stage and the imaging system [198].

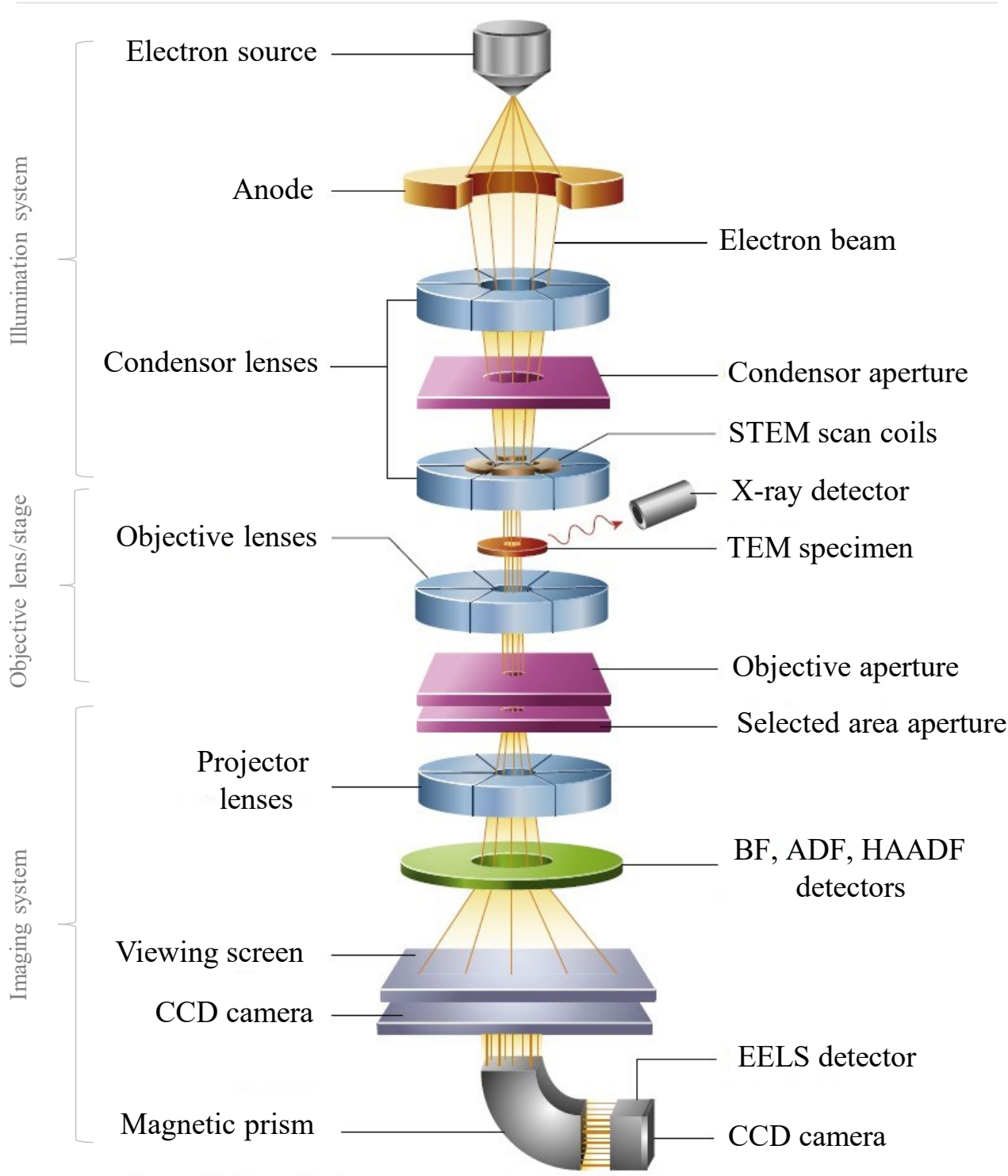


Figure 22 A schematic illustration of a typical TEM set-up, dividing the TEM into three main parts: the illumination system, the objective lens and stage, and the Imaging system. Figure adapted from Ref. [191].

The illumination system containing the electron source, accelerating the electrons in a range of 100-300 keV before traversing them “down” the column [198]. It also contains the condenser lens system, which in a typical column configuration is positioned at the top and serves the purpose of regulating the spot size, as well as focusing or expanding the beam [198]. The illumination system can be operated in two different modes: the parallel and convergent beam mode [198]. The parallel beam mode is mainly used for imaging and selected-area electron diffraction (SAED), whereas the convergent beam mode is

used for scanning transmission electron microscopy (STEM) imaging, analysis via X-ray and electron spectrometry and convergent beam diffraction (CBED) [198]. The objective lens system includes also the holder and stage system, where the sample is positioned within the objective lens, which is divided into an upper and lower polepiece [198]. The objective lens is the most important lens in the TEM and it is also the region in a TEM where all beam-specimen interactions take place [198]. Beneath the objective lens an intermediate lens system (also called the magnifying lenses or diffraction lenses) facilitates the transition between imaging and diffraction modes by either selecting the image plane of the objective lens or its back focal plane, where the diffraction pattern is formed [198]. The projector lens system allows for the adjustment of the desired magnification of the image displayed on the fluorescent viewing screen. Figure 23 schematically depicts the path of the rays within a TEM when operating in diffraction (left) and imaging mode (right), respectively [198].

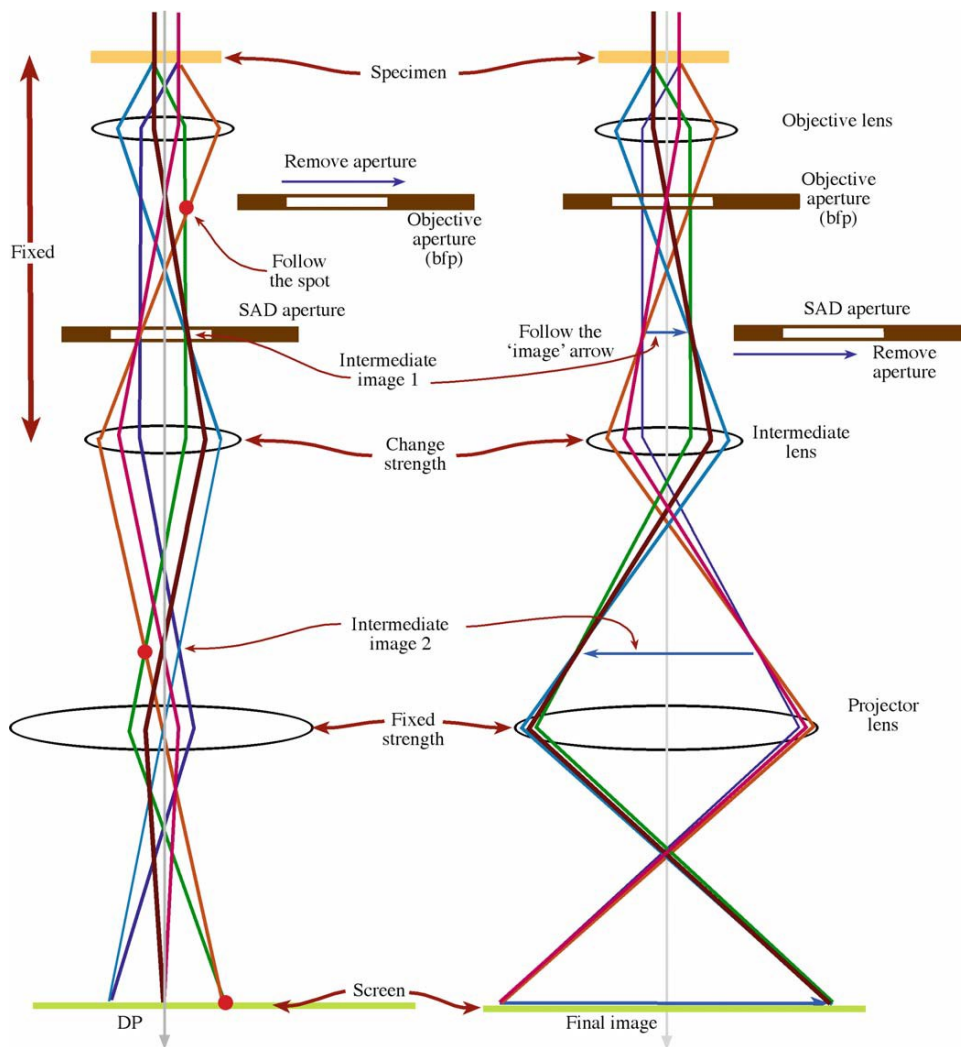


Figure 23 Simplified representation of the two main modes of the TEM imaging system: Diffraction mode (left) and imaging mode (right). In diffraction mode, through the relay lens the back focal plane and in imaging mode the image plane of the objective lens Object selected and magnified on screen. Figure taken from [198].

3.4.3 Lenses, Apertures and Aberrations in TEM

The primary functions of electromagnetic lenses in TEM are twofold: First they capture and redirect the rays originating from a specific point in an object, reproducing a corresponding point in an image and secondly, they concentrate parallel rays onto a specific point within the lens focal plane [198]. In a TEM

the position of the electromagnetic lenses is fixed, in order to control the intensity of the illumination, the magnification or for focusing, the strength of the lenses is changed [198]. Their strength is changed by changing the current through a coil which in turn change the strength of a magnetic field [198].

Apertures in a TEM are located in the lenses and are used to control the size, shape and intensity of the electron beam, the divergence or convergence of electron paths through the lenses, which in turn affects the lens aberrations and controls the current in the beam hitting the specimen [198]. Usually, apertures are circular holes in metal disks, whereas the diaphragm is the metal surrounding the aperture [198]. They help regulate the depth of field, the depth of focus, the collection angle β , reduce aberrations and enhance contrast in TEM imaging [198]. There are apertures which are used to select different electron beams to form different images or they are used to manipulate the image contrast [198]. Other apertures are used to select different regions of the specimen, like the selected area aperture [198].

Electromagnetic lenses suffer from aberrations, which impose limitations on the theoretical resolution of the TEM [198,215,217]. The most relevant are the spherical, chromatic aberration and astigmatism [198,215].

Spherical aberration occurs when electrons passing through the periphery of a lens and are refracted more than those passing through the center [215]. With other words: The lens field behaves different for off-axis rays [198,206]. When the electron is further off-axis, the more strongly it is bent back towards the axis [198]. As a result, the electrons do not reach a common focal point in the Gaussian image plane, but are rather depicted as a disc (also called the disk of least confusion) with a diameter d_s defined as:

$$d_s = \frac{1}{2} C_s (\alpha_{OA})^3 \quad \text{Eq. (6)}$$

where C_s is the spherical aberration coefficient and α_{OA} the aperture angle of the objective lens [215,216]. In particular the objective lens in a TEM is susceptible to the effects of spherical aberration as it affects the level of detail that can be resolved in TEM images [198]. In addition, any errors introduced by the objective lens are magnified by the other lens systems [198].

Electromagnetic lenses suffer from chromatic aberration caused by a certain energy spread, ΔE emerging from different energies of the electromagnetic radiation converging at different focal planes [215]. The energy spread results from the fact that the electron gun does not generate monochromatic electrons. The energy spread is typically in the range of less than ± 1 eV [215]. Further, energy loss happens in the sample because of inelastic scattering [215]. To minimize the blurring of TEM images caused by chromatic aberration, thin specimens are preferred, as they help reduce the effects of inelastic scattering [215]. The disk diameter of the disk of least confusion for chromatic aberration, d_c can be ascribed as:

$$d_c = \frac{\Delta E}{E} C_c \alpha_{OA} \quad \text{Eq. (7)}$$

with $\Delta E/E$ being the fractional variation in the electron beam voltage, ΔE , the energy spread, and E the total energy C_c is the chromatic aberration coefficient and α_{OA} being the aperture angle of the objective lens [206,215,216].

Astigmatism occurs, when electrons experience a non-uniform magnetic field during their spiral motion around the optic axis, resulting from the inability to produce perfect cylindrical symmetry in the polepiece [198]. Moreover, contamination on the apertures can result in charge build-up and deflection of the electron beam [198]. Astigmatism can be adjusted via stigmators, using small octupoles, which introduce a compensating electromagnetic field to balance the inhomogeneities [198,215]. The first condenser lens, C1, and the objective lens must be stigmated to produce a circular incident beam [215].

3.4.4 Scattering, Diffraction and Contrast in TEM

When the electron beam passes through the specimen, the electrons interact with the atomic nuclei and the electrons of the sample material. In this way the electrons are scattered elastically or inelastically due to the Coulomb electrostatic interactions [198]. Electrons emerging from the exit surface of the thin specimen depict a non-uniform distribution, containing all the structural, chemical and all the other information about the specimen [198]. In TEM these non-uniform distributions of electrons are used in two different ways: While the spatial distribution of electron scattering enables for the observation of image contrast, the angular distribution of electron scattering is responsible for the observation of diffraction pattern [198].

Elastically scattered electrons (with less than 0.1 eV change in energy) are responsible for the main amount of intensity in diffraction patterns (DPs) [198,220]. Scattering occurs in all spatial directions with the probability decreasing with the scattering angle [221]. When the electron wave is scattered elastically by the specimen, the electron wave can change both its amplitude and phase as it traverses the specimen, whereas both mechanisms give rise to image contrast [198].

Two fundamental types of contrast are used: the amplitude contrast, which is crucial for lower and intermediate magnifications and the phase contrast, which becomes important for high-resolution TEM (HR-TEM) imaging [198,220].

Amplitude contrast arises from incoherent elastic scattering (Rutherford scattering) and the diffraction contrast arising from coherent elastic scattering under Bragg condition [198].

The mass-thickness contrast depends on the atomic number Z and the thickness, t , of the specimen [198]. For regions with high- Z (i.e., high mass) electrons are scattered more strongly than regions with low- Z of the same thickness [198]. Similarly, thicker regions are responsible for more electron scattering than thinner regions of the same average Z [198]. This means, that thicker and/or higher-mass areas will appear darker in a Bright-Field (BF) image than a thinner and/or lower Z area [198]. In Bright-Field Imaging, the resultant image is formed by the collection of direct-beam electrons with an objective aperture inserted, while strongly diffracted electrons do not contribute to the image forming process [198].

The diffraction contrast is crucial for crystalline materials, as it is controlled by the crystal structure and orientation of the lattice [198]. It arises when the electrons are Bragg scattered. Constructive interference occurs, when the Bragg condition

$$n\lambda = 2d_{hkl} \sin \theta \quad \text{Eq. (8)}$$

is fulfilled. In equation (8) λ is the wavelength of the electron beam, d_{hkl} is the interplanar lattice spacing, and θ is the angle of the incident beam to the interplanar plane hkl , the so-called diffraction angle of the n^{th} order [221].

Therefore, diffraction contrast is defined as special form of amplitude contrast where electron scattering occurs at specific Bragg angles [198]. An overall increase in the BF image contrast is reached by inserting a small objective aperture, excluding many diffracted beams [198]. In Dark-Field (DF) Imaging the direct beam is excluded from the image forming process. By using a small objective aperture, a specific diffracted beam in the SAED pattern is chosen. When returning back to the image mode, the resultant bright areas originate from the specific chosen beam under Bragg condition and therefore appear bright, while the rest of the image remains dark [198].

The intermediate lens allows switching between the imaging and diffraction mode for recording BF- and DF-images [198,216]. SAED patterns are created by inserting the selected area aperture into the image plane of the objective lens [198,216]. Thereby, the DP of the specific area of interest is projected onto

the viewing screen or CCD camera. In order to learn about the crystal structure of the constituting crystalline phases in the ceramics a specific grain has to be oriented along a crystallographic zone axis. Thus, the sample is tilted during convergent beam illumination in diffraction mode. Kikuchi patterns are paired array lines in selected area diffraction patterns (SADPs), emerging due to incoherently scattered, divergent beams of electrons, which are Bragg diffracted by a set of lattice planes [198].

Close to the optical axis, a pair of diffraction cones, so-called Kossel cones appear as parabolas of two parallel lines on the screen/detector [198]. These two Kikuchi lines are sometimes referred as one Kikuchi band [198]. One line therefore corresponds to hkl , the other one to $\bar{h}\bar{k}\bar{l}$ [198]. When Kikuchi bands cross at the center of the optical axis, a crystal is aligned along a specific zone axis (cf. the Kikuchi bands of an aligned TMC in Figure 24 b)). The recorded SAED pattern can then analyzed in the reciprocal space. The discrete length between two diffraction spots in the SAED pattern correspond to the specific lattice spacing d_{hkl} of the corresponding crystal. The lattice spacing, d_{hkl} is equal to the inverse length of the reciprocal lattice vector, g_{hkl} ($d_{hkl} = 1/|g_{hkl}|$) [198]. In this work, the experimental data of SiC, Si₃N₄, HfC, TaC, (Hf,Ta)C, (Hf,Ta)N and C were indexed with the respective lattice spacings given in the Powder Diffraction File (PDF) available in the International Centre for Diffraction Data (ICDD) [222].

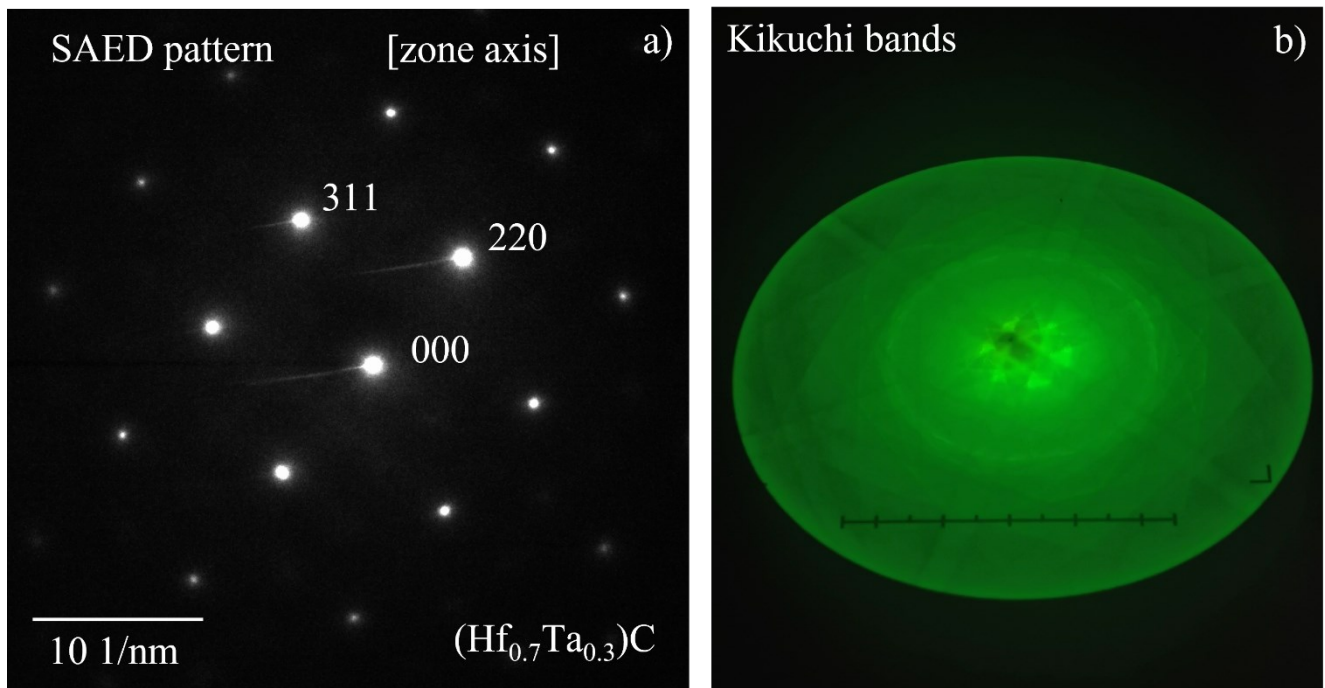


Figure 24 a) SAED pattern of a solid solution of a TMC (Hf,Ta)C crystal displaying discrete diffraction spots. b) Micrograph of the florescent viewing screen, showing the corresponding Kikuchi bands under convergent illumination settings in diffraction mode. The Kikuchi bands cross at the centre, indicating a precise orientation along the zone axis.

The Ewald-sphere construction in Figure 25 is used to demonstrate the relationship between the wave front of the incident and diffracted electron beam and the reciprocal lattice [216,221,223]. For electrons, the radius of the Ewald sphere (given by inverse electron wavelength ($1 / \lambda_e$)) is so large, that the surface of the sphere in the considered area of the reciprocal lattice is approximated by a plane [221]. Figure 25 a) shows the Ewald sphere for the electron beam in the reciprocal lattice of a hypothetical crystal structure. Matching between the Ewald sphere and different order Laue zones gives the reciprocal diffraction pattern, shown in Figure 25 b).

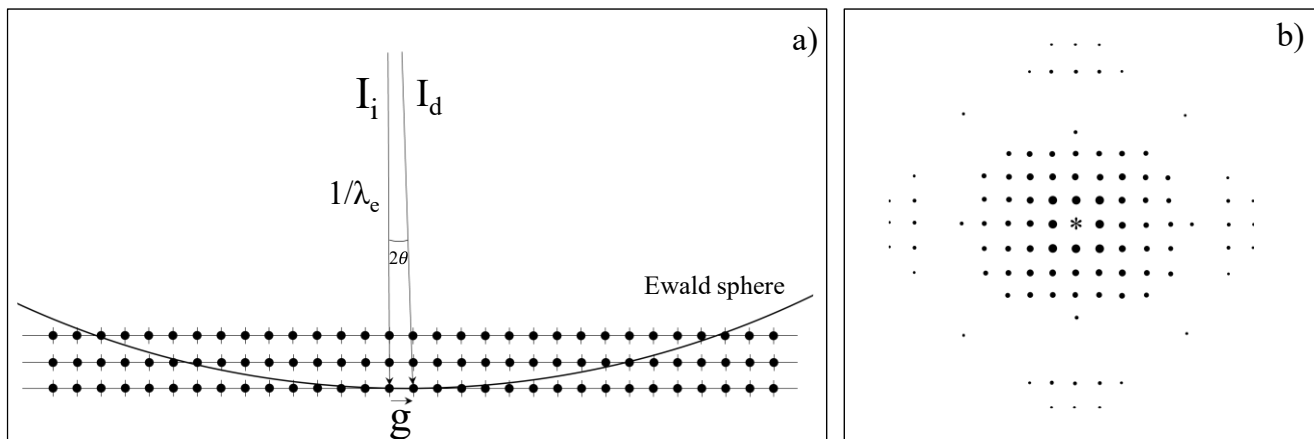


Figure 25 a) Schematic drawing of the Ewald sphere in a hypothetic reciprocal lattice. $1/\lambda_e$ is the radius of the Ewald sphere. I_i is the incident beam, I_d the diffracted beam, θ is the Bragg angle, g the reciprocal lattice vector, which represents the lattice planes. Please note the reciprocal lattice rods, also known as rel-rods. b) corresponding schematic diffraction pattern. The star (*) symbol represents the incident electron beam; the size of the diffraction spots correlates to the differences in the intensity. Figure adapted from Ref. [221].

In Figure 26 the dependence of the intensity of the diffracted beam on the excitation error, s is shown. The wave vector k_i represents the incident wave, with $|k_i| = 1/\lambda_e$. Due to the allowed excitation error, s in electron diffraction, the Bragg condition (Eq. 8) does not have to be fulfilled exactly in order to obtain diffraction reflections [216,221].

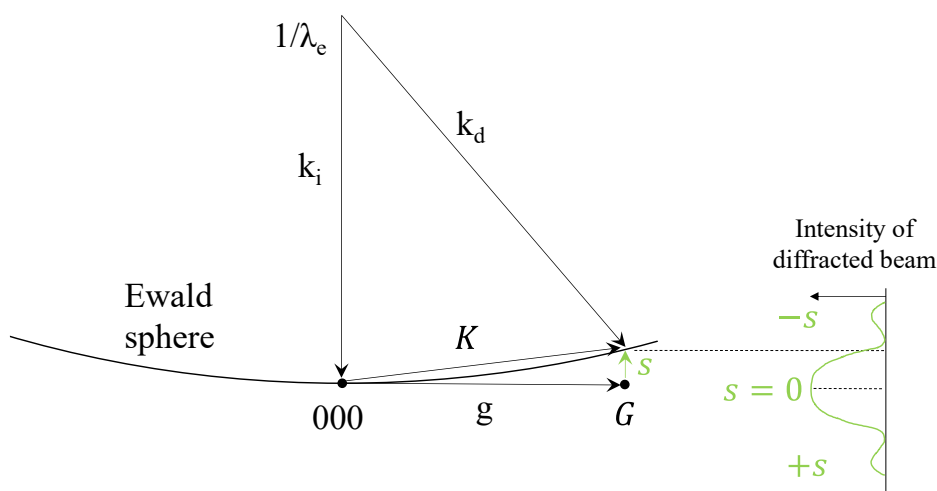


Figure 26 Schematic drawing, showing that the intensity of the diffracted beam beams depends on the excitation error, s . There also will be intensity in a diffraction spot, even when the reciprocal lattice point does not lie exactly on the Ewald sphere and Bragg's condition is not exactly fulfilled. Redrawn after Ref. [224].

Phase contrast is often thought to be synonymous with high-resolution TEM (HR-TEM) but it can also be observed in most TEM images at relatively low magnifications for example in form of moiré patterns [198]. Phase contrast becomes the dominant image forming process for magnifications greater than 150.000 x. HR-TEM imaging requires that both, the transmitted and at least one diffracted beam is included by the objective aperture in the BFP [215]. The phase-contrast imaging is interpreted as lattice fringes or lattice spacing contrast and is sensitive to various factors [198,216]. The appearance of the image shows variations with small changes in the thickness, the orientation, the scattering factor of the

specimen or variations in the focus or astigmatism of the objective lens [198]. The actual location of the atom column cannot be directly interpret from the contrast in the HR-TEM image, instead image simulations are necessary to interpret the HR-TEM image [198].

3.4.5 TEM Experimental Details

The experimental investigations in this work were conducted on a JEM-2100F transmission electron microscope manufactured by JEOL Ltd. (Tokyo, Japan) (cf. Figure 27 a)). The microscope was equipped with a FEG operating at 200 keV ($\lambda = 0.0025$ nm) with a theoretical resolution of 2.2 Å (at 200 keV accelerating voltage). A double-tilt beryllium sample holder (also manufactured by JEOL Ltd.) was employed, enabling controlled tilting of the specimen of $\pm 25^\circ$ in X and Y directions (cf. Figure 27 b), c)). This capability is crucial for achieving a desired orientation along a specific zone axis. Images were captured using an UltraScan 1000 charge-coupled device (CCD) camera produced by Gatan Inc. (Pleasanton, USA). The Gatan Microscopy Suite (Digital Micrograph) software facilitated image acquisition. Selected area diffraction was used to obtain crystallographic information to identify the phase assemblage that formed upon different heat treatments. Structural information was extracted from selected-area electron diffraction (SAED) patterns, which were manually indexed. In this work, some SAED patterns were subjected to color inversion to enhance the visibility of faint reflections. In addition, the JEM-2100F microscope was equipped with a TEM 250 SDD energy-dispersive X-ray spectroscope detector and the corresponding INCA Energy software, both manufactured by Oxford Instruments (Abingdon, UK). This setup enabled the acquisition of EDS data in TEM mode, allowing for elemental analysis during imaging. For the purpose of quantitative EDS analysis, a low beam intensity was necessary to minimize electron beam damage and contamination. To facilitate EDS analysis, the specimen was tilted to an angle of approx. 10° towards the EDS detector. The following operating conditions were applied: an accelerating voltage of 200 keV, a small-sized C2 aperture (which determines the probe current), an objective aperture out, 30 s counting time. Dead time was kept below 30 % for all EDS spectra. In addition, only very thin regions of the specimen in close proximity of perforation were chosen for EDS point measurements. TEM bright-field imaging (TEM-BF), high-resolution TEM (HR-TEM) in combination with SAED was carried out in order to investigate the microstructure of pyrolyzed and annealed ceramic powders as well as thin TEM foils prepared from the sintered ceramic bulk materials. [84,85]

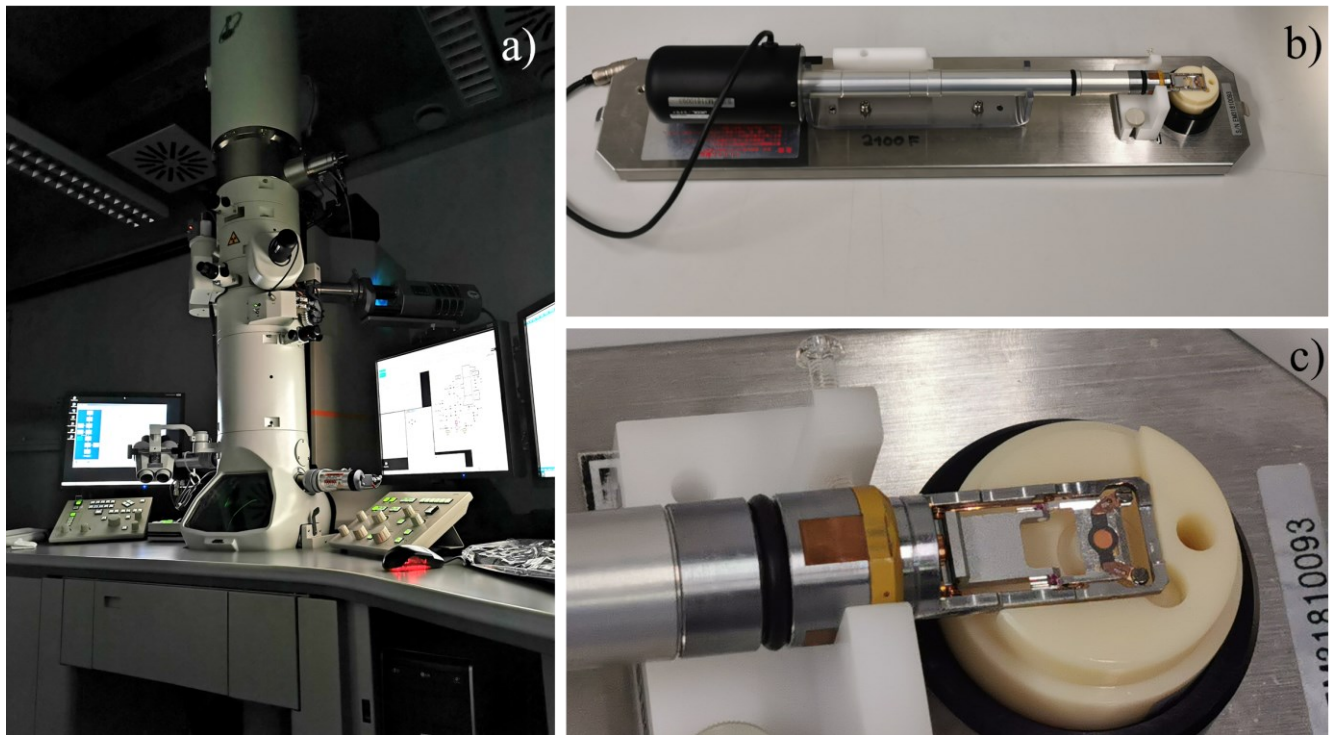


Figure 27 a) Transmission Electron Microscope JEM-2100F (JEOL Ltd., Tokyo, Japan) used for investigations in this study, b, c) Photomicrographs showing the double-tilt holder (JEOL Ltd., Tokyo, Japan).

3.5 Analytical Electron Microscopy - Interaction of Electrons with Materials

3.5.1 Inelastic Electron Scattering

Inelastically scattered electrons suffer from kinetic energy loss due to interaction with other atoms in the specimen. The electron trajectory changes only minimally. [198] The energy, which is lost upon inelastic scattering is transferred to the specimen, generating a range of useful signals as shown in Figure 28 [191]. In Figure 28 there are two illustrations showing the interaction of the incoming primary electrons within a thin TEM specimen in Figure 28 a and a thick SEM sample in Figure 28 b). The electron paths get longer, when the sample is thicker [191]. Thus, the more likely are multiple scattering events [191]. When the electrons lose kinetic energy with each inelastic scattering event, it can also happen that an electron loses all its energy to the sample and gets absorbed [191]. The interaction volume is defined as the volume of electron interaction within the specimen, which is determined by the 3D distribution of several different electron trajectories [191] (cf. Figure 28 b)). In contrast, when the primary beam is transmitted through the TEM specimen, that is thin enough then, the specimen is defined as electron-transparent [191]. Electron transparency is dependent on the kinetic energy of the incident electrons, determined by the accelerating voltage and is also dependent on the chemical composition of the specimen itself (specimen containing higher Z elements absorb electrons faster upon stronger electron interactions) [191].

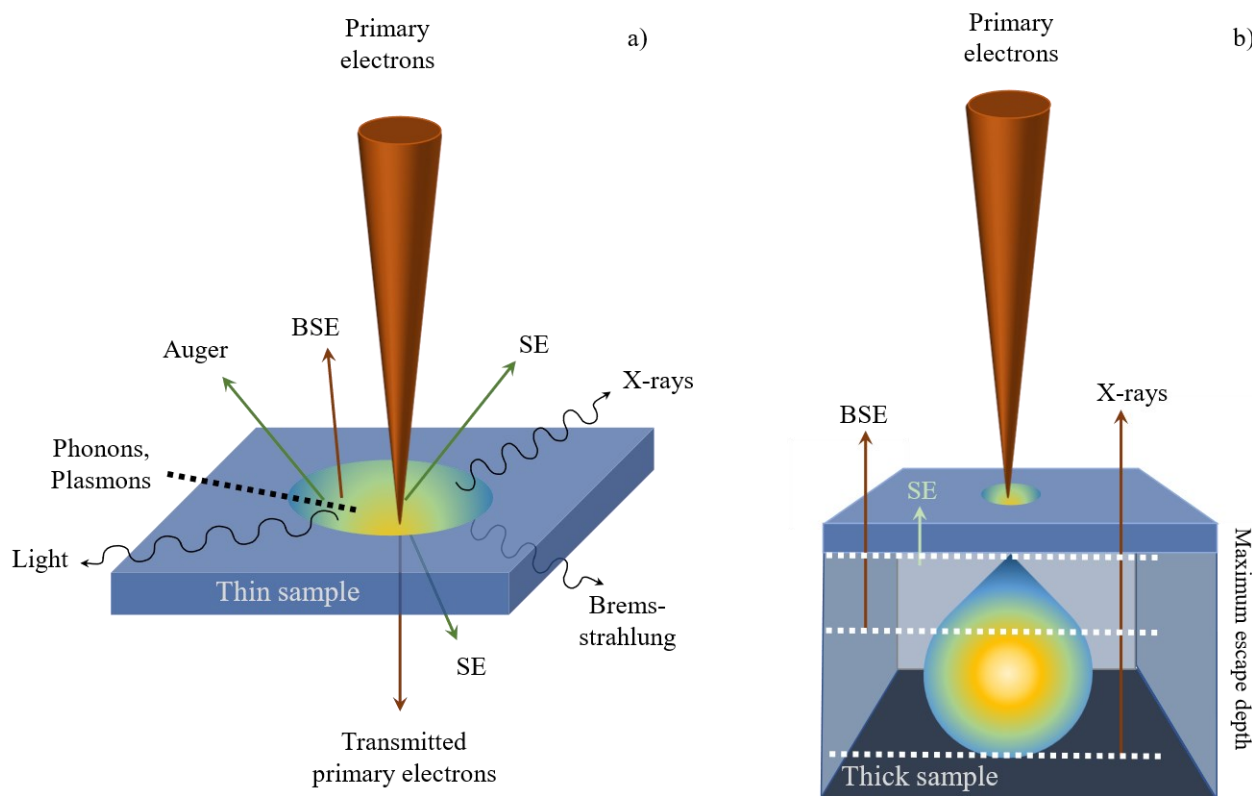


Figure 28 Signals generated by electron-matter interaction in thin (electron transparent) specimen in a), and bulk samples in b). Figure adapted from Ref. [191].

3.5.2 EDX: – Characteristic X-rays

When a high-energy beam electron penetrates through the outer conduction/valence bands materials emit Bremsstrahlung and characteristic X-rays (Figure 29). This electron then interacts with the inner-shell (or core) electrons [191,198]. If the incoming electron transfers more than a critical amount of energy to an inner-shell atom (critical ionization energy), the inner-shell atom is ejected and it escapes the nucleus field [198]. In a solid, this process leaves a hole in the inner shell and the electron escapes above the Fermi level into the unfilled states [198]. By filling the hole with an electron from an outer shell, the ionized atom then returns to its lowest energy (ground state) [198]. This is accompanied by the emission of a characteristic X-ray or an Auger electron. The difference in energy between the two electron shells is characteristic for each atom [198]. The ionization process is shown in Figure 29. By precise focusing the electron beam onto positions of interest, characteristic X-rays are emitted and EDS spectra can be obtained [191]. In order to identify the containing elements in the tested material, the characteristic X-ray peaks in the EDS spectrum are correlated to standardized elemental energies [191]. X-rays can escape from the electron interaction volume, potentially extending up to 1 mm beneath the specimen surface (Figure 28) [191]. Even for a finely focused electron beam, the spatial resolution of X-ray analysis in SEM is limited to approximately $1 \mu\text{m}^3$ in thick samples [191]. EDS spectroscopy in SEM and TEM is applied for non-destructive chemical analysis of materials [191].

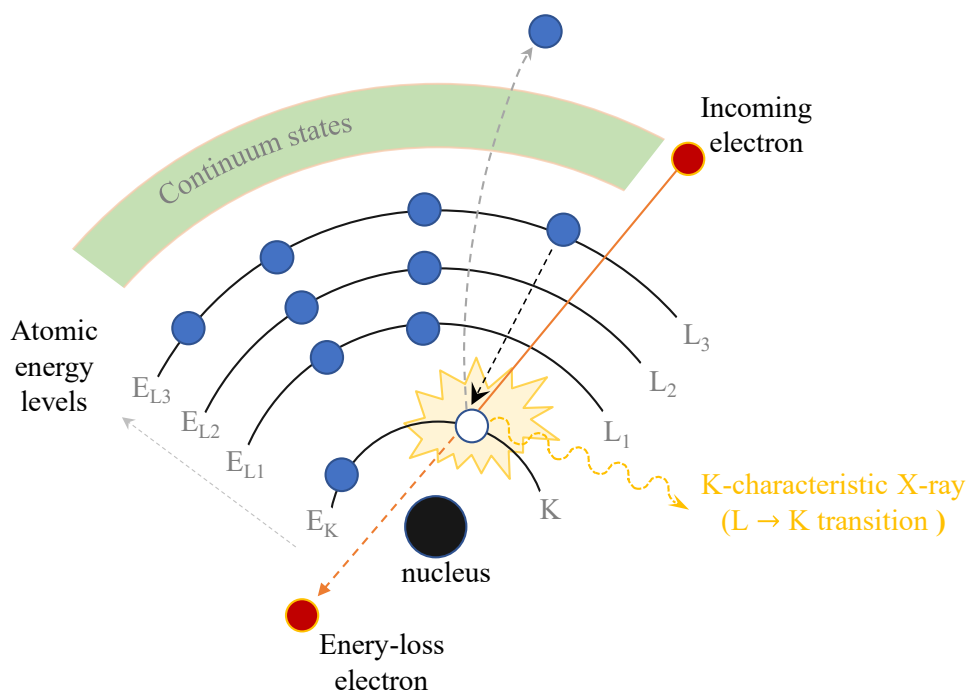


Figure 29 Schematic illustration of the ionization process including the generation of characteristic X-rays. An inner (K) shell electron is ejected from the atom by an incoming high-energy electron. The hole in the K shell is filled with another higher-shell electron (electron from the L3 shell), thereby generating characteristic (K_{α}) X-rays. Figure adapted from Refs. [191,198].

Both microscopes, the scanning electron microscope (SEM) and transmission electron microscope (TEM) used for data acquisition in this work, are equipped with EDS detectors manufactured by Oxford Instruments (Abingdon, UK). Consequently, data acquisition and handling were performed using the INCA Energy software, also developed by Oxford Instruments.

For individual quantitative EDS point measurements, the Point & ID option within the software was employed. Subsequently, the acquired EDS spectra were exported as EMSA (.txt) files. To visualize and analyze the spectra, a Python-based data processing script was employed (cf. Figure A 1 in the appendix). The script parsed the standardized structure of the exported text files and extracted the relevant data points, which were then plotted as a two-dimensional spectrum. This spectrum represents the energy values in keV plotted against the corresponding counts in arbitrary units (a.u.). Thus, each exported text file from the INCA Energy software was processed and plotted using the developed script. The script requires the input of the local file path to the text file, and if needed, the X and Y coordinates can be adjusted to suit the data being analyzed.

In some cases, it was necessary to determine the Hf:Ta ratios of the amorphous matrix phase, the TMCs, or TMCNs using EDS measurements. For this purpose, single EDS point measurements were performed, the spectra were plotted using INCA Energy software and the elements contained in the spectrum were quantified in at-%. The respective at-% values of each element measured in the phases were copied out of the software and normalized using Excel. The values of Hf and Ta were summarized and the respective proportions were calculated.

3.6 X-ray (Powder) Diffraction (XRD) of PDCs

X-ray diffraction analysis were used to obtain global information regarding the phase composition and crystallinity of the prepared ceramic materials. X-ray powder diffraction on the as-pyrolyzed (1000 °C in NH_3) and annealed (1600 °C, N_2) $\text{Si}(\text{Hf}_x\text{Ta}_{1-x})(\text{C})\text{N}$ ceramic powder samples and $\text{Si}(\text{B})\text{C}/(\text{Hf}_{0.75}\text{Ta}_{0.25})\text{C}$

bulk ceramics were carried out by J. Bernauer, using a STOE X-ray diffractometer (STOE & Cie. GmbH, Darmstadt, Germany) equipped with a Debye-Scherrer camera with a monochromatic Mo-K α radiation source ($\lambda=0.7093 \text{ \AA}$) at the Technical University Darmstadt. The measured 2θ range was $5-45^\circ$ at a scan speed of $1^\circ/\text{min}$. Present phases were analyzed using the Match! software (Crystal Impact – Dr. H. Putz and Dr. K. Brandenburg GbR, Bonn, Germany). [84]

The XRD analysis regarding the as-pyrolyzed (1000°C , Ar) $\text{Si}(\text{Hf}_x\text{Ta}_{1-x})\text{C}(\text{N},\text{O})$ ceramic powder and the sintered (2200°C , vacuum) $\text{SiC}/(\text{Hf}_x\text{Ta}_{1-x})\text{C}$ bulk ceramic were carried out by K. Beck, using a D8 Advance X-ray diffractometer (Bruker Corporation, Billerica, USA) utilizing Ni-filtered Cu-K α radiation ($\lambda=1.5406 \text{ \AA}$). The scan step size was 0.015° with 15 s per step. The measured 2θ range was set to $15-100^\circ$. The baseline correction was done by using the Match! Software (Crystal Impact – Dr. H. Putz and Dr. K. Brandenburg GbR, Bonn, Germany). The diffraction peaks were indexed with the Powder Diffraction File (PDF) available in the International Centre for Diffraction Data (ICDD) [222].

3.7 Chemical Composition of PDCs

In order to gain information on the chemical composition of the as-pyrolyzed $\text{Si}(\text{Hf}_x\text{Ta}_{1-x})\text{C}(\text{N},\text{O})$ ceramic powders, and thereof consolidated $\text{SiC}/(\text{Hf}_{0.7}\text{Ta}_{0.3})\text{C}$ ceramics, elemental analysis were carried out at Mikroanalytisches Labor Pascher (Remagen, Germany). To determine the elemental contents, 50 mg of the as-pyrolyzed powder was weighed with an AT261 DeltaRange ultra-precision balance (METTLER Toledo Inc., Greifensee, Schweiz). The as-pyrolyzed powder sample was not additionally pulverized for elemental analysis, whereas the dense sintered bulk ceramic needed a further pulverization with a tungsten carbide (WC) grinder. The elemental contents of Hf, Ta and Si of both samples were determined using inductively coupled plasma atomic emission spectrometry (ICP-AES). The N and O contents were analyzed via hot gas carrier extraction. The elemental content of C was determined via combustion analysis. [85]

3.8 Mechanical Properties via Nanoindentation Tests: Material Hardness

Hardness is defined as the resistance that a material offers to the penetration of another (harder) test specimen [192,225]. A simple technique to measure the hardness is the Brinell-method, where a ball indenter is pressed into the testing material and the diameter of the indentation is measured [225]. Thus, the ratio of the force pressing an indenter into a material P to the indentation area A gives the hardness [226]. There are various other hardness measurement methods using different indenter shapes in order to measure the hardness of the testing materials. For the Rockwell technique, conical indenters are used, whereas the Vickers hardness is tested via pyramids [225]. Since the penetration capacity depends on the shape and inherent hardness of the other body as well as on the type and size of the load, the hardness test method must always be specified when stating hardness values numerically [192].

Nanoindentation allows to assess mechanical properties at small scales [227]. It is a powerful technique for assessing mechanical properties of thin films and bulk materials at low loads and shallow depths [226,228,229]. By applying nanoindentation tests the recorded depth of penetration of an indenter into the specimen along with the measured applied load is used to determine the area of contact and hence the hardness of the test specimen [230]. From the load-displacement curve, the elastic modulus can be extracted [230]. The technique is well established for measuring the properties of homogeneous monolithic materials systems but less research has been done on heterogeneous composite materials [228]. However, most materials relevant in the high-temperature engineering field are heterogeneous and multi-phase materials with structures from the nano- to the micro-meter scale [227]. Therefore, a statistical nanoindentation method, namely the grid indentation technique was developed by Constantinides and others [227,228,231].

Since this work focuses on the characterization of the microstructure, at this point it is referred to further literature. Review articles and books such as Refs. [227,228,232–235] provide a good introduction into the field.

The nanoindentation method was used to obtain information regarding the mechanical properties of the consolidated SiC/(Hf_xTa_{1-x})C ceramics (cf. section 7.3.5). Measurements were carried out in close cooperation with Dr. Jin Wang and G. Winkens at the Institute of Energy and Climate Research at the Forschungszentrum Jülich GmbH. The monolithic bulk samples were cut into small blocks followed by a ceramographic preparation including grinding and subsequent polishing. The samples were glued onto standard aluminium dies using Crystalbond (509-3, Aremco Products Inc., New York, USA). In order to gain information on the elastic modulus and hardness of the samples, the InForce50 actuator in a G200X Nanoindenter (KLA-Tencor, Milpitas, California, USA) equipped with a diamond Berkovich tip was used. The NanoBlitz mapping tool was utilized in order to perform the grid indentation method, whereas 2500 indents were measured, arranged in a 50 x 50 grid with a spacing of 4 μm between each indent, giving a total surface area of 200 x 200 μm². This spacing was chosen in order to avoid overlap of plastic zones and the influence of neighbouring microstructural features in the SiC/(Hf_{0.7}Ta_{0.3})C. The nanoindentation tests were performed at a strain rate of 0.2 s⁻¹ to a maximum load of 50 mN. The InView built-in software package based on the Oliver-Pharr method served to analyze the quasi-static load-displacement data. For the SiC/HfTaC ceramic a Poisson ratio $\nu = 0.2$ [236] was assumed, while for the indenter tip an elastic modulus of $E = 1141$ GPa and a Poisson ratio of $\nu = 0.07$ was assumed. The calibration was performed before data acquisition using a fused silica sample with a known Poisson ratio of $\nu = 0.179$ and elastic modulus $E = 72.12$ GPa.

4 Materials Synthesis and Sample Preparation

All ceramic samples investigated in this work were prepared by J. Bernauer in the laboratory of Prof. R. Riedel, Disperse Solids at the department of Materials Science at the Technical University of Darmstadt. A variety of synthesis papers of Si-based polymer-derived ceramics containing transition metals like Hf and Ta are available in the literature [41,61,64,66] (cf. section 2.10.2). However, a short description of each synthesis is given below. Because this work deals with the characterization of chemically different systems, each system and the individual synthesis and processing routes are briefly presented in 4.1 - 4.3.

4.1 Synthesis and Consolidation of SiHfCN

As already described in section 2.10.2, the single-source-precursors synthesis of the Hafnium-containing UHTC-NC and the preparation of a dense SiHfCN-based ceramic nanocomposites was suggested by J. Yuan et al. in Ref. [66], whereas the preparation of the dense SiHfCN ceramic was reported in Ref. [65]. Its short-term high-temperature oxidation behavior was reported in Ref. [62]. J. Yuan et al. synthesis route for preparing amorphous SiHfCN was performed by J. Bernauer using the suggested single-source precursors. The preparation of the polymeric single-source precursor using a commercial polysilazane (HTT 1800, Clariant, Sulzbach am Taunus, Germany) modified with Tetrakis(diethylamido)hafnium(IV) (TDEAH, Sigma-Aldrich, Chemie GmbH, Taufkirchen, Germany, CAS-no: 19824-55-6) was carried out using the Schlenk technique. Consolidated bulk ceramics were prepared by FAST. Two SiHfCN bulk ceramics were produced with different sintering parameters. As shown in Table 3, the sample noted as SiHfCN_01 differs from the sample noted as SiHfCN_02 only in the dwell time during the FAST process. SiHfCN_01 was sintered with a dwell time of 1 minute, whereas the SiHfCN_02 was sintered with a dwell time of 15 minutes. Otherwise, the same sinter parameters such as a temperature of 1950 °C and a uniaxial pressure of 105 MPa were used for the two ceramics produced. The consolidation of the powders was carried out by M. Eriksson at the national spark plasma sintering facility at the Department of Materials and Environmental Chemistry at the Stockholm University, Sweden. Figure 30 shows the two consolidated ceramic bulk pellets with a diameter of 20 mm and height of ~1.8 mm after sintering. The pellets were then cut into smaller pieces using to prepare the samples for microscopic methods.

Table 3 The FAST sinter parameter of the two prepared SiHfCN bulk ceramics.

sample	Sintering Process	Max. sintering temperature in °C	Uniaxially applied pressure in MPa	Dwell time in °C/min
SiHfCN_01	FAST	1950	105	1
SiHfCN_02	FAST	1950	105	15

SiHfCN_01
1950 °C
105 MPa
1 min

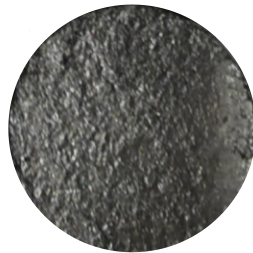


1 cm

→
sawing



SiHfCN_02
1950 °C
105 MPa
15 min



→
sawing



Figure 30 Photographs of the sintered SiHfCN bulk pellets (SiHfCN_01 and SiHfCN_02) after sintering (Dr. M. Eriksson, Stockholm University) and after sawing.

4.2 Synthesis and Annealing of $\text{Si}(\text{Hf}_x\text{Ta}_{1-x})\text{(C)N}$

Si-based polymeric precursors were used to synthesize novel PDCs in the $\text{Si}(\text{M})(\text{C})\text{N}$ system, where $\text{M} = \text{Hf}, \text{Ta}$ (transition metals). The ceramic materials were synthesized by utilizing the polymer-to-ceramic synthesis route (cf. chapter 2.5). Two nanocomposites with different molar ratios $\text{Si}(\text{Hf}_x\text{Ta}_{1-x})\text{(C)N}$, ($x = 0.7$ and $x = 0.2$) were prepared through the pyrolysis-induced transformation of the polymers with a Hf:Ta molar ratio of 7:3 for the Hf-rich ceramic ($\text{Hf}_{0.7}\text{Ta}_{0.3}$) and a Hf:Ta molar ratio of 1:4 for the Ta-rich ceramic ($\text{Hf}_{0.2}\text{Ta}_{0.8}$). In order to generate the single-source precursors for the $\text{Si}(\text{Hf}_x\text{Ta}_{1-x})\text{(C)N}$ ceramics, the Schlenk technique under purified Ar was used. The Schlenk lines and related apparatus are versatile species of laboratory equipment enabling a safe and convenient manipulation of air- and moisture-sensitive compounds [237]. The precursors were synthesized by reacting perhydropolysilazane Durazane-2250 (cf. Figure 10) (PHPS, 20 wt-% in di-n-butyl ether, Merck KGaA, Germany) with tetrakis(dimethylamido)hafnium(IV) (TDMAH, 99.99 %, Sigma-Aldrich, USA, CAS-no: 19782-68-4) and pentakis(dimethylamido)tantalum(V) (PDMAT, 99.99 %, Sigma-Aldrich, USA, CAS-no:19824-59-0) at room temperature. The synthesis route's possible reaction pathways are illustrated in Figure 31. [84]

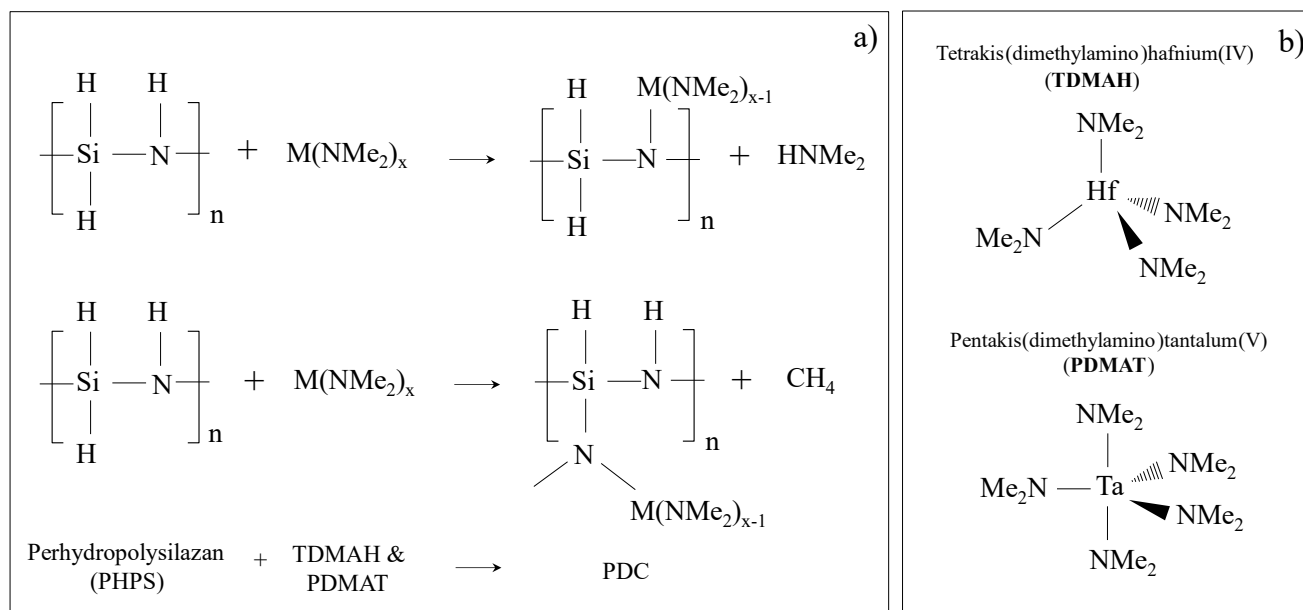


Figure 31 a) Possible reaction pathways during the synthesis of the perhydropolysilazan (PHPS). b) The organo-metallic complexes of $\text{M}(\text{NMe}_2)_x$ with $\text{M} = \text{Hf}, \text{Ta}$ and $\text{Me} = \text{CH}_3$ (TDMAH & PDMAT).

The mass ratio of the organo-metallic complexes (TDMAH + PDMAT) to the Si-polymer (PHPS) was established to 3:7. In the following, the synthesis of the Hf-rich system, $\text{Si}(\text{Hf}_{0.7}\text{Ta}_{0.3})(\text{C})\text{N}$ is described exemplarily: First, 11.66 g of PHPS was dissolved in anhydrous toluene (99.8 %, Sigma-Aldrich, USA) within a 250 ml Schlenk flask equipped with a magnetic stirrer. Subsequently, a solution containing 0.7 g of TDMAH and 0.34 g of PDMAT dissolved in 10 ml of toluene was added dropwise to the mixture. The resulting solution was continuously stirred for 6 hours. The solvent was then removed, yielding a yellow-brown powder. [84]. Figure 32 show various photographs taken by J. Bernauer depicting some synthesis steps during the preparation of the polymer-derived $\text{Si}(\text{Hf}_x\text{Ta}_{1-x})(\text{C})\text{N}$ ceramics, using the Schlenk technique.



Figure 32 Various photographs of the synthesis steps showing a Schlenk flask, the transparent liquid precursor, the metal-modified brown liquid and the obtained brown ceramic powder. All photographs are taken by J. Bernauer.

The powder was crushed using a clean agate pestle and mortar within a glovebox (pressure inside: 3 mbar, O_2 content below 1 ppm, H_2O content below 1 ppm). Subsequently, the powder was sieved, resulting in particle sizes below $100 \mu\text{m}$. The powder material was then pyrolyzed at $1000 \text{ }^\circ\text{C}$ in a flowing ammonia (NH_3) atmosphere at 1 bar pressure for 3 hours. The continuous flow of NH_3 was employed to eliminate the decomposition gases, which develop during the pyrolysis of the polymer-derived material.

Subsequently, the as-pyrolyzed ceramic powders were subjected to annealing at a temperature of 1600 °C in a nitrogen (N₂) atmosphere at 1 bar pressure for a duration of 3 hours. Annealing was performed to characterize the microstructural change and the differences in phase composition afterwards. [84]. Figure 33 shows a photograph of the four obtained polymer-derived ceramic powder samples. On the left, the as-pyrolyzed (green/grey color) and annealed (black color) Hf-rich ceramics (Hf_{0.7}Ta_{0.3}) are shown, on the right the pyrolyzed (green/grey) and annealed (black) Ta-rich ceramics (Hf_{0.2}Ta_{0.8}).

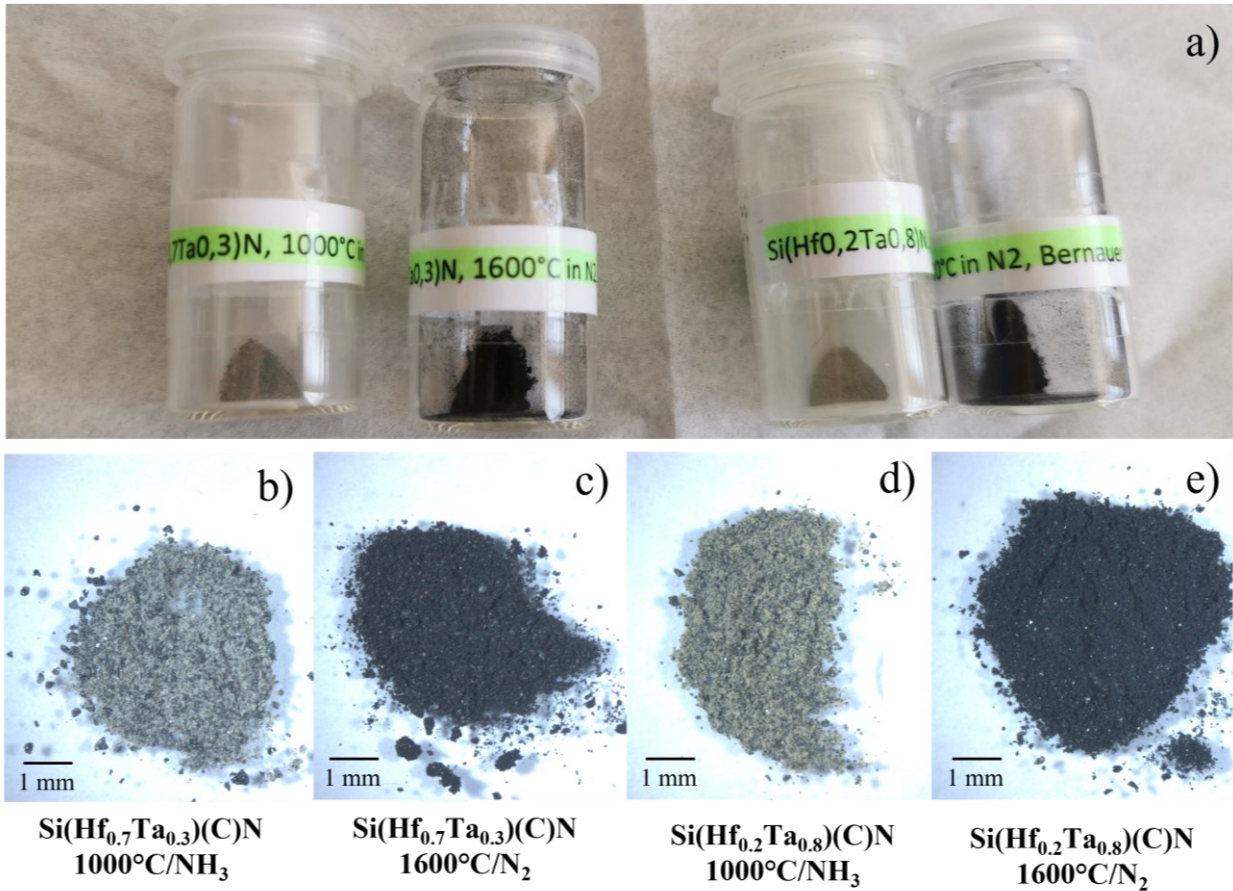


Figure 33 Photomicrographs of the polymer-derived ceramic powders in the Si(Hf_xTa_{1-x})(C)N system. The as-pyrolyzed and annealed Hf-rich Si(Hf_{0.7}Ta_{0.3})(C)N ceramic powders are shown in b) and c), the as-pyrolyzed and annealed Ta-rich Si(Ta_{0.8}Hf_{0.2})(C)N ceramic powders in d) and e).

Table 4 summarizes the processing parameters of the pyrolyzed and annealed polymer-derived ceramic powders as well as the corresponding nomenclature of the prepared ceramics.

Table 4 Processing parameter of the Si(M)(C)N, (M = metal) polymer-derived ceramics. Table adapted from [84].

Sample	metal:metal molar ratio (TDMAH : PDMAT)	metal: polymer molar ratio (TDMAH + PDMAT : PHPS)	Processing temperature in °C	Exposure time in h	Gas atmosphere
Si(Hf _{0.2} Ta _{0.8})(C)N	1:4	3:7	1000	3	NH ₃
Si(Hf _{0.2} Ta _{0.8})(C)N	1:4	3:7	1600	3	N ₂
Si(Hf _{0.7} Ta _{0.3})(C)N	7:3	3:7	1000	3	NH ₃
Si(Hf _{0.7} Ta _{0.3})(C)N	7:3	3:7	1600	3	N ₂

4.3 Synthesis and Consolidation of $\text{Si}(\text{Hf}_x\text{Ta}_{1-x})\text{C}(\text{N},\text{O})$

Ceramic powder samples in the $\text{Si}(\text{M})\text{C}$ system, with $\text{M} = \text{Hf}, \text{Ta}$ (transition metals) were prepared via the polymer-to-ceramic route. Two $\text{Si}(\text{Hf}_x\text{Ta}_{1-x})\text{C}$ single-source precursors with different Hf:Ta ratios ($x = 0.2, x = 0.7$) were synthesized by J. Bernauer. The Schlenk technique under purified Argon was utilized in order to synthesize the single-source precursors for the $\text{Si}(\text{Hf}_x\text{Ta}_{1-x})\text{C}$ ceramics. The molar ratio x determines the proportion of the two transition metal compounds. The precursors were synthesized upon the reaction of the commercially available liquid allylhydridopolycarbosilane (SMP-10, Starfire System Inc., Glenville USA) with tetrakis(diethylamino)hafnium(IV) (also known as TDEAH, 99.99 %, Sigma-Aldrich Chemie GmbH, Taufkirchen, Germany, CAS-no: 19824-55-6) and pentakis(dimethylamino)tantalum(V) (PDMAT, 99.99 %, Sigma-Aldrich Chemie GmbH, Taufkirchen, Germany, CAS-no: 19824-59-0). The metal amino to polymer ratio (TDEAH + PDMAT/SMP-10) was set to 30/70 for both compositions. The metal amino complexes were dissolved in anhydrous toluene. The solution was added dropwise to SMP-10 under stirring conditions at room temperature. The solution was then heated and the solvent was subsequently removed in vacuum. The as-obtained black solid material was ground after evaporation of the solvent in a clean agate pestle and mortar, sieved to a grain size of $\geq 100 \mu\text{m}$ and pyrolyzed at $1000 \text{ }^\circ\text{C}$ in argon atmosphere to prepare the $\text{Si}(\text{Hf}_x\text{Ta}_{1-x})\text{C}(\text{NO})$ ceramic powders. The ceramic nanocomposites are characterized by a Hf:Ta ratio of 7:3 for the Hf-rich ceramic ($\text{Hf}_{0.7}\text{Ta}_{0.3}$) and a Hf:Ta ratio of 1:4 for the Ta-rich ceramic ($\text{Hf}_{0.2}\text{Ta}_{0.8}$).

The ceramic powder sample obtained after pyrolysis are denoted as $\text{Si}(\text{Hf}_x\text{Ta}_{1-x})\text{C}(\text{NO})$ (cf. Figure 34). The as-pyrolyzed ceramic powders were used as initial powder material for the preparation of dense $\text{SiC}/(\text{Hf}_x\text{Ta}_{1-x})\text{C}$ bulk ceramics via FAST. The consolidation was conducted by M. Bram and his team at the Institute of Energy and Climate (IEK), material synthesis and manufacturing processes at the Forschungszentrum Jülich GmbH. For this, the ceramic powder was placed into a graphite die, covered with graphite foil to reduce the damage of the punch and to facilitate the sample removal after consolidation. For consolidation a FCT HP D25/1 FAST apparatus (FCT Systeme GmbH, Frankenblick, Germany) was used. The ceramic powders were densified at $2200 \text{ }^\circ\text{C}$ and a uniaxial pressure of 50 MPa for 20 min in vacuum. The heating rate was set to 100 K min^{-1} , the cooling rate was set to 220 K min^{-1} until RT was reached. To increase the temperature in a controlled way, a pulsed electric current was applied with a pulse duration of 25 ms and pause time of 5 ms throughout the experiment. The temperature was controlled with an optical pyrometer. The samples obtained after consolidation are denoted as $\text{SiC}/(\text{Hf}_x\text{Ta}_{1-x})\text{C}$ bulk ceramics (cf. Figure 34).



Figure 34 Photograph showing the $\text{Si}(\text{Hf}_x\text{Ta}_{1-x})\text{C}(\text{N},\text{O})$ polymer-derived ceramic powders (left) and cut sample pieces of the sintered $\text{SiC}/(\text{Hf}_x\text{Ta}_{1-x})\text{C}$ bulk ceramics (right), with pen for scale. FAST was performed by Prof. Bram and his team, Institute of Energy and Climate (IEK), at the Forschungszentrum Jülich GmbH.

4.4 Nomenclature of PDCs

A note on the nomenclature of the studied PDCs: In the literature, there is no uniform nomenclature for pyrolyzed, annealed or sintered PDC samples. Often, the amorphous single-phase ceramic is named in such a way that all the elements containing the sample are lined up (e.g. Si-Hf-N in Ref. [61]). The annealed ceramic after the polymer-to-ceramic route is then named after the evolving phases written down. In some cases, the matrix phase and the precipitates in the matrix phase are separated by a hyphen (such as SiOC-HfO_2 in Ref. [181], where the matrix phase consists of SiC and SiO_2). In the last decades, PDC syntheses have become more complex and so have the chemical compositions of the evolving PDCs. By adding organometallic complexes as it is for this work, more elements are added to the PDC system. This results in multinary PDCs, which consist of several different phases after the polymer-to-ceramic conversion (cf. chapter 2.5).

In this thesis, the samples of the pyrolyzed, annealed powder samples were named after the respective elements contained. The sintered bulk composites were named after the respective phases contained. For example, the pyrolyzed samples from chapter 7 are given as: $\text{Si}(\text{Hf}_{0.7}\text{Ta}_{0.3})\text{C}(\text{N},\text{O})$ where 0.7:0.3 refer to the molar ratio of the used organometallic complexes. To achieve an Hf:Ta ratio of 0.7:0.3 in at-% in the pyrolyzed and sintered PDC, 0.94 g of TDEAH and 0.34 g of PDMAT were used in the synthesis, (cf. Table 5). The brackets around N and O indicate that these elements are present only in small amounts in the sample. For the FAST-sintered sample, the nomenclature is $\text{SiC}/(\text{Hf}_{0.7}\text{Ta}_{0.3})\text{C}$. This means that the sample is composed of the phases SiC and $(\text{Hf}_{0.7}\text{Ta}_{0.3})\text{C}$, whereas the SiC represents the matrix phase and thus owns a higher volume fraction.

Table 5 summarises the samples examined in the present work. In addition to the sample names, the processing parameters (either from the pyrolysis, annealing or the FAST-sintering process), the used chemicals and exemplarily the elemental analysis after pyrolysis and sintering are given. In Table 5 the data of the elemental analysis in at-% are brought forward from the results section and are used to explain the nomenclature (detailed results on elemental analysis refer to chapter 7.1 and 8.2).

Table 5 Summary of sample names, processing parameters, chemicals used for synthesis and exemplarily elemental analysis in at-%.

Sample name	Processing and parameters	Chemicals for PDC synthesis	Elemental analysis in at-%
SiHfCN_01	FAST (1950 °C/ 105 MPa/ 1 min, in vacuum)	10.8 mL HTT1800, 4.8 mL TDEAH	-
SiHfCN_02	FAST (1950 °C/ 105 MPa/ 15 min, in vacuum)	10.8 mL HTT1800, 4.8 mL TDEAH	-
Si(Hf _{0.7} Ta _{0.3})(C)N	Pyrolysis, 1000 °C, NH ₃	11.66 g PHPS, 0.7 g TDMAH, 0.34 g PDMAT	-
Si(Hf _{0.7} Ta _{0.3})(C)N	Annealing, 1600 °C, N ₂	derived from pyrolized sample Si(Hf _{0.7} Ta _{0.3})(C)N	-
Si(Hf _{0.7} Ta _{0.3})C(N,O) ²	Pyrolysis, 1000 °C, Ar	3 g SMP-10, 0.94 g TDEAH, 0.34 g PDMAT	Si: 35.68, Hf: 1.33, Ta: 0.44, C: 51.64, N: 4.44, O: 5.36
SiC/(Hf _{0.7} Ta _{0.3})C	FAST (2200 °C/ 50 MPa/ 20 min, in vacuum)	derived from sample Si(Hf _{0.7} Ta _{0.3})C(N, O)	Si: 41.79, Hf: 1.57, Ta: 0.53, C: 55.46, N: 0.5, O: 0.24
SiC/(Hf _{0.75} Ta _{0.25})C	FAST (2200 °C/ 50 MPa/ 20 min, in vacuum)	3 g SMP-10, 0.8288 g TDMAH, 0.3125 g PDMAT,	-
Si(Hf _{0.75} Ta _{0.25})BC(N,O)	Pyrolysis, 1000 °C, Ar	3g SMP-10, 0.8288 g TDMAH, 0.3125 g PDMAT, 0.1183 g BH ₃ *SMe ₂	Si: 35.17, Hf: 1.49, Ta: 0.51, B: 0.32 C: 50.28, N: 5.93, O: 6.30
SiBC/(Hf _{0.75} Ta _{0.25})C	FAST (2200 °C/ 50 MPa/ 20 min, in vacuum)	derived from sample Si(Hf _{0.75} Ta _{0.25})BC	Si: 41.7, Hf: 1.69, Ta: 0.57, B: 0.44 C: 48.32, N: 0.97, O: 6.29

² All chemicals listed are oxygen-free chemicals. However, small amounts of oxygen may be introduced into the systems through precursor processing. Small amounts of oxygen were measured in all ceramics via EDS, but only in sample no 5 the oxygen content was determined by elemental analyses, which is why the oxygen then appears in the sample notation.

4.5 Sample Preparation for OLM, SEM and EPMA

In the following the sample preparation techniques for OLM, SEM and EPMA will be briefly explained.

4.5.1 Preparation Methods of Powder Ceramics for OLM and SEM

For initial inspection of the powder particles via optical light microscopy no further sample preparation was necessary. Ceramic powder particles (pyrolyzed and annealed powders) were placed onto slides, which were then suitable for direct inspection under the optical microscope (cf. Figure 35 c)). For SEM imaging powder samples were pulverized by using a clean agate pestle and mortar. The pulverized ceramics were subsequently placed onto adhesive carbon-pads (Plano GmbH, Wetzlar, Germany), which were mounted onto Aluminium stubs for SEM analysis.

In order to obtain information about the microstructural composition of individual powder particles, an additional preparation technique for SEM investigations was required. The original powder particles (not crushed powders) were taken and embedded in Specifix-40 epoxy resin (manufactured by Struers, Copenhagen, Denmark) (Figure 35 b)). The use of epoxy resin at low temperatures ensured the avoidance of potential microstructural variations induced by localized heating. The epoxy with the embedded powder particles was left to cure at room temperature for 24 hours before the embedded powder particles were subsequently subjected to a conventional ceramographic preparation technique involving cutting, grinding with 15, 9, 6, 3, 1 μm diamond lapping films and final polishing with 0.5 μm diamond lapping film and a lubricant consisting of 50 % hexylene glycol and 50 % distilled water was used. Due to the fixation in the epoxy, individual powder particles could be examined and processed in a targeted manner in the SEM and in the FIB-SEM. The sample preparation of ceramic powder samples via FIB-SEM will be explained later in section 4.6.2.

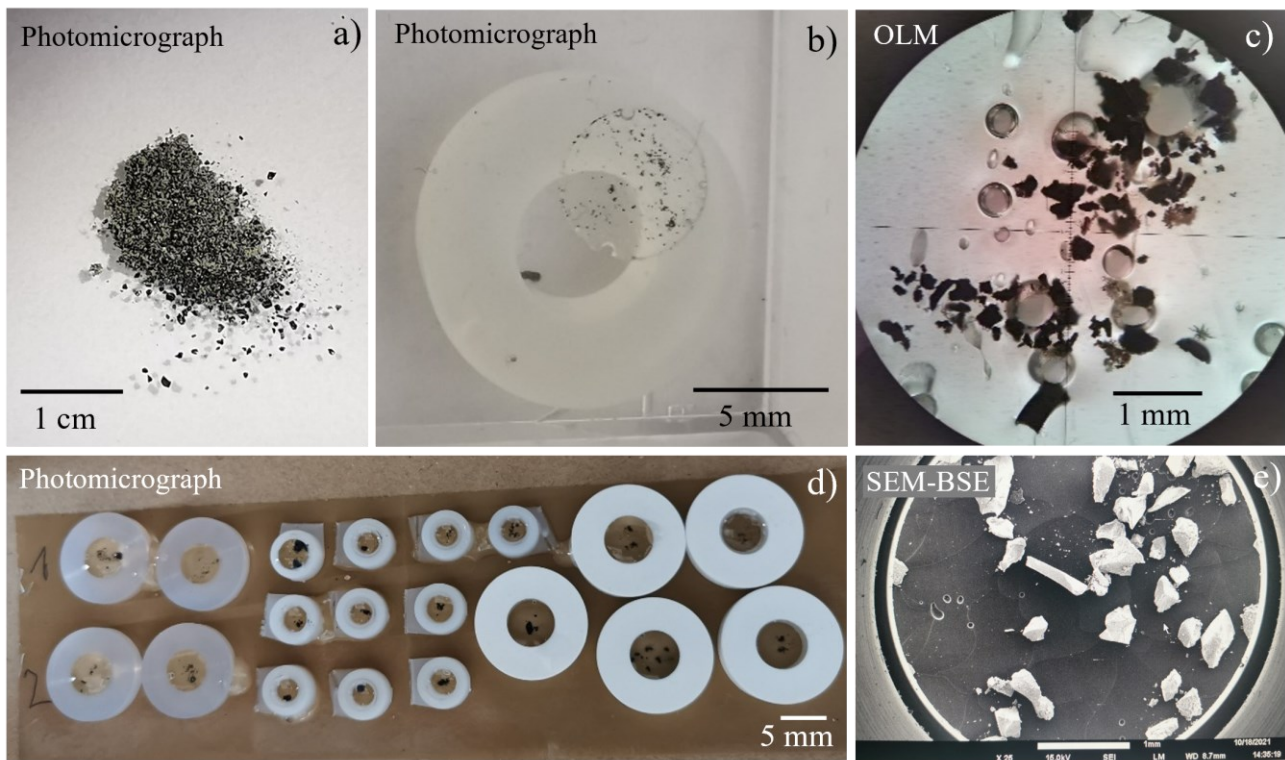


Figure 35 Various sample preparation steps for ceramic powder samples. a) molds filled with small amounts of ceramic powder and resin, b) Low-magnified SEM-BSE image showing ceramic powder particles on a sticky carbon pad for inspection in SEM, c) powder samples for inspection under optical light microscope, d) ceramic powder particles embedded in resin, cured and subsequently polished, e) photomicrograph of embedded powder particles.

4.5.2 Preparation Method of Ceramic Bulk Materials for OLM, SEM and EPMA

To obtain plane-parallel samples for inspection upon OLM, SEM and EPMA, the sintered bulk ceramics were prepared via a ceramographic sample preparation technique including cutting, grinding and polishing. For this, the ceramic pellet was cut into smaller pieces using a slow-speed ISOMET precision saw (Buehler, Leinfelden-Echterdingen, Germany), equipped with a diamond-tipped thin saw blade (dimension of metal bounded diamond saw blade 75 x 0.18 x 12.7 mm, from Cloeren Technology, Germany) to facilitate subsequent processing. The next step involves several steps of mechanical grinding to reduce the thickness of the sample, followed by progressively finer abrasives to remove surface damage caused during grinding. For this, the specimen was mounted onto a sample holder with a mounting adhesive (Crystalbond 509-3, Aremco Products Inc., New York, USA). The specimen is glued onto the sample holder by heating on a heating plate (IKA C-MAG HP 7) to ~ 160 °C, at which temperatures Crystalbond becomes liquid. Subsequently, the specimen undergoes a series of polishing steps using diamond lapping films with grain sizes of 15, 9, 6, 3, 1, and 0.5 μm and running water as lubricant. This polishing process is essential to eliminate scratches and other artifacts that could interfere with imaging. The speed of the rotation platen of the MultiPrep Tripod polisher (Allied High Tech Products Inc., USA), was reduced constantly with each polishing steps from 50 rounds per minute (rpm) to 35 rpm. For the polishing steps utilizing the 1 μm and 0.5 μm diamond lapping films, a lubricant consisting of 50 % hexylene glycol and 50 % distilled water was used.

4.6 Specimen Preparation for TEM Analysis

In the following the preparation methods for specimens resting on a support grid are briefly explained, distinguishing between ceramic powder samples and sintered bulk samples.

4.6.1 Specimen Preparation of Powder Samples for TEM Analysis on Grids

Since the synthesized polymer-derived ceramic of $\text{Si}(\text{Hf}_x\text{Ta}_{1-x})\text{C(N)}$ (cf. chapter 6) and $\text{Si}(\text{Hf}_x\text{Ta}_{1-x})\text{C(N,O)}$ (cf. chapter 7) are present in powder form, the aim was to prepare electron-transparent lamella of individual powder particles and deposit them onto an amorphous thin carbon film on a TEM grid. Firstly, the obtained ceramic powders were prepared by mechanical pulverization in a clean agate pestle and mortar in ethanol. The liquid containing particles are then ultrasonicated for 5 minutes and allowed to settle afterwards. To prepare the specimen for TEM investigations, a small droplet of the settled liquid is pipetted and placed onto a lacy carbon film, supported by a gold grid (Figure 36 a)). In a dry environment, the liquid droplet evaporates, leaving behind a distribution of the particles on the carbon support film. To avoid sample charging the ceramic powders are coated with a thin carbon layer of about several nm. When inspected in TEM, some particles are located over a hole in the lacy carbon film and therefore particles can be studied in the TEM (cf. Figure 36 b), c)).

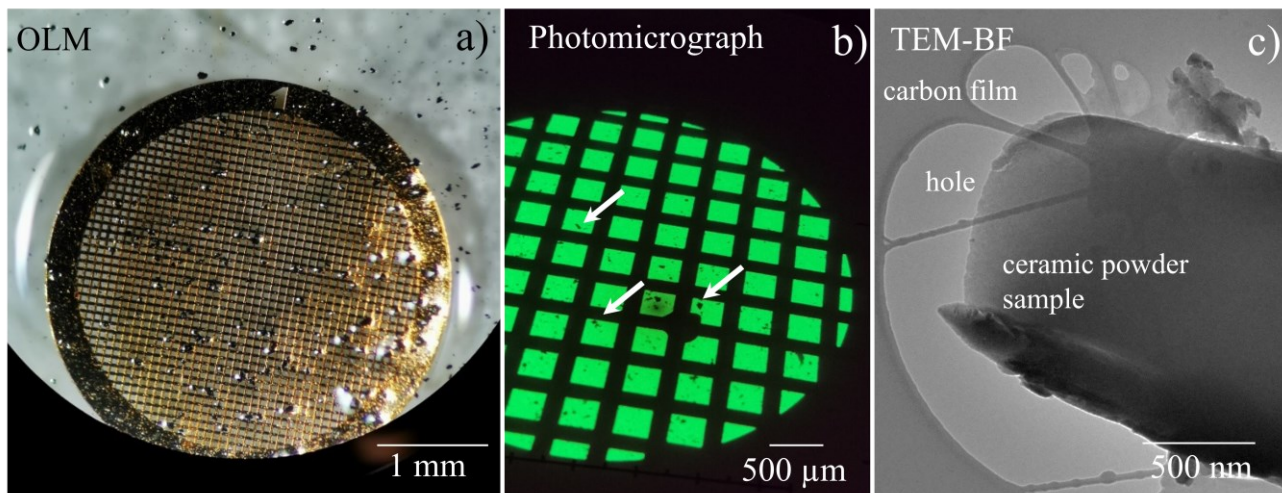


Figure 36 TEM specimen preparation for ceramic powder particles using TEM support grids with carbon film; a) TEM lacy gold grid with freshly pipetted ethanol and pulverized ceramic powder solution, b) photomicrograph of the fluorescent TEM viewing screen showing individual powder particles sitting on the carbon film, c) TEM-BF image showing the carbon film, the hole in the carbon film and the ceramic powder particle located over a hole.

In order to avoid peak overlap between the L_{α} lines of the containing transition metals Hf (7.899 keV) and Ta (8.146 keV) with the K_{α} line of Cu (8.046 keV), which is the material of choice in the commonly used TEM grids, it was necessary to utilize TEM gold grids. The yellow and green marked cells in Table 6 shows that the element-related X-ray energies of Cu, Hf and Ta are very close. The substitution of Cu grids with Au grids provided a definitive distinction between Hf and Ta during EDS analysis. Additionally, for elemental analysis via EDS, the L_{α} -lines of Hf and Ta were preferred over the M_{α} -lines due to the interference caused by peak overlap between the Si- K_{α} peak and the Hf-/Ta- M_{α} peaks (compare blue marked cells in Table 6). In some cases, Mo grids were used instead of gold grids. The characteristic X-ray energies of Mo are also shown in Table 6.

Table 6 Characteristic X-ray energies of C, N, O, Si, Cu, Hf, Ta and Au. Cu and Au are the elements that make up the TEM grids, whereas the other elements listed are those expected chemicals in the prepared ceramics.

Element	Z	$K_{\alpha 1}$	$K_{\beta 1}$	$L_{\alpha 1}$	$L_{\beta 1}$	$M_{\alpha 1}$	$M_{\beta 1}$
C	6	0.277					
N	7	0.392					
O	8	0.525					
Si	14	1.739	1.837				
Cu	29	8.046	8.904	0.928	0.947		
Mo	42	17.479	19.608	2.293	2.394		
Hf	72	55.79	63.23	7.899	9.023	1.644	1.700
Ta	73	57.53	65.22	8.146	9.343	1.712	1.770
Au	79	86.806	77.982	9.713	11.443	2.123	2.203

4.6.2 Specimen Preparation of Ceramic Powder Samples using FIB-SEM

In order to obtain a cross section of an individual powder particle, the FIB lift-out technique was used in this study. A TEM specimen was cut out and deposited on a Molybdenum lift-out grid in collaboration with Dr. S. Schlabach (Institute for Applied Materials, Karlsruhe Institute of Technology). Embedded and ground polished cross-sections of the ceramic $\text{Si}(\text{Hf}_{0.7}\text{Ta}_{0.3})\text{(C)N}$ powder particles shown in Figure 37, were not suited for stable FIB-SEM, (cf. Figure 37 d)). Successful FIB lamella was obtained from a powder particle that was not embedded in resin, but dispersed and stabilized on an adhesive carbon pad.

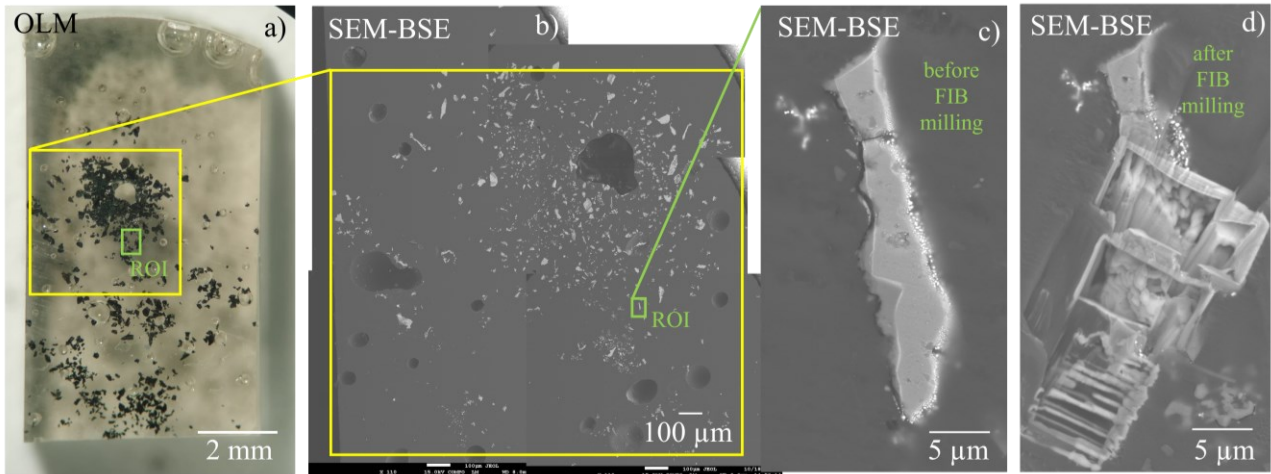


Figure 37 CLEM of the embedded and polished cross-section of the $\text{Si}(\text{Hf}_{0.7}\text{Ta}_{0.3})\text{(C)N}$ ceramic powder particles. a) optical light micrograph of the cold-embedded and subsequently cross-sectioned and polished powder particles, b) correlated sample position in the SEM-BSE image, c, d) SEM-BSE image of the magnified region of interest (ROI) before and after FIB milling.

Figure 38 a) shows a powder particle chosen for the lift-out technique. The region of interest (ROI) was defined from the sample surface using software-controlled tools via marking the region with specific coordinates. Subsequently, a protective Pt layer was deposited with length = $15\ \mu\text{m}$, width = $2\ \mu\text{m}$ and thickness of $0.2\ \mu\text{m}$ (see Figure 38 b), c)), preventing the sample underneath from ion beam damage and Ga^+ implantation. With the focused Ga^+ ion-beam, trenches (dimension of trenches: $x = 20\ \mu\text{m}$, $y = 9\ \mu\text{m}$, $z = 9\ \mu\text{m}$) on both sides of the ROI (cf. Figure 38 b)) were milled via the stairstep milling type with a stage tilt of $\pm 5^\circ$, an ion-beam voltage of 30 keV and beam current of 9.3 nA. For the lift-out a U-cut was performed by using an ion-beam voltage of 30 keV and a beam current of 6.5 nA and a stage tilt of 7° . For the lift-out the stage tilt was 0° . After the lift-out process, several thinning steps were conducted. For the first thinning process, the lamella is upright in 50° stage tilt using an ion-beam current of 30 keV and beam current of 0.46 nA. For the second, third and fourth thinning steps the ion beam current was successively reduced to 0.28 nA, 93 pA and 48 pA. For the two final polishing steps (duration of 5 and 2 minutes), the ion beam current was again reduced from 47 pA to 28 pA. Also, the voltage of the beam was reduced from 5 keV to 2 keV. The extraction process was carried out with the micromanipulator omniprobe 200 to lift the lamella from the substrate. The extracted lamella was then transferred to a suitable Mo lift-out TEM grid (cf. Figure 38 d)).

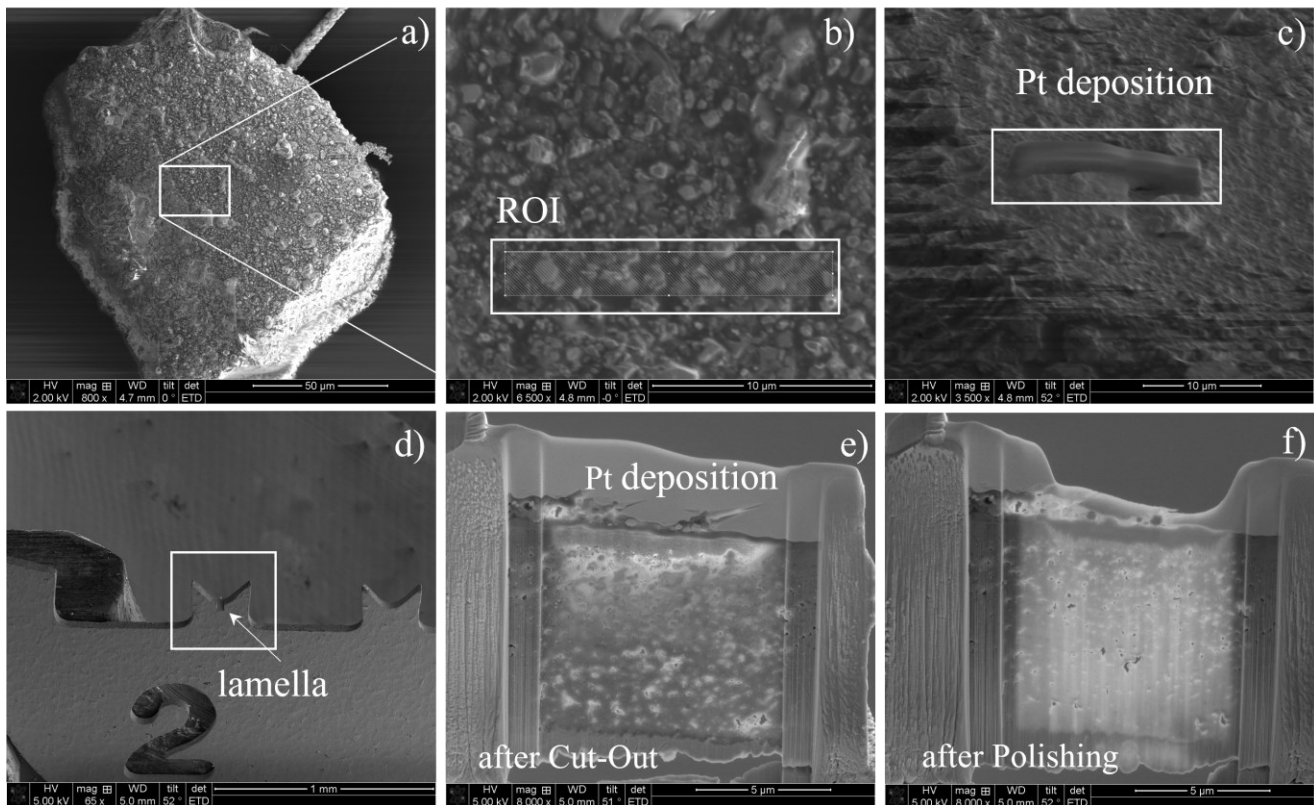


Figure 38 Several SEM images showing the FIB lift-out technique, applied to a single powder particle of the annealed $\text{Si}(\text{Hf}_{0.7}\text{Ta}_{0.3})\text{(C)N}$ PDC, shown in a); b) SEM image, displaying the region of interest (ROI); c) Pt deposition to protect the underlying material; d) extracted lamella (white arrow) transferred and pinned to a Mo lift-out grid; e) pre-thinned FIB lamella with the intact Pt deposition at the top; f) thinned FIB lamella with thinning marks (in vertical direction) from the thinning process. All images in this figure are taken by Dr. S. Schlabach.

4.6.3 Specimen Preparation of Bulk Samples via Conventional TEM Foil Preparation

For the FAST-sintered bulk PDCs (cf. section 4.1 and 4.3), plane-parallel TEM specimens were prepared. The standard ceramographic sample preparation technique for bulk samples via cutting, grinding, polishing was used (cf. Figure 39 a-d)) as already described for the SEM and EPMA analysis in section 4.5.2. The specimen thickness after mechanical grinding and polishing of both specimen sides was around $10\text{-}15\ \mu\text{m}$. In most cases, the ceramic bulk samples slowly got light transparent, as shown in Figure 39 e. After polishing the specimen was glued onto a Mo or Au TEM grid using a two-component adhesive (UHU GmbH & Co. KG, Bühl, Germany) (cf. Figure 39 f)). After 24 h of hardening, Ar^+ Ion-Milling was performed using the precision Duomill 600DIF (Gatan Inc., California, USA) (cf. Figure 39 g), Figure 39 h)). This results in electron transparent sample while preserving the structural integrity and minimizing artifacts that may arise from excessive thinning. The settings used for the ion milling of the sintered PDC ceramics are gun voltages of 4 keV and an aligned ion beam angle of 14° to the surface. Once perforation appears (the thinning time varied from 30 minutes to 2.5 hours), the thinning angle and voltage were reduced to clean the sample of amorphized areas. To avoid sample charging under the incident electron beam, all prepared SEM, EPMA samples and finally thinned TEM specimens were pre-sputtered with a thin carbon layer using a MED 010 deposition system (Balzers Union, Liechtenstein).



Figure 39 Various tools used for sample preparation in the ultra-high temperature laboratory at the Institute for Applied Geosciences at the Technical University Darmstadt; a) ceramic bulk sample glued onto glass slide for sawing; b) handling with heating plate; c) cross-sectioned and polished ceramic bulk sample; d) Tripod polisher; e) final polished TEM specimen, ready to be glued onto TEM grid; f) TEM specimen glued onto TEM grid; g) TEM specimen onto TEM grid, mounted onto sample holder for final Ion-thinning process; h) Gatan Duomill for Ar⁺-ion thinning; i) View onto the fluorescent viewing screen of the TEM.

5 Basic Ceramics: SiHfCN and SiC/Si₃N₄/HfC

Based on the proposed synthesis route for the SiHfCN PDC-NC by J. Yuan in Refs. [65,66] (for details, see preliminary investigations in section 2.10.2) the synthesis route was carried out by J. Bernauer (cf. section 4.1). Basic research on the microstructure development upon high temperatures was carried out by J. Yuan in Ref [65]. However, a detailed microstructure analysis of the FAST-sintered SiHfCN PDC-NCs was missing until yet. The aim of the following chapter is to gain a detailed description of the microstructure evolution upon FAST-sintering at 1950 °C using different dwell times is anticipated. It is expected that the characterization of the constituting phases and grain sizes will enable conclusions on the selection of the Si-based precursor identifying. In this way, it is expected to find a suitable Si-based precursor for TBCs in the high-temperature range.

5.1 Microstructure Analysis by SEM and TEM for SiHfCN_01

After the bulk ceramic was cut and polished for further inspection via SEM and TEM, a heterogeneous microstructure was detected by simply looking at the sample without the aid of electron microscopy. An optical light micrograph (OLM), as shown on the left image in Figure 40, gives a broad overview of the microstructure. 25 individual SEM-BSE images were taken at low magnification and then assembled as one large image (right image in Figure 40) for the same frame. In this way, the assembled collage of the sintered bulk ceramic can easily be compared to the OLM. Both images in Figure 40 show several different microstructural regions of the consolidates SiHfCN_01. They are differentiated in powder particles and sinter necks. In order to characterize the different microstructural regions, the microstructure was analyzed in detail using SEM imaging and TEM analysis.

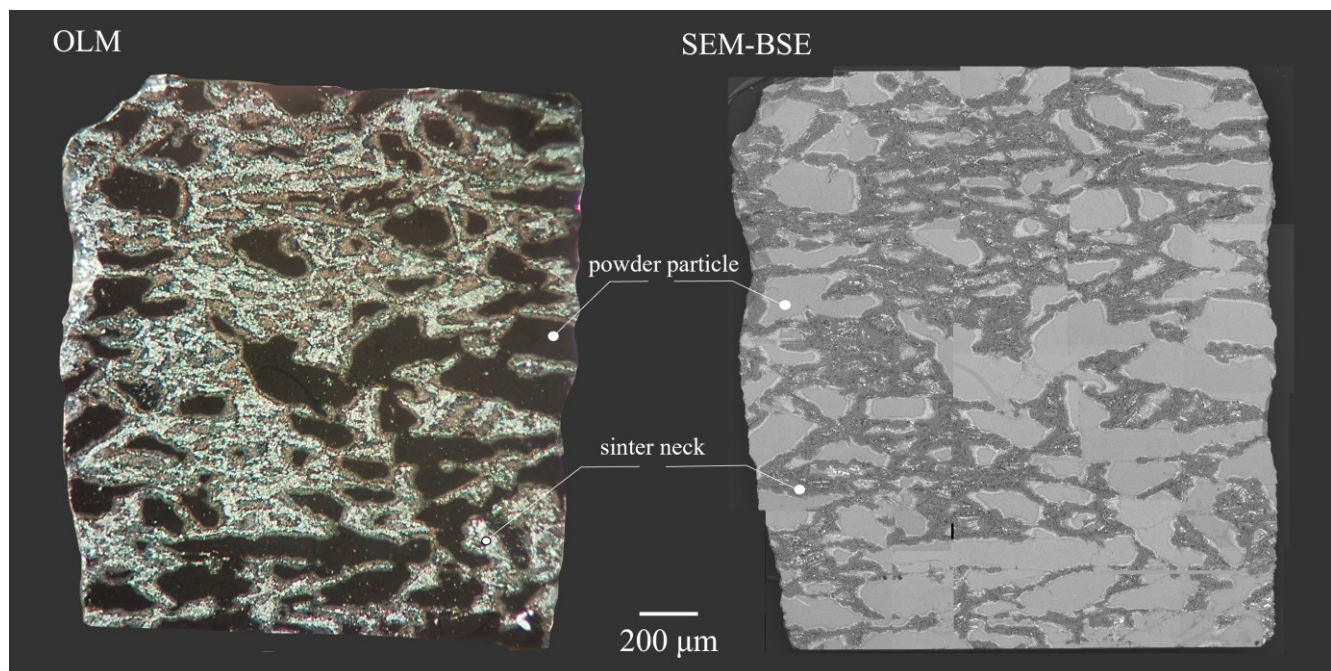


Figure 40 Correlation between OLM and SEM-BSE micrograph. The SEM-BSE image on the right consists of 25 individually mounted SEM-BSE images of the sintered SiHfCN_01 ceramic bulk sample.

Figure 41 illustrates a representative SEM-BSE micrograph, providing an overview of the polished cross-section of the bulk SiHfCN_01 PDC. The microstructure of the bulk ceramic consists of at least four different microstructural regions as detected by four different image contrasts. Figure 41 depicts larger regions with sizes of about 200 - 300 μm (like the three regions shown on each left side of the images) having a bright image contrast in the SEM-BSE image. Because of their size and shape, these regions are

referred to the former powder particles (cf. Figure 41 a)). In addition, one can observe darker areas connecting the former powder particles with each other. They are referred to sinter necks (cf. Figure 41 a)). Furthermore, there are pores, which appear almost black in the BSE image and are almost exclusively present in the sinter necks (cf. Figure 41 a), b)). Another very distinct microstructure region are the transitions zones between the former powder particles and the sinter necks. These areas, which appear very bright in the BSE image, are assigned to crystallization fronts, which extend from the internal surface of the powder particles into the sinter necks. The grain sizes of the very bright appearing Z-rich phases (later identified as HfC with the help of TEM cf. Figure 42) show increasing grain sizes from the particle surface towards the sinter necks. The square marked region in Figure 41 a) is depicted magnified in Figure 41 b), showing the interior of a former powder particle, the crystallization front, the sinter neck and the porosity within the sinter necks. In addition, the microstructural regions of the former powder particles appear very dense. The microstructural regions of the crystallization front also appear very dense, without any porosity present. When examining the microstructural regions of the sinter necks, interconnected pores with the size of $\sim 5 \mu\text{m}$ are visible. The SEM-SE image in Figure 41 c)) supports the assumption that the regions of the former powder particles and also the crystallization fronts are microstructurally very dense and that porosity is particularly present within the sinter necks.

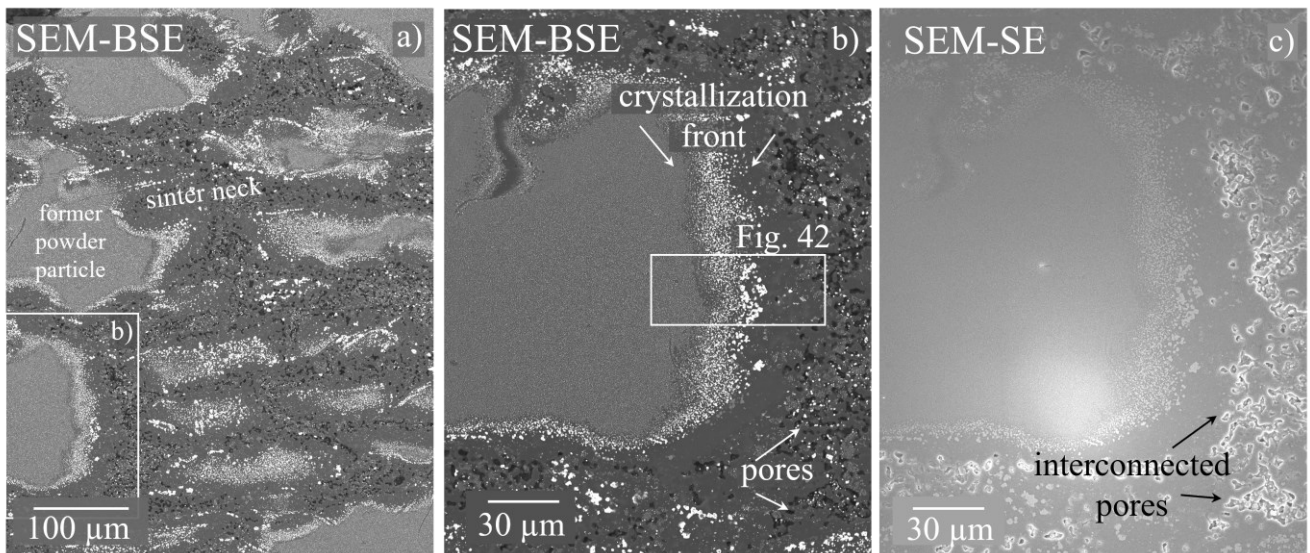


Figure 41 a, b) SEM-BSE images and c) SEM-SE micrograph of the sintered, cross-sectioned and polished SiHfCN_01 ceramic bulk sample show four different microstructural regions: former powder particles, crystallization fronts, sinter necks and porosity.

Figure 42 contains numerous macro- and microstructural but also chemical information as well as electron diffraction regarding the constituting phases within the SiHfCN_01 ceramic. The upper image in Figure 42 displays a magnified SEM-BSE image from the rectangular square in Figure 41 b). Heading from left to right, the interior of a former powder particle, the crystallization front and the sinter neck are depicted. The SEM-BSE image in Figure 42 shows that the crystallization front starts from the inside of the former powder particles heading towards the sinter necks. In addition, two element concentration profiles are plotted at the upper edge of the image. Each element profile contains 251 individual EDS point measurements, providing information about the carbon (green curve) and nitrogen (red curve) content in the respective microstructural regions. Each individual EDS point measurement was placed inside of the SiC/Si₃N₄ matrix (further information see appendix, cf. Figure A2), not in the bright appearing Hf-rich phase. This is done to gain information about the N and C concentration in the matrix phase. It should be considered that the EDS information depth is about $4 \mu\text{m}$. Starting from left to right,

the C and N content within the former powder particle remain at relatively constant concentrations up to the point where the crystallization front starts. There is a brief increase in N and a simultaneous decrease in C within the crystallization front. In addition, the element profiles show, that the N content drops to zero completely as soon as the microstructural region of the sinter neck starts. Thus, there is no N within the sinter neck. Simultaneously the C content increases. Magnified SEM-BSE and correlative TEM-BF images of the three microstructure regions are shown in Figure 42. Each SEM-BSE and TEM-BF image in Figure 42 shows different grain sizes in the constituting phases, in the respective region.

The BSE and TEM-BF images of the microstructural region of the former powder particle show that the constituting phases have similar grain sizes (of up to 100 nm). The SAED pattern obtained at the position of the former powder particle indicates diffraction rings originating from Si_3N_4 , SiC and HfC.

The images of the crystallization front show larger grain sizes of Hf-rich phases in addition to SiC. The SAED pattern in combination with EDS spectra show the presence of HfC and SiC as the two main phases in the crystallization front.

The phase composition in the sinter necks consists of SiC, arranged as very large crystals (grain sizes of up to 4 μm). Rarely, smaller HfC precipitates are also found. As already discussed for the microstructure of the ceramic powders (cf. section 6.4.2), the thermal decomposition of Si_3N_4 in combination with the presence of an increased carbon availability and the absence of nitrogen, grain growth of TMCs has also taken place within the microstructure of the SiHfCN_01 bulk sample. It is evident that nitrogen is still "locked" in the areas of the remnants of the former powder particles. In the transition zone between the crystallization front and the sinter neck, the nitrogen content drops sharply to zero (cf. the nitrogen content in the EDS elemental profile in Figure 42).

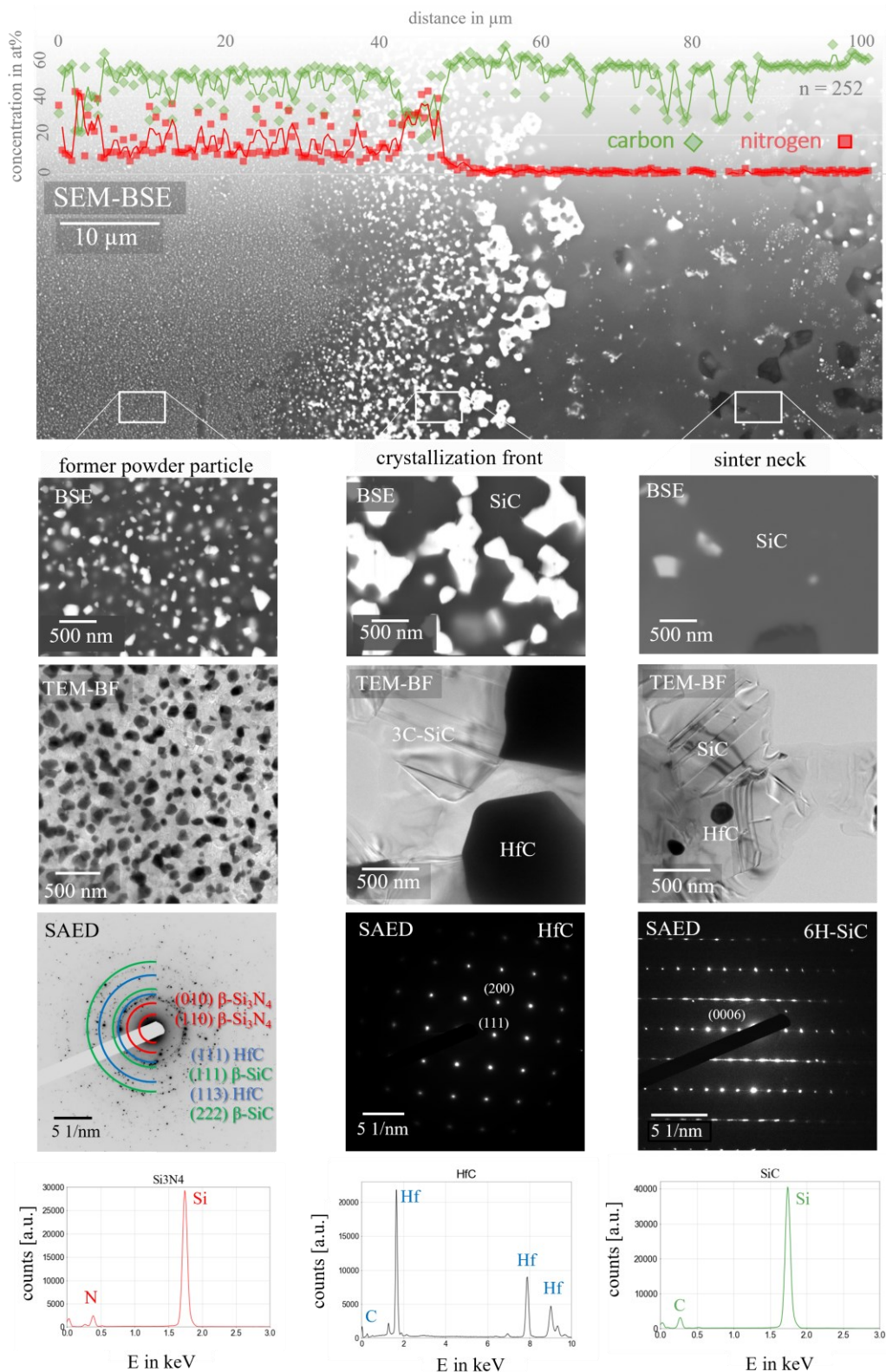


Figure 42 Microstructural characterization of the three different microstructure regions: former powder particle, crystallization front and sinter neck; SEM-BSE images and EDS element concentration profile of carbon and nitrogen of the consolidated SiHfCN₀₁ bulk ceramic. 251 individual point measurements starting from the inside of a former powder particle (left side), continue over to the crystallization front (middle) into the sinter neck (right side) of the cross-sectioned and polished SiHfCN₀₁. TEM-BF and corresponding SAED pattern in addition to EDS spectra of the constituting phases: Si₃N₄, TMC and SiC.

SiC occurs in all three microstructural regions; within the former powder particles, in the crystallization front and in the sinter necks. It occurs in the cubic structure (3C-SiC). Often, it can be seen in the twinned form. Twinning of SiC is observed within the former powder particles (marked with green-red arrows in Figure 43 a)) as well as in the sinter necks (compare Figure 43 b)). The highlighted square in Figure 43 b)) is shown as a HR-TEM image in Figure 43 c) and depicts the twin boundary. The respective diffraction pattern is taken once from the left twin boundary oriented along the $[110]$ zone axis (green label) and from the right twin boundary oriented along the $[-1-10]$ zone axis (red label). In addition, the SAED pattern in the centre shows both orientations (green and red label). The twinned structure is characteristic for SiC in the consolidated sample. It was not found after annealing in the microstructure of the Si(Hf,Ta)(C)N ceramic powder, see chapter 6.3.

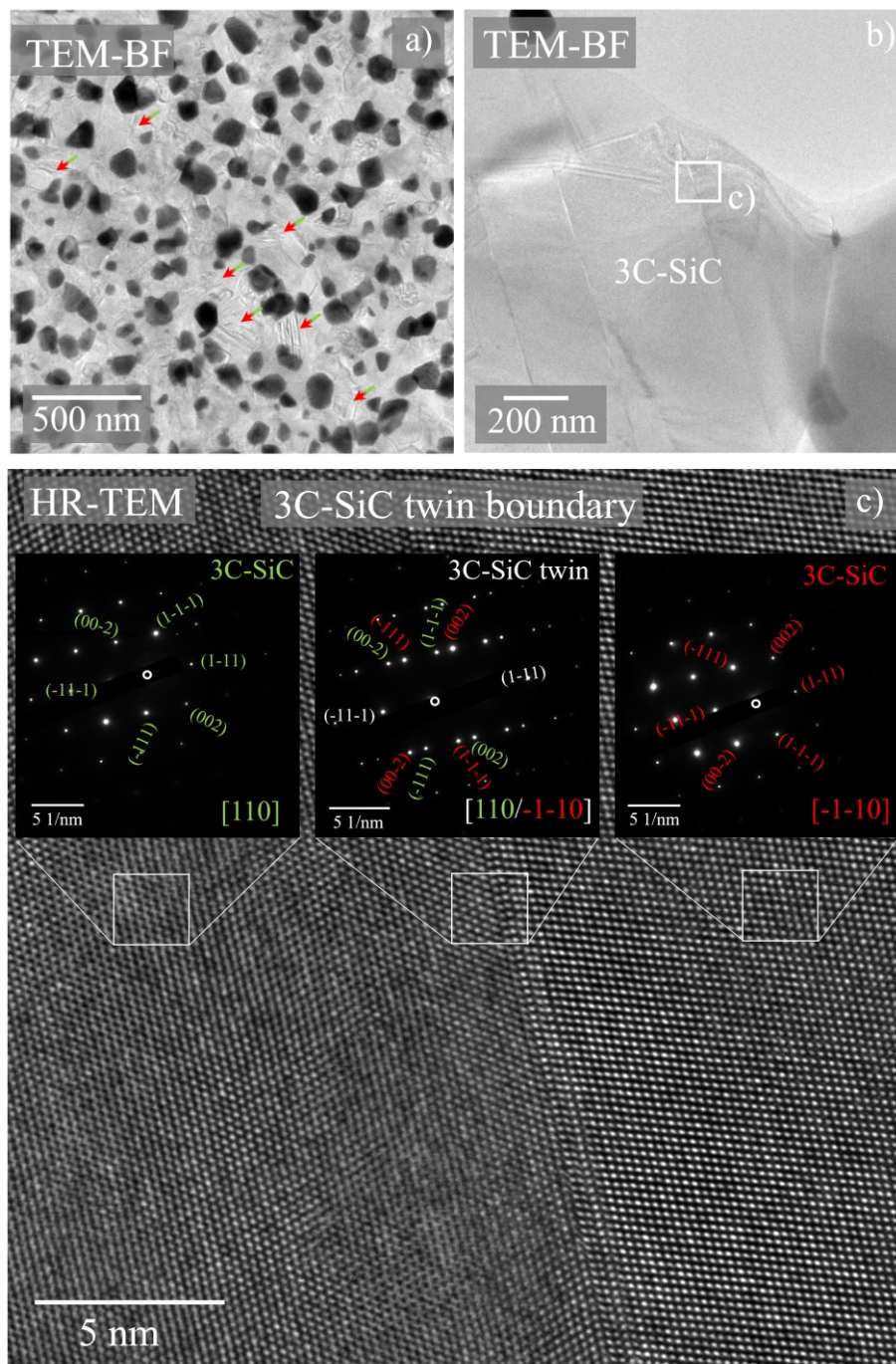


Figure 43 a, b) TEM-BF images, c) HR-TEM image and SAED patterns of the SiC-twin as insets in c).

5.2 Elemental Distribution Maps Using EPMA Analysis for SiHfCN_01

In order to confirm the elemental distribution of C and N on a larger scale, element distribution maps were taken using the electron probe microanalysis (EPMA). Figure 44 shows two distinct SEM-BSE images (upper image → maps are low magnified and lower image → maps are higher magnified) and their respective Si, Hf, C and N element distribution maps. The upper elemental distribution maps in Figure 44 show a large area containing numerous former powder particles, crystallization fronts and sinter necks, whereas the lower figure depicts a single former powder particle, the crystallization front and the surrounding sinter neck. Both EPMA maps show Hf being enriched at the inside of the former powder particles and even more enriched in the crystallization fronts in which predominantly increased grain sizes of HfC are detected (cf. Figure 42). Correlating to the Hf concentration is also the element distribution of C. The sintered necks mostly contain SiC and pores; therefore, the Si element concentration within the sinter necks is high.

The upper element distribution map of N shows that only five of the former powder particles show an enrichment of N. When correlating the N content with the SEM-BSE image, it can be seen that the regions where N is present are the same regions showing the finely dispersed particles in the microstructure, which was described in Figure 41 and Figure 42. As already shown in the EDS profiles in Figure 42, the elemental distribution map of a former powder particle confirms that N is enriched only in the former powder particle. Furthermore, there is a sharp boundary in the transition region between the interior and the crystallization front, where almost no nitrogen is present.

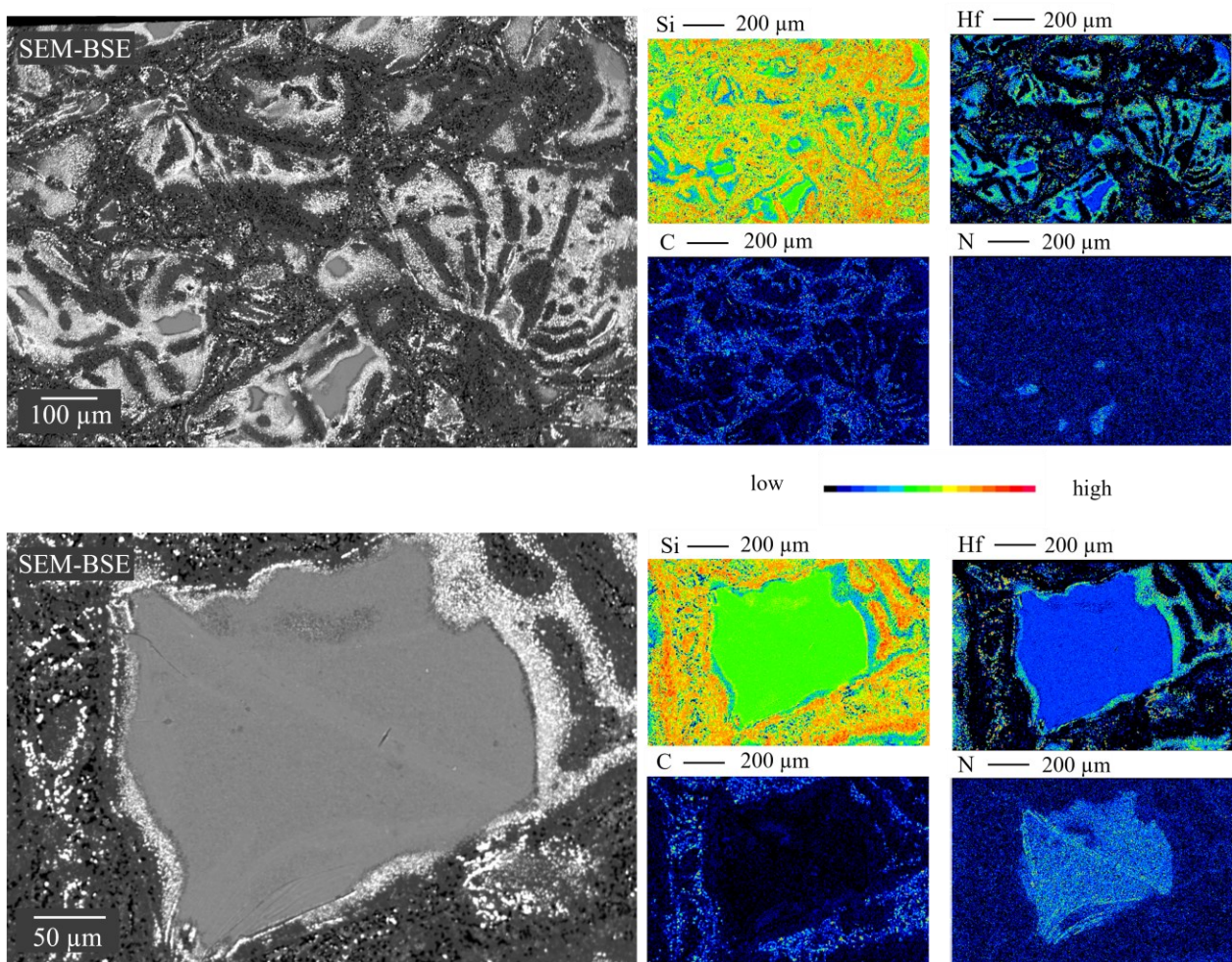


Figure 44 EPMA analysis giving a SEM-BSE image as overview and quantitative element distribution maps of Si, Hf, C, and N for the cross-sectioned and polished SiHfCN_01 bulk ceramic.

5.3 Microstructure Analysis by SEM and TEM for SiHfCN_02

SiHfCN_02 was sintered with a dwell time of 15 minutes. Figure 45 shows the two constituting phases of the SiHfCN_02 ceramic. Using electron diffraction in the TEM, it was shown that the phase composition in the SiHfCN_02 ceramic consists of only two phases, namely SiC and HfC, as confirmed by the SAED patterns and EDS spectra in Figure 45 a-c). The HfC grains in the SiHfCN_02 ceramic achieve large grain sizes, of up to 4 μm , as can be seen in Figure 45 a).

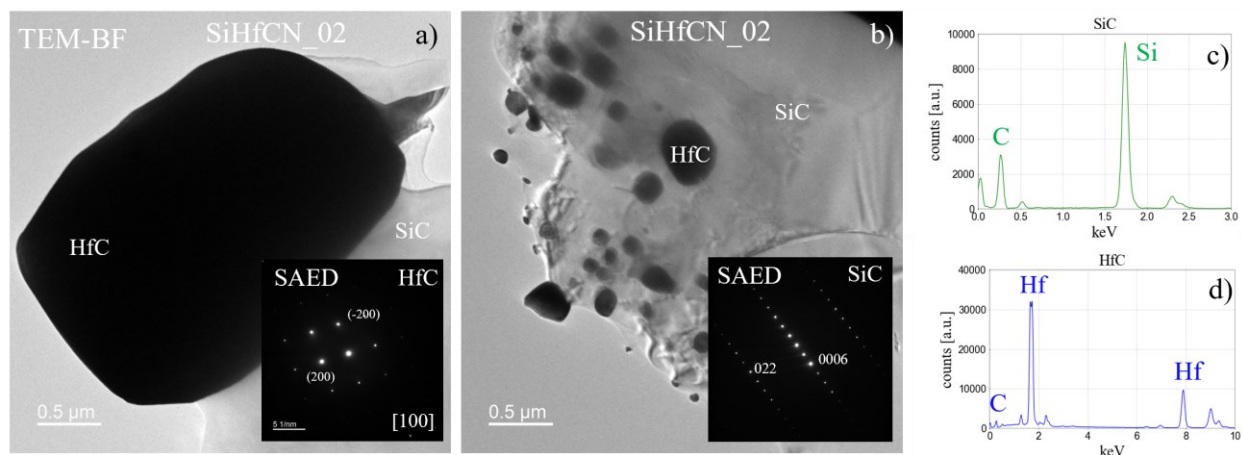


Figure 45 TEM-BF, SAED patterns and EDS spectra of the SiHfCN_02 ceramic.

5.4 Discussion

In the following, a brief comparison regarding the overall microstructures of both ceramics is anticipated. The respective SEM-BSE images of both SiHfCN composites on ground cross-sections are shown in Figure 46 (SiHfCN_01 ceramic, dwell time = 1 minute (left side) and SiHfCN_02, dwell time = 15 minutes (right side)). By comparing the SEM and TEM images of both ceramics, a fundamental difference in the microstructural appearance is noticeable. SiHfCN_01, contains four phases, namely Si_3N_4 , SiC, TMCs and interconnected pores (cf. Figure 42) and the inhomogeneous microstructure with former powder particles and sinter necks are visible. SiHfCN_02 in contrast contains only three phases, SiC, TMC and isolated pores (pores are as well not visible in TEM images in Figure 45). Further, the microstructure of the SiHfCN_02 ceramic is much more homogeneous, it does not show the former powder particle/sinter neck microstructure. Thus, after a dwell time of 15 minutes and a temperature of 1950 $^{\circ}\text{C}$, the thermal decomposition of Si_3N_4 is complete and no more nitrogen remains in the system. In addition, the prolonged dwell time resulted in a massive microstructural change including grain coarsening of TMCs. Furthermore, from the SEM-BSE images it seems as the pores are no longer interconnected but more isolated. Therefore, the microstructure of SiHfCN developed upon sintering from an intermediate stage for the SiHfCN_01 sample into a final sintering stage for the SiHfCN_02 sample (cf. Figure 15).

Although the synthesis and preparation of the SiHfCN ceramics have already been described in Ref. [65,66], a detailed macro- and microstructure analysis of SiHfCN_01 and SiHfCN_02 has been lacking. In previous investigations, attention was paid in particular to the sintering parameters and which sinter temperatures, dwell times and uniaxial pressures were able to achieve the highest density in the SiHfCN composition upon utilization of FAST. Thereby, the densification of SiHfCN at 1950 $^{\circ}\text{C}$ /1 minute/105 MPa and at 1950 $^{\circ}\text{C}$ /15 min/105 MPa both resulted in a density of 3.7 g/cm^3 [65]. The sinter parameters consolidating the as-pyrolyzed SiHfCN ceramic were also used in our study, as described in section 4.1. In particular, the image collage of SiHfCN_01 in Figure 40 displayed a massively heterogeneous microstructure, developed upon sintering. The microstructure contains the

remnants of former powder particles, which are held together by sinter necks, in which interconnected pores are observed. Particularly noticeable are the increased grain sizes of the HfC phase within the microstructural region of the crystallization fronts, as displayed in Figure 42. Nitrogen is still locked in the regions of the former powder particles. The consolidation via FAST leads to an enhanced built-up of sinter necks consisting of large SiC crystals and interconnected pores, which are not yet isolated, indicating that the microstructure of SiHfCN_01 has not reached the final densification state upon sintering with 1 minute of dwell time. In the following work, longer dwell times in the range of 15 - 20 minutes were identified for optimal consolidation during sintering.

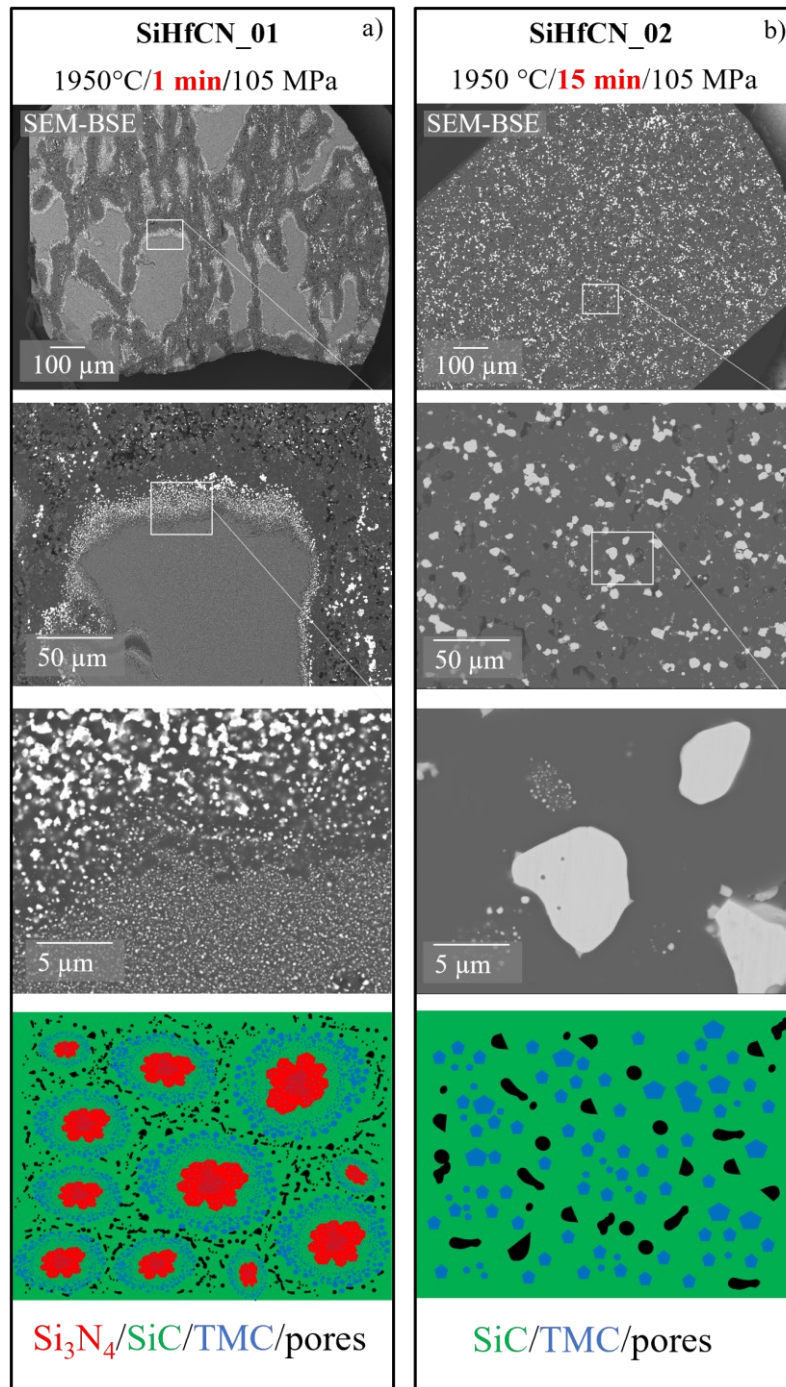


Figure 46 Microstructure comparison between SiHfCN_01 in a) and SiHfCN_02 in b). The difference between the sinter parameters of both ceramics lies in the dwell time. The microstructure and densification state of SiHfCN_01 are assigned to the intermediate sinter stage, whereas SiHfCN_02 is assigned to the final sinter stage with grain coarsening and isolated pores.

6 The Influence of Tantalum: $\text{Si}(\text{Hf}_x\text{Ta}_{1-x})\text{(C)N}$ and $\text{Si}_3\text{N}_4/\text{SiC}/(\text{Hf}_x\text{Ta}_{1-x})\text{(C)N}$

Based on the preliminary investigations by C. Zhou, J. Yuan and Q. Wen in Refs [41,47,61,62,65,66] (cf. section 2.10.1 and 2.10.2), Tantalum was added to allow the formation of a solid solution of a transition metal carbide $(\text{Hf}_x\text{Ta}_{1-x})\text{C}$, which shows the highest ever known melting temperature (cf. chapter 2.2). A chemical modification in the synthesis procedure of the single-source precursor in terms of the organometallic complex was introduced by J. Bernauer (cf. section 4.2). The addition of PDMAT (as organo-metallic complex for Tantalum) to the known $\text{SiHf}(\text{C)N}$ [66] nanocomposite (cf. chapter 5) results in a novel ceramic nanocomposite, namely $\text{Si}(\text{Hf}_x\text{Ta}_{1-x})\text{(C)N}$ (cf. section 4.2). Because the synthesized material represents a new material, which to the best of our knowledge was not previously reported in the literature, a fundamental characterization is necessary. Thus, the microstructure development as well as phase characterization and crystallization behaviour are unknown until yet. Accordingly, the following chapter focuses on the detailed characterization of the novel as-pyrolyzed (1000 °C) and annealed (1600 °C) $\text{Si}(\text{Hf}_x\text{Ta}_{1-x})\text{(C)N}$ system, where $M = \text{Hf}$ and Ta with $x = 0.7$ and $x = 0.2$. By analyzing the phase assemblage in combination with the high-temperature microstructural evolution, valuable feedback on the evolving phases is given to J. Bernauer, in order to adjust the synthesis. It is expected that this novel as-pyrolyzed $\text{Si}(\text{Hf}_x\text{Ta}_{1-x})\text{(C)N}$ ceramic powder is suitable for high-temperature sintering in order to prepare a dense bulk ceramic on which mechanical properties and oxidation tests will be carried out.

In general, the microstructure characteristics of the novel polymer-derived ceramics in the Hf-rich $\text{Si}(\text{Hf}_{0.7}\text{Ta}_{0.3})\text{(C)N}$ or the Ta-rich $\text{Si}(\text{Hf}_{0.2}\text{Ta}_{0.8})\text{(C)N}$ compositions were found to be very similar. Consequently, the electron microscopy results are shown as example for either the Hf-rich or the Ta-rich ceramics, as only the molar Hf:Ta ratios were altered during the polymer synthesis.

6.1 Phase Assemblage Determined via XRD Analysis

Figure 47 a) illustrates the X-ray diffractograms of the $\text{Si}(\text{Hf}_{0.2}\text{Ta}_{0.8})\text{(C)N}$ ceramic (black line) and the $\text{Si}(\text{Hf}_{0.7}\text{Ta}_{0.3})\text{(C)N}$ ceramic (red line) powder particles after pyrolysis at 1000 °C for 3 hours in an ammonia (NH_3) atmosphere (cf. Figure 12). The patterns exhibit two broad peaks at around 17° and 30° which demonstrate a mainly XRD-amorphous structure. The shape of the first peak suggests the additional presence of nanoparticles. X-ray diffraction (XRD) has a detection limit of approximately 1-2 vol%, which makes the identification of low-content and nano-sized precipitates challenging [54]. However, high-resolution scanning electron microscopy (HR-SEM) and TEM imaging clearly confirmed the existence of such nanocrystals at the surface of the as-pyrolyzed ceramic powder particles (cf. Figure 49, Figure 50 and Figure 52).

The X-ray powder diffractogram of the $\text{Si}(\text{Hf}_{0.2}\text{Ta}_{0.8})\text{(C)N}$ ceramic powder sample (black line) and the $\text{Si}(\text{Hf}_{0.7}\text{Ta}_{0.3})\text{(C)N}$ ceramic powder sample (red line) after an 3 h annealing step at 1600 °C in a nitrogen (N_2) atmosphere is shown in Figure 47 b). The amorphous pattern observed in the as-pyrolyzed ceramic powder samples disappeared completely, and sharp reflections become visible. According to the XRD pattern in Figure 47 b), annealing at high temperatures induced the crystallization of $\alpha\text{-Si}_3\text{N}_4$ (PDF 41–0360), $\beta\text{-Si}_3\text{N}_4$ (PDF 33–1160), $\beta\text{-SiC}$ (PDF 29–1129) and solid solutions of the two TMCs, namely $(\text{Hf}_{0.2}\text{Ta}_{0.8})\text{C}$ and $(\text{Hf}_{0.7}\text{Ta}_{0.3})\text{C}$. The reflections of the Hf-rich solid solution $(\text{Hf}_{0.7}\text{Ta}_{0.3})\text{C}$ refer to pure HfC (PDF 39–1491), while the reflections of the Ta-rich solid solution $(\text{Hf}_{0.2}\text{Ta}_{0.8})\text{C}$ refer to pure TaC (PDF 35–0801). [84]

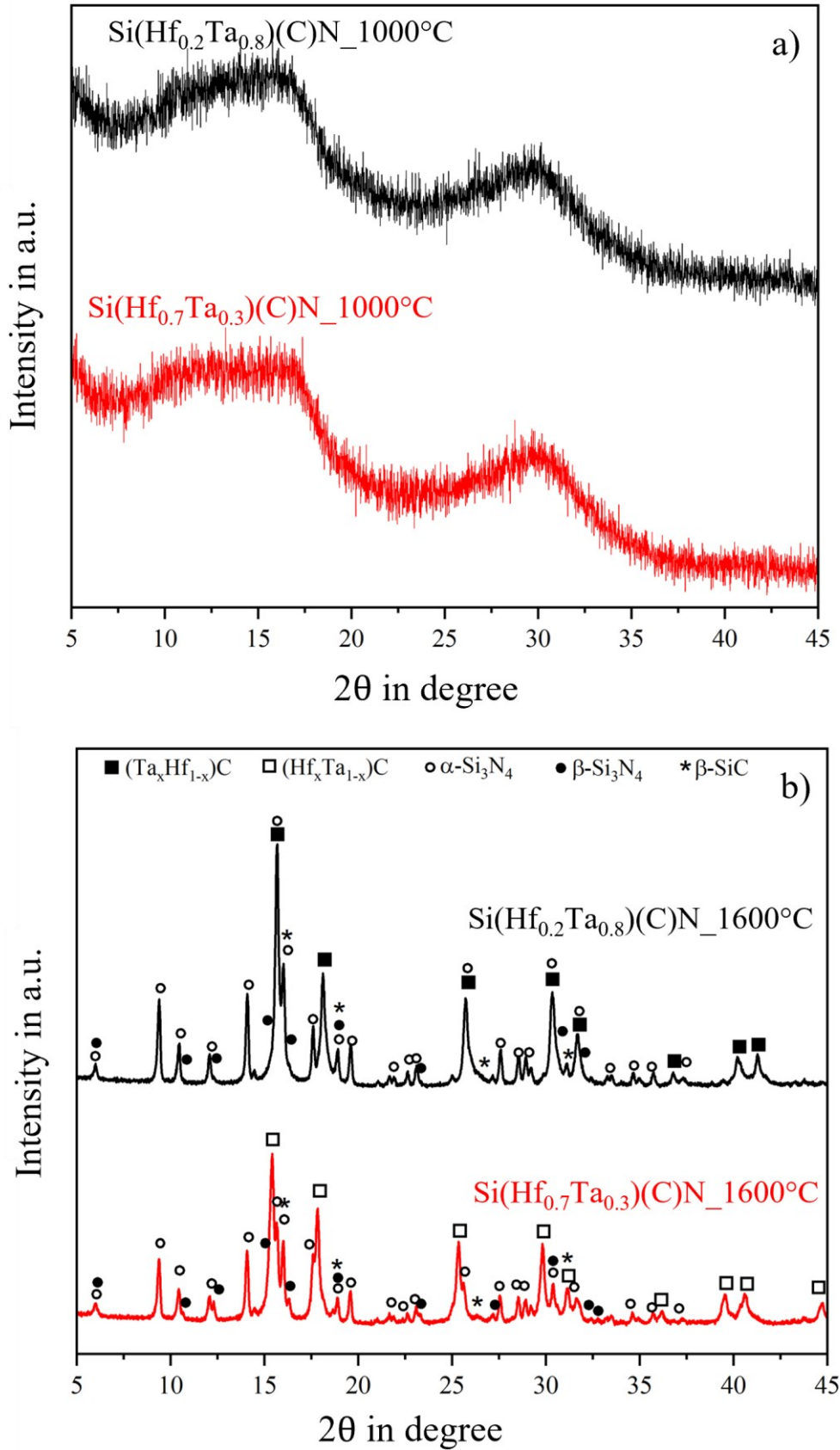


Figure 47 XRD patterns of the as-pyrolyzed and annealed Hf-rich and Ta-rich Si(Hf_xTa_{1-x})(C)N polymer-derived ceramic powders. X-ray powder diffraction diffractogram of a) both as-pyrolyzed ceramic samples. and b) the annealed ceramic samples. The Ta-rich compositions are shown in black color, the Hf-rich compositions are presented in red. Figure adapted from Ref. [84].

6.2 Microstructure of As-pyrolyzed $\text{Si}(\text{Hf}_x\text{Ta}_{1-x})\text{(C)N}$ PDCs, ($x=0.7$ and $x=0.3$)

The microstructure of the $\text{Si}(\text{Hf}_{0.7}\text{Ta}_{0.3})\text{(C)N}$ ceramics, pyrolyzed for 3 hours at $1000\text{ }^\circ\text{C}$ in a NH_3 atmosphere was examined using SEM. In low magnified SEM-BSE images, the surface of the powder particles presents a mostly featureless morphology, showing only a few crystallites/precipitates or individual grains. Figure 48 shows the overall appearance of the pulverized powder particles. [84]

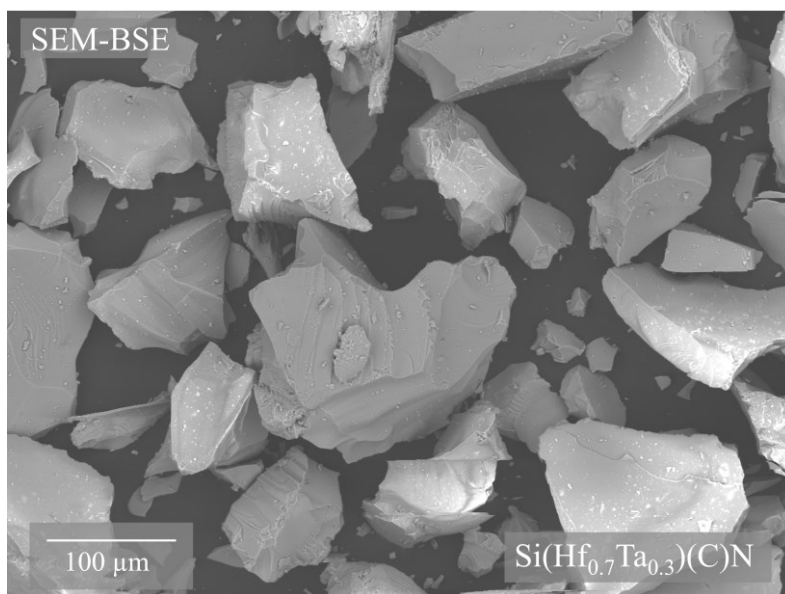


Figure 48 SEM-BSE image of the as-pyrolyzed $\text{Si}(\text{Hf}_{0.7}\text{Ta}_{0.3})\text{(C)N}$ ceramic powder. Figure taken from Ref. [84].

Further investigations revealed two microstructurally different regions present within some of the imaged powder particles. This becomes particularly clear in Figure 49, where a fracture surface of a powder particle is depicted. Finely distributed, small, roundish precipitates are visible on the surface of this particle, see Figure 49 b). Within the SEM-BSE image a distinction between two microstructure regions is possible: the initial particle surface area with small precipitates (sizes of up to $\sim 0.5\ \mu\text{m}$) and a bulk area with a very massive microstructure, labeled as bulk region in Figure 49 b). [84]

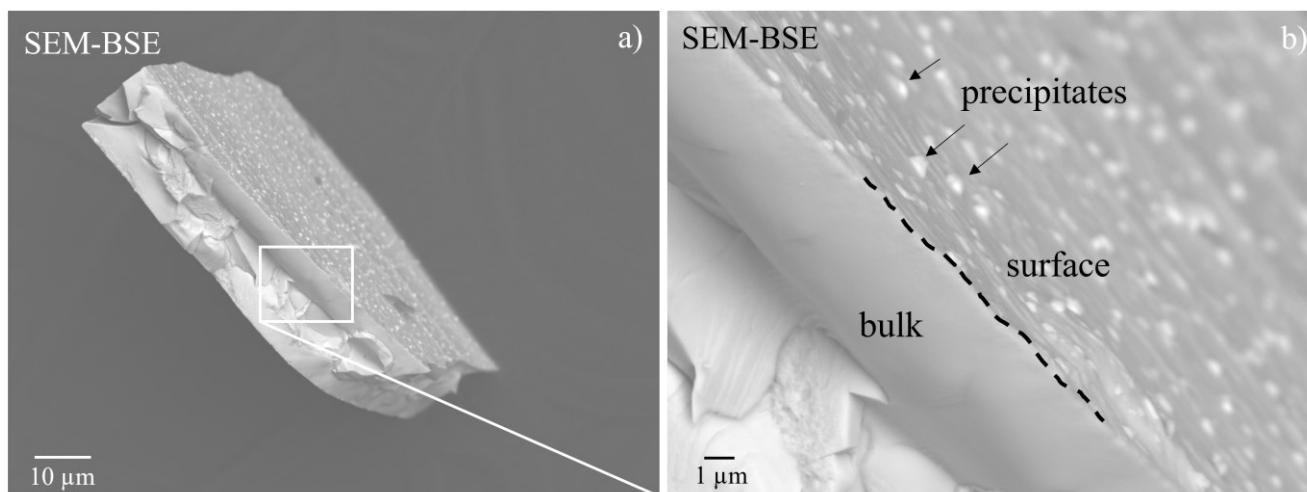


Figure 49 SEM-BSE images showing a fracture surface of a the as-pyrolyzed $\text{Si}(\text{Hf}_x\text{Ta}_{1-x})\text{(C)N}$ polymer-derived ceramic powder particle with two microstructurally different regions present: the surface region and the bulk region; a) Overview of the whole particle; b) on the surface, nano-sized precipitates are marked with black arrows.

High-resolution SEM images (cf. Figure 50) revealed dispersed precipitates on the surface of individual powder particles (cf. Figure 50 a)). also visible in the SE image (cf. Figure 50 b)) and BSE image (Figure 50 d)). These nanoparticles exhibited particle sizes ranging from 5 to 50 nm, and their morphology appeared nearly spherical (Figure 50 b)). The SEM-SE image in Figure 50 b)) provided information about surface topography and nanoparticle size, while the SEM-BSE image in Figure 50 d) highlighted the chemical contrast between the nanoparticles (appearing bright) and the underlying matrix phase (appearing darker) due to its atomic number sensitivity (Z-contrast, see section 3.5.1). Chemical analysis using EDS indicated an enrichment of Hf and C, and a depletion in N in the nanoparticles when compared to the matrix (dashed red lines), which is shown by the continuous blue line in the EDS spectrum in Figure 50 c)). It is important to note that the EDS measurements on nano-sized crystallites in SEM are affected by the large interaction volume (of about $4\ \mu\text{m}$) of the incident electron beam. Additionally, background and/or underlying phases also contribute to the recorded EDS spectra at single measurement points. This leads to deviations from the exact composition (cf. Figure 28). Consequently, the relatively strong N peak (Figure 50 c)) originates from the underlying matrix phase, which is primarily composed of Si, N, and C, and is depicted by the dashed red line in the EDS spectrum in Figure 50 c)). It is reduced by the presence of the nanoparticles laying on its surface.[84]

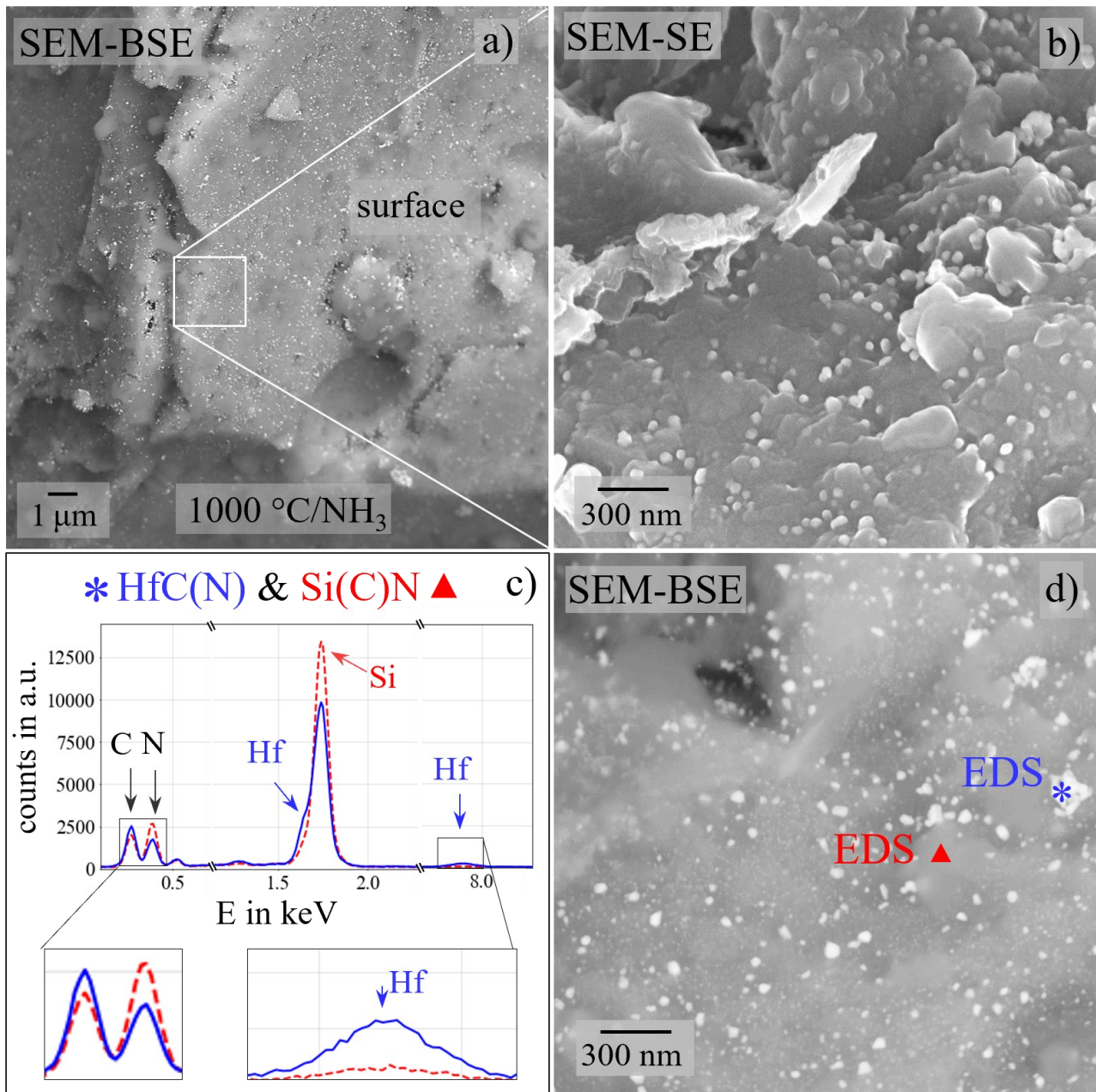


Figure 50 SEM-BSE (a, d) and SEM-SE (b) images of the as-pyrolyzed $\text{Si}(\text{Hf}_{0.7}\text{Ta}_{0.3})(\text{C})\text{N}$ polymer-derived ceramic powder sample, showing the powder particle surface with nano-sized precipitates; c) EDS spectra showing the difference between the two microstructural regions. The Hf-rich precipitate is marked with the blue star symbol in d), the corresponding spectrum is shown in blue in c), whereas the red triangle in d) represents the SiCN phase; the respective spectrum is shown in red in c). The indexed elements correspond to the characteristic X-ray energies: C ($K\alpha$), N ($K\alpha$), Si ($K\alpha$), Hf ($M\alpha$, $L\alpha$). Figure adapted from Ref. [84].

Also, TEM bright-field (TEM-BF) images revealed a distinct microstructure within the two different regions. Again, these two regions were identified as bulk and surface region of individual powder particles. Since the investigated samples were powders, each individual powder particle within the powder sample is considered as an individual system in this study. The bulk region displayed a featureless microstructure with a homogeneous amplitude contrast as shown in Figure 51. The selected area electron diffraction (SAED) pattern (inset in Figure 51 a)) along with the high-resolution TEM (HR-TEM) image (Figure 51 b)) confirmed that the bulk regions were amorphous. EDS point measurements

within the bulk region confirm the presence of Si, Hf, Ta, C, N and O (cf. Figure 51 c)). [84] The Hf:Ta ratio was determined with Hf:Ta = 0.19:0.81 (± 0.01) (for details see Table A 2 in the appendix).

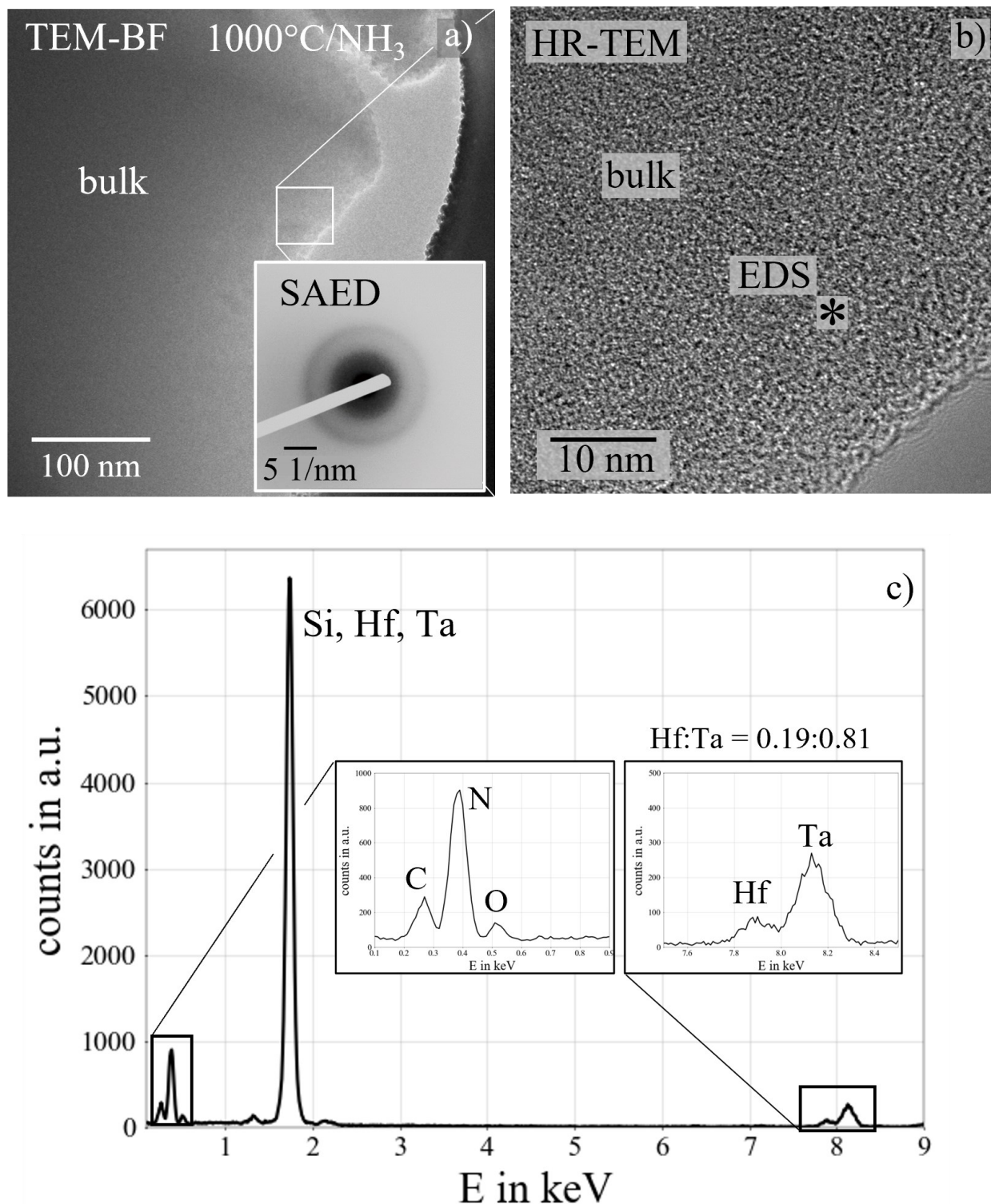


Figure 51 TEM-BF and HR-TEM images representing the amorphous microstructure of the bulk region within the as-pyrolyzed $\text{Si}(\text{Hf}_{0.2}\text{Ta}_{0.8})(\text{C})\text{N}$ polymer-derived ceramic powder. The inset in a) shows a distinct diffuse SAED pattern; the HR-TEM image in b) depicts the amorphous nature of the bulk regions, where the star symbol marks the location of the EDS point measurement; c) the corresponding EDS spectrum of the amorphous bulk region is shown exemplarily with the containing elements correlated as follows: C (K_{α}), N (K_{α}), O (K_{α}), Si (K_{α}), Hf (M_{α} , L_{α}), and Ta (M_{α} , L_{α}). The Hf:Ta ratio is Hf:Ta = 0.19:0.81 (± 0.01).

The surface regions of the powder particles exhibited a different microstructure. As observed in the SEM micrographs (cf. Figure 49, Figure 50), TEM analysis confirmed the presence of small crystallites (nanoparticles) in the surface regions of the powder particles. The HR-TEM micrographs in Figure 52 a) and b) revealed nano-sized crystallites ranging from 5 to 20 nm, as indicated by black arrows. The size of these nanoparticles was slightly smaller than those observed in SEM, which can be attributed to the specific region studied in TEM. The SAED pattern originating from this surface region displayed distinct diffraction rings (cf. inset in Figure 52 a)) and some broad spots related to dispersed crystalline nano-sized particles. The SAED ring pattern was indexed as $(\text{Hf}_{0.2}\text{Ta}_{0.8})\text{CN}$, indicating the presence of transition metal carbonitrides (TMCNs). The EDS spectra presented in Figure 52 c) provided the chemical compositions of the residual amorphous phase (shown in red) adjacent to the nano-crystalline TMCN precipitates (shown in blue), which are present in/or on the surfaces of the powder particles. The EDS spectrum of the amorphous area (depicted with the red line) mainly showed element intensities of Si, Hf, Ta, N and slight peaks of C and O, while Si is missing in the crystalline precipitates in the surface regions (depicted with the blue line). The Hf:Ta ratio of the TMCNs is $\text{Hf:Ta} = 0.19:0.81 (\pm 0.03)$ determined via individual EDS measurements (for details see Table A 3 in the appendix). Based on the chemical analysis in conjunction with electron diffraction, the precipitation of nano-sized crystalline TMCNs on the surface of individual powder particles was confirmed. The TMCNs at the surface and in the surface-near regions exhibited a wide particle-size distribution, ranging from approximately 5 nm (Figure 52 b)) to about 500 nm (observed in SEM, Figure 49 b)) for the largest crystallite size. The crystalline TMCN particles possess a thin layer (1-2 nm) of residual carbon surrounding the TMCNs (cf. Figure 52 b)). The two studied systems (Hf-rich vs. Ta-rich) exhibited very similar micro- and nanostructures upon pyrolysis at 1000 °C, with an amorphous bulk region and the nano-sized precipitates of TMCNs surrounded with a carbon shell at powder particle surface regions. No significant difference was observed between the two novel polymer-derived ceramic systems. [84]

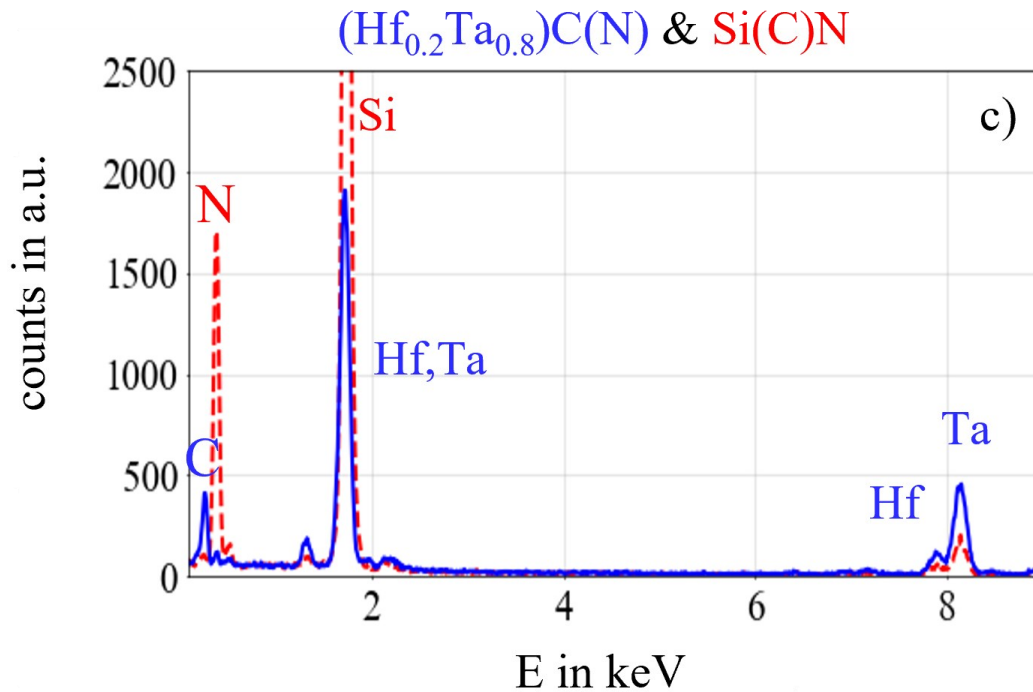
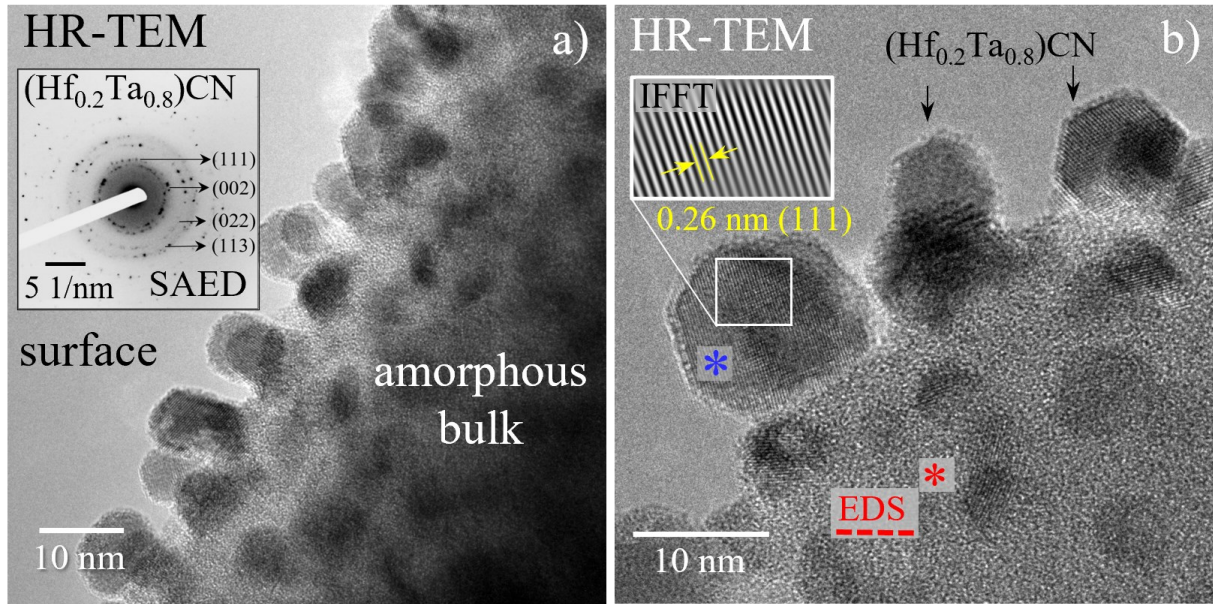


Figure 52 TEM micrographs of the $\text{Si}(\text{Hf}_{0.2}\text{Ta}_{0.8})\text{(C)N}$ polymer-derived ceramic powder sample pyrolyzed at $1000\text{ }^\circ\text{C}$ in NH_3 atmosphere; a) TEM-BF image of the particle surface with nano-sized TMCN precipitates, b) HR-TEM image with inset of IFFT image, giving information of the lattice spacings of the TMCN, c) two EDS spectra of the mostly amorphous bulk region (shown in red) and the nano-sized TMCN phase (shown in blue). The elements in the EDS spectra are indexed via their characteristic X-ray energies as follows: C (K_α), N (K_α), Si (K_α), Hf (M_α, L_α), Ta (M_α, L_α). The Hf:Ta ratio of the precipitates (blue EDS spectrum) is Hf:Ta = 0.19:0.81 (± 0.03).

6.3 Microstructure of Annealed $\text{SiC/Si}_3\text{N}_4/(\text{Hf}_x\text{Ta}_{1-x})\text{(C)N}$ PDCs, ($x=0.7$ and $x=0.3$)

The microstructure of the polymer-derived ceramics within the $\text{Si}(\text{Hf}_x\text{Ta}_{1-x})\text{(C)N}$ system was investigated after pyrolysis and a subsequent annealing step at $1600\text{ }^\circ\text{C}$ for 3 hours in a nitrogen (N_2) atmosphere. Upon annealing a fully crystalline ceramic powder was obtained, as shown in the XRD pattern of Figure 47 b). Individual powder particle microstructure are characterized at surface and bulk regions, in accordance to chapter 6.2 and the corresponding Figure 49 - 47). [84]

6.3.1 Microstructure of the Surface Region

SEM imaging of the powder sample after the heat treatment gives a completely different topography of the powder particles with respect to the pyrolyzed powder, as can be seen by comparing Figure 48 with Figure 53. The annealed powder particles no longer show any featureless microstructure like it was the case for the pyrolyzed powder particles. Instead, each individual powder particle depicts an individual microstructural appearance, as can be seen in Figure 53.

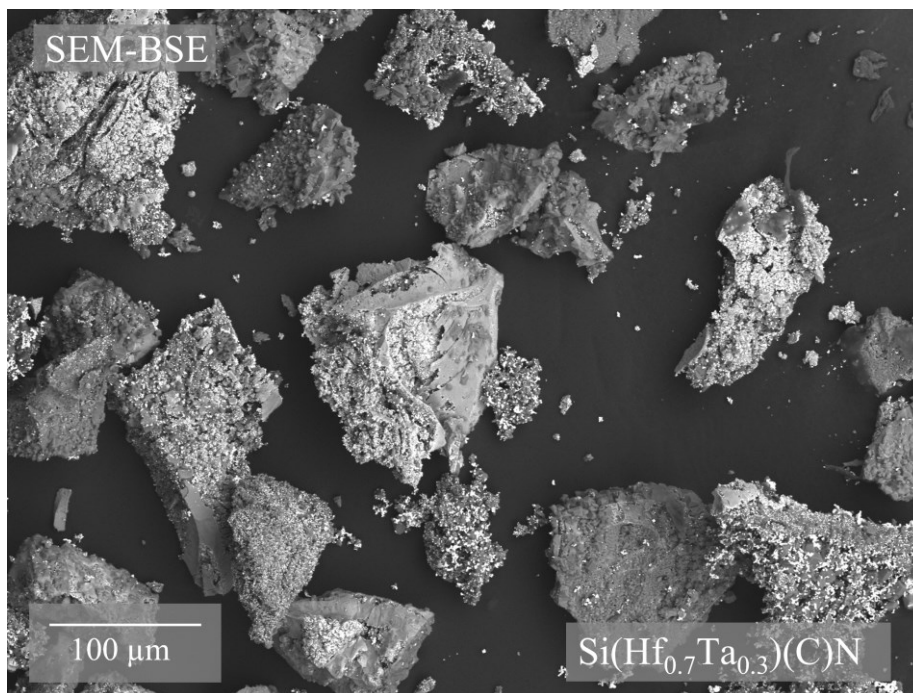


Figure 53 SEM-BSE image of the surface topography of the annealed $\text{Si}(\text{Hf}_x\text{Ta}_{1-x})(\text{C})\text{N}$ ceramic powders. Figure published in Ref. [84].

The microstructure of an individual powder particle, with specific emphasis on the surface region, is depicted in the SEM-SE and SEM-BSE micrographs as well as the EDS measurements presented in Figure 54. The surface region exhibits a rough topography characterized by relatively coarse $(\text{Hf}_{0.2}\text{Ta}_{0.8})\text{C}$ grains with idiomorphic crystals with sizes of up to $\sim 1 \mu\text{m}$ (cf. Figure 54 a-f)). Figure 54 e) shows the surface region where two different phases are present. Based on EDS point measurements, shown in Figure 54 g) and h), the constituting phases in the surface region are SiC and TMC (this will be confirmed later with electron diffraction in TEM, cf. Figure 55). The bulk region, indicated as "bulk" in Figure 54 a) and d) consist of a dense structure, where no individual particles are observable. A detailed description regarding the microstructure of the bulk region will be given later in section 6.3.2.

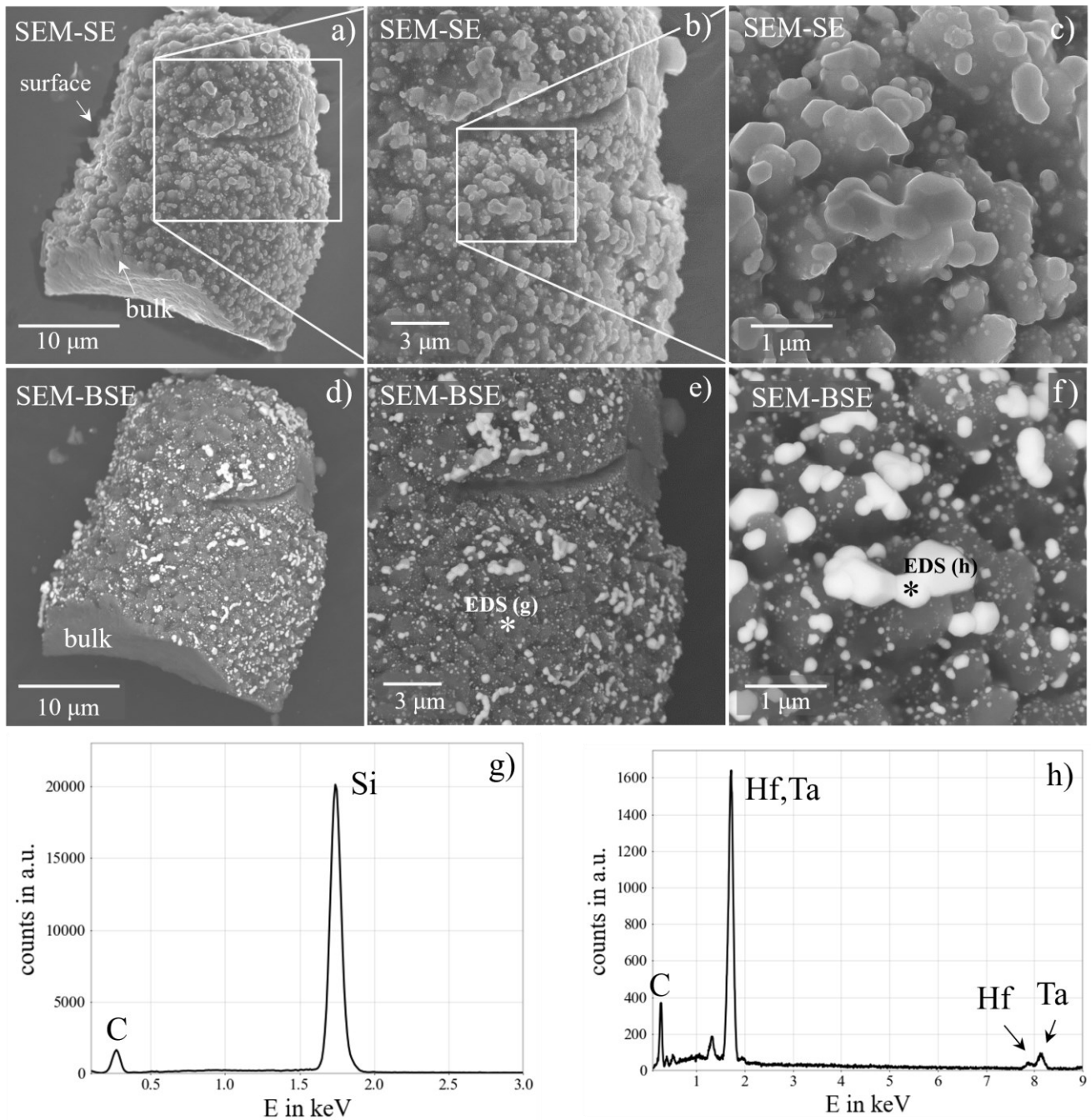


Figure 54 SEM-SE, SEM-BSE micrographs of an individual powder particle of the annealed $\text{Si}(\text{Hf}_{0.2}\text{Ta}_{0.8})\text{CN}$ polymer-derived ceramic. In addition, g) and h) show two EDS spectra giving information on the chemistry of the constituent phases present at the surface region. For the spectrum in g) the constituting elements are: C (K_{α}) and Si (K_{α}). For the spectrum in h) the elements are: C (K_{α}), Hf (M_{α} , L_{α}) and Ta (M_{α} , L_{α}). Figure adapted from Ref. [84].

The microstructure of a typical surface region is presented in Figure 55 utilizing various conventional TEM techniques such as TEM-BF, HR-TEM, the SAED technique, and EDS. The TEM-BF images in Figure 55 a) and d) exhibit dark grains, representing Ta-rich TMCs ($\text{Hf}_{0.2}\text{Ta}_{0.8})\text{C}$. The chemical information is given in the EDS spectrum in Figure 55 h). The Hf:Ta ratio of the TMC is Hf:Ta = 0.22:0.78. HR-TEM images shown in Figure 55 b) and e) reveal the presence of a thin carbon layer of 3 - 5 nm, encapsulating the constituent phases. HR-TEM imaging and the corresponding SAED pattern identify the crystalline phases as β -SiC and ($\text{Hf}_{0.2}\text{Ta}_{0.8})\text{C}$, respectively. Figure 55 b) and c) show the HR-TEM image and the

corresponding SAED pattern of SiC, whereas Figure 55 e) and f) depict the HR-TEM image and the SAED pattern of the TMC. It is known from literature and the phase diagram shown in Figure 7, that cubic HfC and TaC form solid solutions, denoted as $(\text{Hf}_x\text{Ta}_{1-x})\text{C}$, with a rock-salt (NaCl) structure [42] (refer to chapter 2.2). The relationship between the lattice parameters and the x-values follows Vegard's law [42,46]. The standard lattice parameters for stoichiometric HfC and TaC are 4.641 Å and 4.456 Å, respectively [238]. After Vegard's law the lattice parameter for $(\text{Hf}_{0.7}\text{Ta}_{0.3})\text{C}$ is calculated with 4.585 Å, for $(\text{Hf}_{0.2}\text{Ta}_{0.8})\text{C}$ it is 4.493 Å. In addition to solid solutions carbides $(\text{Hf}_x\text{Ta}_{1-x})\text{C}$, pure TaC was sporadically observed within the phase assemblage of the Ta-rich powder, as depicted in Figure 58. [84]

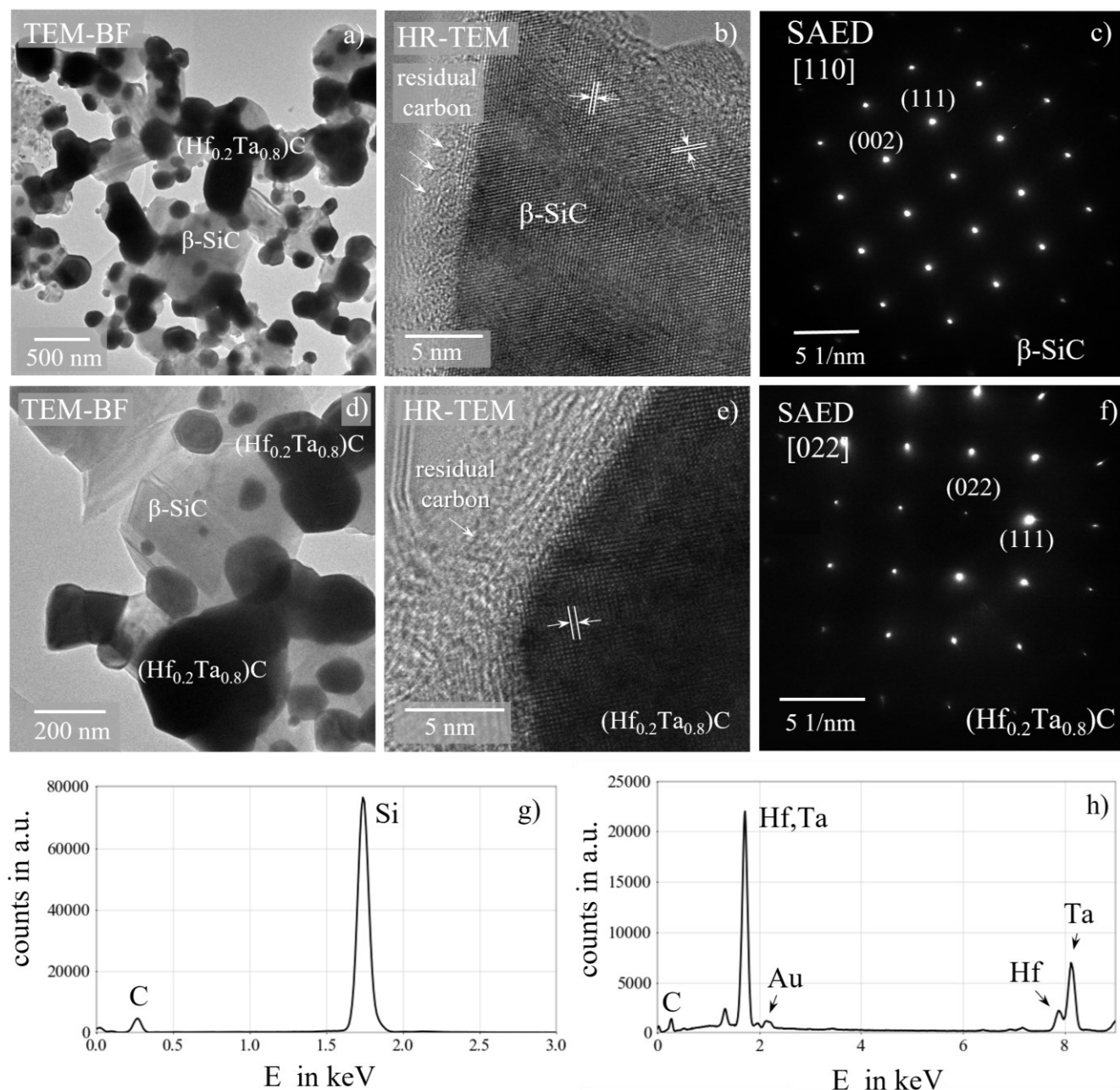


Figure 55 a, d) TEM-BF, b, e) HR-TEM images, c, f) SAED patterns and g, h) EDS spectra showing the phase assemblage of the surface region within the annealed $\text{Si}(\text{Hf}_{0.2}\text{Ta}_{0.8})(\text{C})\text{N}$ PDC. The surface regions constitutes SiC and $(\text{Hf}_{0.2}\text{Ta}_{0.8})\text{C}$ with a Hf:Ta ratio = 0.22:0.78. Each carbide is encapsulated by a thin residual carbon layer/shell. For the EDS spectrum in g) the characteristic X-ray energies are correlated as follows: C (K_α) and Si (K_α). For the spectrum in h) the elements are: C (K_α), Hf (M_α , L_α) and Ta (M_α , L_α). Figure adapted from Ref. [84].

Imaging of the annealed powder samples shows that various crystal sizes and shapes have formed on the surfaces of individual ceramic powder particles. Figure 56 shows large idiomorphic Si_3N_4 crystals, and also SiC whiskers (cf. Figure 56 h), i)). Furthermore, idiomorphic crystal shapes of the TMCs have formed. In general, these images demonstrate the grain size variations of the TMCs. In particular, relatively large TMCs with grain sizes of up to $\sim 3 \mu\text{m}$ can be seen very well in Figure 56 b), whereas rather small developed TMCs with grain sizes smaller than 200 nm are depicted on Figure 56 c). In addition, the different surface regions shown in Figure 56 point out that no powder particle is like the other. Furthermore, it can be seen that surface crystallization has produced very inhomogeneous shapes and sizes of the constituting phases.

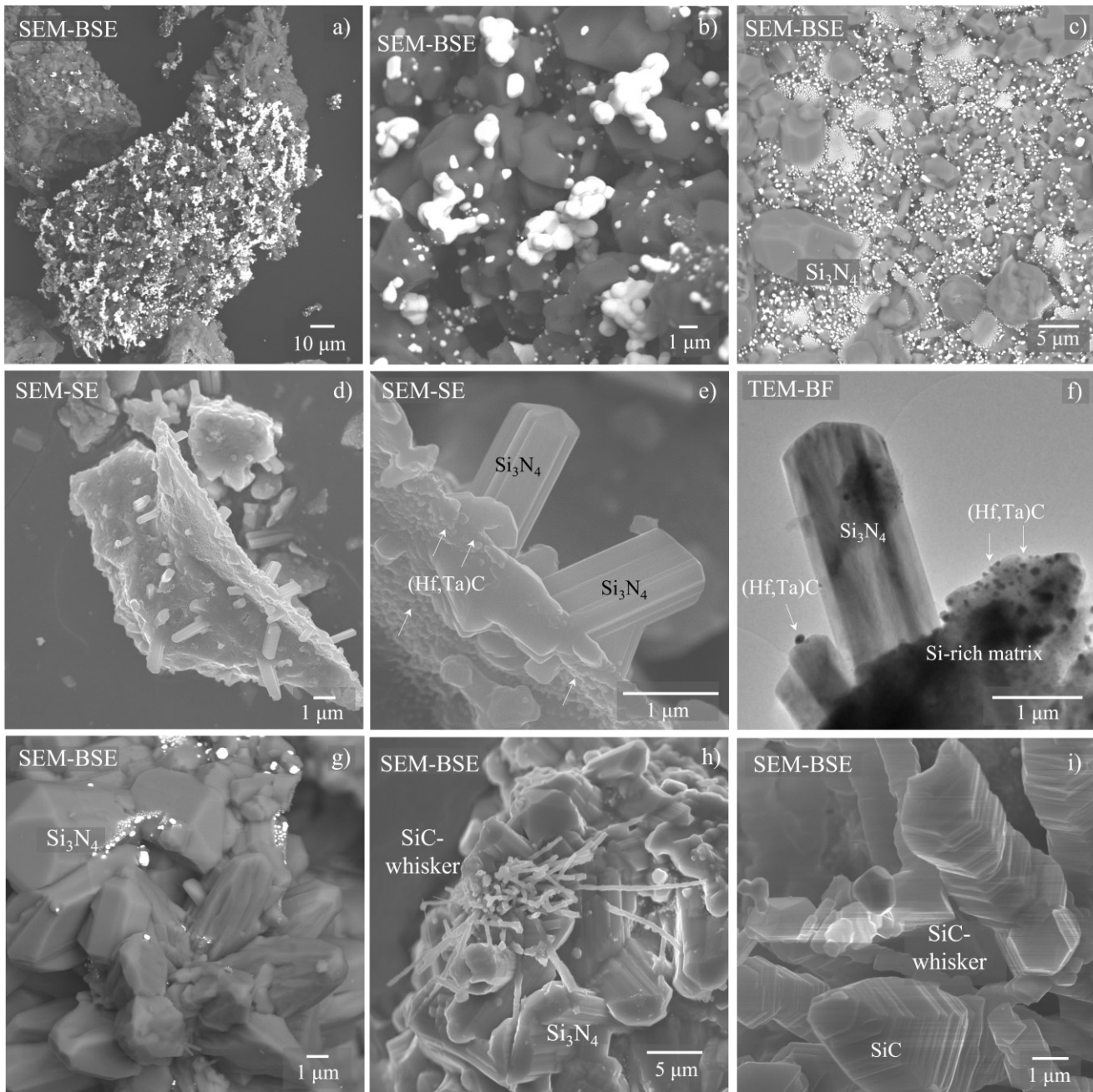


Figure 56 SEM and TEM images showing pronounced crystal growth at surface regions of the annealed $\text{Si}(\text{Hf}_{0.7}\text{Ta}_{0.3})(\text{C})\text{N}$. a, b, c, g, h, i) SEM-BSE images, d, e,) SEM-SE images and f) TEM-BF micrograph of idiomorphic silicon nitride (Si_3N_4) next to silicon carbide (SiC) whiskers.

6.3.2 Microstructure of the Bulk Region

A typical appearance of the microstructure in the bulk region is shown in the TEM-BF images presented in Figure 57 a), b). Upon the annealing temperature of 1600°C , the initially amorphous bulk material underwent crystallization and phase separation, resulting in the formation of Si_3N_4 as matrix phase with embedded small crystallites of TMCNs. The EDS spectrum in Figure 57 c) obtained at one of the small crystallite shows the presence of elements such as Hf, Ta, C and N with a Hf:Ta ratio of Hf:Ta=0.72:0.28 (± 0.14) (for details see Table A 4 in the appendix), while the EDS spectrum in Figure 57 f) taken from the surrounding matrix indicates the presence of Si and N. The HR-TEM image in Figure 57 d) reveals the presence of beta-silicon nitride ($\beta\text{-Si}_3\text{N}_4$) within the bulk region, along with embedded nano-sized TMCNs ($(\text{Hf}_{0.7}\text{Ta}_{0.3})\text{CN}$). The SAED pattern shown in Figure 57 e) demonstrates that the Si_3N_4 is oriented

along the $[1\bar{1}1]$ zone axis. Thus, the matrix phase is composed of Si_3N_4 grains, which can reach sizes of up to $1\ \mu\text{m}$. Within the Si_3N_4 matrix phase, the nano-sized $(\text{Hf}_{0.7}\text{Ta}_{0.3})\text{CN}$ particles with sizes of up to $10\ \text{nm}$ were the first to crystallize. Consequently, during the crystallization process, the TMCNs become enclosed within the Si_3N_4 matrix. [84]

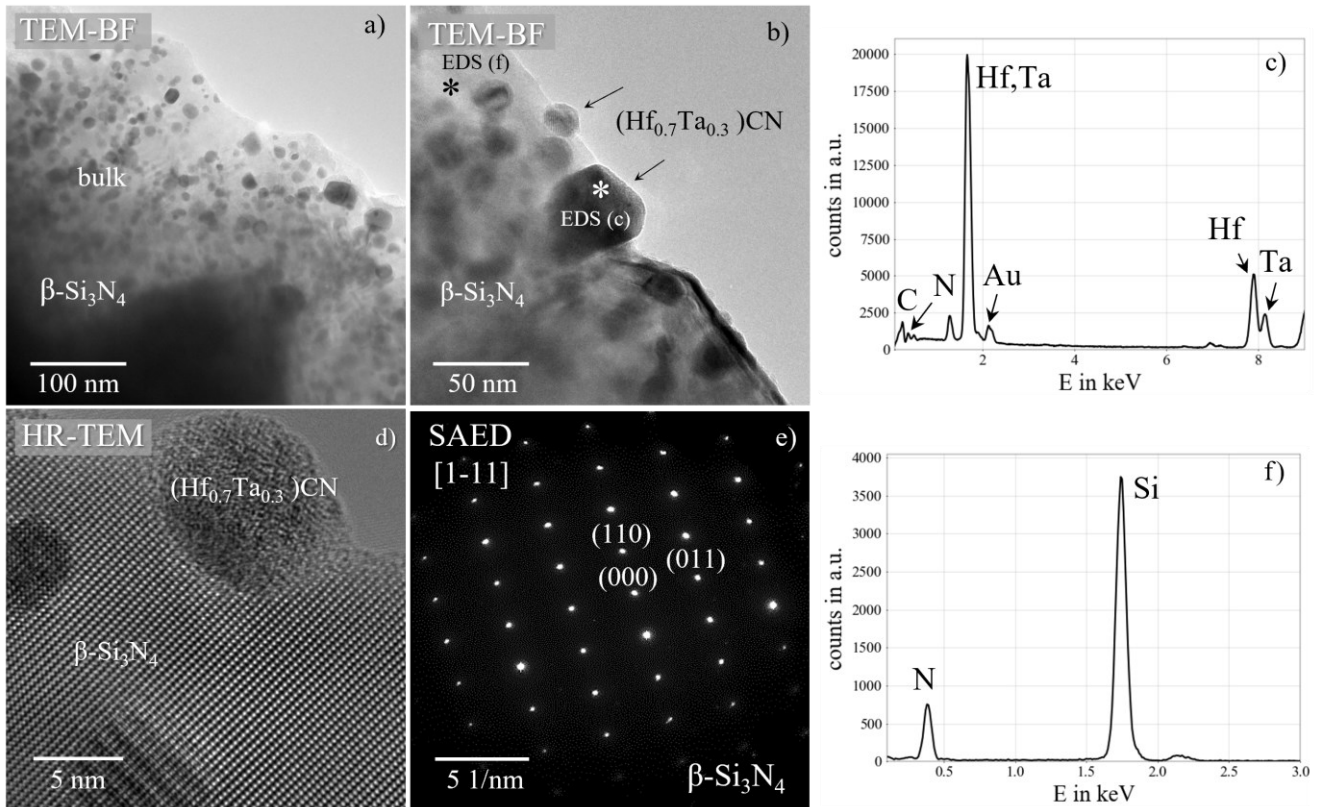


Figure 57 a, b) TEM-BF and d) HR-TEM images, e) SAED pattern and c, f) EDS spectra showing the microstructure and chemistry of the annealed $\text{Si}(\text{Hf}_{0.7}\text{Ta}_{0.3})(\text{C})\text{N}$ polymer-derived ceramic powder samples. The phase assemblage constitutes of $\beta\text{-Si}_3\text{N}_4$ and embedded nano-sized Hf-rich TMCNs $(\text{Hf}_{0.7}\text{Ta}_{0.3})\text{CN}$ with a Hf:Ta ratio of Hf:Ta=0.72:0.28 (± 0.14). The SAED pattern of the oriented Si_3N_4 phase in e) corresponds to the HR-TEM image in d). The exact EDS point measurement positions are indicated in the TEM-BF image with an asterisk in b). The corresponding EDS spectrum in c) represent the TMCN phase, with the elements indexed as follows: C (K_α), N (K_α), Hf (M_α , L_α) and Ta (M_α , L_α). The EDS spectrum in f) represents the Si_3N_4 phase with the following elements indexed: N (K_α) and Si (K_α). Figure adapted from Ref. [84].

In both ceramic samples, the Hf-rich and Ta-rich $\text{Si}(\text{Hf}_x\text{Ta}_{1-x})(\text{C})\text{N}$ polymer-derived ceramic, annealed at $1600\ ^\circ\text{C}$ in a N_2 atmosphere, amorphous free carbon was observed in surface regions (cf. Figure 58). In particular, the HR-TEM micrographs in Figure 58 revealed a thin carbon layer encapsulating the TMC particles. This carbon shell with $2\text{-}5\ \text{nm}$ in thickness was consistently observed around each carbide and carbonitride, as was also reported in studies by Q. Wen et al. in Ref [41]. [84]

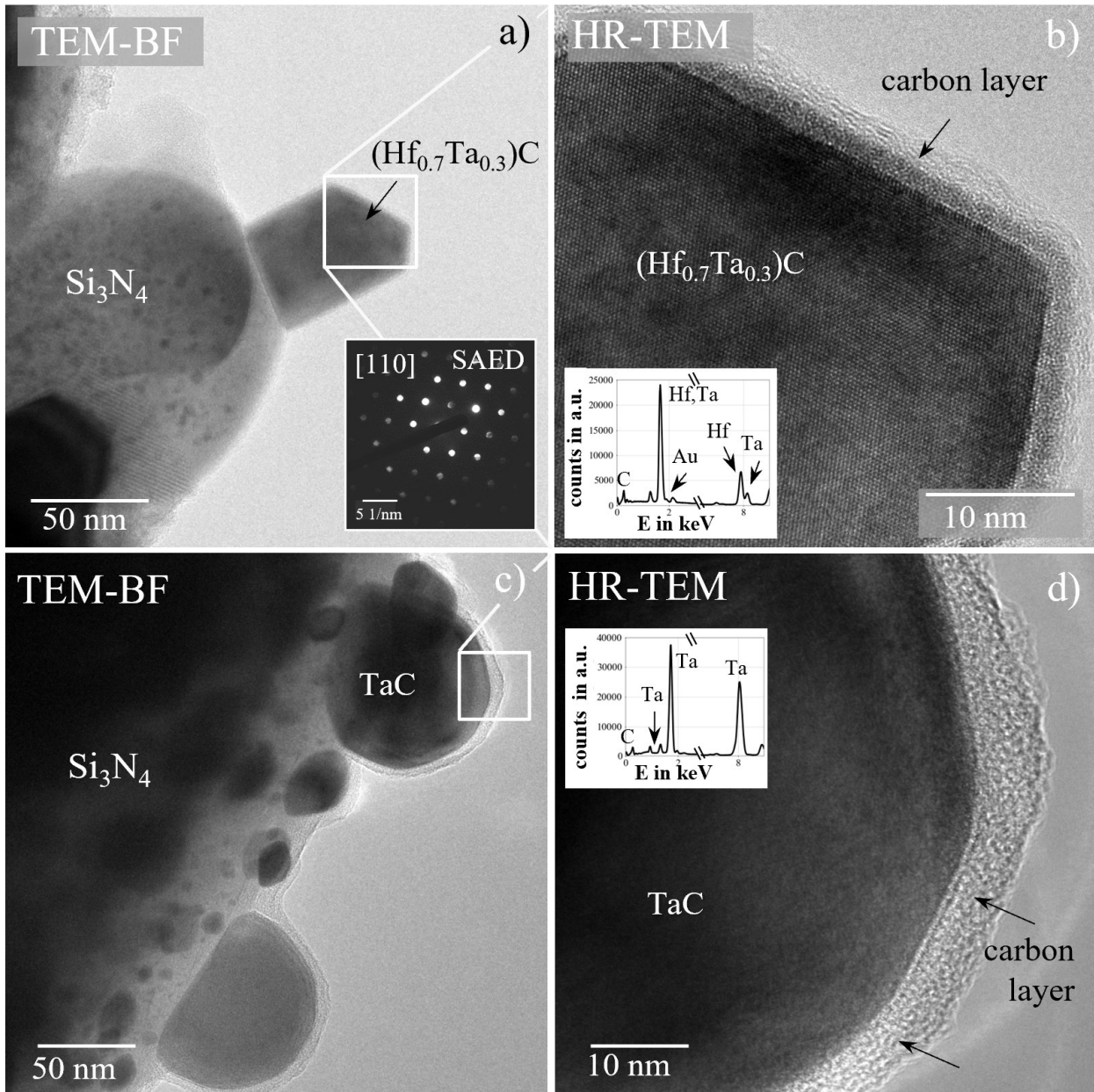


Figure 58 a, c) TEM-BF and b, d) HR-TEM micrographs of the Hf-rich $\text{Si}(\text{Hf}_{0.7}\text{Ta}_{0.3})\text{C}$ N (a, b) and Ta-rich $\text{Si}(\text{Hf}_{0.2}\text{Ta}_{0.8})\text{C}$ N (c, d) annealed polymer-derived ceramics. Amorphous carbon was detected around TMCs in both Hf-rich and Ta-rich ceramic powder samples. c, d) Besides solid solutions of TMCs, also pure TaC was found within the Ta-rich PDC. The insets in b, d) show the EDS spectra of $(\text{Hf}_{0.7}\text{Ta}_{0.3})\text{C}$ in b) and TaC in d) where the peaks are correlated as follows: C ($\text{K}\alpha$), Au ($\text{M}\alpha$), Hf ($\text{M}\alpha$, $\text{L}\alpha$), and Ta ($\text{M}\alpha$, $\text{L}\alpha$).

6.3.3 Cross Sections of Bulk and Adjacent Surface Region

As result of the preparation technique including the grinding of powder particles to achieve electron transparency for TEM analysis using a clean pestle and mortar, (cf. section 4.6.1) the original microstructure of the annealed powder particles was destroyed. Consequently, it was challenging to observe both, the bulk and surface regions of the powder particles using TEM. Hence, the transitional zone between the bulk and surface could not be visualized via TEM imaging. To confirm the existence of a microstructural transition zone between the bulk and surface region, additional SEM analysis was conducted on polished cross-sections of individual powder particles (see section 4.5.1 for description of sample preparation). [84]

In Figure 59 a) selection of SEM-BSE images is shown, depicting cross-sections of embedded and polished annealed polymer-derived $\text{Si}(\text{Hf}_{0.7}\text{Ta}_{0.3})\text{(C)N}$ powder particles. Within these images, the TMCs and TMCNs have a high Z-contrast, which let them appear as bright particles within the BSE images. In contrast, the Si-based matrix phases (Si_3N_4 and SiC) appear darker due to their lower average Z-numbers.

Figure 59 shows that the bulk regions of the powder particles make up the largest part of the particles in terms of area. However, the surface regions show different thicknesses for each powder particle. For example, the surface region in Figure 59 a) has a thickness of up to $3\ \mu\text{m}$, whereas the surface region in Figure 59 b) is slightly thinner, only reaching a thickness of $\sim 400\ \text{nm}$. The surface thickness is in general thicker, when larger TMCs constitute the surface region. For example, the surface region in Figure 59 a) in the upper part of the image contains very large TMCs, with grain sizes up to $700\ \text{nm}$, giving a total surface thickness of roughly $3\ \mu\text{m}$, while the TMC crystal sizes at the bottom surface of the same particle in the lower part of the image are much smaller (grain sizes up to $100\ \text{nm}$), which leads to a total thickness of only $0.5\ \mu\text{m}$. This shows clearly, that the surface regions even within a single powder particle are not equally in size. Furthermore Figure 59 e), f), j) and k) show, how the grain size of the TMCs gradually increase from the bulk direction to the surface region.

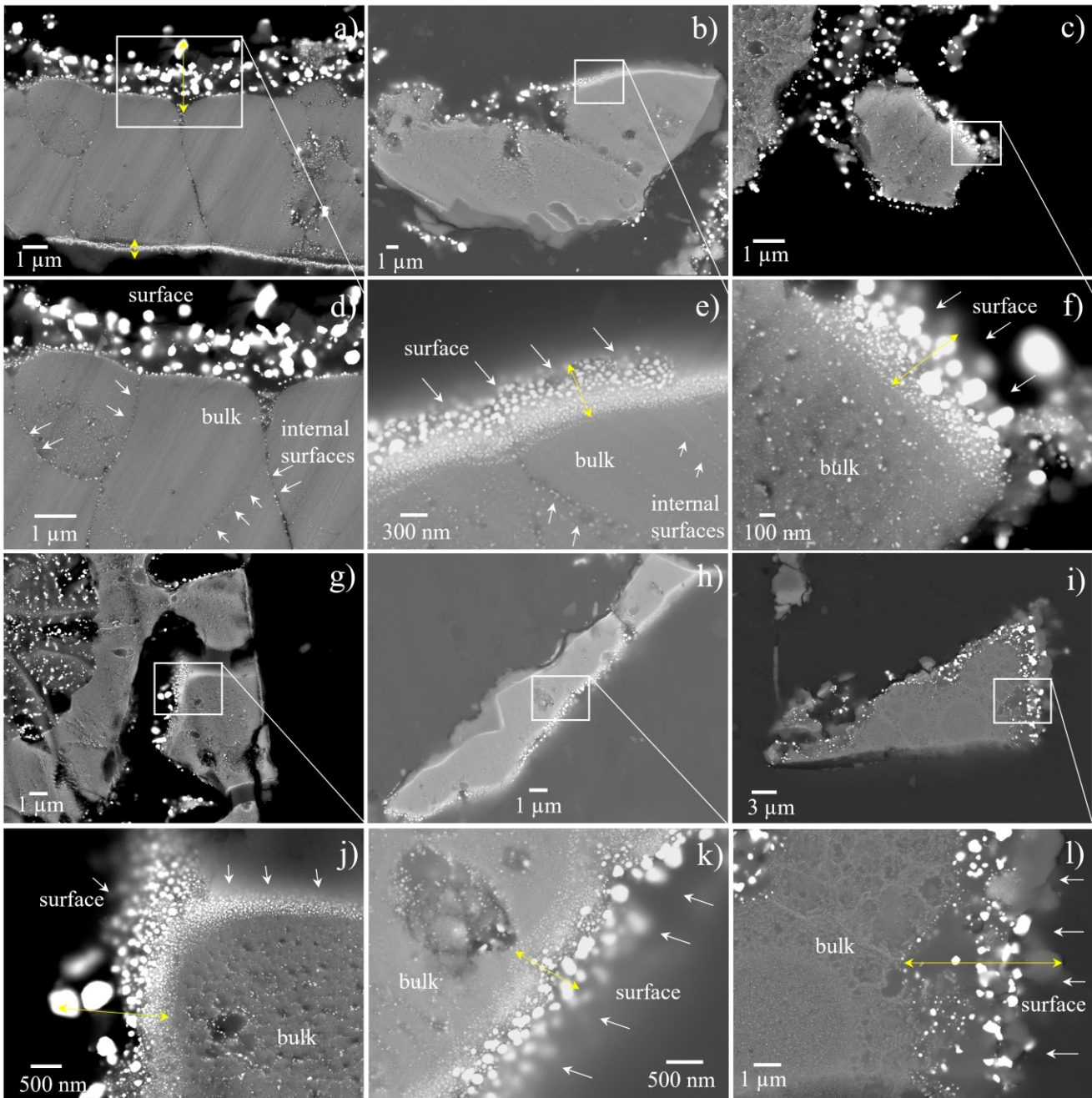


Figure 59 Various SEM-BSE images of the embedded $\text{Si}(\text{Hf}_x\text{Ta}_{1-x})(\text{C})\text{N}$ polymer-derived ceramic powder particles after annealing at 1600°C . Images in a), b), c), g), h) and i) show an overview of the whole powder particle, whereas the micrographs in d), e), f), j), k), and l) depict enlarged areas of the surface and bulk regions. Surface regions are characterized by an enrichment of TMCs (appearing bright in SEM-BSE images). The thickness of the surface regions is marked with yellow arrows in each magnified BSE image and the thickness of the surface region differs in each powder particle. An increase in the TMC grain sizes is visible from bulk to surface, in particular in e), f), j) and k). Internal surfaces are detected within an individual powder particle (Figure 55a, and d).

In Figure 60 a) and b) two SEM-BSE images are shown, providing an overview of an embedded, cross-sectioned and polished powder particle. Thus, the microstructure of the annealed $\text{Si}(\text{Hf}_{0.7}\text{Ta}_{0.3})(\text{C})\text{N}$ ceramic powder particles is depicted. Figure 60 b) again shows the increase in TMC crystal size from the inner bulk towards the outer surface region. TMCN particles found within the bulk region exhibit grain sizes of up to 50 nm, whereas in surface-near regions, the TMCs (in surface-near regions) can reach particle diameters as large as 500 nm, which is 10 times larger. These variations in particle size result

from localized chemical differences occurring within the bulk and surface-near regions of each powder particle. In order to verify this, a distinct region exhibiting grain coarsening from bulk to surface was analyzed using individual EDS point measurements. Figure 60 b) illustrates the SEM-BSE image of the transition zone from the bulk region (depicted in red) into the surface region (depicted in green). Within this selected region, 47 individual EDS point measurements were measured and subsequently analyzed. Individual EDS measurements were set within the Si-based matrix phase (excluding the white TMC precipitates) to obtain information regarding the chemical changes in the transitional zone between the bulk and surface region. The corresponding graph in Figure 60 c) presents the change of the relative element concentrations including Si, C, N, O, Hf, and Ta (in at-%) while moving from the bulk to the surface region (from left to right and from red to green). In particular, the two concentration profiles of C and N, represented by circle and diamond symbols respectively, demonstrate an inverse curve characteristic. The C content increases from the bulk to the surface, whereas the N concentration exhibits the opposite trend and decreases from the bulk to the surface. These two profiles (C and N) intersect at approx. 1.2-1.4 μm from the starting point of the EDS measurement, precisely matching the transition zone between the bulk and surface as observed in the SEM-BSE image (cf. transition zone between red and green marked region in Figure 60 b)). These findings support the observations made via TEM (cf. section 6.3.2 and Figure 57), where N is primarily present in the bulk region, predominantly forming silicon nitride (Si_3N_4). On the other hand, carbon tends to concentrate in the surface regions, forming β -SiC and residual carbon layers (cf. section 6.3.1 and Figure 55). Moreover, the oxygen concentration (indicated by the blue triangle symbol) exhibits a notable increase ranging from approx. 2 at-% up to 8 at-%, which is comparably high for carbonitride containing PDCs. [84]

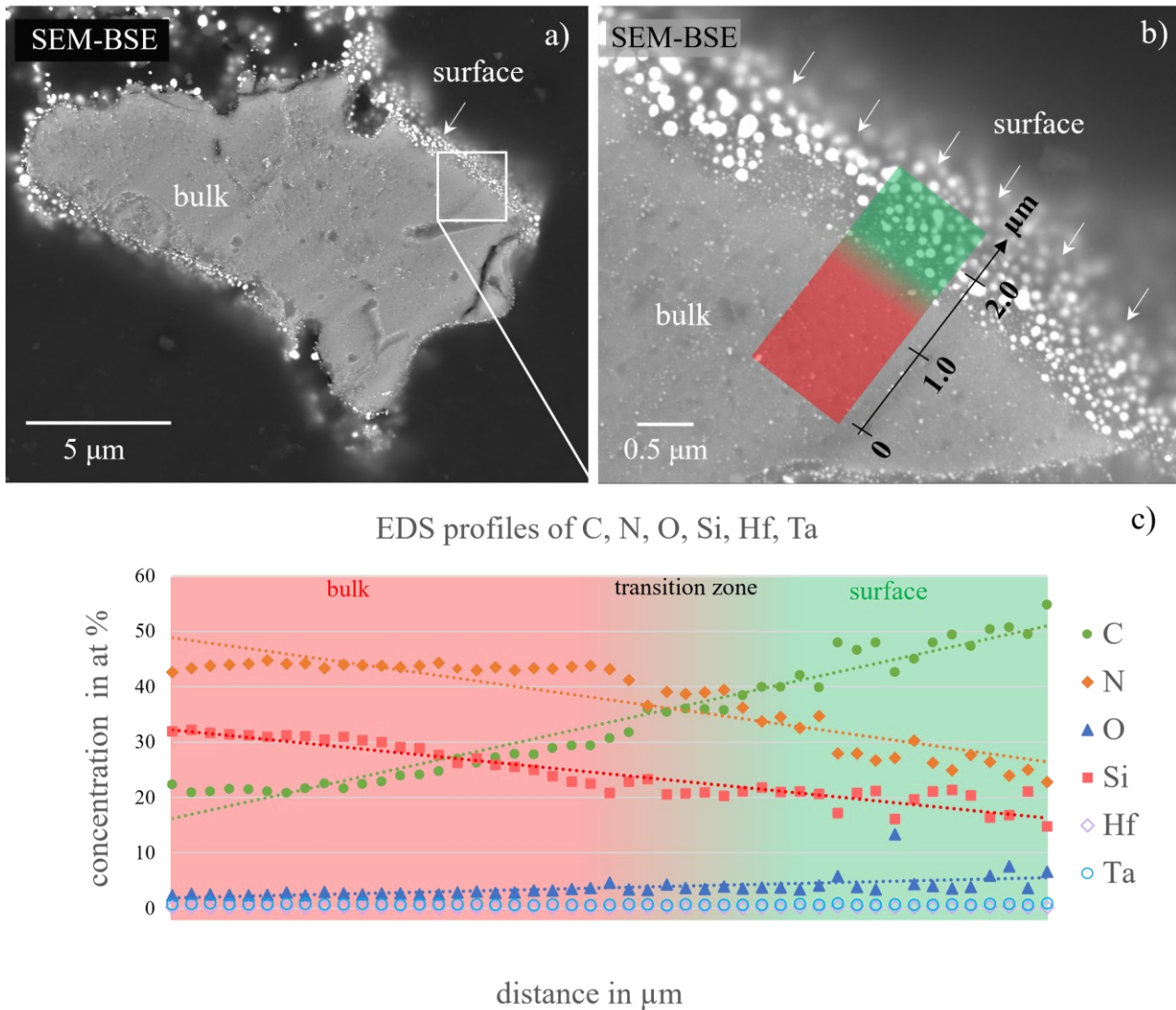


Figure 60 a, b) SEM-BSE micrographs showing a cross-section of an individual annealed polymer-derived ceramic powder particle in the $\text{Si}(\text{Hf}_{0.7}\text{Ta}_{0.3})\text{(C)N}$ system. TMC(N)s grains increase in size from inner bulk (TMCN) to outer surface regions (TMC); c) Relative elemental concentrations of C, N, O, Si, Hf, and Ta based on EDS point profiles in the red and green marked regions. The TMC(N) particle size increases in the surface-near region, coinciding with an elevated C and O content. The Si and N elemental concentrations are depleted, in the near-surface region. Figure published in Ref. [84].

6.3.4 Microstructure and Chemical Details of the Transition zone

In order to confirm the measured element concentrations from the previous EDS single point measurements in SEM, to gain local chemical details and to further add electron diffraction information generated via TEM analysis, a lamella was prepared via FIB-SEM. For the exact preparation steps, please refer to section 3.2.2. The FIB lamella shown in Figure 61 a) depicts a cross-section through the bulk and surface region of the annealed $\text{Si}(\text{Hf}_{0.7}\text{Ta}_{0.3})\text{(C)N}$ powder particle. The white rectangle in Figure 61 a) is shown enlarged in Figure 61 b). In Figure 61 b), 26 TEM-BF images were put together to form a collage of the entire width of the TEM lamella. In the bulk region at the bottom of the image, Figure 61 b) shows finely distributed TMCNs in a Si_3N_4 -rich matrix phase. By moving further up in the lamella, a very thin region consisting of nanosized TMCs (approx. 20 nm in size) occurs. The TMCNs in this region lie very close together. This region of nanosized TMCs is followed by a SiC layer. The SiC crystals

make up the transition zone with a thickness of approx. 200 nm. The last region is the surface region. As already described in the previous chapters, this region contains large TMCs.

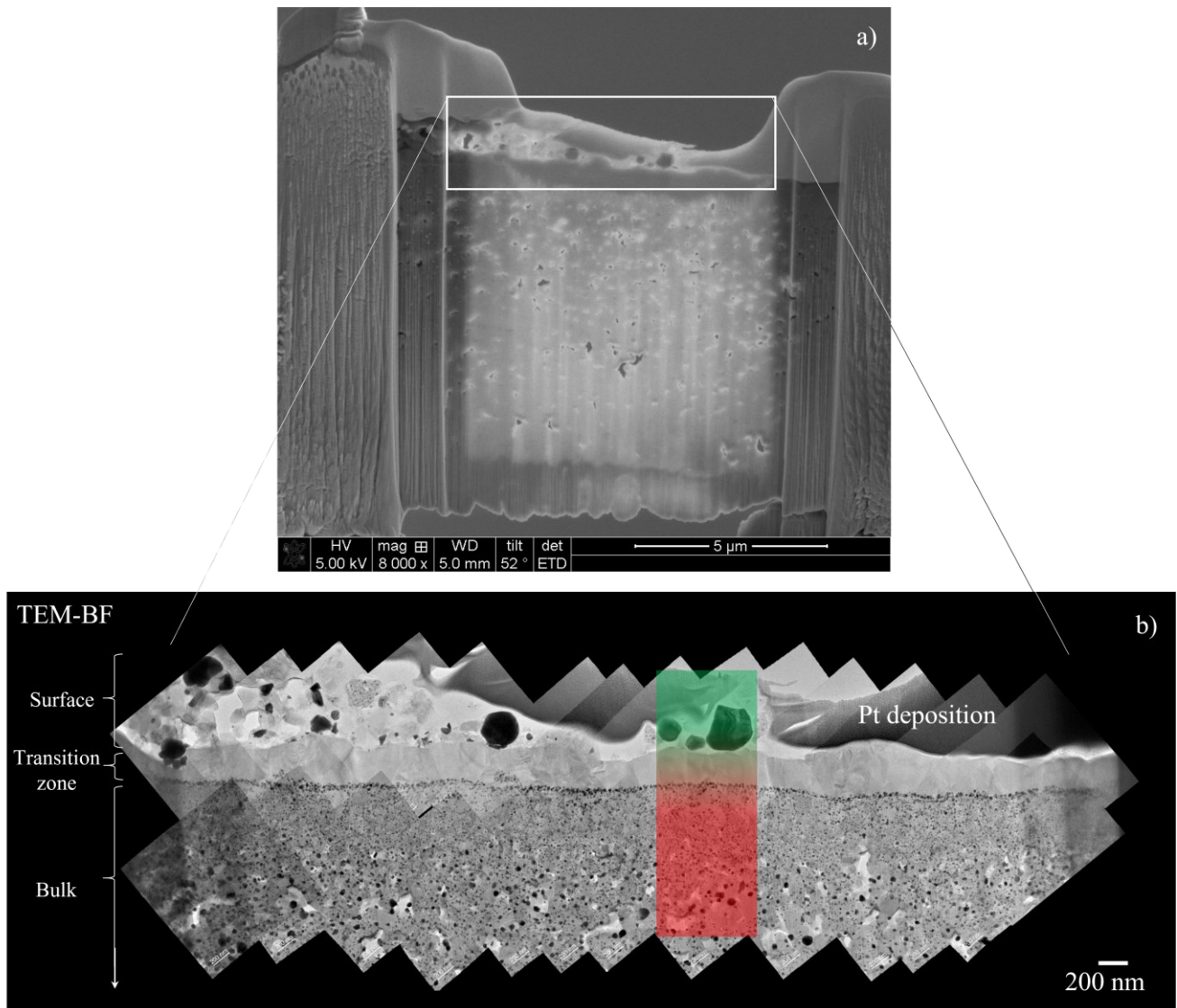


Figure 61 a) SEM-SE image of the TEM lamella prepared from the annealed $\text{Si}(\text{Hf}_{0.7}\text{Ta}_{0.3})\text{CN}$ polymer-derived ceramic powder particle via FIB-SEM. b) Collage of TEM-BF images showing the cross-section through the bulk-to-surface transition zone of an individual powder particle. Slight contrast variations enhance the edges of the frame and do not contribute to the microstructure. TEM lamella preparation was carried out by Dr. S. Schlabach, KIT.

Figure 62 shows the transition zone enlarged in TEM-BF mode. Amorphous residual phases can be found in the gaps between the large TMCs of the surface regions and the SiC layer. A series of individual EDS point measurements (star symbols) and three colored rectangles (blue, green and red) as insets are shown in Figure 62 a). In Figure 62 b-d) the respective diffraction patterns from the colored insets are shown. In Figure 62 e-h) the element concentration profiles in at-% across the different regions are plotted. As already described earlier, the TEM analysis of the FIB-lamella again confirms, that the bulk region is rich in Si_3N_4 , while Si and N decrease in its concentration very strongly in the transition zone and in the surface zone (cf. Figure 62 g), and f)). However, the element distributions of C and O show the opposite trend. C and O increase in the transition zone and in the surface region. The enrichment of O in the amorphous areas is particularly noticeable. Upon electron diffraction, it was shown that the transition zone consists of SiC. The residual phases in the gaps between enlarged TMCs in the surface region are indeed amorphous, shown by the diffuse diffraction ring in Figure 62 b).

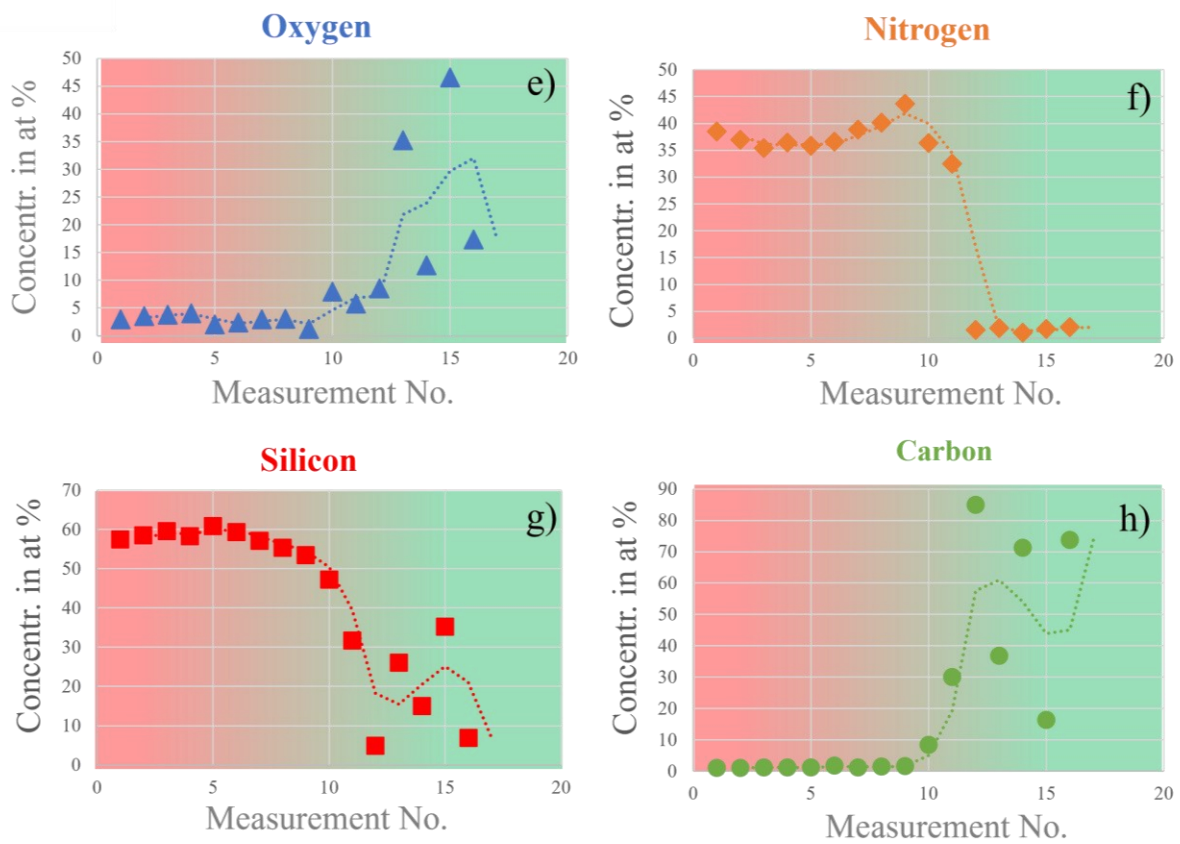
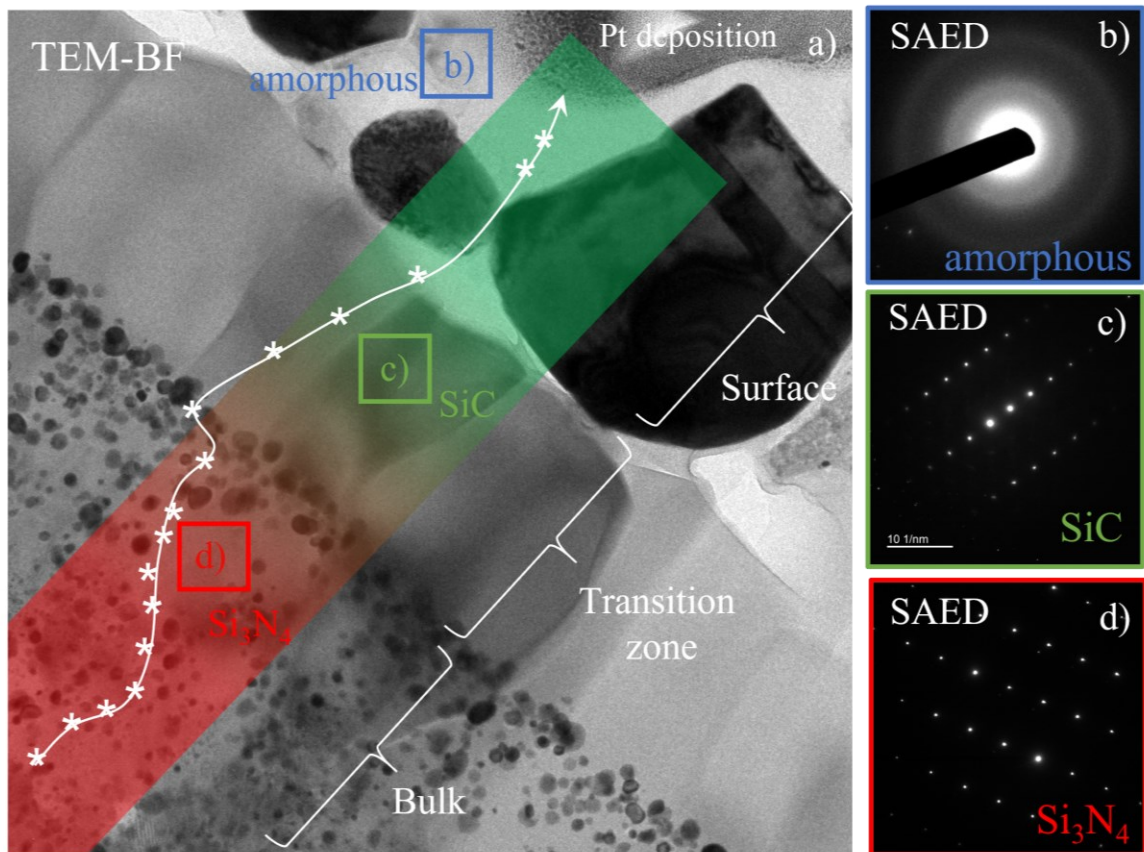


Figure 62 a) TEM-BF image, b-d) SAED patterns and e-h) O, N, Si, C element concentration profiles in at-% from bulk and transition zone into the surface region, as marked by the line.

6.4 Discussion

In the following, the evolution of the $\text{Si}(\text{Hf}_x\text{Ta}_{1-x})\text{(C)N}$ polymer-derived ceramic powders and the phase composition upon annealing is discussed with respect to literature.

6.4.1 Evolution and Phase Composition in the $\text{Si}(\text{Hf}_x\text{Ta}_{1-x})\text{(C)N}$ PDCs upon Annealing

According to the binary phase diagram published by Gusev et al. [106], HfC and TaC exhibit a continuous series of solid solution formation at temperatures above 887 °C (cf. Figure 7). Further, the phase diagram (cf. Figure 7) illustrates the existence of a miscibility gap at lower temperatures, explaining the presence of pure TaC beneath solid solutions of $(\text{Hf}_x\text{Ta}_{1-x})\text{C}$ which was found in the Ta-rich sample (cf. Figure 58 c), d)). During TEM analysis TMCNs and TMCs were formed upon high-temperature anneal at 1600° C. Figure 63 shows the structural formula of the organometallic complexes. An explanation is the availability of carbon within the system, originating from residual CH_3 groups of the organometallic precursors of PDMAT and TDMAH, after the pyrolysis. The remaining methyl groups therefore serve as a carbon source required for carbide or carbonitride formation. Figure 63 shows that the ratio of Ta:C in PDMAT is Ta:C = 1:10, the ratio of Hf:C in TDMAH is Hf:C=1:8. A ratio of Ta:C=1:1 or Hf:C=1:1 is sufficient for the formation of a stoichiometric TMC. Thus, the observed carbon shells (cf. Figure 58) may form due to an excess of carbon originating from the organometallic complexes (both PDMAT and TDMAH). The formation of these thin carbon shells is therefore assumed to be a consequence of carbon diffusion towards the surfaces.

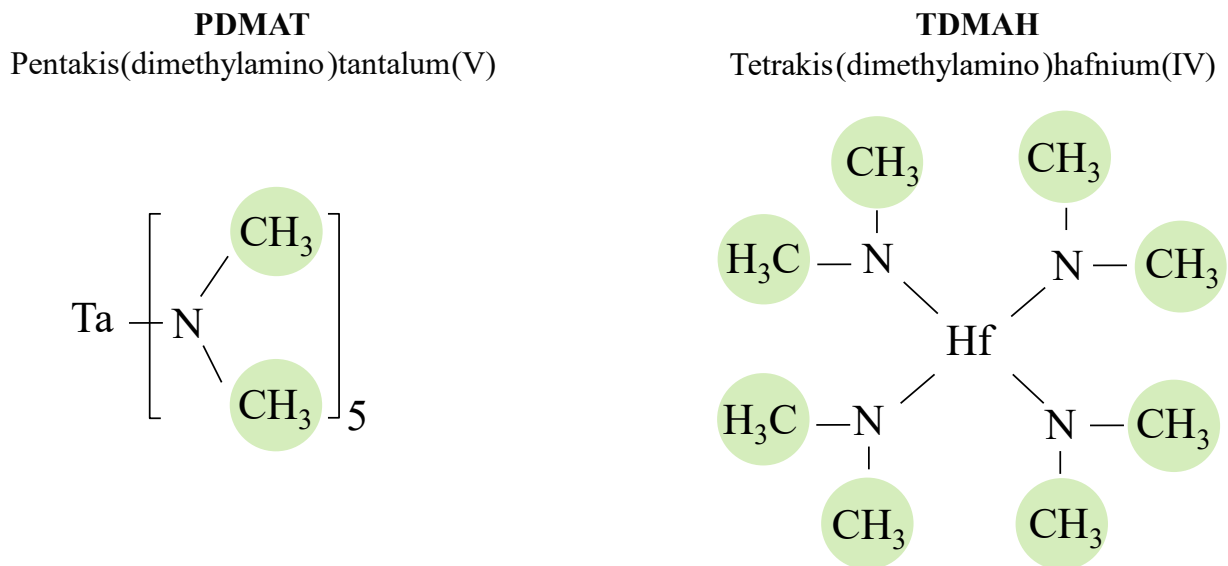
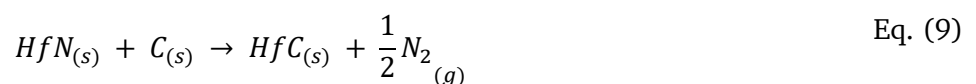


Figure 63 Structural formula of the organo-metallic complexes PDMAT and TDMAH used to modify the polymeric precursors.

J. Yuan et al. [66] provided an explanation for the presence of carbides, utilizing thermodynamics and the corresponding Ellingham diagram. As depicted in Figure 64 and Equation 9, hafnium nitride (HfN), along with segregated carbon, decompose into hafnium carbide (HfC) and gaseous nitrogen (N_2) at temperatures exceeding 1500 °C [66,239]. [84]



In this study, X-ray diffraction (XRD) data, combined with TEM analysis, confirm the presence of TMCs at 1600° C. Despite the thermodynamic stability of TMN suggested by the Ellingham diagram at 1000 °C, both Ta- and Hf-carbonitrides were observed in the polymer-derived ceramic Si(Hf_xTa_{1-x})(C)N samples. Although the pyrolysis in an ammonia atmosphere would favour TMN formation, the crystallization of TMCN at low temperatures is attributed to the higher carbon content in the amorphous bulk.

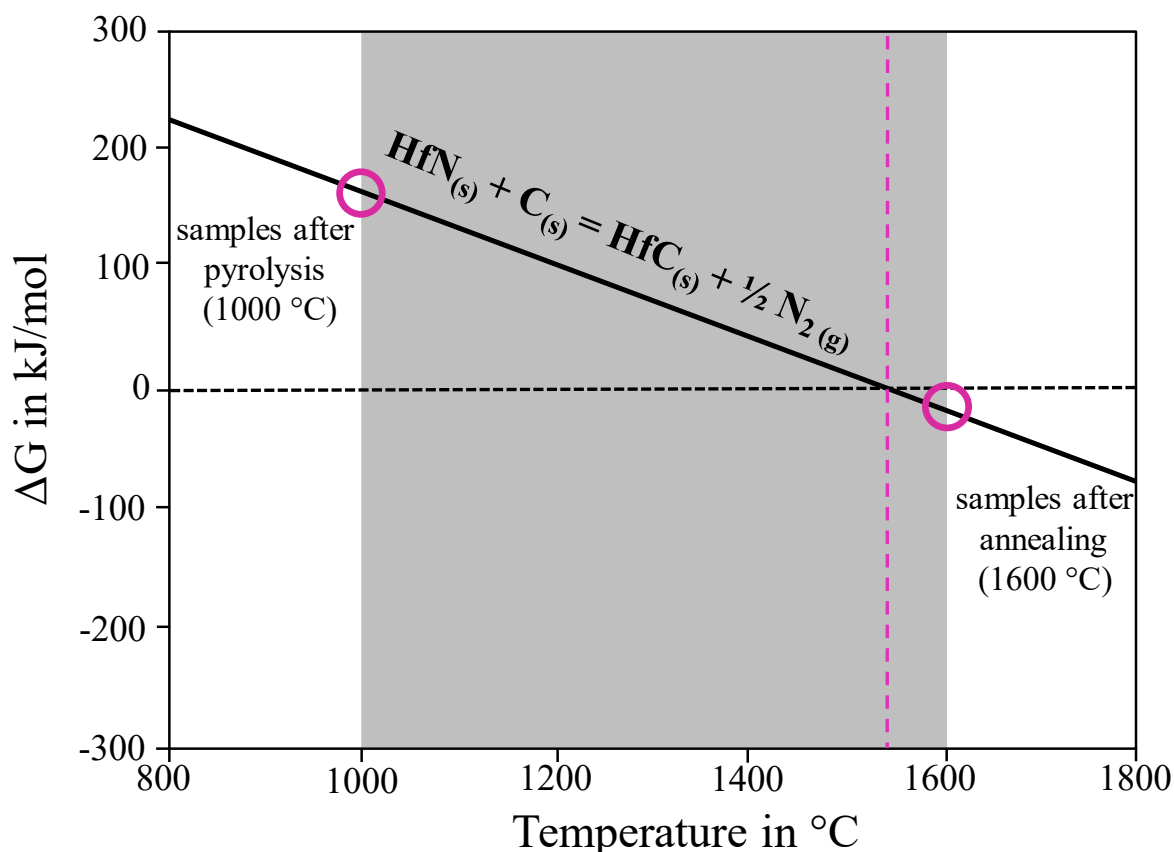
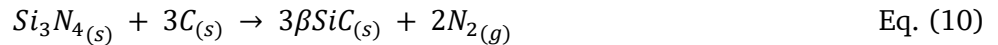


Figure 64 Ellingham diagram showing the temperature as a function of the Gibbs free energy. The temperature dependence of the change in the Gibbs free energy of the possible reactions of HfN plus free C decomposing into HfC plus gaseous N₂ at high temperatures. The temperature range between 1000 °C and 1600 °C represents the pyrolysis temperature and annealing temperatures of the here studied Si(Hf_xTa_{1-x})(C)N PDCs (redrawn after Ref. [66], data taken from Ref. [239]).

6.4.2 Thermal Decomposition Reaction

The grain size of the TMCs and TMCNs, varies depending on their location within the bulk or surface region either in the as-pyrolyzed powders as well as in the annealed ceramic powders. This variation was investigated by examining the pulverized as-pyrolyzed and polished cross sections of the annealed powder particles (cf. Figure 59) as well as the FIB lamella in Figure 61. After pyrolysis the microstructure consists mainly of a glassy Si-Hf-Ta-C-N-(O) network (cf. Figure 51). Within surface regions, mainly TMCNs are present, showing grain sizes of up to 50 nm (cf. Figure 52). High-temperature anneal at 1600° C leads to the formation of Hf- and Ta-carbides at the particle surfaces, characterized by larger particle sizes with a maximum diameter of about 500 nm up to 700 nm. These carbides coexist with β-SiC and a residual amorphous O-rich phase at the surface regions. During the annealing process, the decomposition of Si₃N₄ occurs and is accompanied by an enhanced depletion of volatiles, such as N₂, at surface-near regions (for comparison see EDS data in Figure 60 c). This well-known decomposition

reaction involves the solid-state decomposition of Si_3N_4 in the presence of free carbon to form solid SiC and gaseous nitrogen, as shown in Equation 10.



This thermal decomposition reaction typically starts at temperatures exceeding 1440 °C in a N_2 containing atmosphere [240–243], and thus this process is assumed to take place during the annealing at 1600 °C. The decomposition of Si_3N_4 leads to an increased volume fraction of SiC in the surface regions. It is assumed that the diffusion of transition metals in surface regions (rich in SiC and residual amorphous phases as depicted in Figure 62) occurs more rapidly along amorphous carbon layers compared to diffusion in the Si_3N_4 -rich bulk regions. As a result, small TMCN precipitates are present in the bulk region where Si_3N_4 remains, while larger TM-carbides and large β -SiC grains are found in surface-near regions. This decomposition reaction is a significant factor contributing to the observed differences in microstructural evolution between the surface and bulk regions during high-temperature annealing, which actually begins at temperatures around 1000 °C (pyrolysis temperature). [84]

6.4.3 Vapor-phase Reactions

Individual powder particles exhibit anomalous grain growth of Si_3N_4 and SiC at surface regions. The analysis conducted using SEM and TEM revealed the presence of columnar Si_3N_4 and whisker-like SiC crystallites with high aspect ratios (cf. Figure 56). These formations are assumed to result from local vapor-phase reactions occurring during the high-temperature annealing process. The nitrogen atmosphere in combination with the release of nitrogen due to the decomposition of Si_3N_4 , promotes vapor-phase reactions, particularly on the surface of the powder particles. This phenomenon leads to a conspicuous decoration of the outer particle surface with substantial idiomorphic Si_3N_4 grains and SiC whiskers, as shown in Figure 56. Comparable findings have also been reported in relation to SiCN- and SiCO-based polymer derived ceramics (PDCs) [244–246]. [84]

6.4.4 Diffusion Phenomena, Coarsening and the Influence of Oxygen

An inverse behaviour of C and N in the transition zone between bulk and surface, as well as the increase of O in the near-surface regions was found (cf. elemental profiles of C, N and O in Figure 60 c) and Figure 62). This finding leads to the assumption that the elements of C, N and O are mainly responsible for the grain coarsening of TMCs in surface-near regions. The coarsening phenomenon observed here, coupled with the localized changes in chemical composition (C, N, O contents), is comparable to findings from literature [67,74,180,181,247]. Kleebe and co-workers [181] previously investigated the coarsening behaviour of HfO_2 particles within a SiHfCO polymer-derived matrix upon isothermal heat treatment at 1300 °C. They interpreted the pronounced grain coarsening of hafnia in the surface-near regions by a reduced carbon content, that should lead to an enhanced diffusion coefficient of Hf in the silica matrix, thereby promoting particle growth. They proposed a decomposition-coarsening model to elucidate the variations in particle size observed in the Si-Hf-C-O PDCs. Anand et al. [74] described a Zr-diffusion-controlled coarsening process of ZrO_2 crystallites in a Si-C-N-O ceramic. Furthermore, Sujith et al. [67] also reported significant coarsening of nano-sized hafnia (HfO_2) in Si-Hf-C-N-O, which the authors attributed to diffusion-controlled mechanisms governed by Ostwald ripening mechanism. In the context of the here examined $\text{Si}(\text{Hf}_x\text{Ta}_{1-x})(\text{C})\text{N}$ samples, it is suggested here that the oxygen content influences the diffusivity of Hf and Ta, thereby enabling a distinct coarsening of TMCs in surface-near regions. As illustrated in Figure 60 c) and Figure 62 e), the oxygen concentration increases in surface-near regions due to the residual amorphous phase (cf. Figure 62) and the impurities coming from the

polymer synthesis process. The combination of the increased oxygen concentration coupled with a decrease in nitrogen (due to Si_3N_4 decomposition) and the presence of amorphous carbon in the surface-near regions, might account for the increased elemental diffusion of Hf and Ta leading to the observed TMC coarsening. [84]

6.4.5 Microstructural Evolution from 1000 °C to 1600 °C

The scheme in Figure 65 illustrates the microstructural evolution of the $\text{Si}(\text{Hf}_x\text{Ta}_{1-x})\text{(C)N}$ system upon pyrolysis at 1000 °C and subsequent thermal treatment at 1600 °C. Four distinct microstructural stages of an individual powder particle are shown. Each illustration shows the stepwise crystallization process upon the different temperatures of the pyrolysis and heat treatment. The powder particle develops from an initially fully amorphous state at temperatures below 1000 °C into a crystallized and phase separated final microstructure at an annealing temperature above 1600 °C.

After pyrolysis at 1000 °C, the powder sample shows an X-ray amorphous structure, comprising a glassy Si-Hf-Ta-C-N-(O) network (Figure 65 a)). SEM and TEM analysis reveal that only the bulk region of the powder particles is amorphous and featureless in microstructure (cf. Figure 51), while the surface regions show small TMCN particles, hinting on early crystallization at the surface (cf. Figure 52). Regarding the amorphous bulk regions, a small amount of carbon was also detected by EDS (cf. inset Figure 51 c)), indicating that carbon is still incorporated within the glass network and has not yet undergone phase separation.

After annealing at 1600 °C, both the bulk and surface regions are crystalline. The microstructure evolution of the bulk and surface regions in the PDC powder samples annealed at 1600 °C is more advanced compared to samples pyrolyzed at 1000 °C (Figure 65 b)). The early crystallization of TMCNs observed on the surface regions at 1000 °C transforms upon annealing at 1600 °C into a matrix primarily composed of SiC with larger crystalline TMC particles. The surface regions experience a carbothermal decomposition reaction, where Si_3N_4 in the presence of free carbon decomposes into SiC and gaseous nitrogen (Eq. 10). The bulk region consists of large crystalline Si_3N_4 grains with embedded TMCNs (Figure 65 c)). In these inner regions, the decomposition of Si_3N_4 has not yet initiated. Thus, the crystallization/decomposition process occurs from the outer surface towards the inner parts of the powder particles. It is suggested here that the formation of $(\text{Hf}_x\text{Ta}_{1-x})\text{C}$ with increased particle size at the surface results from Hf- and Ta-diffusion-controlled coarsening. As temperatures surpass 1600 °C, a further progression of Si_3N_4 decomposition and coarsening is suggested to take place, ultimately leading to the formation of thermodynamically stable phases such as SiC and $(\text{Hf}_x\text{Ta}_{1-x})\text{C}$ (Figure 65 d)). [84]

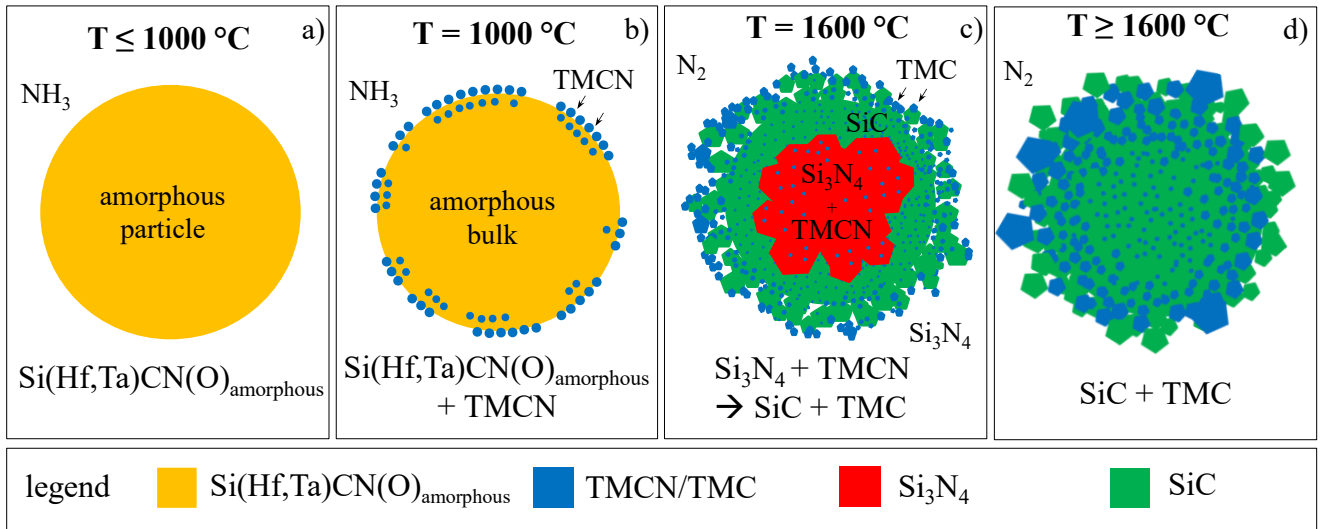


Figure 65 Schematic illustration of the microstructural evolution of the polymer-derived ceramic $\text{Si}(\text{Hf}_x\text{Ta}_{1-x})(\text{C})\text{N}$ upon pyrolysis at $1000\text{ }^\circ\text{C}$ and subsequent heat treatment at $1600\text{ }^\circ\text{C}$.

6.5 Conclusion

Polymer-derived ceramic powder samples with a $\text{Si}(\text{Hf}_x\text{Ta}_{1-x})(\text{C})\text{N}$ composition synthesized using the single-source-precursor method shows a manifold microstructure. Upon pyrolysis at $1000\text{ }^\circ\text{C}$, the resulting powder samples exhibited early crystallization of TMCNs primarily in the surface-near regions. The formation of TMCNs was attributed to a higher carbon content, specifically to residual CH_3 -groups present in the organometallic complexes. The carbon is suggested to react with Hf, Ta and N, forming $(\text{Hf}_x\text{Ta}_{1-x})\text{CN}$. The bulk regions remain predominantly amorphous. In particular noteworthy is the different microstructural evolution at the surface and in bulk regions, which is already initiated at temperatures around $1000\text{ }^\circ\text{C}$, but becomes even more pronounced at elevated temperatures, such as at an annealing temperature of $1600\text{ }^\circ\text{C}$.

At temperatures around $\sim 1440\text{ }^\circ\text{C}$, a thermal decomposition reaction occurred predominantly at surface-near regions, leading to the decomposition of the matrix phase (Si_3N_4) into SiC and gaseous nitrogen. Parallel to this decomposition another decomposition reaction takes place: In the presence of free carbon, TMCNs decompose into TMCs and gaseous nitrogen (after Eq. 9). The TMC at internal and surface-near regions undergo pronounced grain coarsening. Local variations in the chemical composition of C, N and O are suggested to influence the diffusion of the transition metals. This, in turn, contributes to the increased TMC grain size, particularly in the surface-near region, where a higher oxygen content and the presence of amorphous carbon layers were observed. Si_3N_4 and small TMCNS are still present in the bulk, while SiC is exclusively observed in the surface regions. The local decomposition in the surface-near regions and the corresponding coarsening of TMC particles represent an active and characteristic mechanism in the $\text{Si}(\text{Hf}_x\text{Ta}_{1-x})(\text{C})\text{N}$ -based polymer-derived ceramics during annealing. It is mandatory to consider this process when contemplating high-temperature applications of this material class. [84]

7 The Influence of Polysilan: Si(Hf_xTa_{1-x})C(N,O) and SiC/(Hf_xTa_{1-x})C

Based on the synthesis proposed by Q. Wen in Ref. [41,47], a commercially available polysilane was modified with different molar ratios of Hf- and Ta metal complexes (TDEAH and PDMAT) and subsequently sintered by FAST (cf. chapter 2.10.2). The synthesis of the Si(Hf_xTa_{1-x})C(N,O) single-source precursor with $x=0.2$ and $x=0.7$ was performed by J. Bernauer and presented in section 4.3. The sintering parameters for the FAST process were given with 2200 °C/50 MPa/20 min. In contrast to the two previously investigated systems in chapter 5 and 6, where a commercially available polysilazane (PHPS) was used as precursor, a polysilane precursor was used here instead (refer to chapter 2.4 for the difference between both precursors). It is expected, that the change in the precursor results in a ceramic with little to no nitrogen content in the microstructure. In this way it is expected, that the formation and therefore also the thermal decomposition of nitrides will not occur. Since the materials prepared are novel systems and have only been reported on in Ref. [41] so far, no mechanical parameters are known yet. Thus, the mechanical properties have been determined.

The Hf-rich (Hf_{0.7}Ta_{0.3}) and the Ta-rich (Hf_{0.2}Ta_{0.8}) PDC-NC show very similar results, both in terms of microstructure and the mechanical behaviour. As the Hf-rich sample showed a promising oxidation resistance, (see Nils-Christian Petry Ref. [248]) the focus here is on presenting the microstructure and mechanical properties for the SiC/(Hf_{0.7}Ta_{0.3})/C PDC-NC.

7.1 Chemical Composition and Phase Assemblage

Table 7 provides the results from the elemental analysis from Mikroanalytisches Labor Pascher (Remagen, Germany), giving the chemical composition of the metal-containing as-pyrolyzed Si(Hf_{0.7}Ta_{0.3})C(N,O) and the sintered SiC/(Hf_{0.7}Ta_{0.3})C PDC in weight percentage (wt-%) and atomic percent (at-%). Both ceramics consist of Si, Hf, Ta, C, N and O. In addition, the empirical formula of both ceramics is given. The difference in the chemical composition between the ceramic powder after pyrolysis (1000 °C) and the resulting sintered bulk ceramic (2200 °C) is the concentration of the N and O content, as shown in Table 7. The as-pyrolyzed Si(Hf_{0.7}Ta_{0.3})C(N,O) powder contains a N and O content of ~3.6 and ~4 wt-%, whereas in contrast the N and O contents in the sintered bulk sample are ~0.3 wt-% and ~0.2 wt-%, respectively. Thus, there is a loss in N and O during the consolidation process. [85]

Table 7 Chemical composition of the as-pyrolyzed Si(Hf_{0.7}Ta_{0.3})C(N,O) and sintered SiC/(Hf_{0.7}Ta_{0.3})C ceramics. Table taken from Ref. [85].

sample	elemental analysis						
		Si	Hf	Ta	C	N	O
Si(Hf _{0.7} Ta _{0.3})C(N,O)	wt-%	46.9	11.1	3.75	29.03	3.64	4.01
Si(Hf _{0.7} Ta _{0.3})C(N,O)	at-%	35.68	1.33	0.44	51.64	5.55	5.36
empirical formula	Si(Hf _{0.04} Ta _{0.01})C _{1.45} N _{0.16} O _{0.15}						
	elemental analysis						
SiC/(Hf _{0.7} Ta _{0.3})C	wt-%	51.8	12.4	4.25	29.34	0.31	0.17
SiC/(Hf _{0.7} Ta _{0.3})C	at-%	41.79	1.57	0.53	55.46	0.50	0.24
empirical formula	Si(Hf _{0.04} Ta _{0.01})C _{1.33} N _{0.01} O _{0.01}						

Figure 66 displays the X-ray diffraction (XRD) patterns of the as-pyrolyzed ceramic Si(Hf_{0.7}Ta_{0.3})C(N,O) powder and the sintered SiC/(Hf_{0.7}Ta_{0.3})C bulk ceramic. The ceramic powder, pyrolyzed at 1000 °C in an Argon atmosphere, exhibits an X-ray amorphous structure, no distinct diffraction peaks are present. However, a broad peak around $2\theta = 36^\circ$ corresponds to the (111) peak of β -SiC, as shown in Figure 66.

The XRD pattern of the sintered bulk ceramic indicates a fully crystalline structure with three phases present: β -SiC, the TMC ($\text{Hf}_{0.7}\text{Ta}_{0.3}\text{C}$), and graphitic carbon. The six sharp peaks at 35.7° , 41.5° , 60.1° , 71.9° , 75.6° , and 90.2° correspond to the diffraction of (111), (200), (220), (311), (222), and (400) crystal planes of β -SiC (PDF 29–1129) and are represented by a closed rectangle symbol. The presence of a diffraction peak around 33.7° , denoted by a star symbol, indicates the existence of stacking faults (SF) in SiC, while the sharp peak of the TMC overlaps with the weak SF peak. This phenomenon will be shortly discussed in section 7.4.5. The remaining sharp peaks are assigned to the TMC of ($\text{Hf}_{0.7}\text{Ta}_{0.3}\text{C}$), represented by a half-filled, lying triangle symbol (PDF 19-6861). Additionally, the small peak at 26.2° is attributed to the presence of graphitic carbon, represented by a closed triangle symbol. [85]

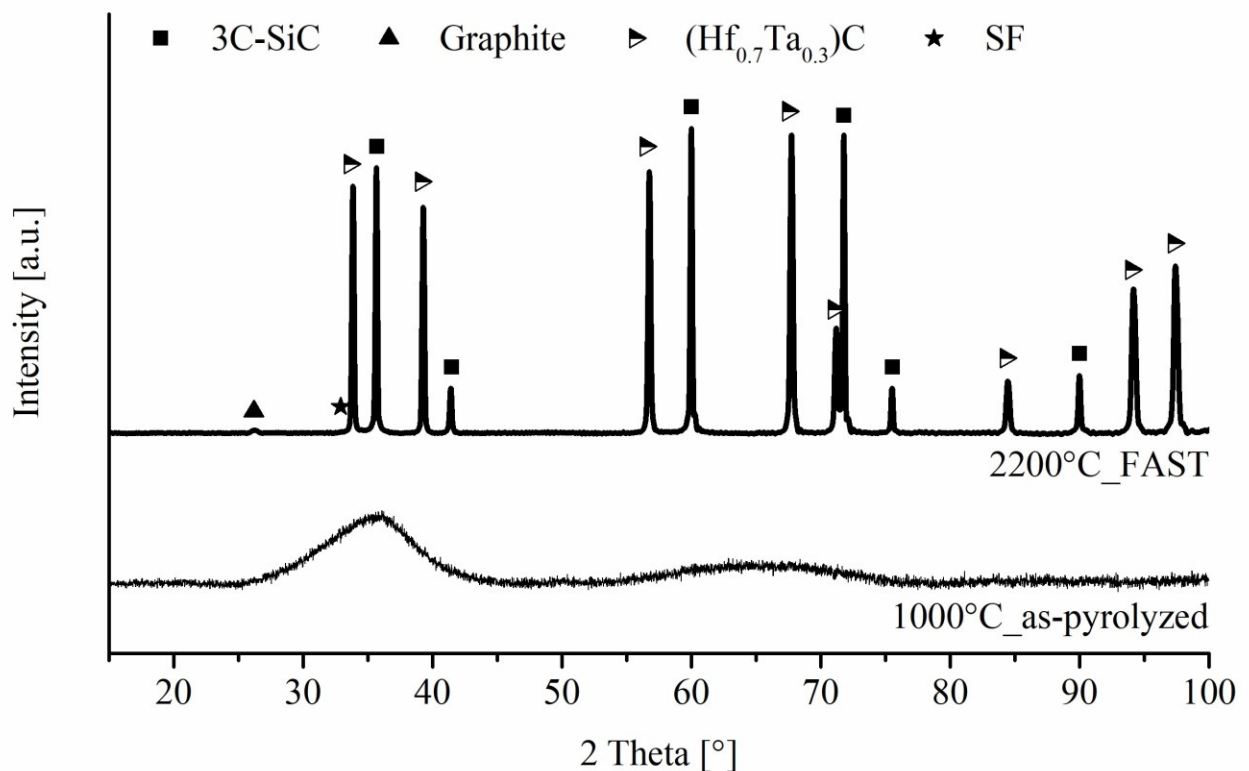


Figure 66 XRD pattern of the as-pyrolyzed $\text{Si}(\text{Hf}_{0.7}\text{Ta}_{0.3})\text{C}(\text{N},\text{O})$ ceramic powder pyrolyzed at 1000°C in Ar (bottom) and XRD pattern of the bulk $\text{SiC}/(\text{Hf}_{0.7}\text{Ta}_{0.3})\text{C}$ ceramic sintered at 2200°C (top).

7.2 Microstructure of As-pyrolyzed $\text{Si}(\text{Hf}_{0.7}\text{Ta}_{0.3})\text{C}(\text{N},\text{O})$ Powders at 1000°C in Ar

Comprehensive electron microscopic investigations were conducted on as-pyrolyzed $\text{Si}(\text{Hf}_{0.7}\text{Ta}_{0.3})\text{C}(\text{N},\text{O})$ powder particles using SEM and TEM in conjunction with energy-dispersive X-ray spectroscopy (EDS) and electron diffraction. Figure 67 illustrates a representative SEM-BSE micrograph, providing an overview of the as-pyrolyzed PDC powder. After pyrolysis at 1000°C in an argon atmosphere, the microstructure of the powder particles appeared featureless, meaning that distinct grain boundaries or crystalline features are lacking. The EDS spectrum presented in Figure 67 b) was acquired by an individual point measurement on the surface of a powder particle and depicts the presence of Si, Hf, Ta, C, N, and a relatively strong O peak. The elemental composition obtained through EDS analysis is in good agreement with the results of elemental analyses displayed in Table 7. [85]

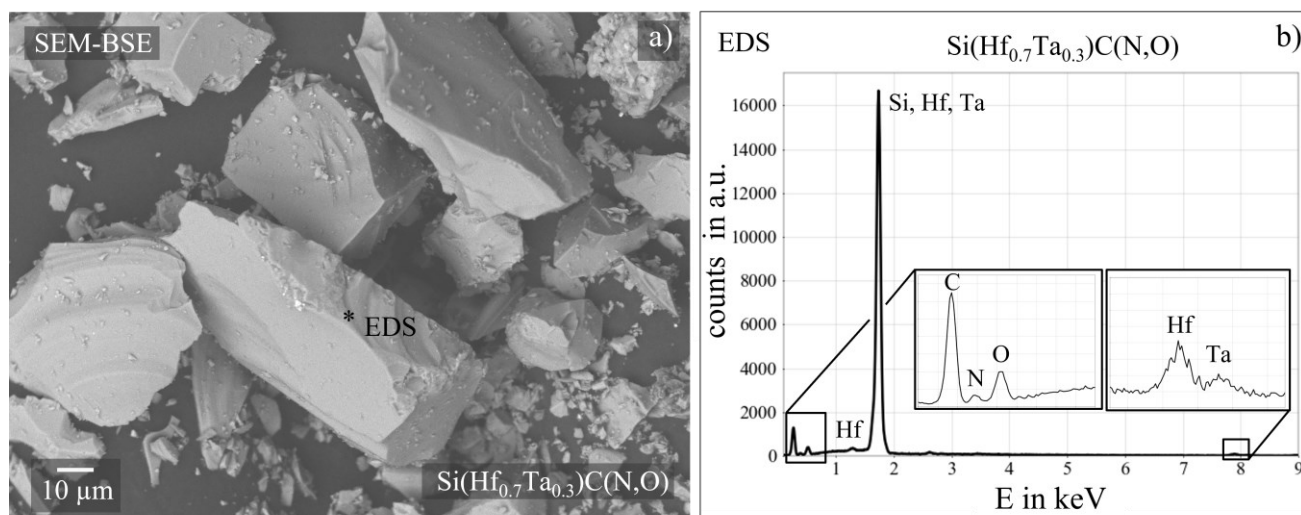


Figure 67 a) SEM-BSE micrograph and b) EDS spectrum of the as-pyrolyzed $\text{Si}(\text{Hf}_{0.7}\text{Ta}_{0.3})\text{C}(\text{N},\text{O})$ polymer-derived ceramic. The containing elements in b) are indexed following the characteristic X-ray energies with: C (K_{α}), N (K_{α}), O (K_{α}), Si (K_{α}), Hf (M_{α} , L_{α}) and Ta (M_{α} , L_{α}).

TEM analyses allow a more detailed insight into the microstructure compared to SEM. Figure 68 presents a TEM-BF and HR-TEM image, in addition to a SAED pattern, and an EDS spectrum of an individual point measurement of the amorphous as-pyrolyzed powder sample. Consistent with the X-ray amorphous XRD pattern (cf. Figure 66) and the featureless structure observed via SEM (cf. Figure 67), TEM analysis also exhibits a predominantly amorphous microstructure. The amorphous structure is evident from the homogeneous amplitude contrast observed in the TEM-BF image in Figure 68 a) as well as the HR-TEM image in Figure 68 b) and the diffuse halo ring pattern within the SAED in Figure 68 c). Also, EDS analysis in TEM (Figure 68 d)) confirms the presence of Si, Hf, Ta, C, N and O, aligning well with the SEM results and elemental analyses presented in Table 7. The presence of small amounts of N is attributed to the nitrogen content in the polymeric metal complex of PDMAT and TDEAH (cf. the structural chemical formula in Figure 31 b). The incorporation of oxygen into the glass network is an inherent outcome of polymer processing. Minor amounts of oxygen are challenging to avoid. [85]

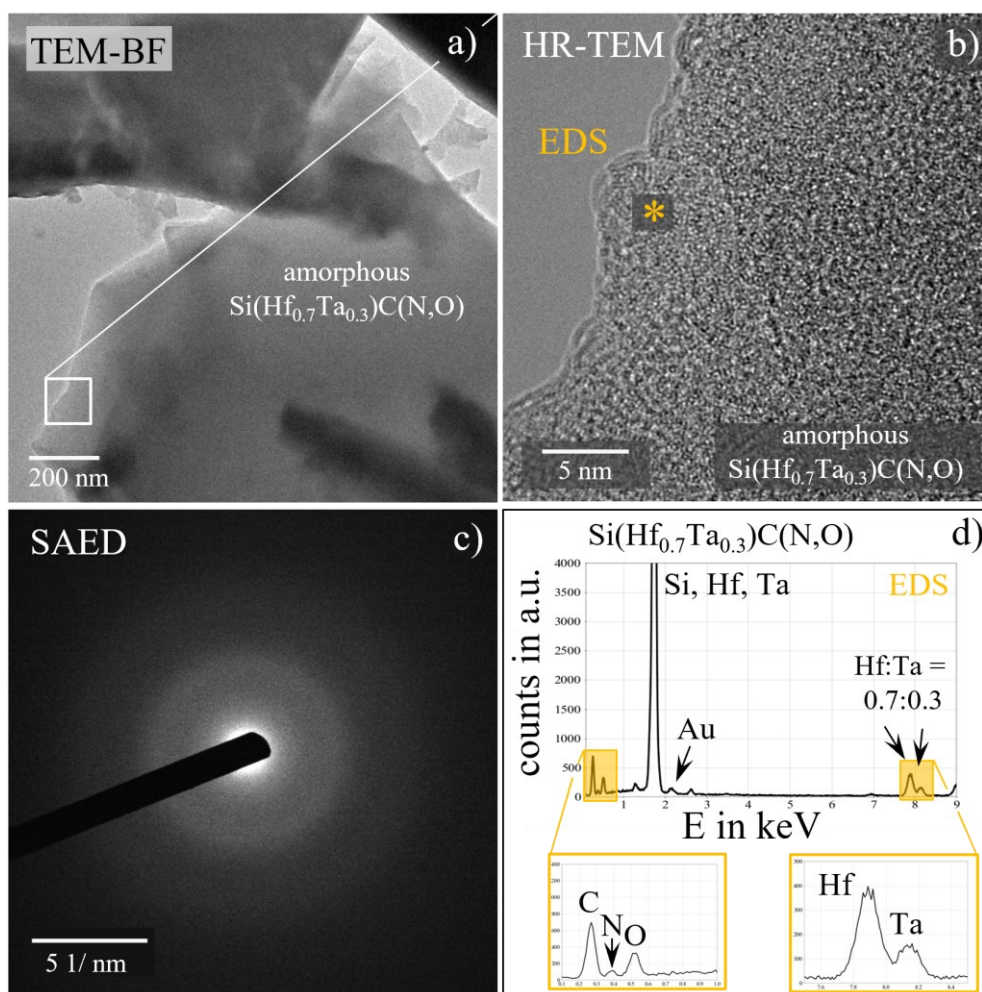


Figure 68 a) TEM-BF image, b) HR-TEM image, c) SAED pattern and d) EDS spectrum of the amorphous as-pyrolyzed $\text{Si(Hf}_{0.7}\text{Ta}_{0.3}\text{)C(N,O)}$ polymer-derived ceramic with a Hf:Ta ratio of Hf:Ta = 0.70:0.30 (± 0.06). The EDS spectrum in d) represent the amorphous $\text{Si(Hf}_{0.7}\text{Ta}_{0.3}\text{)C(N,O)}$ phase, with the elements indexed as follows: C (K_{α}), N (K_{α}), O (K_{α}), Si (K_{α}), Hf (M_{α} , L_{α}) and Ta (M_{α} , L_{α}).

While the XRD pattern and SEM analysis indicate an X-ray amorphous structure, inspections via TEM imaging reveal the presence of a small number of Hf- and Ta-rich nanoparticles, as shown in the TEM-BF and HR-TEM images in Figure 69. With this observation, the microstructure of the as-pyrolyzed $\text{Si(Hf}_{0.7}\text{Ta}_{0.3}\text{)C(N,O)}$ polymer-derived ceramic powder is defined as pseudo-amorphous rather than fully amorphous. Figure 69 a) depicts two distinct diffraction contrasts. Due to a higher mass contrast the observed Hf-Ta-rich nanoparticles appear darker than the amorphous $\text{Si(Hf}_{0.7}\text{Ta}_{0.3}\text{)C(N,O)}$ glass network. The particle size of the Hf,Ta-rich nanoparticles range from approximately 5 nm up to 100 nm (Figure 69 a)). EDS analysis, combined with HR-TEM imaging, SAED pattern, and IFFT images (Figure 69), reveal the presence of an intermetallic ($\text{Ta}_x\text{Hf}_{1-x}\text{)C(O)}$ compound phase with small amounts of oxygen incorporated. In addition, the HR-TEM image, FFT and IFFT images in Figure 69 b), e) and f) demonstrate that the TMC nanoparticles are encapsulated with a thin 2-4 nm graphitic carbon layer/shell (this was also observed for the annealed $\text{Si(Hf}_{0.7}\text{Ta}_{0.3}\text{)(C)N}$ powders, cf. Figure 58). The presence of these carbon shells has been reported in the literature, and their evolution during pyrolysis may be due to a carbon excess within the organometallic complexes, as explained in section 6.4.1.

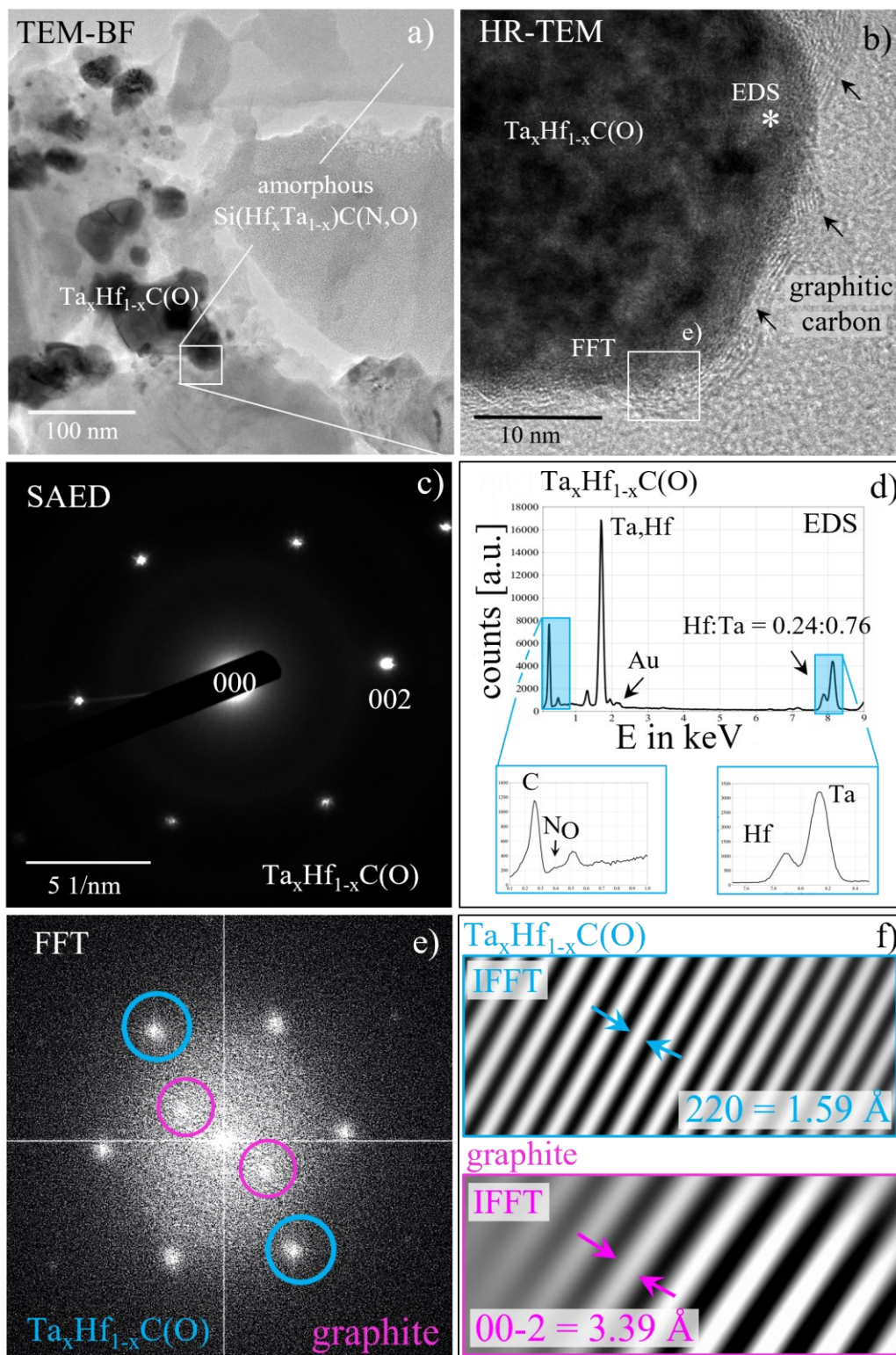


Figure 69 $\text{Si}(\text{Hf}_{0.7}\text{Ta}_{0.3})\text{C}(\text{N},\text{O})$ polymer-derived ceramic microstructure and elemental distribution after pyrolysis at 1000 °C, a) TEM-BF image, b) HR-TEM micrograph, c) SAED pattern, d) EDS spectrum and f) IFFT images. A amorphous $\text{Si}(\text{Hf}_{0.7}\text{Ta}_{0.3})\text{C}(\text{N},\text{O})$ glass network is visible by the homogeneous amplitude contrast in a), and Ta-rich nanoparticles via higher mass contrast in a). The EDS spectrum in d) at the position “*” b) shows a Ta-rich nanoparticle with a Hf:Ta ratio of Hf:Ta = 0.24:0.76 (± 0.04) with the elements indexed as follows: C ($K\alpha$), N ($K\alpha$), O ($K\alpha$), Hf ($M\alpha$, $L\alpha$) and Ta ($M\alpha$, $L\alpha$); e) FFT image with discrete diffraction spots (pink) showing the presence of graphite around the Ta-rich particle, exact position of FFT is indicated as small rectangle in b); IFFT images in f) give information about the lattice spacings of $(\text{Ta}_x\text{Hf}_{1-x})\text{C}(\text{O})$ in blue and the graphitic carbon in pink.

The EDS spectrum of the amorphous $\text{Si}(\text{Hf}_{0.7}\text{Ta}_{0.3})\text{C}(\text{N},\text{O})$ glass network shown in Figure 68 d) depicts the representative Hf:Ta ratio of 0.7:0.3 (± 0.06), which is consistent with the anticipated ratio upon synthesis (cf. section 4.3). The Hf:Ta ratio is assessed by measuring different powder particles of the amorphous $\text{Si}(\text{Hf}_{0.7}\text{Ta}_{0.3})\text{C}(\text{N},\text{O})$ glass network via 27 EDS point measurements. However, the Hf:Ta ratio within the TMC nanoparticles formed after pyrolysis at 1000 °C no longer correspond to that of the residual amorphous $\text{Si}(\text{Hf}_{0.7}\text{Ta}_{0.3})\text{C}(\text{N},\text{O})$ structure, as can be seen by comparing the heights of the Hf:Ta peaks in Figure 68 d) and Figure 69 d). The Hf:Ta ratio within 18 EDS point measurements of the TMC nanoparticles is 0.24:0.76 (± 0.04), indicating a different composition for the nanoparticles compared to the surrounding material. A detailed demonstration of the exact position of each EDS point measurement (amorphous structure and crystalline nanoparticles) in the corresponding $\text{Si}(\text{Hf}_{0.7}\text{Ta}_{0.3})\text{C}(\text{N},\text{O})$ polymer-derived ceramic powder sample and the evaluated elemental Hf:Ta ratios taken from the respective EDS spectra can be found in the appendix shown in Figure A3 and Table A 5.

7.3 Microstructure of Sintered $\text{SiC}/(\text{Hf}_{0.7}\text{Ta}_{0.3})\text{C}$ at 2200 °C in Vacuum

7.3.1 Microstructure Analysis by OLM and SEM

The microstructural of the consolidated $\text{SiC}/(\text{Hf}_{0.7}\text{Ta}_{0.3})\text{C}$ bulk ceramic after the FAST sintering process was studied by OLM and SEM. The consolidation resulted in the formation of a crystalline ceramic material, as depicted in the XRD pattern in Figure 66. Correlative light and electron microscopy (CLEM) technique was employed, enabling the comparison of the same area of interest using both microscopy methods. The results are depicted in Figure 70, including two optical light micrographs correlated to the respective area also shown in two SEM-BSE images of the sintered $\text{SiC}/(\text{Hf}_{0.7}\text{Ta}_{0.3})\text{C}$ composites. The analysis of the polished cross sections of the bulk ceramic reveals three distinct microstructural regions. Firstly, there are the remnants of the former powder particles with sizes of 50 μm up to 100 μm (cf. Figure 70 a)). Secondly, the microstructure consists of sinter necks, which are formed during the sintering process. Lastly, there is residual porosity present within the ceramic. In Figure 70 b) and d), the microstructure of the $\text{SiC}/(\text{Hf}_{0.7}\text{Ta}_{0.3})\text{C}$ ceramic is depicted, including the former powder particles and sinter necks labelled accordingly. These components constitute the majority of the microstructure. Porosity appears in three distinct forms, represented by different colored arrows in Figure 70 b) (white, black, and yellow). The black arrow in Figure 70 b) points to small-scaled intragranular pores within the former powder particles, characterized by pore sizes of approximately ~ 30 nm. In comparison to the sinter necks, the former powder particles appear darker in OLM micrographs (cf. Figure 70 a) and b)) due to the distribution of the small-scaled pores and the resulting diffuse scattering of light. Porosity is also observed at the interface between the former powder particles and the sinter necks (indicated by yellow arrows in Figure 70 b)). Furthermore, large macro pores are visible (white arrows) in both the OLM and SEM-BSE images (Figure 70 b) and d)), exhibiting considerable variation in pore morphology and sizes (up to 3 μm), particularly in the area of the sinter necks. The white rectangle in Figure 70 d) is shown as magnified SEM-BSE image in Figure 71 a), showing the sinter neck in the middle of the image and microstructural regions of the former powder particles in the left and right, respectively.

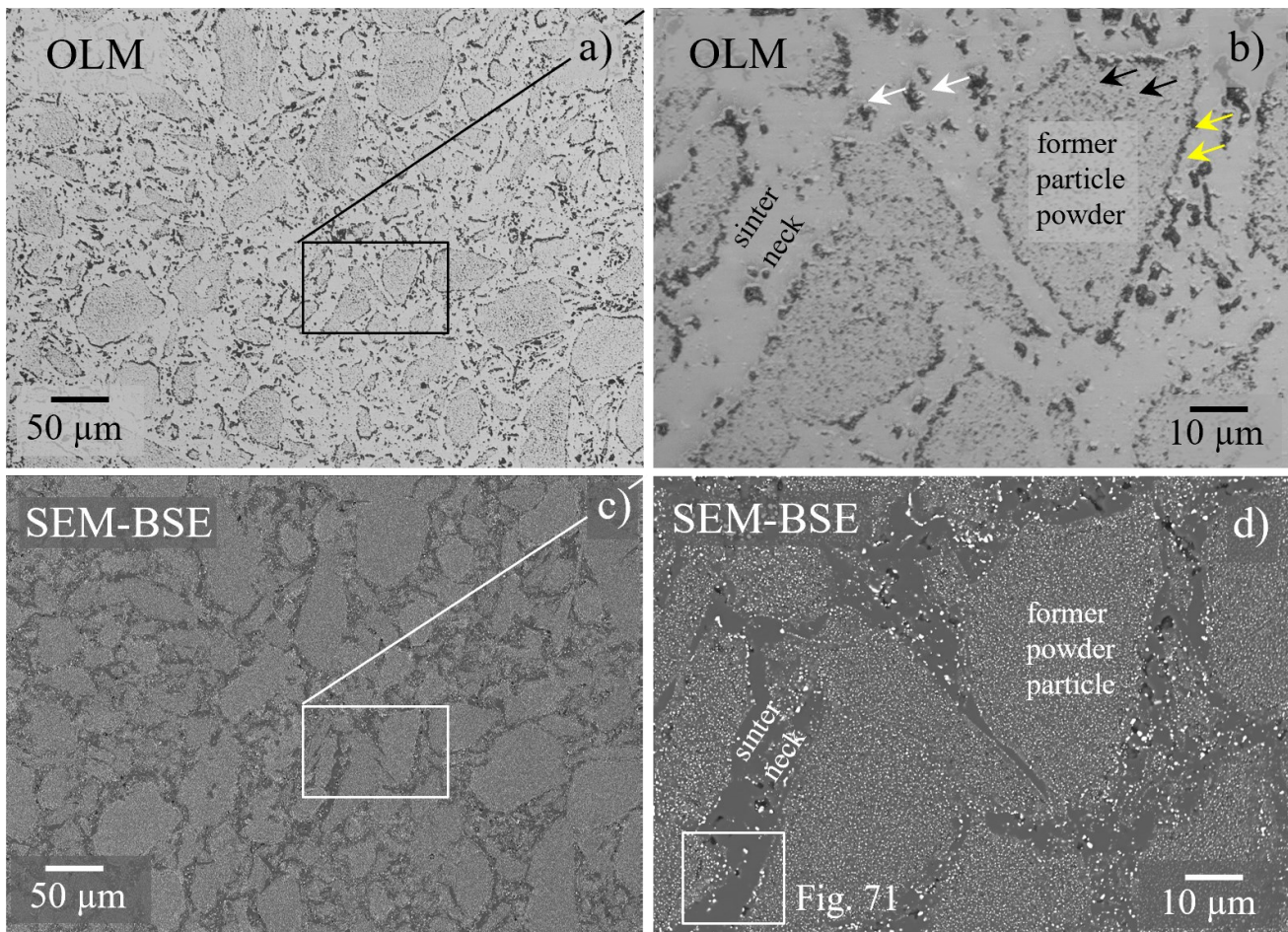


Figure 70 Correlative light and electron microscopy (CLEM) showing the three distinct microstructural regions of the consolidated SiC/(Hf_{0.7}Ta_{0.3})C PDC: former powder particles, sinter necks and porosity; a, b) optical light micrographs with three different colored arrows depicting the different appearance of pores within the sintered ceramic; the white arrow depicts the macropores in the sinter neck, the black arrows depict the pores within the former powder particle and the yellow arrows depict the pores, present c, d) SEM-BSE images showing the exact the same area of interest as in the optical light micrographs in a, b).

Analysis of the SEM-BSE micrographs reveal that the regions of the former powder particles consist of two finely dispersed phases. Through X-ray diffraction and chemical analysis (EDS) combined with electron diffraction (SAED in TEM, see section 7.3.4), the dark-appearing phase in the SEM-BSE images is identified as silicon carbide (SiC). On the other hand, the bright-appearing particles are identified as solid solutions of TMCs, specifically (Hf_{0.7}Ta_{0.3})C (as will be shown later in Figure 76 d), e), g)). The microstructure within the former powder particles is characterized by homogeneously distributed TMCs (with grain sizes of up to ~500 nm) embedded in a SiC matrix. This stands in contrast to the microstructure in the sinter necks, which primarily consist of SiC with enlarged grain sizes of TMCs with grain sizes of up to 1 μm. TMCs within the sinter necks are often found in close proximity to the internal surfaces of the former powder particles. Another microstructural feature near the internal surfaces of the former powder particles is depicted in Figure 71 b). TMCs in this region exhibit increased grain sizes and appear to be aligned in the microstructure, as indicated by red arrows.

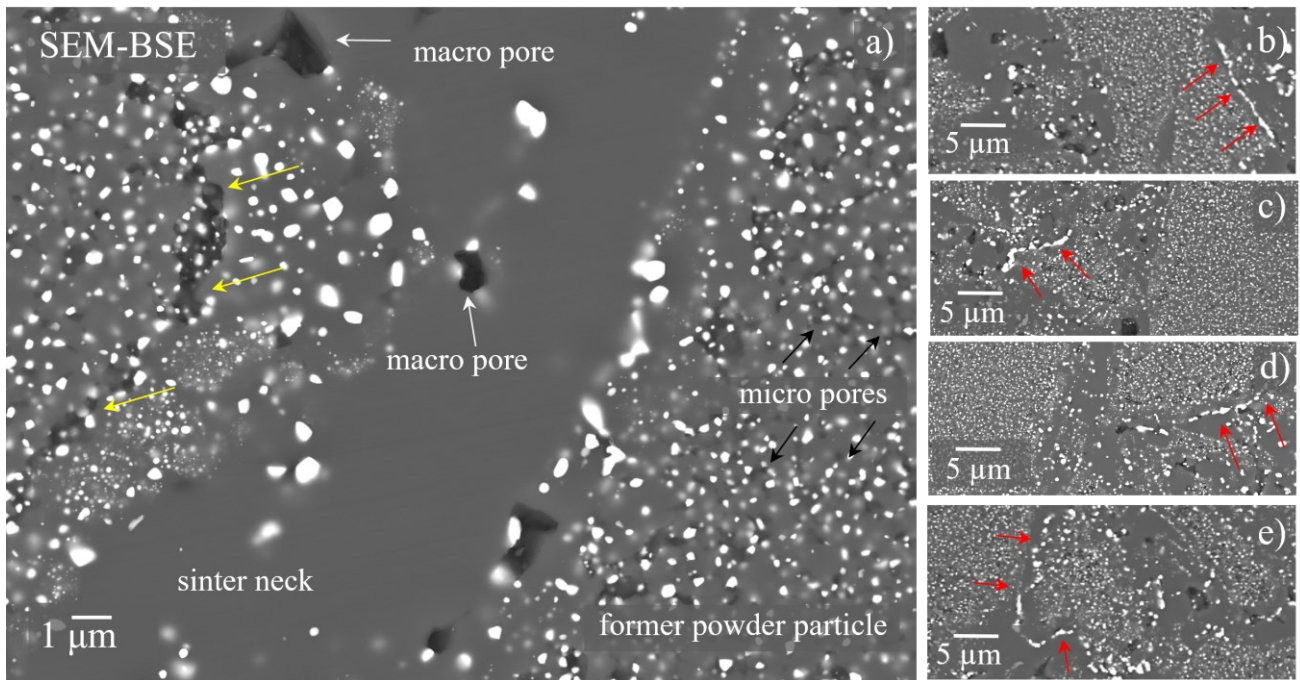


Figure 71 SEM-BSE images showing the constituting microstructural regions of the sintered bulk ceramic. a) magnified SEM-BSE image showing the sinter neck in the middle of the image and two former powder particles on the left and right. The three different appearances of pores within the microstructure of the sintered SiC/(Hf_{0.7}Ta_{0.3})C PDC are depicted with yellow, white and black arrows. SEM-BSE images in b, c, d and e) show TMCs very well aligned at or near the internal surface of the former powder particles.

7.3.2 Porosity Determination in SiC/(Hf_{0.7}Ta_{0.3})C

The residual porosity of the SiC/(Hf_{0.7}Ta_{0.3})C ceramic was determined via semiautomated image analysis using SEM-BSE images of polished cross sections obtained from the sintered bulk material. For large scale information, individual SEM-BSE images were captured at 11 different positions and assessed with a magnification of 500x and with a magnification of 1000x, as shown in Figure 72.

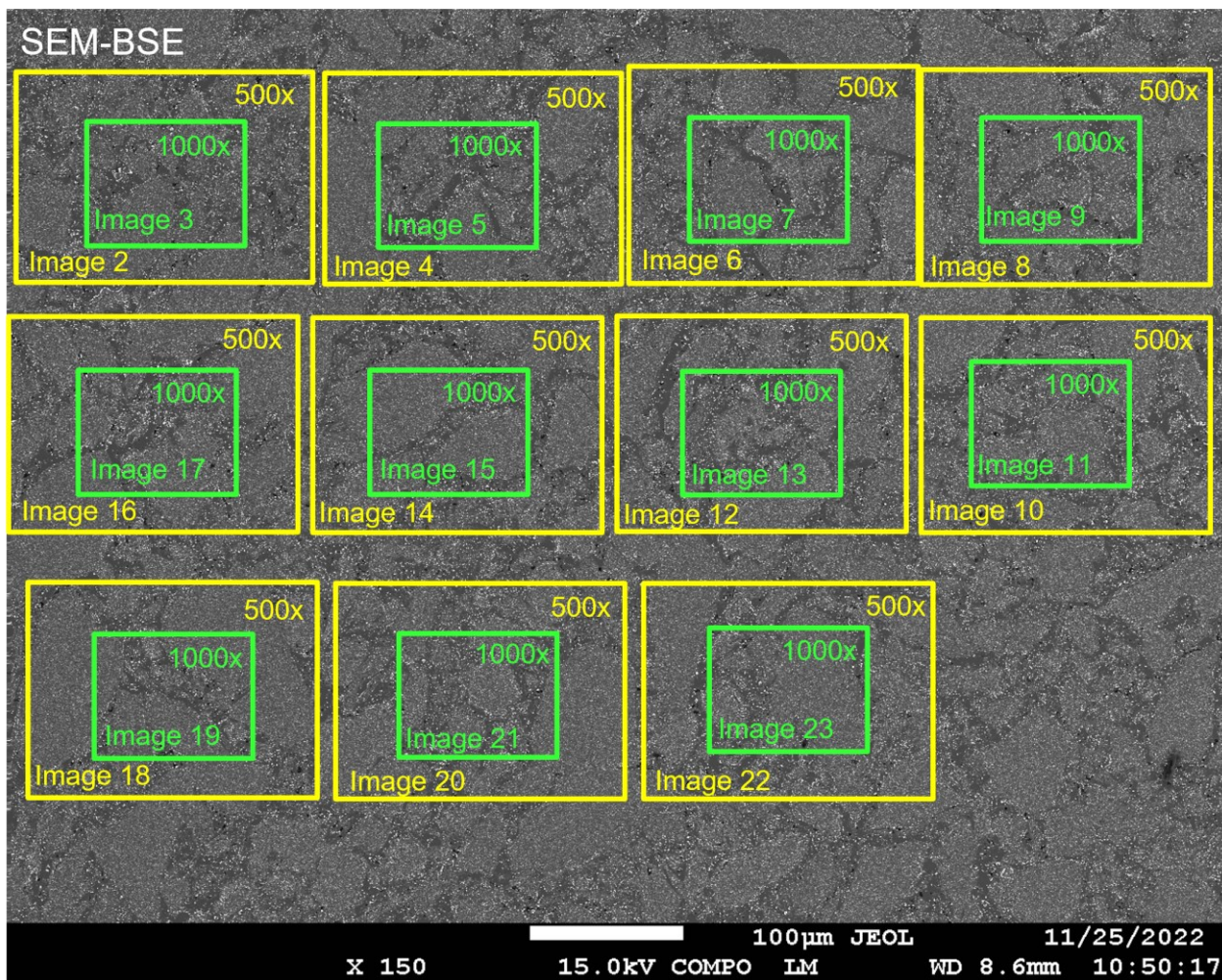


Figure 72 Low-magnified (LM) SEM-BSE image giving an overview where the total of 22 pictures were taken for the evaluation of the quantitative image analysis enabling for the determination of the porosity values. Yellow marked image frames were taken at a magnification of 500x, image frames depicted in green were taken at a magnification of 1000x.

Pores appear black in the SEM-BSE images. Thresholding via ImageJ gives the cross-sectional area percentage of the detected pores relative to the total area providing an area pore density. To evaluate the porosity of the series of images with magnifications of 500x and 1000x, gray values between 0-85 and 0-87 respectively were selected for each individual image using the thresholding tool in the histogram. Table 8 shows the results of the semiquantitative image analysis giving porosity values for the two different magnifications. The mean porosity value for the SiC/(Hf_{0.7}Ta_{0.3})C sample, based on the results from the eleven images, is determined to be 2.4 ± 0.7 area % for the images with a magnification of 500x and 4.6 ± 0.9 area% for the images with a magnification of 1000x. The given uncertainty was based on a standard uncertainty multiplied by a coverage factor $k = 2$ to achieve a confidence level of approximately 95 % [249].

Table 8 Resulting porosity values for eleven BSE images at magnifications of 500x and 1000x.

Frame no.	porosity (500x) in area %	porosity (1000x) in area %
2, 3	2.8	4.3
4, 5	3.1	5.0
6, 7	2.2	5.3
8, 9	2.6	5.3
10, 11	2.6	4.2
12, 13	2.1	3.8
14, 15	2.0	4.6
16, 17	2.4	4.3
18, 19	1.9	4.5
20, 21	2.0	4.8
22, 23	2.4	4.4
mean	2.4	4.6
2σ	0.7	0.9

Figure 73 presents a comparison of the results gained upon the two investigated magnifications of 500x and 1000x. In Figure 73 a) and b) two original SEM-BSE images for the selected magnifications are shown. Figure 73 c) and d) show the further processed images in which the quantitatively analyzed pores are depicted in blue. Additionally, Figure 73 e) and f) show the final processed images of the indexed pores in black after the thresholding via ImageJ. Images taken upon a magnification of 1000x show a representative distribution of pores in the microstructural region of the sinter necks containing larger pores as well as in the microstructural regions of the former powder particles containing smaller pores (cf. blue marked pores in Figure 73 c), d)). As can be seen in Figure 73 images with a magnification of 500x loose pore information, in particular regarding the smaller pore sizes in the microstructural regions of the former powder particles. Therefore, the determined porosity values within the images with the 1000x magnification were preferred due to a representative pictorial presentation of pores in both microstructural regions, i.e., former powder particles and sinter necks. This ensured a more accurate representation of the porosity distribution, avoiding an overestimation of one or another microstructural region [202]. The relatively high material density determined for eleven images at a magnification for 1000x reaching $\sim 95\%$ in the ceramic bulk sample is attributed to the efficient consolidation achieved through FAST.

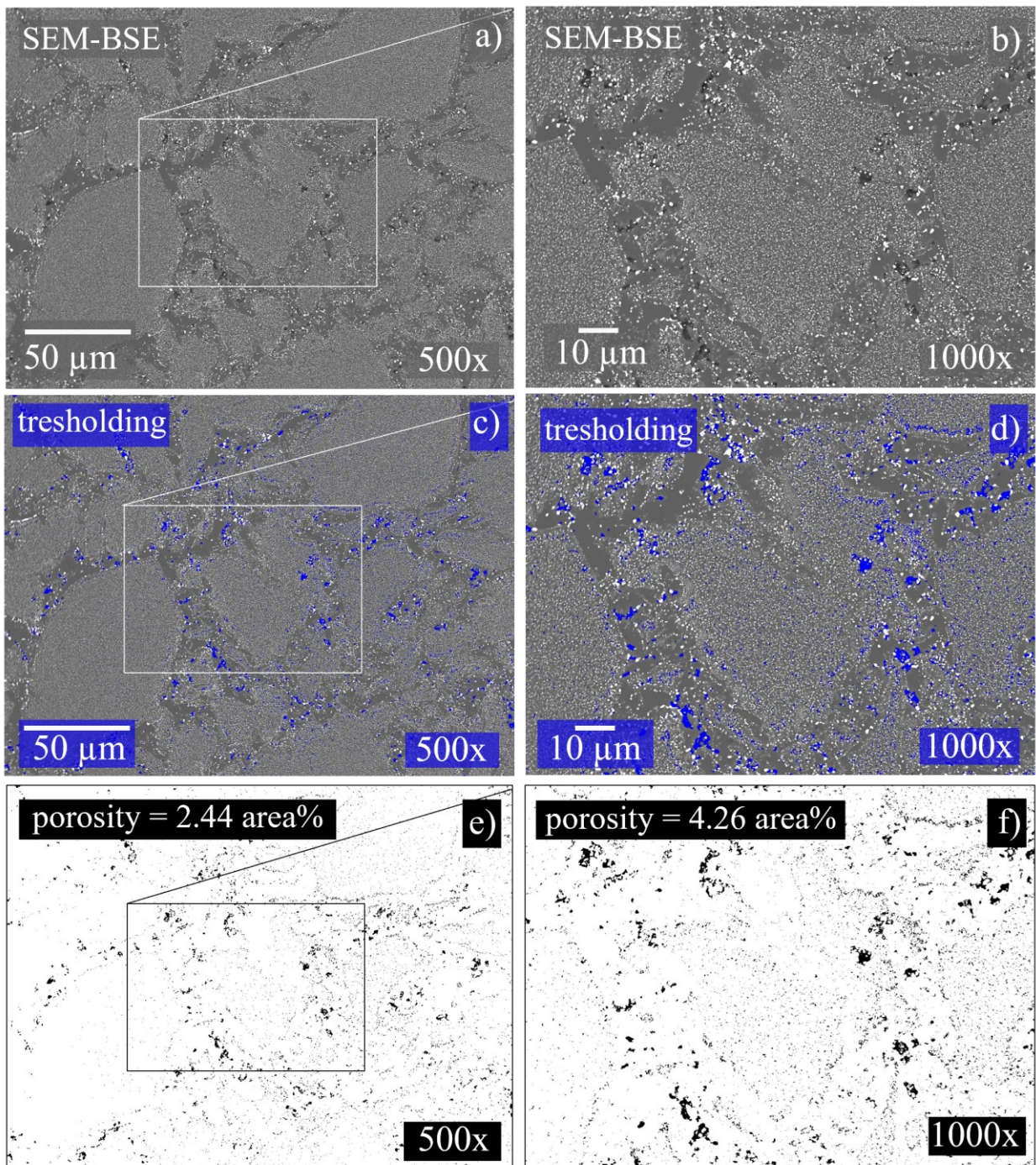


Figure 73 SEM-BSE images and further processed images used for the determination of the porosity in the $\text{SiC}/(\text{Hf}_{0.7}\text{Ta}_{0.3})\text{C}$ bulk sample. a, b) original SEM-BSE images with magnifications of 500x and 1000x. c, d) Thresholding of the darkest contrast in a, b) leads to the blue-marked pores. e, f) Final image after thresholding gives the indexed pores in black.

7.3.3 Elemental distribution maps using EPMA analysis

Figure 74 displays an SEM-BSE image and the correlated elemental distribution maps of the Si, Hf, Ta, C, N and O, obtained via electron microprobe analysis (EPMA). The SEM-BSE image in Figure 74 a) depicts the analysed microstructure region, comprising the former powder particles and sinter necks. Dark blue marked pixels indicate a low element concentration, while red and orange indicate a high element concentration at that location. The elemental distribution maps reveal an enrichment of Si

within the sinter necks (cf. Figure 74 b)). Hf, Ta, and C show a slight enrichment (light blue) within the former powder particles and a predominant enrichment (green, yellow and red) at/near the internal surfaces of the former powder particles (Figure 74 c), d), e)). These findings are consistent with the SEM analysis, where TMCs with larger grain sizes were observed at the internal surfaces of the former powder particles. The elemental distribution maps for O and N indicate no significant enrichment (cf. Figure 74 f), g)). This is again consistent with the elemental analysis presented in Table 7. The elemental difference between the sinter necks and the former powder particles is nicely detected within the element distribution maps in Figure 74. However, a distinction between individual SiC and TMC grains within the former powder particles is not clearly detectable due to the relatively large beam diameter in the EPMA. This is because the TMCs, especially within the former powder particles, have sizes below 500 nm which is smaller than the beam diameter ($< 1 \mu\text{m}$).

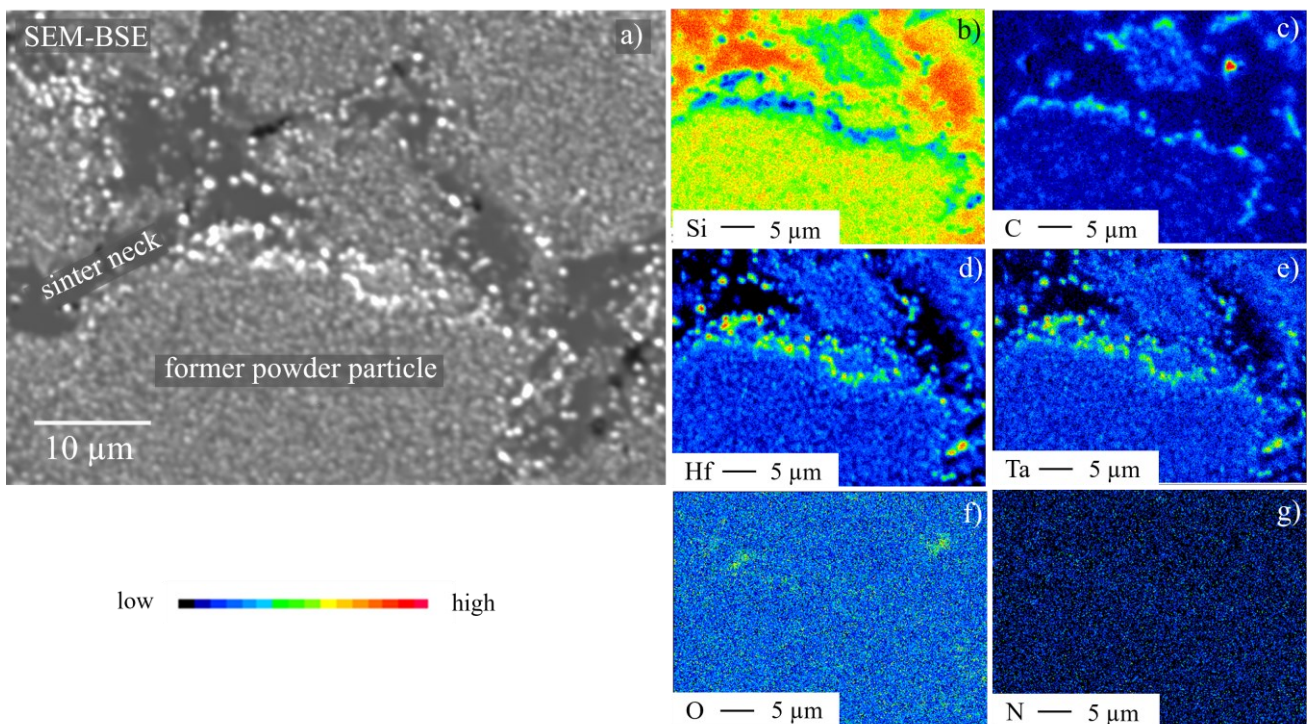


Figure 74 SEM-BSE image (a) and correlative EPMA element distribution maps of Si, C, Hf, Ta, O and N in b-g) of a cross-sectioned and polished sintered SiC/(Hf_{0.7}Ta_{0.3})C bulk ceramic. Dark blue equals low element concentrations, red equals high element concentrations.

7.3.4 Microstructure of SiC/(Hf_{0.7}Ta_{0.3})C using TEM Analysis Methods

Figure 75 depicts a collage of TEM-BF images, comprising 253 individual images, acquired from an Ar⁺-ion-milled sintered SiC/(Hf_{0.7}Ta_{0.3})C TEM specimen. It offers a combination of high magnification and a large field of view. Each image is captured at the smallest possible magnification of 5000x to visualize the grain-like microstructure, encompassing the former powder particles and the sinter necks. Within the image composition, two distinct phases are present, namely SiC and the TMC of (Hf_{0.7}Ta_{0.3})C, forming the overall phase assemblage. These phases exhibit noticeable differences in mass contrast in the TEM-BF images, enabling easy differentiation between both phases. Consistent with observations from OLM and SEM, the TEM imaging also confirms the relatively homogeneous microstructure of the former powder particle regions. In contrast, the region of the sinter necks displays a more heterogeneous microstructure concerning grain size, phase distribution, and grain morphology. Figure 76 provides a

closer view of the area within the white rectangle shown in Figure 75, further magnifying the microstructural regions, i.e., the former powder particle and sinter neck for detailed analysis.

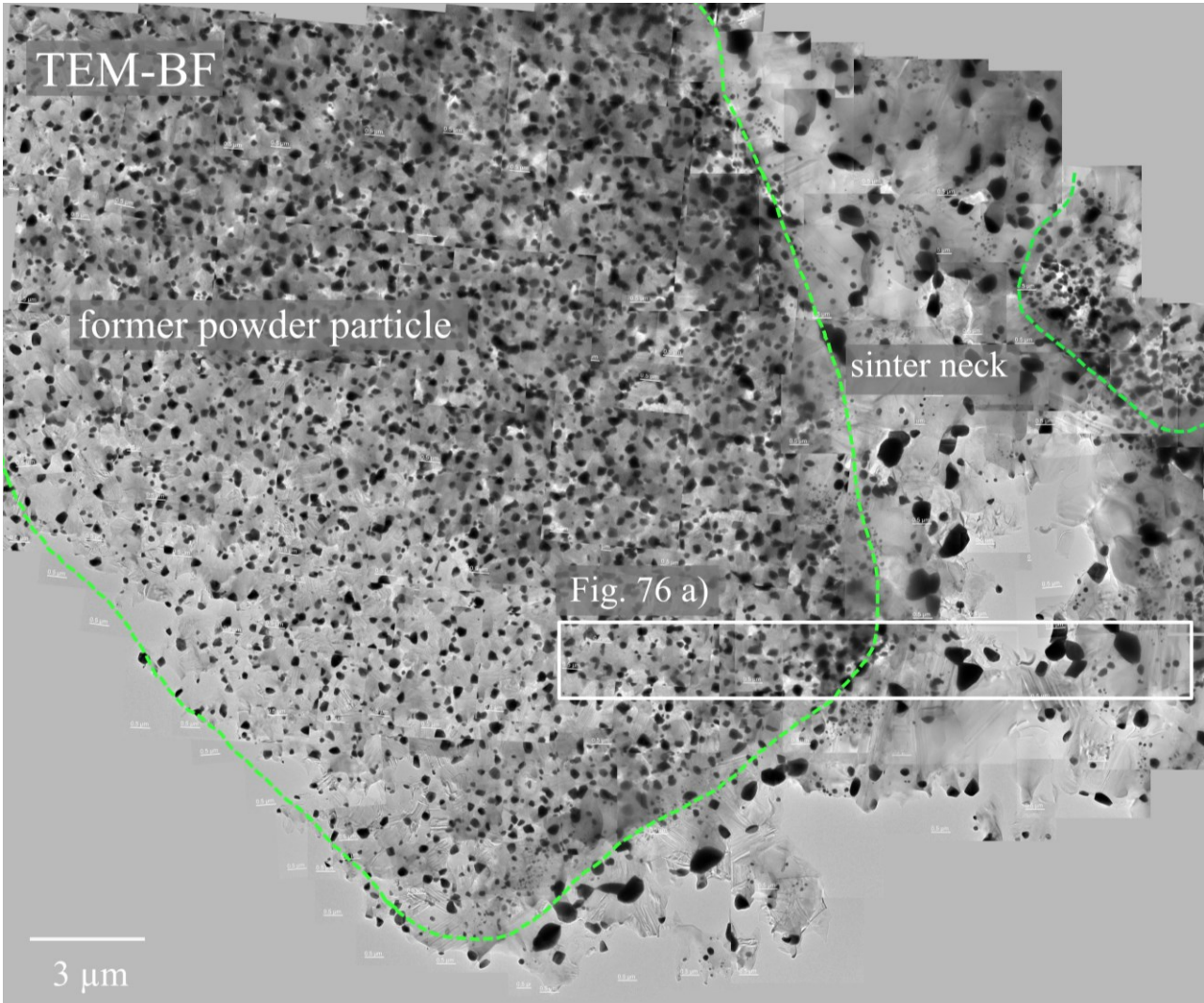


Figure 75 TEM-BF collage composing 253 individual TEM-BF images giving a high magnification with a large field of view of the microstructure of the consolidated PDC. Two microstructural regions are shown: the former powder particles and the sinter neck. The dashed green line separates the former powder particle from the sinter neck.

Figure 76 provides a detailed analysis of the two distinct microstructural regions. As shown in Figure 76 b), the former powder particles exhibit finely dispersed particles in the matrix, according to EDS (Figure 76 e)) related to TMCs embedded in a SiC-rich matrix phase. The grain sizes of both phases within the former powder particles show a homogeneous distribution. SiC particles are equiaxed in shape, ranging from 400 up to 700 nm in size, while (Hf,Ta)C particles are slightly smaller, with sizes ranging from 100 up to 400 nm (cf. Figure 76 b)). The grain size distribution in the sinter necks region differs significantly. Both SiC and TMCs show increased grain sizes near the internal surfaces of the former powder particles. Particularly noteworthy are the (Hf_{0.7}Ta_{0.3})C grains, with a maximum measured size of up to 800 nm, which is almost twice as large as the grain sizes in the former powder particles. The sinter necks mainly consist of large SiC crystals, with a maximum grain size of up to 3 μm (Figure 76 d)). The Hf:Ta ratio of the observed TMC particles formed upon crystallization during the sintering process, were assessed by EDS point measurements on 33 individual particles (see exact positions in Figure A4 and the corresponding data in Table A6 in the appendix). The measured EDS data are close to the anticipated

composition of the precursors (Hf:Ta = 0.7:0.3). The mean Hf:Ta ratio within the $(\text{Hf}_{0.7}\text{Ta}_{0.3})\text{C}$ grains is measured as 0.74:0.26 (± 0.04). Thus, the compositions of the respective crystallites of $(\text{Hf}_{0.7}\text{Ta}_{0.3})\text{C}$ are presented in the molar ratios of the precursors within the text and the anticipated images. Two exemplary EDS spectra of a TMC (depicted in blue) and SiC (depicted in green) are shown in Figure 76 e). The EDS measurements provide no indication of residual nitrogen within the TMC or SiC of the sintered sample. However, small amounts of oxygen are incorporated in the TMC, rather than in the SiC.

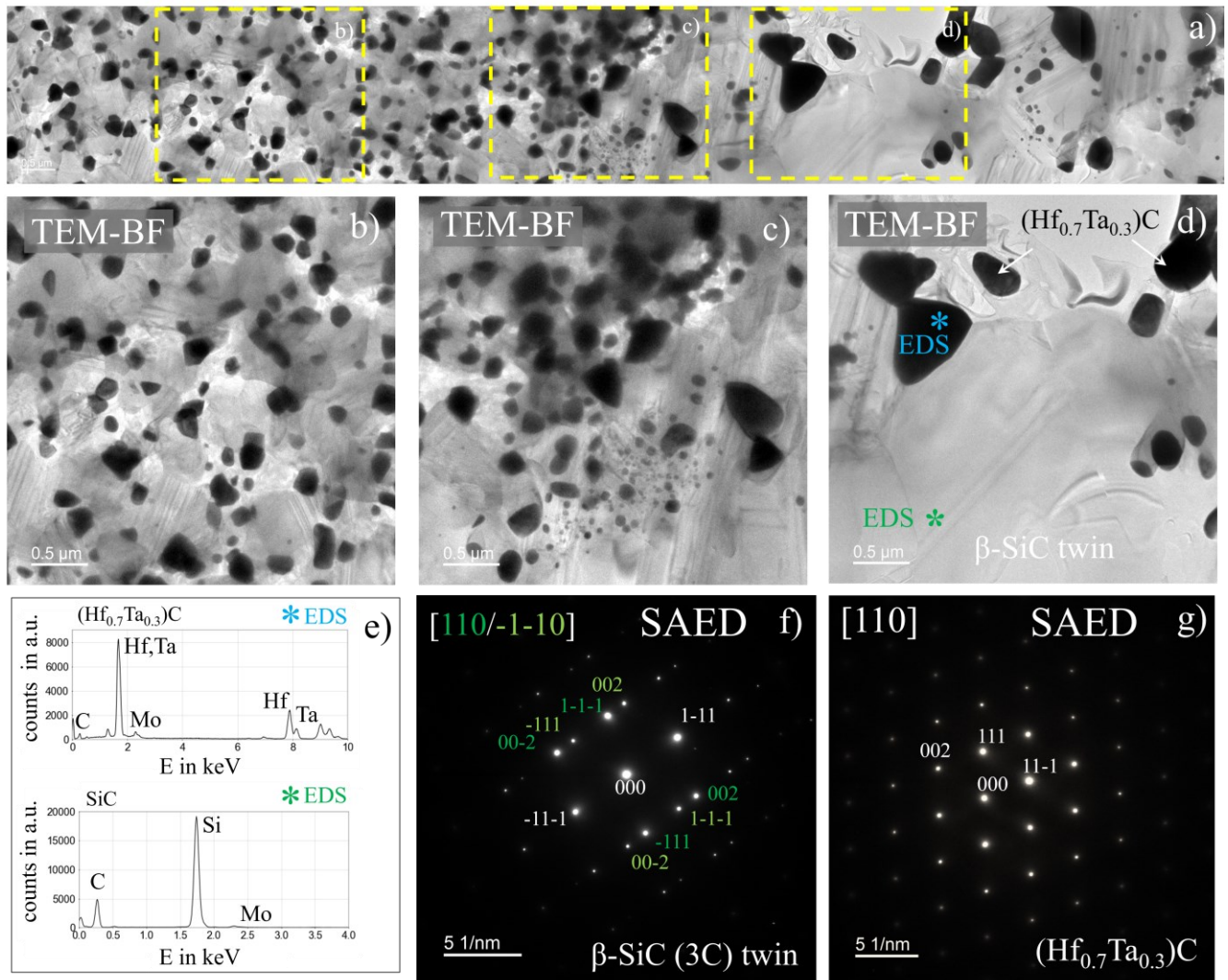


Figure 76 a-d) TEM-BF images showing the transition zone between the former powder particles and the sinter neck; d) EDS point measurement of the TMC is marked with blue asterisk and EDS point measurement of SiC is marked with a green asterisk; e) the EDS spectra from the corresponding asterisks in d). Elements are indexed as follows: for $(\text{Hf}_{0.7}\text{Ta}_{0.3})\text{C}$ in blue: C ($K\alpha$), Mo ($L\alpha$), Hf ($M\alpha$, $L\alpha$), Ta ($M\alpha$, $L\alpha$) and for SiC in green: C ($K\alpha$), Si ($K\alpha$), Mo ($L\alpha$); f, g) SAED patterns of $(\text{Hf}_{0.7}\text{Ta}_{0.3})\text{C}$ TMC and SiC, both aligned to a specific zone axis.

Electron diffraction analysis of SiC reveals its cubic phase (F-43m, zinc-blende structure), commonly known as 3C-SiC or β -SiC. Twinning of 3C-SiC is frequently observed (cf. Figure 76 b) and Figure 77). Under specific imaging conditions close to the $[110]$ zone axis, the selected area electron diffraction (SAED) pattern of a SiC single-twin is depicted in Figure 76 f), where the $\langle 111 \rangle$ plane represents the twin boundary. Apart from single-twins, SiC contains stacking faults (SF) in the sintered bulk sample. These SFs are visible in the high-resolution transmission electron microscopy (HR-TEM) image of Figure

77 c), displaying a sequence of bright/dark contrasts. During TEM analysis, two polytypes of SiC are identified: 3C-SiC and 6H-SiC, as evident from the SAED patterns in Figure 77 d) and f).

Additionally, the FAST sintered sample exhibits segregated carbon, which is observable in the form of thin graphitic carbon layers/shells around the TMCs. This has been reported for earlier systems in section 6.4.1 and already for the as-pyrolyzed Si(Hf_{0.7}Ta_{0.3})C(N,O) in section 7.2 (cf. Figure 69) as well as in the literature in Ref. [41].

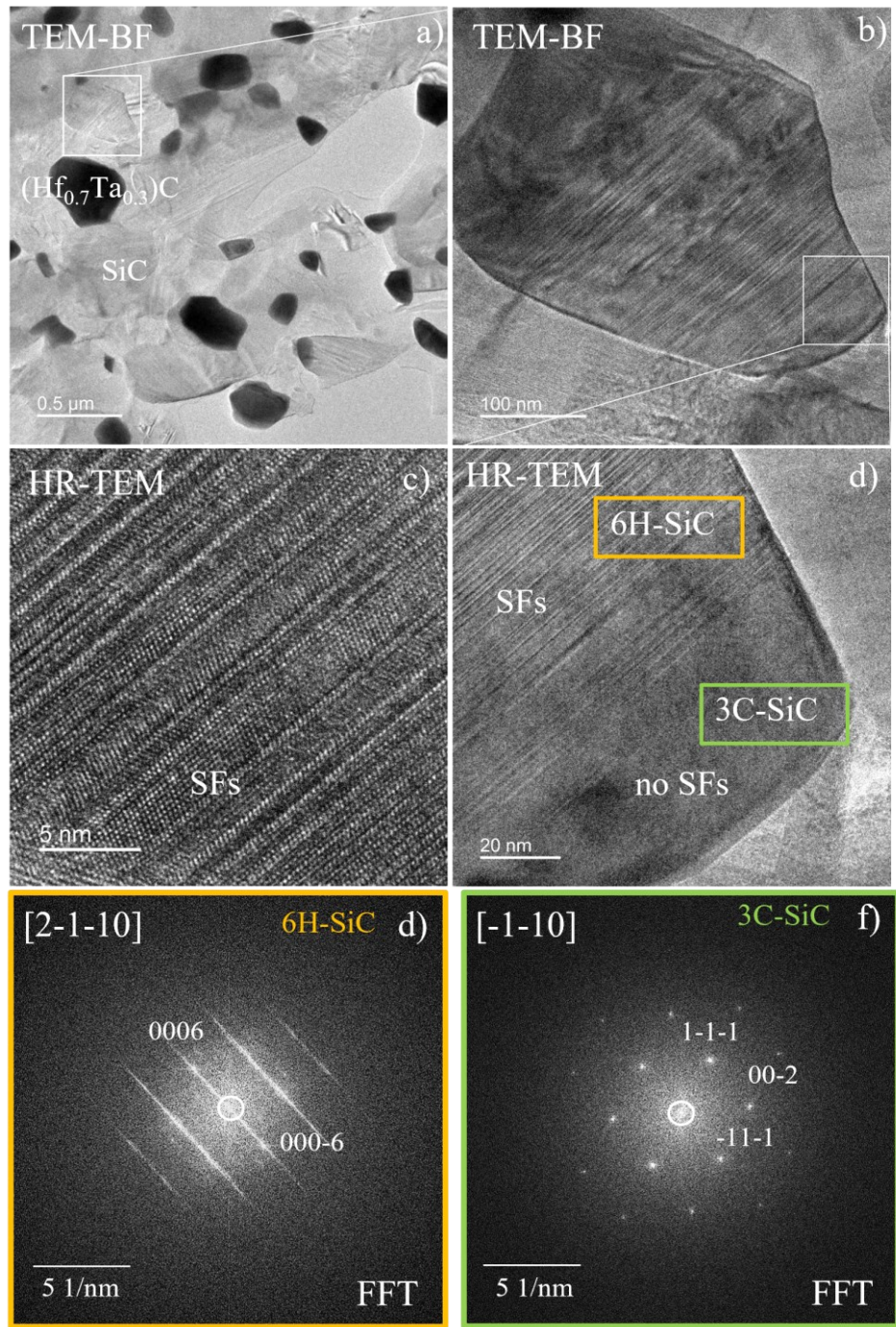


Figure 77 a, b) TEM-BF images of the sintered SiC/(Hf_{0.7}Ta_{0.3})C PDC, focusing on a SiC grain with regions, enriched in stacking faults. c, d) HR-TEM images showing a region where no SFs are present, and a region where SFs are depicted as bright/dark contrast. d, f) FFT images of the corresponding regions marked in d).

7.3.5 Mechanical Properties of the Different Microstructural Regions

Mechanical properties are measured by nanoindentation, as described in chapter 3.8. After the data acquisition including the sample mapping, the resulting data set was analysed via cumulative frequency (cf) plots in collaboration with G. Winkens based on the considerations from Randall [228]. Focus was on identifying the mechanical properties of the three different microstructural regions, which were described in detail in section 7.3.1, namely the sinter necks, the former powder particles, and the porous region. These components rationalize the usage of a three-component fit within the cf plots. In each microstructural component, a Gaussian distribution for the hardness H and the Young's Modulus E was assumed. Thus, the sum of three cumulative Gaussian distributions with variable fraction was fitted to the cf plots. Three distinct hardness values and mean elastic moduli, their respective standard deviation and the relative occurrence of each microstructural component were characterized. The mechanical properties of each individual indent were attributed to one of the three microstructural regions. In addition, the mapping is reconstructed accordingly. In comparison to a two-component fit, the three-component fit yielded far better results.

Figure 78 a) presents an optical light micrograph of the 50 x 50 indentation grid, while Figure 78 b) exhibits maps of the measured mechanical properties. Each indent shown in the grid in Figure 78 b) was attributed to one microstructural region. Specifically, the low-hardness/low-modulus component is represented by blue regions, while medium and high-value components are indicated by yellow and red regions, respectively.

The analysis of the maps in Figure 78 b), alongside with the optical micrograph, allows the extraction of correlations between the mechanical properties and the microstructure. For instance, former powder particles containing SiC, $(\text{Hf}_{0.7}\text{Ta}_{0.3})\text{C}$, and nanopores, situated in the center left and lower left regions of Figure 78 b), belong to the yellow component, exhibiting medium hardness ($H = 27.3 \pm 3.3$ GPa) and medium modulus ($E = 444 \pm 24$ GPa). On the other hand, areas displaying macro pores visible in the optical micrograph (e.g., the large pore in the center left of Figure 78 a)) correspond to the blue component, characterized by low values ($H = 22.5 \pm 7.3$ GPa; $E = 367 \pm 78$ GPa). Sinter necks with minimal or no porosity, mainly composed of SiC, belong to the red component, showing the highest values for mean hardness ($H = 36.7 \pm 2.9$ GPa) and mean modulus ($E = 549 \pm 62$ GPa). The large relative standard deviation of 33 % and 21 % for H and E , respectively, in the blue region (cf. Table 9; porous regions) can be attributed to the inclusion of porous areas of the two other microstructural components (red and yellow), where no distinct materials properties were identified within the cf. Notably, the maps in Figure 78 b) indicate relatively low values for hardness and modulus at the top edge. Although these areas were predominantly attributed to the blue component, the optical micrograph reveals the presence of powder particles. The low mechanical properties in this region can be explained by the presence of subsurface porosity, which is not observable in the optical micrograph. As a result, the mechanical properties determined through nanoindentation may not necessarily correlate with the microstructural components identified through surface characterization, owing to potential differences in subsurface microstructures.

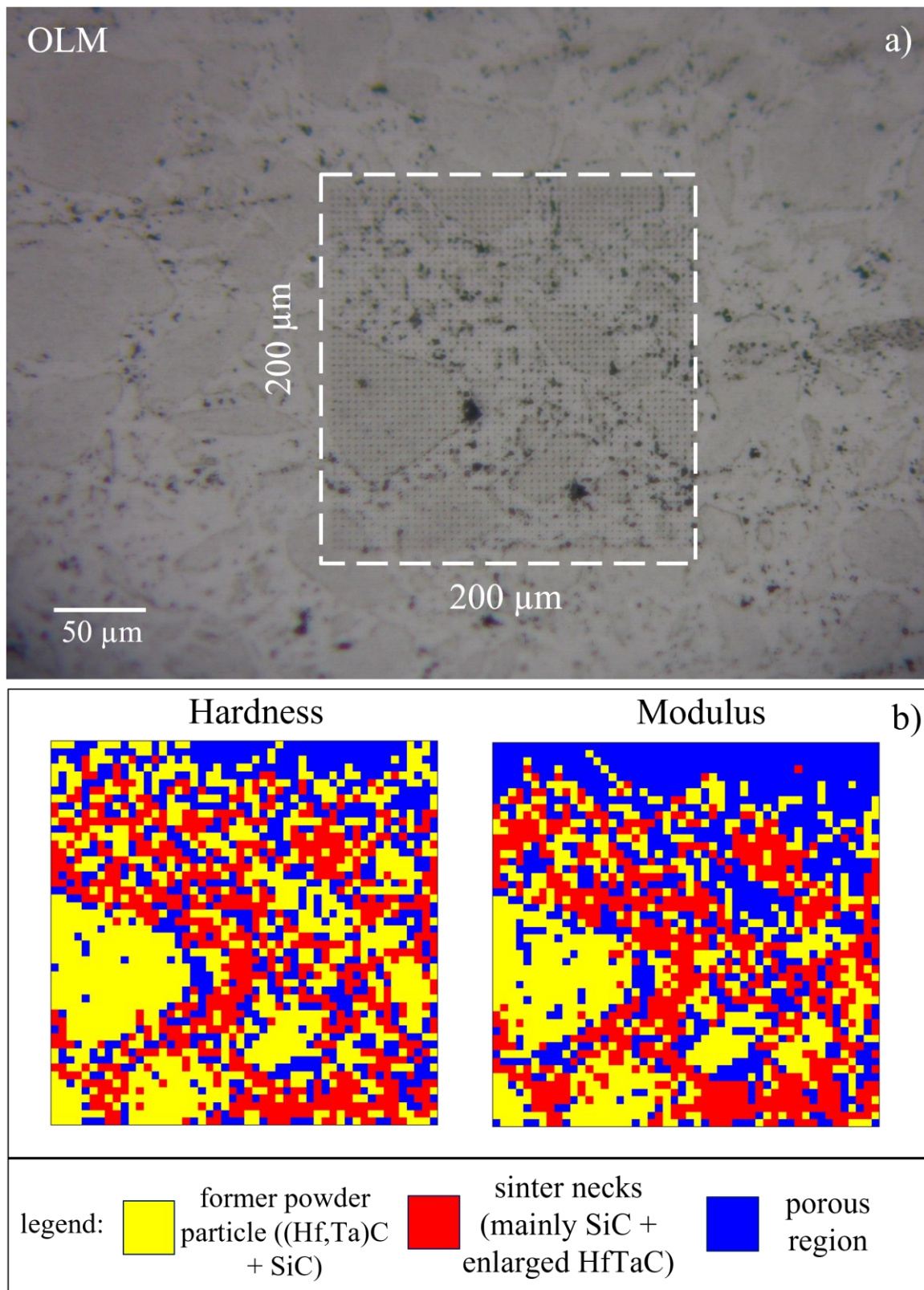


Figure 78 a) Optical light micrograph showing the probed 50 x 50 indentation grid. b) Hardness and Modulus maps of the corresponding area indented in a). Each indent was attributed to one of the three microstructural components: yellow for the former powder particle constituting small-scaled and homogeneous distributed $(\text{Hf}_{0.7}\text{Ta}_{0.3})\text{Cs}$ in a SiC matrix, red for the sinter necks, mainly constituting SiC and enlarged $(\text{Hf}_{0.7}\text{Ta}_{0.3})\text{Cs}$ and blue for porous regions.

Table 9 shows the results of the mechanical properties revealed upon the fit of the three Gaussian-distributed components.

Table 9 Mechanical properties of the three microstructural regions in the monolithic SiC/(Hf_{0.7}Ta_{0.3})C ceramic.

	Former powder particle (TMC + SiC + nanopores)	Sinter necks (mainly SiC + enlarged TMCs)	Porous regions
Hardness in GPa ± standard deviation (σ)	27.3 ± 3.3	36.7 ± 2.9	22.5 ± 7.3
E Modulus in GPa ± standard deviation (σ)	444 ± 24	549 ± 62	367 ± 78

7.4 Discussion

7.4.1 As-pyrolyzed 1000 °C Si(Hf_{0.7}Ta_{0.3})C(N,O) Powder Sample

The investigation of the as-pyrolyzed Si(Hf_{0.7}Ta_{0.3})C(N,O) polymer-derived ceramic powders, synthesized using the PDC approach, revealed the presence of nanocrystalline particles within a predominantly amorphous matrix (cf. Figure 69 a), b)). It indicates that the X-ray amorphous powder (cf. Figure 66) exhibits a microstructure, which is not fully homogeneous upon pyrolysis temperatures of 1000 °C. The phenomenon that PDCs undergo local early crystallization upon pyrolysis was reported for nanocrystalline TMCNs in the novel Si(Hf_xTa_{1-x})(C)N described in chapter 6.4 and for nano-sized ZrO₂ in a SiZrCN PDC as reported in Ref. [60]. As shown in Figure 69 d), the Hf:Ta ratio of the early formed crystalline TMCs indicate a Ta-rich (0.2:0.8) Hf:Ta ratio, deviating from the overall anticipated Hf-rich (0.7:0.3) Hf:Ta ratio. With reference to the HfC-TaC phase diagram in Figure 7 Ta-rich TMCs are thermodynamically stable, as there opens a two-phase region at low temperatures. According to the quasi-binary phase diagram, also Hf-rich carbides should be present. However, by local TEM measurements it is possible, that the Hf-rich precipitates were not sampled here. It should be considered that the system does not consists of three elements only, and other phases can occur in the higher-level phase diagram.

7.4.2 Microstructural Evolution of the Sintered SiC/(Hf_{0.7}Ta_{0.3})C Bulk Sample

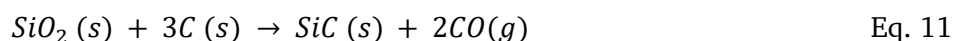
Numerous characteristics of the amorphous Si(Hf_{0.7}Ta_{0.3})C(N,O) and dense SiC/(Hf_{0.7}Ta_{0.3})C ceramic concerning the chemical composition, phase assemblage and the microstructural evolution upon sintering have been described via ex-situ analysis in the chapters 7.1, 7.2 and 7.3. The microstructure characterization include the evolution of a mostly amorphous Si(HfTa)C(NO) precursor into a crystalline SiC/(Hf_{0.7}Ta_{0.3})C ceramic via phase separation and crystallization. The consolidation of the initial powder particles is activated via sintering mechanisms, through matter transfer, leading to SiC-rich sinter necks between the former powder particles. In addition, as shown in Figure 75, internal surfaces of the former powder particles depict increased grain sizes of TMCs. Stacking faults in Silicon carbide is an often observed microstructure characteristics within the sintered SiC/(Hf_{0.7}Ta_{0.3})C bulk ceramic (cf. Figure 77). Residual closed porosity is found to be entrapped within both microstructural regions (cf. Figure 70, Figure 71). The combination of the FAST sinter parameters, including mechanical, thermal, and electrical effects, lead to various mechanisms such as densification, Joule heating, thermal gradients, percolation effects, Peltier effect, electromigration, and/or electrochemical reduction, as well as diffusion

processes [168,169,250]. All these mechanisms collectively contribute to the observed microstructural evolution in the investigated SiC/(Hf_{0.7}Ta_{0.3})C PDC. Notably, the final microstructure evolution is not solely determined by the sintering parameters [54]. It also significantly depends on the size distribution of the starting powder particles, which is influenced by ball milling and sieving processes. Furthermore, the chemical composition of the starting powder plays a crucial role in shaping the final microstructure [12,54]. Chemical reactions occurring during the FAST process, such as phase separation, crystallization, decomposition and therefore also the formation of gaseous species have also a profound impact on the final microstructure of the PDC. In the subsequent sections, the influence of various processing parameters on the microstructure and chemistry of the SiC/(Hf_{0.7}Ta_{0.3})C ceramic is discussed.

7.4.3 Role of Atmosphere/Gaseous Species Influencing the Evolving Microstructure

The starting powder primarily comprises an amorphous Si(Hf_{0.7}Ta_{0.3})C(N,O) glass. However, during the sintering process, various reactions occur, such as crystallization, phase transitions, vaporization, and condensation reactions, which significantly influence the sinter behaviour of the system. This is particularly evident in UHTC and PDC systems, where thermal decomposition reactions lead to local chemical variations upon high-temperature annealing or where sintering leads to the release of volatile substances into the sintering chamber [84,99,180,181]. The microstructural evolution of amorphous polymer-derived ceramics upon ultra-high temperature sintering involves numerous reaction steps and processes which are not fully understood yet. Some critical sub-reactions during sintering in SiC-based systems have been recently described in the literature [251–253].

For instance, Saha et al. reported the phase separation of amorphous SiOC ceramics into SiO₂, SiC, and C at temperatures starting from 1300°C [252]. Also, Liu and co-workers assume that smaller amounts of oxygen impurities (SiO₂) and residual carbon are present in the HfC-SiC system [253]. With reference to thermodynamic calculations and previous studies, the authors assume that the sub-reactions (Equations 11, 12) will occur at different temperatures during sintering [253].



$$(T > 1530 \text{ }^\circ\text{C}, P_{CO} = 1 \text{ atm}, \Delta G < 0)$$



$$(T > \sim 1700 \text{ }^\circ\text{C}, P_{SiO} = 3P_{CO} = 0.25 \text{ atm}, \Delta G < 0)$$

Thus, it is assumed that various sub-reactions also occur during the transition from amorphous Si(Hf_{0.7}Ta_{0.3})C(N,O) into the crystalline SiC/(Hf_{0.7}Ta_{0.3})C ceramic upon sintering at 2200 °C. EDS point measurements in SEM and TEM reveal the presence of oxygen and nitrogen in the as-pyrolyzed Si(Hf_{0.7}Ta_{0.3})C(N,O) ceramics, as indicated by the corresponding element peaks in the EDS spectra (see Figure 67 b) and Figure 68 d)). In accordance with EDS analyses, elemental analysis via the hot gas carrier extraction measurements showed an oxygen content of approximately 4 wt-% in the as-pyrolyzed Si(Hf_{0.7}Ta_{0.3})C(N,O) ceramics (refer to elemental analysis Table 7). However, after consolidation via FAST, the oxygen content was found to be less than 0.2 wt-%, suggesting a loss of oxygen during sintering. Based on these observations, it is suggested that the decreased oxygen content in the sintered ceramics is attributed to the carbothermal reduction reaction between silica and carbon (Equation 11).

If the decomposition reaction of Eq. 11 occurs within the $\text{Si}(\text{Hf}_{0.7}\text{Ta}_{0.3})\text{C}(\text{N},\text{O})$ system during consolidation, even to a minor extent, it may influence the sintering behaviour due to the formation of gaseous species. The importance and influence of the atmosphere during densification is described theoretically [168]. However, no silica was detected via the analytical measurements in SEM and TEM within the glassy $\text{Si}(\text{Hf}_{0.7}\text{Ta}_{0.3})\text{C}(\text{N},\text{O})$, but a nitrogen content of ~ 3.6 wt-% (cf. Table 7). In contrast, the nitrogen content in the sintered $\text{SiC}/(\text{Hf}_{0.7}\text{Ta}_{0.3})\text{C}$ ceramic decreased to ~ 0.3 wt-%, indicating a N-mass loss during sintering. These findings align with results from Q. Wen et al., where the authors also reported relative mass loss due to carbothermal reactions in as-pyrolyzed and subsequently annealed ceramics [41]. This raises the question of whether gaseous nitrogen plays a role in the sintering process and to what extent. EDS analysis did not detect nitrogen in the constituent phases of SiC and TMCs in the sintered sample (cf. Figure 76 e)), suggesting that gaseous nitrogen forming during the sintering process, becomes entrapped in closed pores and thereby impedes complete densification, as it is described for BaTiO_3 in Refs. [168,254]. In summary, the evaporation of volatile species triggered by carbothermal reduction reactions, and the generation of gaseous species are a very likely phenomena to occur in the microstructural evolution of initially amorphous $\text{Si}(\text{Hf}_{0.7}\text{Ta}_{0.3})\text{C}(\text{N},\text{O})$ polymer-derived ceramics during the sintering process.

7.4.4 The Influence of Sinter Additives

Section 7.3 provides a detailed description of the microstructure of the dense $\text{SiC}/(\text{Hf}_{0.7}\text{Ta}_{0.3})\text{C}$ ceramic. Of particular interest are the observed sinter necks composed of large SiC grains (of up to $3\ \mu\text{m}$ in particle size), which raise the question how these sinter necks evolve during the sintering process via FAST. Earlier studies have shown that sinter aids could lower the sintering temperature [255]. For example, the consolidation of SiC powders using sintering aids such as the $\text{Y}_3\text{Al}_5\text{O}_{12}$ or Al_2O_3 could enhance the densification rate and slow down grain growth kinetics [255–257]. Similar effects have been studied separately in the case of carbon and boron additives on the sintering behaviour of SiC by Stobierski and Gubernat [258,259]. Their research indicated that carbon used as sinter additive limits mass transport mechanisms and restricts SiC grain growth [259]. Recently, Rau et al. reported that transition metal fillers can lower the formation temperature of SiC through the generation of transition metal carbides, silicides, and oxides [260]. Previous research has also shown that metals such as Fe can influence the crystallization temperature of β -SiC through catalytic effects [260]. According to the authors, SiC formation becomes feasible at temperatures around $1300\ \text{°C}$, primarily due to the presence of Fe, which locally reduces the energetic barrier for β -SiC crystallization [260]. Our findings suggest similar processes, in which the transition metals Hf and Ta influence the formation temperature of SiC. The incorporation of the transition-metal amino complexes on the molecular level of the polysilan may also exert catalytic effects, influencing phase formation and sintering behaviour of SiC. However, further investigations are required to explore these possible catalytic effects.

7.4.5 Mechanical Effects

TEM investigations reveal the presence of SiC single-twins and stacking faults (Figure 77). From early crystallography studies it is known that SiC exhibits polytypism, a crystallographic property characterized by the stacking of structural cubic modules, which is closely related to twinning and stacking faults [261,262]. The addition of fully ordered twinned modules in the structure of the cubic 3C-SiC (β -SiC, space group F-43m (zinc blende structure)) leads a reduction of the symmetry, namely to the non-centrosymmetric 6H-SiC structure (α -SiC, space group P63mc) [262,263]. While the X-ray diffraction (XRD) pattern predominantly shows 3C-SiC, TEM imaging clearly indicates the presence of 6H-SiC, as shown by the bright/dark (B/D) contrast (cf. Figure 77 c)), a phenomenon attributed to

dynamical diffraction [262]. The B/D contrast arises when the crystal is slightly tilted away from the Bragg condition, and its intensity is enhanced along the polytype-sensitive rows, particularly in the [11-20] zone axis of 6H-SiC [262]. Indexing SiC polytypes in XRD pattern is challenging [264]. However, previous studies have identified a very weak diffraction peak at 34.2° in the XRD pattern of 3C-SiC, which is attributed to the <10-11> plane of 6H-SiC [264–266]. Unfortunately, this weak diffraction peak in the XRD pattern (Figure 66) coincides with the (111) peak of (Hf_{0.7}Ta_{0.3})C, present at 34.8°. The origin of the SF's in SiC remains unclear, as it is uncertain whether they form during the phase transformation and accompanied change in crystal structure from α -SiC to β -SiC upon cooling or through deformation induced by mechanical load during the sintering process.

7.4.6 Electrical Current

As described in chapter 2.9, the initial powder is thermally conducting since Hf and Ta as transition metals show excellent electrical conductivity. Thus, high-electric currents flow directly through the green body consisting of powder particles, resulting in interactions between the electric current and the microstructure [168]. This leads in addition, to high temperature gradients within the sample, which are much higher than in non-conducting sample materials as it was shown by temperature field simulations (comparison between electrically conducting TiN and insulating 3Y-ZrO₂) in Ref. [267]. Since the green body is not dense, the electric current flows unevenly through the material [168]. Consequently, a complicated network of percolation current pathways is formed along the contact regions between adjacent powder particles, leading to increased Joule heating along those pathways [167,168]. In theoretical considerations the percolation network causes fluctuating hot spots, which are characterized by high local current densities and overheating [167,168,173] with temperatures surpassing the average temperature significantly [168]. In consequence, microstructures will form, deviating from conventional sintering scenarios [168]. Indeed, FAST mechanisms include phenomena such as partial melting at surfaces and recrystallization [167,168,173]. The microstructure of the SiC/(Hf_{0.7}Ta_{0.3})C ceramic observed in Figure 71 indicate the presence of percolation current pathways during the consolidation. These pathways are likely to occur, particularly in the contact regions of the former powder particles, where sinter necks and grain coarsened TMCs are present. Figure 71 shows several regions displaying pearl-like structures. This could be regions where the pulsed direct current and intense local Joule heating leads to temperature gradients and subsequently also to sintering inhomogeneity, which then induce non-uniform microstructures [267]. Interestingly, increased grain sizes of the TMC appear at or near internal surfaces of the former powder particles (see also Figure 75), which can possibly be explained by the flow of pulsed direct current (DC) along the grain boundaries and the emerging inhomogeneous energy distribution within the compacted powder particles. In particular local temperature variations are assumed to dominate the development of such special microstructures [168].

The binary carbides HfC, TaC, and their solid solutions (Hf_xTa_{1-x})C exhibit a combination of metallic, covalent, and ionic bonding, contributing to high thermal and electrical conductivity [9,41,45,130,268]. The thermal conductivity κ of TMCs displays several unusual characteristics; unlike ordinary crystalline solids, the thermal and electrical conductivity of sintered TMCs increase with rising temperature, as can be seen in Figure 79 [100,238,269].

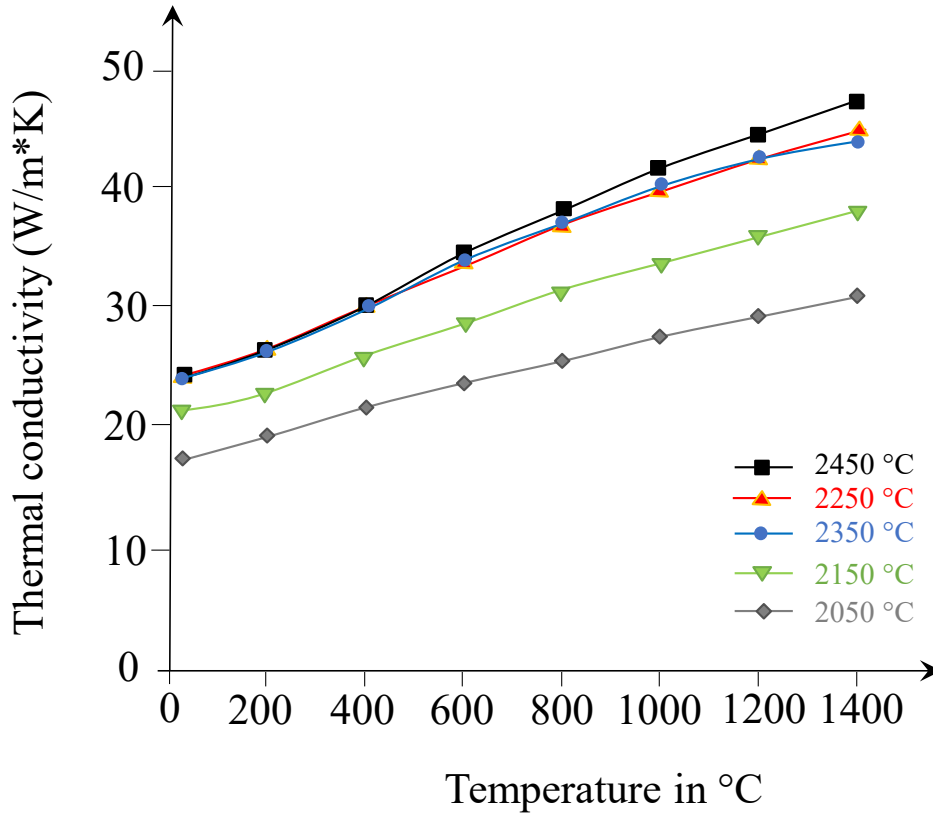


Figure 79 The thermal conductivity of $(\text{Ta}_{0.8}\text{Hf}_{0.2})\text{C}$ (sintered at 5 different temperatures) plotted against the temperature. Measured from room temperature to 1400 °C. Figure redrawn after Ref. [238].

The pulsed electric current utilized in the FAST process induces additional heating, leading to a further rise in sample temperature, and is expected to influence the grain growth of TMCs on internal surfaces (compare the grain sizes of TMCs inside former powder particles versus the grain sizes of TMCs on the internal surface of former powder particles in Figure 75). Furthermore, the pulsed current results in local higher temperatures due to the Joule heating effect, which enhance matter transport through increased diffusivity, thereby contributing to additional grain growth of TMCs, as illustrated in the schematic drawing in Figure 80 [45,79,164,165,168,170,270–272]. The influence of the electric current on the mass transport, leading to the development of distinct microstructures, has been previously documented for metallic glasses [271] and ceramic materials [161].

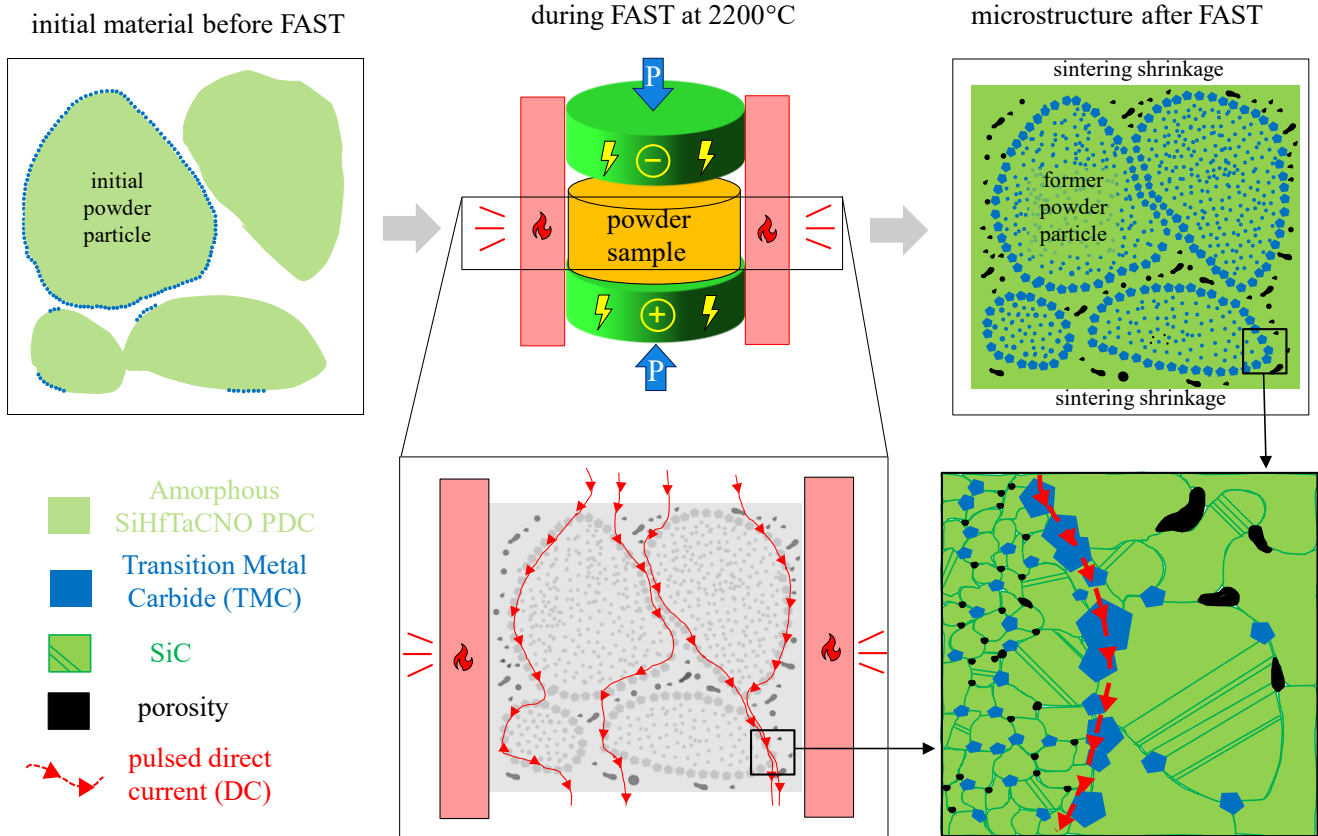


Figure 80 Influence of the electric current on the microstructural evolution within the SiC/(Hf_{0.7}Ta_{0.3})C PDC. Schematic drawing showing the microstructure of the initial amorphous Si(Hf_{0.7}Ta_{0.3})C(N,O) powder during FAST, and the microstructure of the consolidated SiC/(Hf_{0.7}Ta_{0.3})C bulk ceramic after FAST. The current pathways along the internal surfaces of adjacent powder particles (red lines and arrows) and the increase grain size of TMCs (in blue) on internal particles, as well as increased SiC crystals (in green) in the sinter necks are shown. Further, the different pore sizes (black) are shown: In the former powder particles, the pores are small, in the sinter necks, pores are bigger in size.

7.4.7 Grain Size Effects and the Influence of Oxygen

The microstructural analysis of the SiC/(Hf_{0.7}Ta_{0.3})C ceramic showed two distinct grain size distributions within the consolidated ceramic, as illustrated in Figure 75. The grain sizes of both phases within the former powder particle (SiC and TMC) are significantly smaller than their respective grain sizes within the sinter necks. This phenomenon may be attributed to the presence of micropores at grain boundaries within the region of the former powder particles, as indicated in Figure 71 and Figure 81 b). The pinning effect of the secondary phase seems to prevent an exaggerated grain growth of SiC and TMC in the microstructural region of the former powder particles. This is advantageous because with the microstructure within the former powder particles, the thermal conductivity is assumed to be kept low by the homogeneous distribution of the nanosized TMCs in the SiC matrix (phonon scattering see section 1.2). Similar observations regarding grain growth stagnation due to pinning effects were reported for other ceramics processed via FAST/SPS, such as nanocrystalline yttria [272], B₄C-TiB₂ composites [273], or TaC/SiC composites [99]. Comparing the grain sizes within the consolidated SiC/(Hf_{0.7}Ta_{0.3})C ceramic, Figure 75 shows that the SiC grain sizes within the sinter necks are approximately twice as large as those within the microstructure of the former powder particles. Increased SiC grain sizes in the sinter necks might result from the combination of high temperatures and the presence of enlarged "free" space in the particle-to-particle contact zones. Additionally, the oxygen impurities present in the starting

powder (as evidenced by the EDS spectrum in Figure 68 d) and elemental analysis in Table 7) might favour exaggerated grain growth through evaporation-condensation mechanisms at high temperatures [168]. This was reported before in Ref. [99] for FAST-sintered TaC/SiC. The slightly increased oxygen content is assumed to influence the particle size of the TMCs located on the internal surfaces of the former powder particle, as already discussed for the Si(Hf_xTa_{1-x})(C)N PDCs in section 6.4.4. Several studies in the literature report that sintering of non-oxide ceramics poses challenges due to oxygen impurities, which promote coarsening phenomena [88,99,146,163,253,274]. Table 10 gives an overview about non-oxide ceramic systems, in which coarsening was attributed to an increased oxygen impurity content. It is noted here that even minor oxygen impurity contents in the range of 0.2-1.7 wt-% are sufficient to promote coarsening. The oxygen impurities are considered to be introduced either by synthesis or other preparation processes, i.e., ball milling. However, the grain growth (coarsening) mechanism due oxygen impurities is not fully understood [163]. Liu and co-workers stated that oxide impurities are extremely harmful to TaC densification since the oxides form a liquid or vapor at high temperatures, and therefore evaporation-condensation or other non-densifying mechanisms then cause coarsening [99].

Table 10 Literature review giving an idea about the oxygen impurities promoting grain coarsening in actual oxygen-free Si-based ceramic systems.

Materials	Processing and Temperature in °C	Oxygen content in wt-%	Publication year	Authors	Refs.
BC	Pressureless Sintering (1000-2300 °C)	1.2	1989	Dole et al.	[274]
ZrB ₂ -ZrC-SiC	SPS (2100 °C)	-	2005	Medri et al.	[88]
TiB ₂	HP (1300-1800 °C)	1.3-1.7	2009	Jensen et al.	[163]
TaC/SiC	SPS (1800 °C)	0.2	2012	Liu et al.	[99]
HfC-SiC	Pressureless sintering (2300 °C)	<1.04	2013	Liu et al.	[253]
ZrB ₂ and TiB ₂	SPS (1700-2000 °C)	-	2021	Oguntuyi et al.	[146]
SiHfTa(C)N	Annealing (1600 °C)		2023	Thor et al.	[84]
SiC/(Hf _{0.7} Ta _{0.3})C	SPS (2200 °C)	~4.0	not published yet	Thor et al.	[85]

7.4.8 Porosity

Pores are a common structural three-dimensional defect of ceramic materials. Its origin can be divers; pores are often the result of a too short sintering time or too low sintering temperature [186] (compare the different sintering stages in Figure 15). However, particularly with respect to the densification of polymer-derived ceramic amorphous powders, porosity can also arise from gas evolution in an already dense body due to the evaporation of attached side groups of the polymers, such as CH₂ or CH₃. The microstructure of multinary PDCs is highly complex and incorporates open, closed pores, or cracks. Porosity within sintered SiC/(Hf_{0.7}Ta_{0.3})C PDC is a prevalent feature in the microstructure and affects a wide range of properties, such as the elastic modulus or thermal conductivity. The specification of the

porosity is in particular essential in order to compare the mechanical properties measured in section 7.3.5 with already published values from literature.

7.4.9 Discussion of Local Mechanical Properties

Referring to the characterization of the microstructure in chapter 7.3, it was expected that the microstructural region of the former powder particles (yellow component in Figure 78) will show the highest values regarding the elastic modulus (E) and hardness (H). In particular, it was thought that this is because precipitation hardening³ arises from the secondary phase (TMCs) within the SiC matrix. But in fact, the mechanical properties are lowered. They result from the simultaneous indentation of SiC, TMCs and numerous nanopores found within the initial powder particles (cf. Figure 71). Figure 81 a) depicts a schematic illustration of the observed microstructure with nano-sized pores present. Consequently, it is very likely that the indentations from the Berkovich indenter tip, with an assumed cross-sectional area of approx. $2 \mu\text{m}^2$ will also indent into porous regions, which then will contribute to decreased mechanical properties. The dependence of the cross sections of the nano indenter imprints and the presence of micro/nanopores is clearly depicted in the SEM-BSE image in Figure 81 b). It shows a high-magnified microstructural region of a former powder particle including the theoretical cross-section of the nano-indenter imprints, schematically drawn into the image. Nanoindentation imprints are depicted as triangles with set distances of $4 \mu\text{m}$ to each. This concept is called grid indentation technique and was described by Randell and co-workers [228].

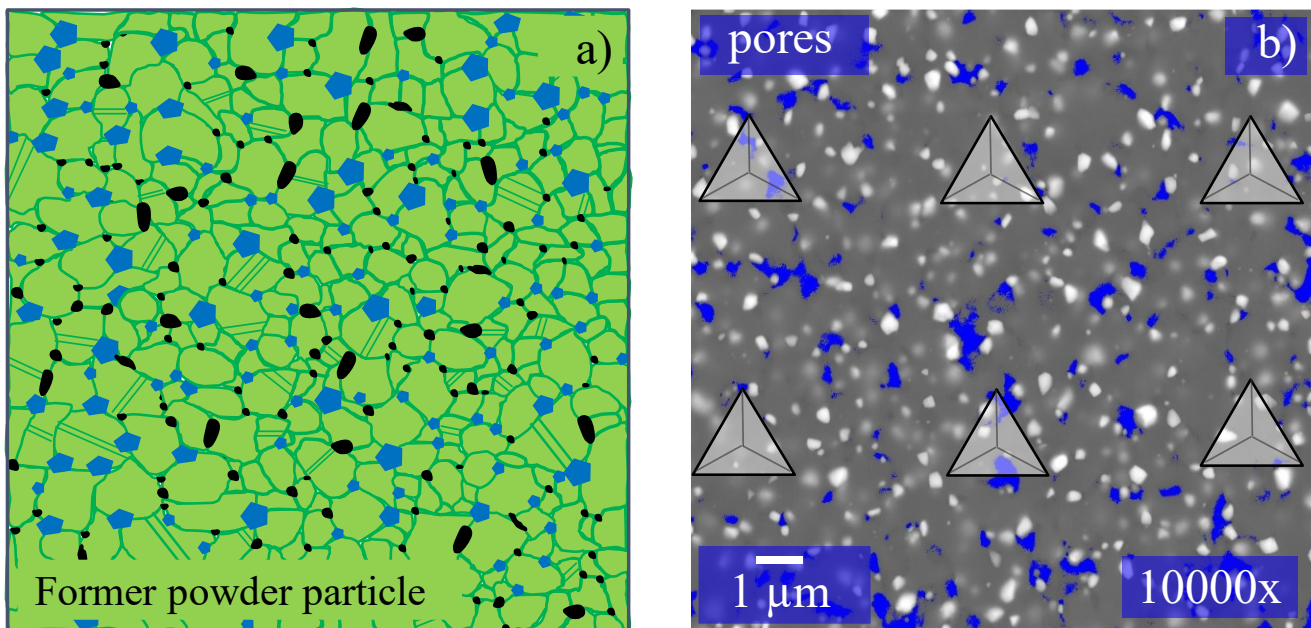


Figure 81 Microstructure of the former powder particle region; a) schematically drawn microstructure with twinned SiC as the matrix phase depicted in green, the TMCs as secondary phase depicted in blue and micro-/nano pores represented in black color. b) SEM-BSE image with blue-marked pores (thresholding via ImageJ). The triangles show schematically the cross-sections of the nano indenter.

³ Precipitation hardened materials contain extremely fine particles of a second phase (in this study TMCs in SiC matrix), whose dimensions are much smaller than $1 \mu\text{m}$. Due to the resulting hindering effect on dislocations these precipitation hardened materials have high strength values [275].

Comparison with literature data is difficult here, as there are not yet many data reported on mechanical properties of PDCs consolidated by FAST. In fact, there are many UHTC-based composite ceramics that have been prepared using the PM method and subsequent sintering via FAST. However, this also means that in these ceramics prepared via PM synthesis, the final composition in terms of chemistry is usually already present in the initial powder form and only the compaction, so to speak, needs to be fulfilled by FAST, meaning there is probably little change in chemistry during the sintering process. For PDC composites, the initial powders are present in the as-pyrolyzed state, which usually means that the powders are amorphous. Thus, crystallization, phase separation and also decomposition reactions take place upon sintering. This means that the microstructure of ceramic composites produced via the PM route in general will be different compared to ceramic composites produced via the PDC route, which inevitably affects the mechanical properties. As already described above, investigations regarding the mechanical properties of SiC/(Hf_{0.7}Ta_{0.3})C PDCs consolidated via the FAST within the existing literature are very scarce. However, in Table 11 mechanical properties of SiC-based ceramic composites manufactured either by PDC or PM routes, and subsequently consolidated via FAST are listed for comparison. In bold type are the three microstructure regions and mechanical properties studied here. Listed below are comparable ceramics which are chemically similar, have similar densities and, in the best case, were produced via FAST.

Table 11 Mechanical Properties of the three microstructural regions detected within the SiC/(Hf_{0.7}Ta_{0.3})C ceramic composite, listed alongside to chemically similar SiC-based ceramics published in literature.

Material	Processing route	Consolidation	FAST Parameter	Vickers hardness (GPa)	Nanohardness (GPa)	Elastic Modulus (GPa)	Ref.
			sinter temperature in °C/ pressure in MPa/ dwell time in min				
former powder particle (TMC + SiC + micropores)	PDC	FAST	2200/50/20	-	27.3 ± 3.3	444 ± 24	this work
SiC/HfC	PDC	FAST	2200/50/20	-	25.6 ± 4.9	324.5 ± 47.6	[183]
TaC/SiC	PM	FAST	1900/40/5	21.0 ± 10	-	498 ± 10	[99]
HfC + MoSi ₂	PM	FAST	1900/100/15	19-21	26-28	450-500	[276]
sinter necks (mainly SiC)	PDC	FAST	2200/50/20	-	36.7 ± 2.9	549 ± 62	this work
SiC/C	PDC	FAST	2200/50/20	-	24 ± 3	309 ± 29	[277]
SiC	PM	FAST	2050/69/10	32 ± 0.7	-	440 ± 20	[278]
SiC	Single crystal	-	-	-	41.0 ± 1.2	549 ± 20.6	[279]
porous regions	PDC	FAST	2200/50/20	-	22.5 ± 7.3	367 ± 78	this work

The elastic modulus and hardness values of the microstructural region of the former powder particle (depicted as the yellow component in Figure 78) are closely comparable to literature values of similar ceramic composites. The determined Young's modulus value of the former powder particle, $E = 444 \pm 24$ GPa, falls right between the values for the documented HfC/SiC composite with $E = 324 \pm 48$ GPa from Ref. [183] and the TaC/SiC composite with $E = 498 \pm 10$ GPa from Ref. [99],

as expected for intermediate compositions. Although the values measured in this work are very close to the mechanical properties of the HfC/MoSi₂ composite with $E = 450\text{-}500$ GPa and $H = 26\text{-}28$ GPa, published by Sciti and co-workers in Ref. [276], significant differences in the microstructure of the two compared ceramics are visible. The sinter necks (represented by the red component in Figure 78) exhibit the highest measured E and H values within the SiC/(Hf_{0.7}Ta_{0.3})C ceramic composite. Since the sinter necks consisted mainly of large grains of SiC (cf. Figure 76) with grain sizes up to $3\ \mu\text{m}$, only SiC ceramics were used for comparison. Actually, it was expected that the mechanical properties of the sinter necks measured here would show very similar results to those of the SiC/C ceramics in Ref. [277], because they were produced with the same precursors and the same FAST sinter parameters. Nevertheless, the SiC-rich sinter necks from this work show much higher values. Instead, the mechanical properties reported in Hayun et al., Ref. [278] show very close results to the here measured mechanical properties. Hayun and co-workers reported dense ($\text{RD} = 99.4\%$) FAST-processed covalent SiC ceramics containing an E-Modulus of $\sim 440 \pm 20$ GPa and Hardness of 32 ± 0.7 GPa [278]. However, even closer to the herein measured values are the mechanical properties of SiC single crystals, published by Datye and coworkers [279]. The authors reported an E-modulus of SiC single crystals with $E = 549 \pm 21$ GPa showing almost the same extremely high values as the E modulus measured for the sintered bridges with $E = 549 \pm 62$. One reason for such extremely high values is the formed microstructure of the sinter necks and the grain size of the SiC crystals, which in some cases are larger than $3\ \mu\text{m}$ and thus show values comparable to single crystals. As described earlier in chapter 7.3 the sinter necks contain a few large pores (cf. Figure 71), which are at least of similar size compared to the indenter. Thus, any detected macropore within the sinter neck is accurately identified as porous region (blue component in Figure 78) and thus do not contribute the mechanical properties of the sinter necks (red component). To summarize, the comparative analysis underlines that the microstructural regions of the sinter necks within the SiC/(Hf_{0.7}Ta_{0.3})C PDC composite exhibit the highest recorded E and H values within the literature. Furthermore, high-throughput nanoindentation enables the opportunity to establish correlations between the mechanical properties and distinct microstructural regions, especially within heterogeneous microstructures.

7.5 Summary

The microstructure development upon FAST-sintering was conducted. While the as-pyrolyzed polymer-derived ceramic powders possess an amorphous structure (cf. chapter 7.2, Figure 68), consolidation upon FAST resulted in dense SiC/(Hf_{0.7}Ta_{0.3})C ceramic composites (cf. chapter 7.3). The overall microstructure of the ceramic material after sintering exhibited three distinct microstructural regions: the former powder particles, which are held together through sinter necks, and some remaining isolated pores (cf. Figure 71 a)). Notably, regions with larger TMCs were found to be concentrated along internal surfaces which are surfaces of the former powder particles (cf. Figure 75). This phenomenon was attributed to enhanced diffusion facilitated by Joule heating (cf. Figure 80) and the presence of oxygen, promoting grain growth. The microstructural evolution of the polymer-derived ceramics (PDCs) during FAST was influenced by multiple factors including thermal, electrical, and mechanical mechanisms. The application of pulsed electric current induced Joule heating traveling along grain boundaries within the initial powder particles, impacting the growth of TMCs and leading to an inhomogeneous microstructure development in the SiC/(Hf_{0.7}Ta_{0.3})C PDC system, which has never been reported in literature before. Excessive grain growth of TMCs within the microstructural region of the former powder particles was prevented and attributed to the pinning effect of the (secondary) SiC phase and the existence of nanopores (cf. Figure 81a)). High-throughput nanoindentation on polymer-derived bulk ceramics effectively revealed their mechanical properties and established connections with the identified

microstructural constituents (cf. section 7.3.5). The comparison between optical micrographs and the provided mechanical property maps supported these relationships (cf. Figure 78). In addition, the presence of sample porosity significantly affected the statistical assessment of nanoindentation results, necessitating its consideration when determining the number of components for fitting and interpreting the mechanical properties.

8 The Influence of Boron Additive – Si(B)C/(Hf_{0.75}Ta_{0.25})C

Based on the preliminary results regarding the detailed phase characterization of the FAST-sintered SiC/(Hf_{0.7}Ta_{0.3})C in chapter 7, two novel Hf- and Ta-modified precursors with minor adjustments in their Hf:Ta ratio were synthesized via the single-source precursor route by J. Bernauer. Subsequently these single-source precursors were consolidated upon FAST. In comparison to the synthesis and preparation of the SiC/(Hf_{0.7}Ta_{0.3})C composite described in section 4.3 the here presented ceramics are SiC/(Hf_{0.75}Ta_{0.25})C and SiBC/(Hf_{0.75}Ta_{0.25})C. These two novel composites are anticipated as potential coating materials used for the protecting top coat for high temperature application materials. The slight change in the Hf:Ta ratio from 0.7:0.3 to 0.75:0.25 is to an expected improved oxidation behaviour and is thought to be beneficial due to the phase transformation from the (Hf_{0.75}Ta_{0.25})C (crystallized upon sintering at high temperatures) into the Hf₆Ta₂O₁₇, forming upon oxidation tests (see Diss. N. Petry in Ref. [248]). The Hf₆Ta₂O₁₇ phase is stable up to 2250 °C (no phase transformation from RT up to melting point), has a low thermal conductivity of ~2.89 W/m*K at 1200 °C and a thermal expansion coefficient of ~8.91 x 10⁻⁶/°C and therefore has been reported as a potential TBC material [39,280–282]. Furthermore, one of the novel single-source precursors is additionally tailored with a small amount of a borane dimethylsulfide complex. As it is known from several earlier studies regarding polysilazane-related systems, it is expected that the addition of boron leads to an enhanced thermal stability with respect to crystallization and decomposition as described earlier in chapter 2.6. Details can be found in Refs. [57,68,108,133]. As in the previous chapters 5-7, feedback on the microstructure development will be given regarding the precursors used and especially the influence of B on the microstructure. It is expected that the microstructure of the SiC/(Hf_{0.75}Ta_{0.25})C composite does not show major microstructural deviations from the SiC/(Hf_{0.7}Ta_{0.3})C sample, but the boron-added sample does. Thus, microstructure characterization of the novel FAST-sintered Si(B)C/(Hf_{0.75}Ta_{0.25})C PDC-NC is given.

8.1 Synthesis and Consolidation of Si(Hf_{0.75}Ta_{0.25})(B)C

A commercially available polycarbosilane (cf. Figure 11) (SMP-10, Starfire System Inc., Glenville USA) was modified with dimethylamine complexes of hafnium (Hf(NMe₂)₄, TDMAH, Sigma-Aldrich, USA, CAS-no: 19782-68-4) and tantalum (Ta(NMe₂)₅, PDMAT, Sigma-Aldrich, USA, CAS-no: 19824-59-0, where Me = CH₃) (cf. Figure 63). The molar ratio of the TDMAH:PDMAT was set to 0.75:0.25 for each preceramic single-source precursor. Molar ratios of the metal:metal and metal:polymer in addition to the exact quantities of the chemicals used in the synthesis to prepare the single-source precursors are listed in Table 12. For the preparation of the SiBC/(Hf_{0.75}Ta_{0.25})C ceramic, a small amount of 0.1183 g borane dimethylsulfide complex ((CH₃)₂S BH₃, BMS) was added. The metal to boron ratio was set to 2:1. After the synthesis of the single-source precursors, the obtained materials were subsequently pyrolyzed in 1000 °C in an Argon atmosphere and ground using a clean pestle and mortar to achieve particle sizes smaller <100 μm. The as-pyrolyzed ceramic powders were successfully consolidated into monolithic bulk samples using FAST, as can be seen in Figure 82. Based on the results in chapter 7, the sinter parameters were set as follows: sinter temperature of 2200 °C, pressure of 50 MPa, and a dwell time of 20 minutes under vacuum (cf. Table 12). The heating and cooling rates were set to 100 °C/min.

Table 12 Molar ratios and quantities of the used chemicals in addition to the FAST parameter used for the preparation of SiC/(Hf_{0.75}Ta_{0.25})C and SiBC/(Hf_{0.75}Ta_{0.25})C.

sample	TDEAH: PDMAT (metal: metal ratio)	(TDEAH+ PDMAT): PHPS (metal: polymer) molar ratio	SMP-10 in g	TDMAH in g	PDMAT in g	(CH ₃) ₂ S BH ₃ in g	Sinter tempe rature in °C	Applied pressure in FAST in MPa	Dwell time in FAST (min)
SiC/ (Hf _{0.75} Ta _{0.25})C	75:25	30:70	3	0.8288	0.3125	-	2200	50	20
SiBC/ (Hf _{0.75} Ta _{0.25})C	75:25	30:70	3	0.8288	0.3125	0.1183	2200	50	20

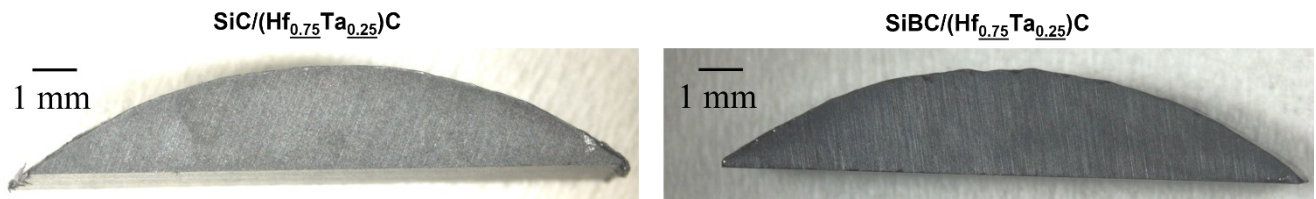


Figure 82 Micrographs showing the cut sintered pellets of SiC/(Hf_{0.75}Ta_{0.25})C (left) and SiBC/(Hf_{0.75}Ta_{0.25})C (right) for further sample SEM and TEM preparation steps .

8.2 Chemical Composition and Phase Assemblage

Figure 83 displays the X-ray diffraction (XRD) patterns of the as-pyrolyzed Si(B)(Hf_{0.75}Ta_{0.25})C(N,O) ceramic powders and the sintered Si(B)C/(Hf_{0.7}Ta_{0.3})C bulk ceramics. The ceramic powder, pyrolyzed at 1000 °C in an Argon atmosphere, exhibits an X-ray amorphous diffraction pattern, broad diffraction hills are present. The broad peak around $2\theta = 17^\circ$ corresponds to the (111) peak position of β -SiC. The two XRD pattern of the sintered dense bulk ceramics of Si(B)C/(Hf_{0.75}Ta_{0.25})C indicate a fully crystalline structure with β -SiC, TMC (Hf_{0.7}Ta_{0.3})C, and graphitic carbon present. The sharp peaks of β -SiC (PDF 29-1129) are represented by a closed rectangle symbol. The remaining sharp peaks are assigned to the TMC of (Hf_{0.7}Ta_{0.3})C, represented by a half-filled, lying triangle symbol (PDF 19-6861). Additionally, the small peak at $\sim 11^\circ$ is attributed to the presence of graphitic carbon, represented by a closed triangle symbol.

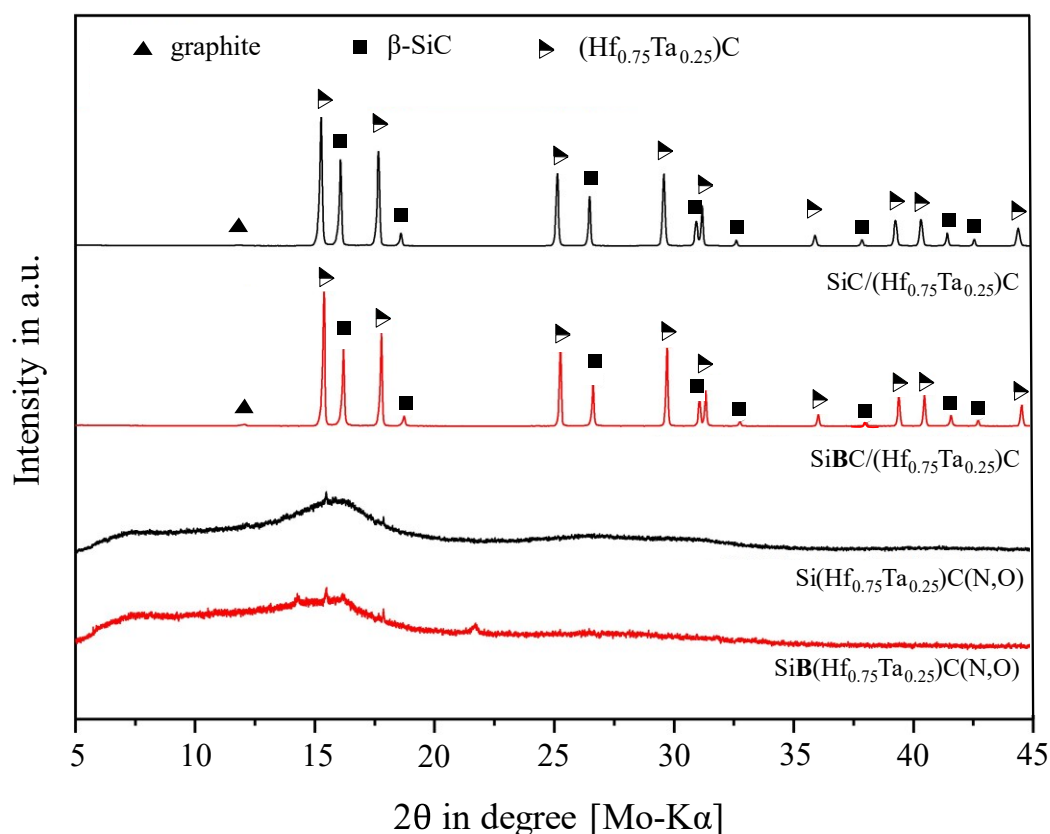


Figure 83 XRD patterns of the as-pyrolyzed Si(B)(Hf_{0.75}Ta_{0.25})C(N,O) ceramic powder pyrolyzed at 1000 °C in Ar (bottom) and XRD pattern of the bulk Si(B)C/(Hf_{0.75}Ta_{0.25})C ceramic sintered at 2200 °C (top). Diffraction analysis was performed by J. Bernauer.

Table 13 provides the results from the elemental analysis from Mikroanalytisches Labor Pascher (Remagen, Germany), giving the chemical composition of the boron-modified metal-containing PDC after the pyrolysis and sintering in weight percentage (wt-%). Values given in wt-% were converted into at-%. Furthermore, the empirical formula of each sample is given. Both ceramics consist of Si, Hf, Ta, C, N, O and small amounts of B. The difference in the chemical composition between the Si(B)(Hf_{0.75}Ta_{0.25})C(N,O) ceramic powder after pyrolysis and the resulting sintered Si(B)C/(Hf_{0.75}Ta_{0.25})C bulk ceramic is the concentration of the N (cf. Table 13). The as-pyrolyzed ceramic powder contains a N content of ~ 3.85 wt-%, whereas in contrast the N content in the sintered bulk sample is decreased to ~ 0.57 wt-%.

Table 13 Chemical composition of the as-pyrolyzed SiB(Hf_{0.75}Ta_{0.25})C(N,O), sintered SiBC/(Hf_{0.75}Ta_{0.25})C ceramic samples in wt-% and at-% and the empirical formula of each sample.

sample	elemental analysis								
		Si	Hf	Ta	B	C	N	O	
SiB(Hf _{0.75} Ta _{0.25})C(N,O)	wt-%	45.8	12.4	4.25	0.16	28	3.85	4.67	
SiB(Hf _{0.75} Ta _{0.25})C(N,O)	at-%	35.17	1.49	0.51	0.32	50.28	5.93	6.30	
Empirical formula		Si(Hf_{0.04}Ta_{0.01})B_{0.01}C_{1.43}N_{0.17}O_{0.18}							
sample	elemental analysis								
		Si	Hf	Ta	B	C	N	O	
SiBC/(Hf _{0.75} Ta _{0.25})C	wt-%	49.5	12.8	4.38	0.2	24.52	0.572	4.25	
SiBC/(Hf _{0.75} Ta _{0.25})C	at-%	41.7	1.69	0.57	0.44	48.32	0.97	6.29	
Empirical formular		Si(Hf_{0.04}Ta_{0.01})B_{0.01}C_{1.16}N_{0.02}O_{0.15}							

8.3 Microstructure of SiC/(Hf_{0.75}Ta_{0.25})C and SiBC/(Hf_{0.75}Ta_{0.25})C

Figure 84 shows comparatively six SEM-BSE images depicting the microstructure of the sintered SiC/(Hf_{0.75}Ta_{0.25})C (cf. Figure 84, top row) and the SiBC/(Hf_{0.75}Ta_{0.25})C ceramic (cf. Figure 84, bottom row). In Figure 84 a) and d), a comparatively low magnification was selected in order to obtain an overview of the entire microstructure. Figure 84 b), c) and e), f) in contrast show enlarged images from the insets in Figure 84 a) and d), respectively. The microstructure of the SiC/(Hf_{0.75}Ta_{0.25})C bulk ceramic is very comparable to the dense SiC/(Hf_{0.7}Ta_{0.3})C bulk ceramic described earlier in chapter 7.3. Also, the three different microstructural regions are present: former powder particles, sinter necks and porous regions in the sinter necks (compare Figure 70 with Figure 84b), c)). This is in accordance with the former results, since only the Hf:Ta ratio was slightly adjusted from 0.7:0.3 to 0.75:0.25 for the ceramic shown in Figure 84 a-c). The sintering conditions were chosen to be the same as those described for the SiC/(Hf_{0.7}Ta_{0.3})C ceramics in chapter 7.3 (2200 °C sinter temperature, 20 minutes dwell time and a pressure of 50 MPa). For this reason, the microstructure of the SiC/(Hf_{0.75}Ta_{0.25})C bulk ceramic will not be discussed further in the following.

The microstructure of the boron-modified ceramic in Figure 84 d-f) strongly differs from the other ceramics (compare the top row with the bottom row in Figure 84). The SEM-BSE images shown in Figure 84 d-f) show an inherently homogeneous distribution of the containing phases. No morphology remaining from former powder particles can be seen, nor can sinter necks be discerned as such. Furthermore, no large pores are visible as in the other composites. As can be seen from the XRD patterns, the phase composition is composed of SiC as the matrix phase with finely dispersed TMCs and graphite. A boron containing phase was not identified in XRD nor in EDS measurements in SEM.

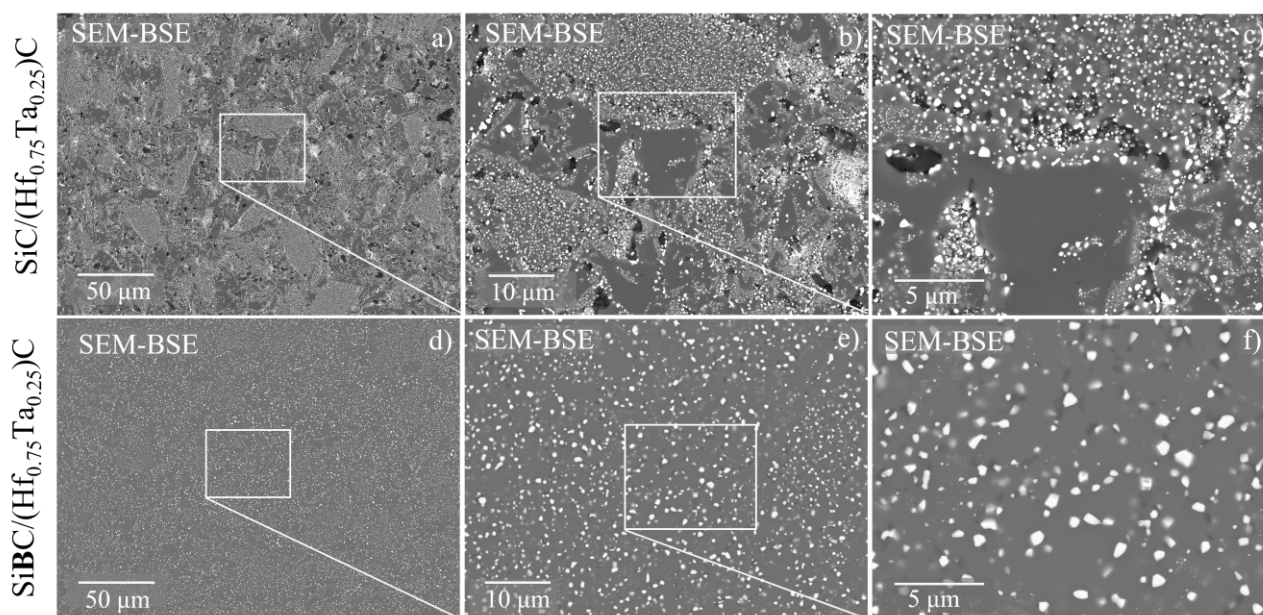


Figure 84 Comparison of the SEM-BSE images of SiC/(Hf_{0.75}Ta_{0.25}) (top row) and SiBC/(Hf_{0.75}Ta_{0.25})C (bottom row).

Figure 85 gives a more detailed view of the microstructure of the SiBC/(Hf_{0.75}Ta_{0.25})C ceramic. In Figure 85 a), numerous individual TEM-BF images were combined to form an image collage to provide a general overview of the microstructure (cf. Figure 85 a)). TMCs reach grain sizes of up to 1 μm, as detectable by the dark phases in Figure 85 a). Also visible is the SiC matrix, where the SiC grains reach sizes of up to 2.5 μm. Figure 85 b) shows a single TEM-BF image in which stacking faults (SFs) in the SiC phase are detectable by bright-dark contrasts. This is also particularly visible in the HR-TEM image in Figure 85 c)

and the corresponding SAED pattern (cf. inset in Figure 85 c)). Beside the HR-TEM image of a SiC crystal, also a TMC crystal is shown in high resolution. In addition to the lattice fringes of the Hf-Ta carbide in Figure 85 d), an amorphous carbon layer is visible at the top of the image. Figure 85 e) shows an example of an EDS spectrum of a SiC crystal. Besides the expected elements Si and C, a small oxygen peak appears. In total, 14 SiC crystals were analyzed chemically upon EDS measurements in TEM. The mean measured oxygen concentrations in the SiC phase is approx. $\sim 1.2 \pm 0.7$ at-% in the EDS measurements. Figure 85 f) shows an example of an EDS spectrum of a TMC. Besides C, Hf and Ta, a small oxygen peak was found here as well. In total, eleven TMC grains were measured using single point EDS measurements. The results show an average oxygen content of $\sim 3.7 \pm 1.7$ at-%. The detailed EDS measurement results of SiC and TMC can be found in the appendix in Figure A5 and Table A7. The exact EDS point measurements from Figure 85 e) and f) are indicated in Figure 85 a) and b) with a red asterisk for SiC and a blue asterisk for the TMC. Also, no boron-containing phase was found via EDS measurements in TEM.

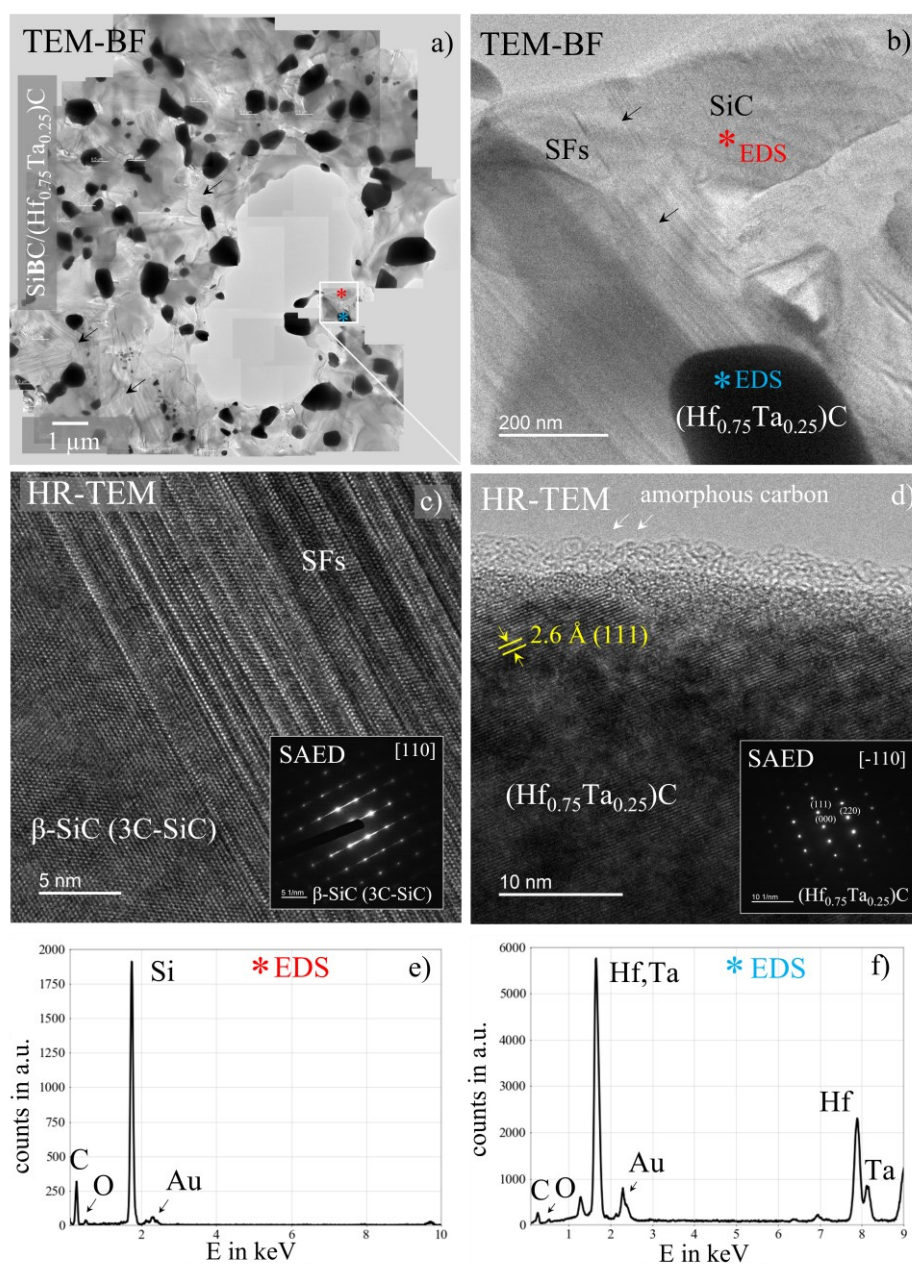


Figure 85 a, b) TEM-BF images, c, d) HR-TEM images with SAED pattern as insets and e, f) EDS spectra of the constituting phases SiC and $(\text{Hf}_{0.75}\text{Ta}_{0.25})\text{C}$ in the sintered $\text{SiBC}/(\text{Hf}_{0.75}\text{Ta}_{0.25})\text{C}$ ceramic.

8.4 Image Analysis for Determination of Porosity in SiBC/(Hf_{0.75}Ta_{0.25})C

The residual porosity of the SiBC/(Hf_{0.75}Ta_{0.25})C ceramic was determined via semiautomated image analysis using SEM-BSE images of polished cross-sections obtained from the sintered bulk material. In total, 40 individual SEM-BSE images were captured and assessed; twenty with a magnification of 1000x and twenty with a magnification of 3000x, as shown in Figure 86.

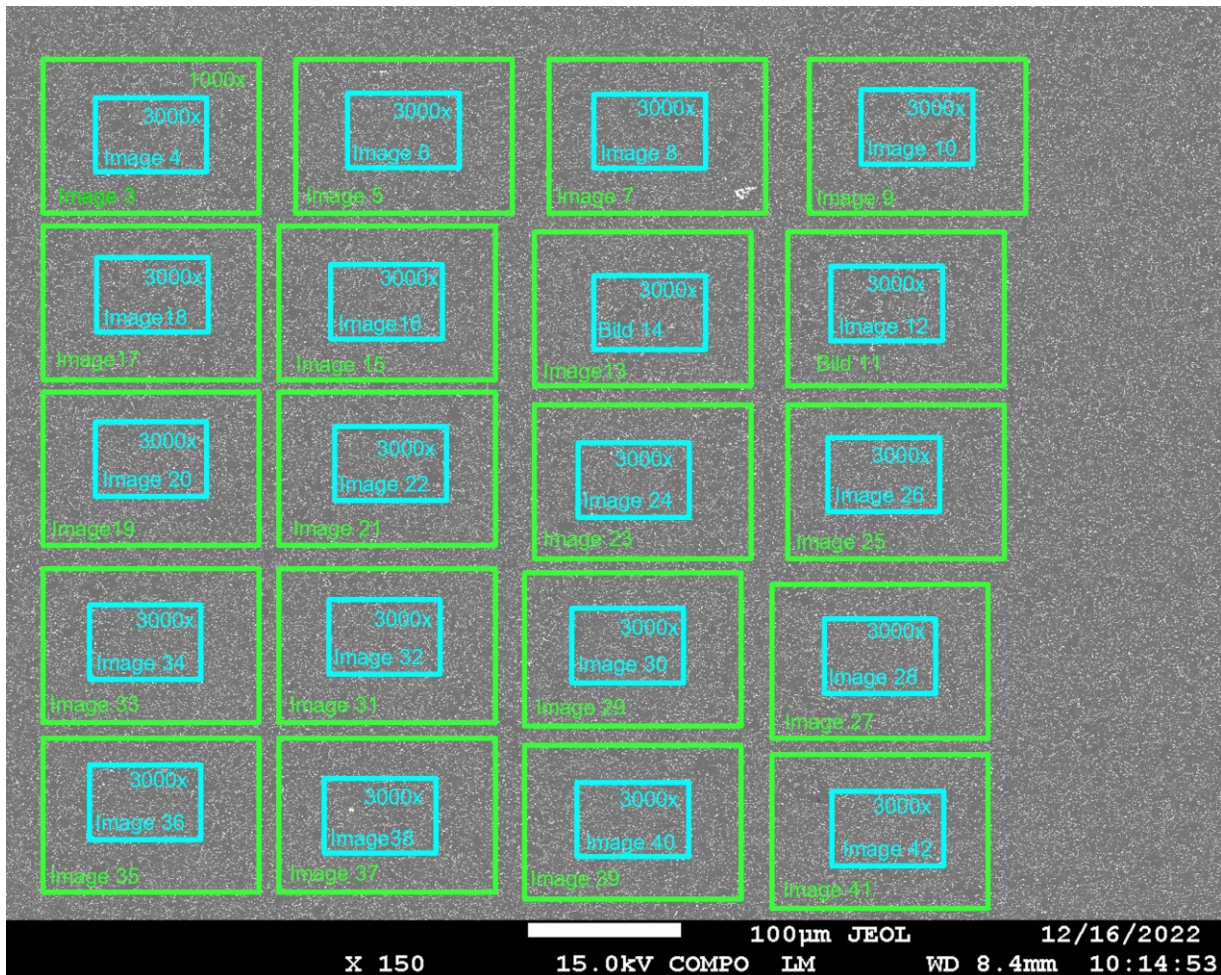


Figure 86 Low-magnified (LM) SEM-BSE image highlighting the 40 BSE image positions for evaluating the sample porosity. Green marked image frames were taken at a magnification of 1000x, image frames depicted in blue were taken at a magnification of 3000x.

Pores appear black. Thresholding via ImageJ gives the cross-sectional area percentage (area %) of the detected pores relative to the total area providing an area pore density. To evaluate the porosity of the series of images with magnifications of 1000x (green image frames) and 3000x (blue image frames), gray values between 0-86 and 0-102 respectively were selected for each individual image using the thresholding tool in the histogram. Table 14 shows the results of the semiquantitative image analysis giving porosity values for the two different magnifications. The mean porosity value for the SiBC/(Hf_{0.75}Ta_{0.25})C sample, based on the results from the twenty images, is determined to be 1.54 ± 0.2 area % for the images with a magnification of 1000x and 1.85 ± 0.3 area% for the images with a magnification of 3000x. The given uncertainty was based on a standard uncertainty multiplied by a coverage factor $k = 2$ to achieve a confidence level of approximately 95 % [249].

Table 14 Resulting porosity values for eleven SEM-BSE images at magnifications of 500x and 1000x.

Freame no.	porosity in area %	porosity in area %
3, 4	1.72	2.25
5, 6	1.83	2.46
7, 8	1.26	1.85
9, 10	1.37	1.37
11, 12	1.47	1.66
13, 14	1.58	2.24
15, 16	1.5	1.54
17, 18	1.64	1.82
19, 20	1.57	1.75
21, 22	1.75	1.83
23, 24	1.51	1.44
25, 26	1.1	1.42
27, 28	1.38	2.08
29, 30	1.71	1.76
31, 32	1.22	2.0
33, 34	1.57	2.41
35, 36	1.17	1.4
37, 38	1.14	1.87
39, 40	1.28	1.82
41, 42	1.23	2.12
mean	1.45	1.85
2σ	0.2	0.3

Figure 87 presents a comparison of the results gained upon the two investigated magnifications of 1000x and 3000x. In Figure 87 a) and b) two original SEM-BSE images for the selected magnifications (1000x vs. 3000x) are shown. Figure 87 c) and d) show the further processed images in which the quantitatively analyzed pores are depicted in blue. Additionally, Figure 87 e) and f) show the final processed images of the indexed pores in black after the thresholding via ImageJ. In the images taken upon a magnification of 1000x pores are hardly detectable in the microstructure. In contrast, images with a magnification of 3000x give much more information regarding the porosity. Figure 87 d) shows that pores generally tend to occur close to or in direct contact with TMCs, whereas hardly any pores occur within the SiC matrix. Large pores are more likely to occur near larger TMCs, while small pores are concentrated near smaller TMCs. There are also areas in the microstructure where there are small clusters of nanometre-sized TMCs, where no pores occur, or they are so small that they cannot be depicted via SEM imaging.

Therefore, the determined porosity values within the images with the 3000x magnification were preferred. The relatively high material density determined for twenty images at a magnification for 3000x reaching $\sim 98\%$ in the ceramic bulk sample is attributed to the efficient precursor modification with boron in combination with the consolidation achieved through FAST.

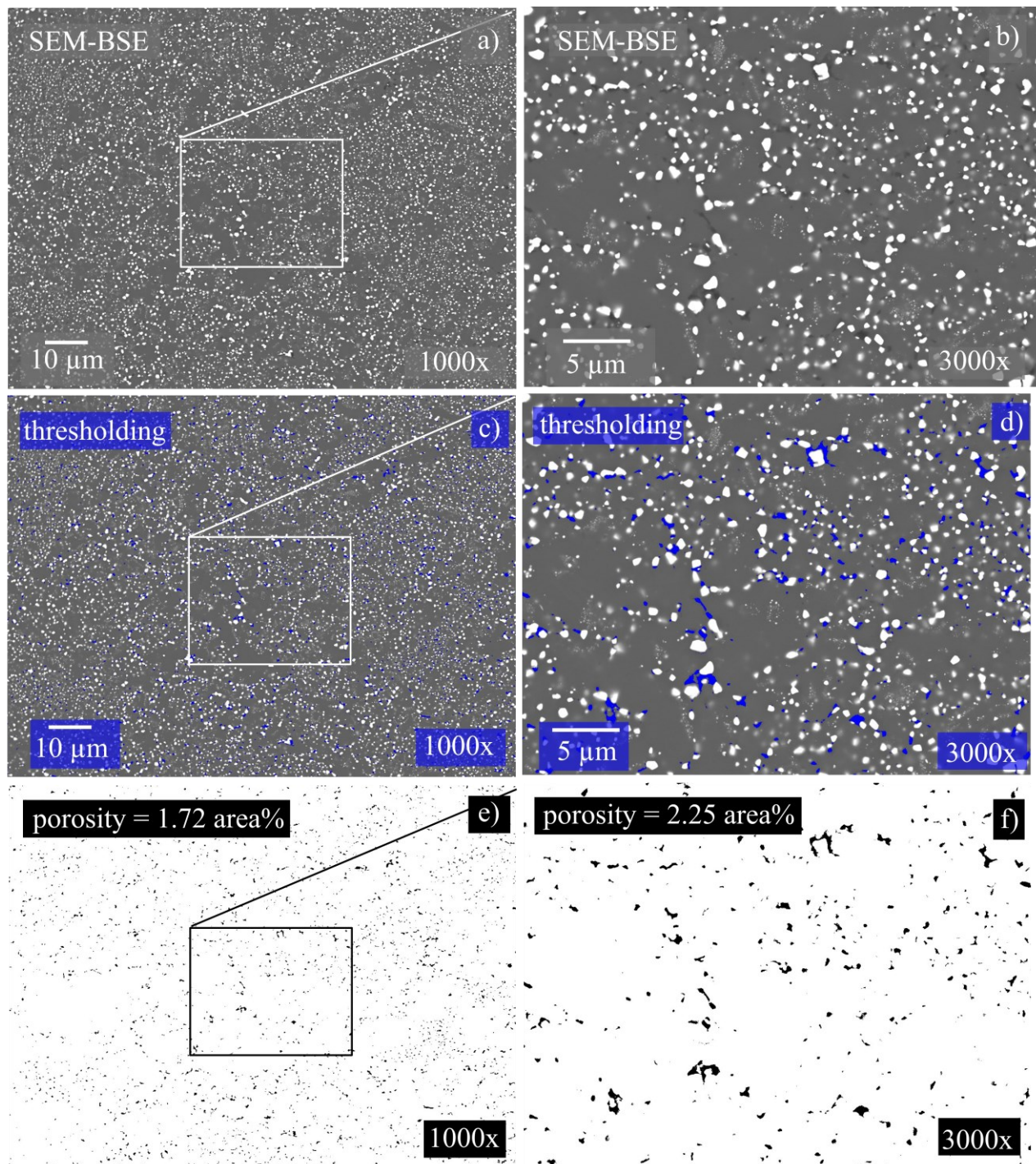


Figure 87 SEM-BSE images and further processed images used for the determination of the porosity in the SiBC/(Hf_{0.75}Ta_{0.25})C bulk sample. a, b) original SEM-BSE images with magnifications of 1000x and 3000x. c, d) Thresholding of the darkest contrast in a, b) leads to the blue-marked pores. e, f) final image after thresholding gives the indexed pores in black as sum of the porosity in area%.

8.4.1 Estimation of the boron distribution in SiBC/(Hf_{0.75}Ta_{0.25})C

The microstructural variations between the sintered SiC/(Hf_{0.75}Ta_{0.25})C and SiBC/(Hf_{0.75}Ta_{0.25})C ceramic was described in section 8.3. Consistent with earlier studies from literature, the introduction of small amounts of boron exerts a profound influence on the microstructure of the sintered SiBC/(Hf_{0.75}Ta_{0.25})C (cf. Figure 84). With the application of XRD or EDS a boron-containing phase could not be detected. However, from the elemental analysis (cf. Table 13) it is known that an average boron content of 0.44 at-

% is present in the sintered SiBC/(Hf_{0.75}Ta_{0.25})C sample. Literature suggests that the boron is distributed within the carbon shell surrounding each TMC [283,284]. To estimate the distribution of boron atoms within the sample, it is assumed that the boron atoms are uniformly distributed within the TMC (neglecting that the TMCs have different grain sizes). To estimate the number of boron atoms per TMC in the SiBC/(Hf_{0.75}Ta_{0.25})C ceramic sample, the number of boron atoms in the sample frame (cf. Figure 87) was calculated by:

$$n_{atoms\ boron}(at\%_{Boron}) = 0.44\% * N_A * \frac{\rho * V}{M} \quad \text{Eq. 13}$$

With N_A representing the Avogadro constant (6.022*10²³ mol⁻¹), ρ signifies the density of the sample (determined as ρ = 3.669 g*cm⁻³ through the Archimedes method in Ref. [283]), V denotes the sample volume where from Figure 87 d) the volume of the cross section is assumed as a cuboid, with A = cross sectional area of the image with a width = 30.17 μm and a length = 40.31 μm and height = 1 μm (for the sake of simplicity), which then gives V = 1216 μm³. M is the molecular weight of the sample (calculated from Table 13) with M ≈ 23.76 g/mol. Given the overall composition of 0.44 at-% boron from the elemental analysis (cf. Table 13), the boron concentration within the sample is known.

Inserting the values into Eq. 13, the number of boron atoms ($n_{atoms\ boron}(at\%_{Boron})$) in the sample is calculated with:

$$\begin{aligned} n_{atoms\ boron}(at\%_{Boron}) & \quad \text{Eq. 14} \\ = 0.44\% * 6.022 * 10^{23} \text{ mol}^{-1} * \frac{3.669 \text{ g} * \text{cm}^{-3} * 1216 \mu\text{m}^3}{23.76 \text{ g/mol}} \\ n_{atoms\ boron}(at\%_{Boron}) & = 4.9 * 10^{11} \text{ atoms} \end{aligned}$$

The area-percentage and number of TMC particles in the microstructure can be estimated by using the thresholding in ImageJ on Figure 88 a). By utilizing the SEM-BSE image obtained from Figure 87 d), and further processed images in Figure 88 b) and c), the area percentage (A_{TMC}) and number (n_{TMC}) of TMC particles in the SiBC/(Hf_{0.75}Ta_{0.25})C bulk sample was determined. This yielded an estimated number of TMCs $n_{TMC} = 1879$ and an $A_{TMC(area\%)} = 14.25 \text{ area}\%$ in the microstructure. This corresponds to a total TMC particle area of $A_{TMC} = 173.3 \mu\text{m}^2$.

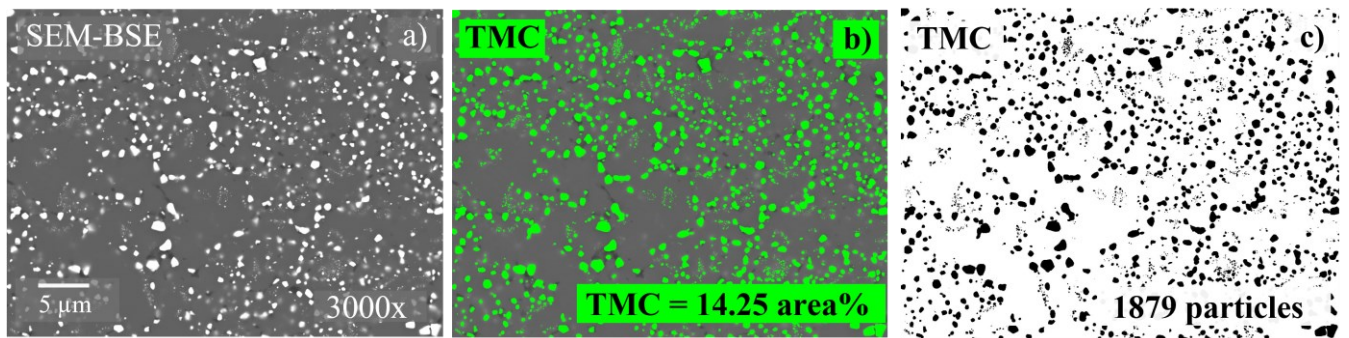


Figure 88 a) SEM-BSE image taken from Figure 87 d) and further processed images in b) and c) used for the determination of the area% and numbers of TMC particles in the SiBC/(Hf_{0.75}Ta_{0.25})C bulk sample.

With this the number of TMC atoms in the sample can be obtained by:

$$n_{atoms\ TMC} = N_A * \frac{\rho * V_{TMC}}{M} \quad \text{Eq. 15}$$

where ρ signifies the density of the TMC = (Hf_{0.75}Ta_{0.25})C (determined as $\rho = 12.725 \text{ g}\cdot\text{cm}^{-3}$), V_{TMC} denotes the TMC volume from Figure 87 d), where the volume of the TMCs is estimated via thresholding via ImageJ with = 14.15 area%, which then gives $V_{TMC} = 173.3 \mu\text{m}^3$. M is the molecular weight of the (Hf_{0.75}Ta_{0.25})C with $M \approx 191.1 \text{ g/mol}$.

Inserting the values into Eq. 15, the number of TMC atoms ($n_{atoms\ TMC}$) in the sample is calculated with:

$$n_{atoms\ TMC} = 6.022 * 10^{23} \text{ mol}^{-1} * \frac{12.725 \text{ g} * \text{cm}^{-3} * 173.3 \mu\text{m}^3}{191.12 \text{ g/mol.}} \quad \text{Eq. 16}$$

$$n_{atoms\ TMC} = 6.9 * 10^{12} \text{ atoms}$$

This gives the Boron-to-TMC atom ratio within the TMC particles of

$$\frac{n_{atoms\ boron}}{n_{atoms\ TMC}} = \frac{4.9 * 10^{11}}{6.9 * 10^{12}} = 0.071612 \quad \text{Eq. 17}$$

Thus, having about 7% boron to TMC atom ratio suggests that boron may act as nucleation aid for the formation of the TMCs either by acting as nucleation center for the formation of TMCs or by enhancing the Carbon outdiffusion-mobility in the lattice.

8.5 Discussion

This chapter addresses the impact of slight materials composition changes and perspectives of a novel polycarbosilane-based and boron-modified single-source precursor, prepared into a dense ceramic nanocomposite upon consolidation with FAST (cf. chapter 8.1).

The slight change in the ratio between Hf and Ta has notably affected the final microstructure. The reaction of the (Hf_{0.75}Ta_{0.25})C into the stable Hf₆Ta₂O₁₇ upon oxidation which is stable up to 2250°C, has to be tested.

Consolidation of the boron-modified SiBC/(Hf_{0.75}Ta_{0.25})C upon FAST resulted in a dense crystalline ceramic composite (cf. Figure 87). The overall microstructure of the ceramic material after sintering exhibited a completely different microstructure compared to the other characterized composites in this work (cf. chapter 6-7). Small amounts of boron (0.1183 g of BMS, cf. chapter 8.1) suppress a grain coarsening in this polysilane-based system during sintering, as it was already described for polysilazane-derived ceramics in Refs [57,68,108,133,258]. Thereby, the addition of boron seems to prevent the evolution of sinter necks and the coarsening of TMCs on internal surfaces during the FAST process. The distribution of TMCs in SiBC/(Hf_{0.75}Ta_{0.25})C is more homogeneous as it is in SiC/(Hf_{0.75}Ta_{0.25})C. Furthermore, boron has a huge influence on the densification upon sintering, as the densified SiBC/(Hf_{0.75}Ta_{0.25})C composites yielded a density of nearly ~98 %. In comparison, the dense SiC/(Hf_{0.7}Ta_{0.3})C ceramic (cf. section 7.3.2) only reaches a density of ~95%. Observations within the microstructure of the sintered SiBC/(Hf_{0.75}Ta_{0.25})C ceramic show that larger pores are found near or in close vicinity to TMCs and no pores are found in the SiC matrix (cf. section 8.4). It is assumed that the porosity emerges through the different shrinkage behaviour and the different viscosity of the

organometallic complexes (TDMAH and PDMAT) and organosilicon polymer (SMP10) during the cooling. The volume shrinkage during the transformation of TDMAH and PDMAT into the TMC particles ($\rho_{\text{HfC}} = 12.2 \text{ g/cm}^3$, $\rho_{\text{TaC}} = 14.3 \text{ g/cm}^3$) compared to the transformation of SMP10 into SiC ($\rho_{\text{SiC}} = 3.2 \text{ g/cm}^3$) is higher in comparison. Thus, a greater degree of shrinkage is expected within the TMCs. This complex transformation is accompanied by an outward diffusion of carbon in the regions of the Carbides and a different change in viscosity. This may lead to mechanical stress and explain the larger pores occurring near or in close vicinity to the TMCs.

With the help of the elemental analyses, a boron content of 0.2 wt-% (cf. Table 13) was analyzed. Due to the homogeneous distribution of TMCs, the decreased grain sizes of TMCs and the decrease of the overall porosity compared to SiC/(Hf_{0.75}Ta_{0.25})C ceramic, it is assumed that boron may act as a nucleation centre for the TMCs. However, boron was not found in XRD nor via EDS analysis in TEM. Based on earlier studies from Q. Wen and co-workers in Refs. [183,285] it is anticipated, that the boron is located in the thin carbon-film/carbon-shells around the TMCs. The estimation of the boron-to-TMC atom ratio in section 8.4.1 reveals a 7 % boron-to-TMC atom ratio. With this, investigations using electron-energy loss spectroscopy (EELS) could be indeed helpful, since EELS allows particularly a determination of the light elements such as oxygen or boron. Based on the current state of knowledge, this novel ceramic composite is the most suitable ceramic in terms of the microstructure. Therefore, further measurements regarding the microstructure (determine where the boron is located in the microstructure), thermal and mechanical properties on the SiBC/(Hf_{0.75}Ta_{0.25})C are highly recommended.

9 Conclusion

Divers microscopic and analytic methods such as OLM (cf. chapter 3.1), SEM (cf. chapter 3.2), EPMA (cf. chapter 3.3), CTEM (cf. chapter 3.4) in conjunction with EDS (cf. section 3.5.2), XRD (cf. chapter 3.6), elemental analysis (cf. chapter 3.7) and nanoindentation (cf. chapter 3.8) allowed for a detailed investigation of the microstructure of a series of PDCs. In a first step, basic polysilazane-based Hf-modified SiHfCN composites (cf. chapter 5) and Hf/Ta-modified $\text{Si}(\text{Hf}_x\text{Ta}_{1-x})(\text{C})\text{N}$ UHTC-NCs (with $x = 0.7$ and $x = 0.2$) (cf. chapter 6) were studied. Then, polycarbosilane-based $\text{Si}(\text{Hf}_{0.7}\text{Ta}_{0.3})\text{C}$ (cf. chapter 7) and $\text{Si}(\text{Hf}_{0.75}\text{Ta}_{0.25})(\text{B})\text{C}$ (cf. chapter 8) PDC-NCs were characterized. Thereby, the focus laid on the detailed characterization of the microstructural evolution for different temperature protocols after pyrolysis, annealing or sintering with different dwell times. Either polysilazane (cf. section 4.1 for the preparation of SiHfCN and cf. section 4.2 for the preparation of $\text{Si}(\text{Hf}_x\text{Ta}_{1-x})(\text{C})\text{N}$) or polycarbosilane (cf. section 4.3 for the preparation of $\text{Si}(\text{Hf}_{0.7}\text{Ta}_{0.3})\text{C}$ and chapter 8.1 for the preparation of $\text{Si}(\text{Hf}_{0.75}\text{Ta}_{0.25})(\text{B})\text{C}$) were modified with different molar ratios of transition metal complexes (TDMAH, PDMAT). Subsequently, the as-pyrolyzed powders were either annealed at 1600 °C in inert gas atmosphere (N_2) (for the $\text{Si}(\text{Hf}_x\text{Ta}_{1-x})(\text{C})\text{N}$), or the as-pyrolyzed powders were used as initial powder material for the consolidation of dense bulk composites via FAST at 1950 °C (for the SiHfCN) and at 2200 °C (for the $\text{Si}(\text{Hf}_{0.7}\text{Ta}_{0.3})\text{C}$ and $\text{Si}(\text{Hf}_{0.75}\text{Ta}_{0.25})(\text{B})\text{C}$). By providing constant feedback on the synthesis and the effects of the different sintering parameters on the microstructure, it was possible to tailor specific chemical compositions and their final microstructures.

SiHfCN ceramic nanocomposites were reported to be oxidation-resistant in preliminary investigations described in section 2.10.2 and Refs. [65,66]. Here, the microstructures of two newly synthesized and consolidated SiHfCN bulk ceramics (cf. chapter 5) were characterized and subsequently compared to each other in section chapter 5.4. These experiments have shown that the dense SiHfCN bulk ceramics exhibit different microstructures depending on the dwell time during sintering. A short dwell time (SiHfCN_01) resulted in an inhomogeneous microstructure, including different microstructural regions. The microstructure observed within the SiHfCN_01 bulk ceramic constitutes of former powder particles, sinter necks, interconnected pores within the sinter necks and crystallization fronts starting from the internal surface of the former powder particles (cf. section 5.1). An improvement of this inhomogeneous microstructure was then achieved by increasing the dwell time from 1 minute to 15 minutes. As shown in Figure 46 the microstructure of the related SiHfCN_02 sample changed strongly, from an inhomogeneous to a homogeneous distribution of the TMCs (cf. section 5.3). The increased dwell time led to completely different microstructure. Increased TMC grain sizes (cf. Figure 46) and no Si_3N_4 in the microstructure was observed. As described for the sintered SiHfCN_02 bulk ceramic, also the annealed $\text{Si}(\text{Hf}_x\text{Ta}_{1-x})(\text{C})\text{N}$ ceramic powder particles in section 6.4.2 underwent a thermal decomposition reaction, resulting in a phase composition, where Si_3N_4 is completely absent due to the presence of free carbon and its thermal decomposition into SiC and gaseous nitrogen at high temperatures (cf. Equation 10). A detailed study of the microstructure and phase characterization of individual $\text{Si}(\text{Hf}_x\text{Ta}_{1-x})(\text{C})\text{N}$ powder particles led to a detailed description of the microstructure evolution (cf. chapters 6.1 - 6.3). This enabled for a microstructural evolution model, as described and discussed in section 6.4.5. The $\text{Si}(\text{Hf}_x\text{Ta}_{1-x})(\text{C})\text{N}$ powder particles microstructure does not develop homogeneously from an amorphous into a crystalline state when exposed to high temperatures (cf. Figure 65). Instead, crystallization and subsequent phase separation processes lead to the thermal decomposition of Si_3N_4 , loss of gaseous nitrogen and coarsening of TMCs observed particularly at the surface regions of individual powder particles. The powder particles annealed at 1600 °C in the $\text{Si}(\text{Hf}_x\text{Ta}_{1-x})(\text{C})\text{N}$ system showed increased grain sizes of TMCs especially in surface-near regions (cf. section 6.3.1). In addition, gas phase reactions lead to the development of very large and high-aspect ratio SiC whisker and Si_3N_4 crystals (cf. section 6.3.2). Remnants of the N-

containing phases were still present in the bulk region of the powder particles; the phase assemblage of the bulk is composed of TMCNs embedded in a Si_3N_4 matrix. The surface region, on the other hand, consists of large-grown TMCs, SiC, and a residual amorphous C-O-rich phase. As discussed in chapter 6.4, it was shown that the local chemical differences within the microstructural regions of the surface and bulk regions are jointly responsible for the microstructure evolution. It was concluded, that N-containing PDCs are rather prone to crystallization upon high temperatures ($\sim 1600^\circ\text{C}$), and tend to undergo phase separation and coarsening phenomena in temperatures around 1600°C . This heterogeneous microstructure regarded as unfavourable with respect to the intended applications as TBC. Originally, the idea was that the as-pyrolyzed $\text{Si}(\text{Hf}_x\text{Ta}_{1-x})\text{CN}$ ceramic powders should be compacted into a bulk ceramic using FAST. In this way mechanical properties could be determined and oxidation tests performed. Due to the detailed microstructure characterization and thus a monitoring of the synthesis, this material could not be successfully densified.

In summary, there are strong parallels between the high-temperature microstructure development upon FAST-sintering of bulk ceramics and microstructure development during annealing of ceramic powders. This gets particularly evident through the observation of the microstructure of the FAST-sintered SiHfCN bulk ceramics and the annealed $\text{Si}(\text{Hf}_x\text{Ta}_{1-x})(\text{C})\text{N}$ powder particles and (compare Figure 59 and Figure 41).

The similarities of the internal surface coarsening (crystallization front) in the bulk ceramics and the surface coarsening in the ceramic powders is obvious and develops regardless of whether the FAST-sintering or a high-temperature process is used during the heat treatment of the powders (annealing). In chapter 6 it was expected that the microstructure characterization will enable conclusions on the selection of the Si-based precursor. For chapters 5 and 6, it can be concluded that the nitrogen-rich systems, prepared via the PDC route using polysilazane precursors suffer from high temperatures during the sintering and annealing steps. Due to the decomposition of Si_3N_4 in the presence of free carbon it is suggested that N-rich polymer-derived ceramic systems will not find an application as coating material for application temperatures greater than or equal to 1600°C . In particular Figure 89 displays the precursor system plotted against the temperature. It shows, that decomposition of materials resulting from precursors ranging from SiCN to SiCNO is given above a certain temperature.

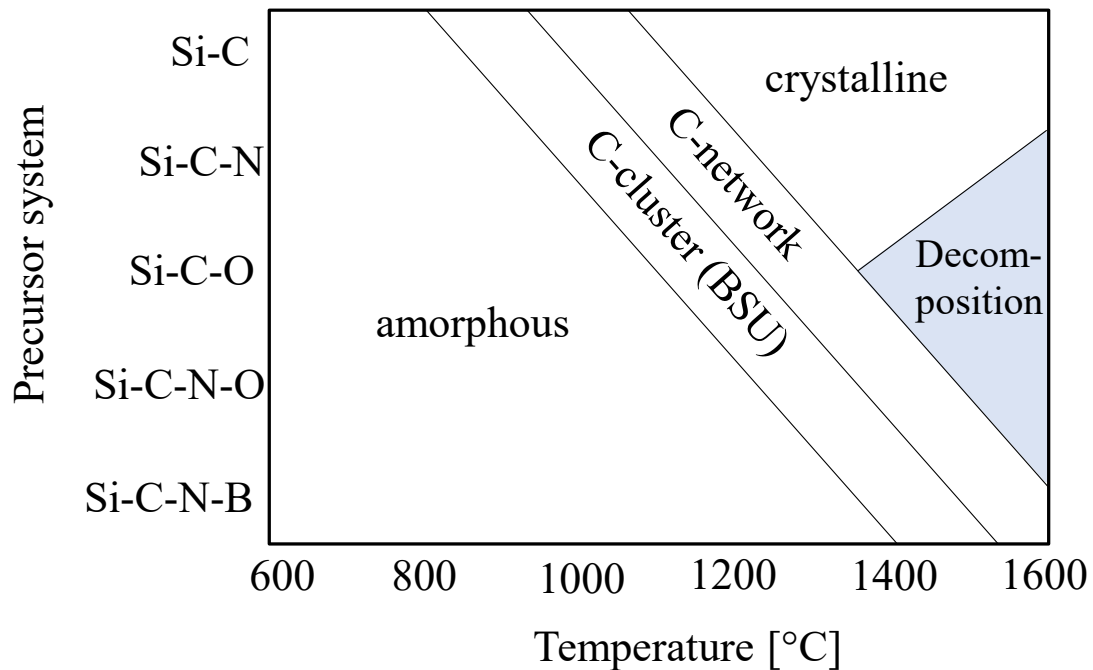


Figure 89 Different polymeric precursor systems plotted against temperature in °C. Figure redrawn after Ref. [128].

Consequently, no further investigations on N-containing systems were undertaken in this work. Instead, a change in the modified single-source precursor was anticipated. Thus, the focus was laid on systems with polycarbosilanes as polymeric precursor, which develop into SiC ceramics. In chapter 7 a detailed microstructural characterization of FAST-sintered SiC/(Hf_{0.7}Ta_{0.3})C was anticipated. It was expected, that the change in the precursor results in a ceramic with little to no nitrogen content in the microstructure. In this way it was expected, that the formation and therefore also the thermal decomposition of nitrides will not occur. It was shown that although the microstructure of the dense-sintered SiC/(Hf_{0.7}Ta_{0.3})C sample shows less severe surface coarsening of the TMCs, but that in general the microstructure is still inhomogeneous, similar to that of the dense SiHfCN_01 ceramic (cf. chapter 5) and the Si(Hf_xTa_{1-x})(C)N powder samples (cf. chapter 6). Furthermore, elemental analysis of as-pyrolyzed Si(Hf_{0.7}Ta_{0.3})C(N,O) and FAST-sintered SiC/(Hf_{0.7}Ta_{0.3})C (cf. chapter 7.1) confirmed that the nitrogen content in the samples after the sintering process was very low. No nitride formation and the associated thermal decomposition and generation of gases occurred.

To assess the mechanical properties of distinct microstructural regions within such an inhomogeneous microstructure (containing sinter necks and former powder particles), high-throughput NI was performed (cf. section 7.3.5). The mechanical properties were characterized for each microstructure region and give the highest modulus and hardness values for the sinter necks with $E = 549$ GPa (± 62 GPa) and $H = 36.7$ GPa (± 2.9 GPa). The findings demonstrate, that the grit-indentation technique utilized on inhomogeneous microstructures within FAST-sintered bulk PDCs is an effective method to identify mechanical properties and correlate those to microstructural regions. This grit-indentation method was never reported for PDCs before.

Another final modification of the molar Hf:Ta ratio in the single-source precursor (cf. chapter 8) was shifted from 0.7:0.3 to 0.75:0.25. This modification is expected to enable for the phase transition of the TMC (Hf_{0.75}Ta_{0.25})C into the oxidation resistant Hf₆Ta₂O₁₇ oxide phase, when exposed to synthetic air during oxidation experiments. It was expected that the addition of boron leads to an enhanced thermal stability with respect to crystallization and decomposition. It was shown that the addition of small amounts of boron (cf. chapter 8.1) resulted in a completely different microstructure development upon

FAST-sintering. The addition of small amounts of boron has indeed yielded a very homogeneous distribution of the constituting phases. Thus, TMCs are finely dispersed in a SiC matrix phase. Within this microstructure there are hardly any open pores visible. Quantitative image analysis yielded a closed porosity value of $\sim 1.85 \pm 0.3$ area%, which in contrast to the other systems gives an extremely reduced porosity ($\sim 98\%$ density in SiBC/(Hf_{0.75}Ta_{0.25})C vs. $\sim 95\%$ density in SiC/(Hf_{0.7}Ta_{0.3})C). Furthermore, there are no signs of former powder particles or sinter necks left. Also, no grain coarsening of TMCs at internal surfaces were observed, as it was the case in the previously investigated systems of SiHfCN (cf. chapter 5), Si(Hf_xTa_{1-x})(C)N (cf. chapter 6) and Si(Hf_{0.7}Ta_{0.3})C (cf. chapter 7).

In summary, the evolution of the microstructures upon different heat treatments in the respective composite materials is shown schematically in Figure 90.

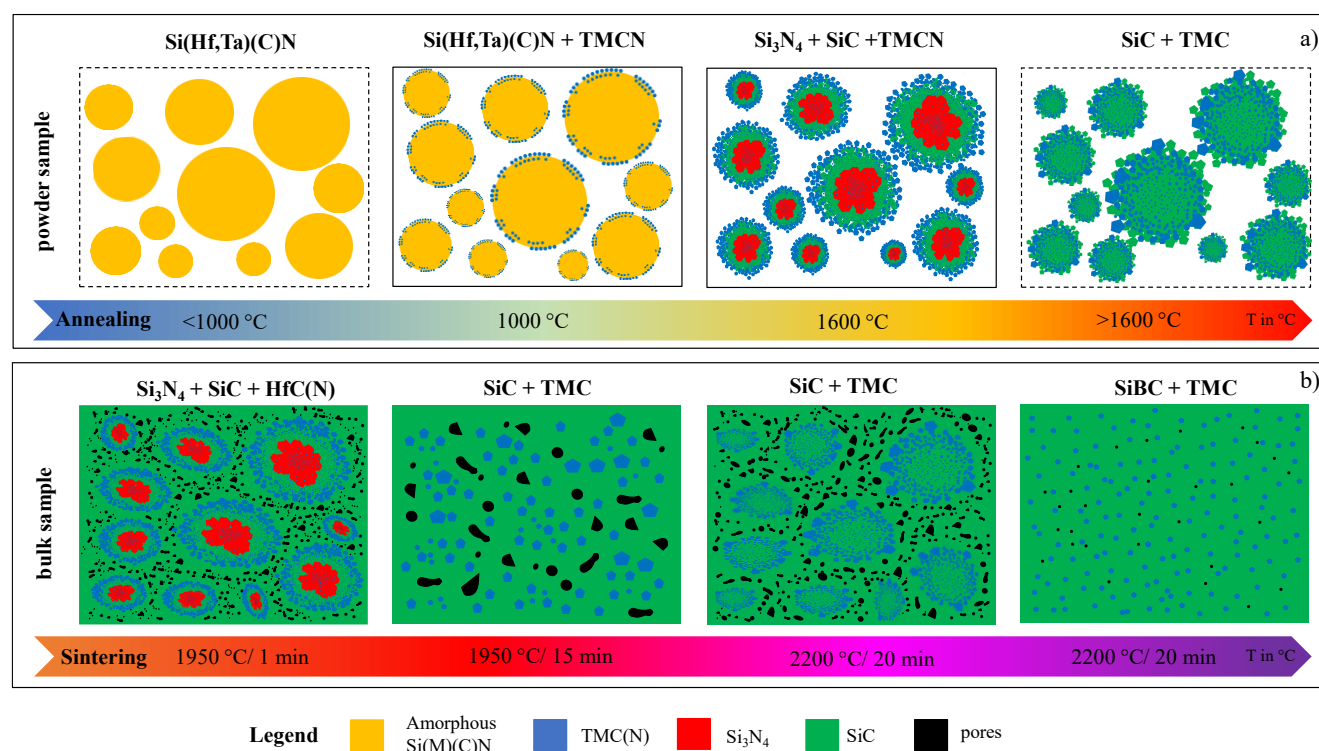


Figure 90 Schematic drawing and comparison between the final microstructures of pyrolyzed and annealed ceramic powders in a), and FAST-sintered bulk ceramics prepared upon different polymers and sintered at different temperatures and dwell times in b). The first and last frames of the top row are shown as dashed lined because the model drawings for these temperatures are hypothetical and have not been supported by experimental data.

The top row in Figure 90 shows the schematic developments in the ceramic powders upon annealing. The bottom row in Figure 90, on the other hand, shows schematically how the various microstructures of the as-pyrolyzed powders developed after different sintering temperatures and dwell times. Starting with the amorphous as-pyrolyzed Si(Hf_xTa_{1-x})(C)N powders (top row in Figure 90 a)), which were subsequently annealed at high temperatures and underwent phase separation, thermal decomposition and coarsening phenomena (cf. Figure 90 a)). Repeated experiments in the SiHfCN systems followed (Figure 90 b)), and the emerging microstructures can be very well compared to the emerging microstructures of the annealed powders. A final precursor change (from polysilazane to polysilane) led to the nitrogen being kept out of the system, avoiding the thermal decomposition of Si₃N₄ (Figure 90 b)). The slight adjustment of the Hf:Ta ratio from 0.7:0.3 to 0.75:0.25 and the incorporation of small

amounts of boron, led to a very homogeneous microstructure with a low porosity and in comparison, to fine-grained TMCs in a SiC matrix (Figure 90 b)).

In conclusion, for the development of novel PDC-NCs for TBC materials, a detailed microstructure characterization is essential for giving feedback in order to adjust the precursors and the process parameters of the sintering.

10 Outlook

To characterize novel PDC-NCs in future studies, a combination of different methods to assess the micro- and nanostructure is indispensable. This work has demonstrated that OLM and HR-SEM is suitable for a basic overview of the microstructure of the particle surface (cf. chapter 3.1 and 3.2). However, it should always be kept in mind that thermal treatments will cause microstructural changes, which can not only be observed on direct surfaces, but also take place inside single powder particles [84]. This study has shown local chemical variations occurring at submicro- and nanometer scales in the PDCs (cf. the transition zone between bulk and surface regions ~ 200 nm, cf. Figure 61). Thus, TEM, HR-TEM and other methods like atom probe tomography (APT), are needed to image microstructures on a nano-scale and analyze chemical/atomic variations in order to understand the structure property relationships. To characterize closed porosity gas physical adsorption or computed tomography (here especially Nano-CT due to the small sizes of the pores and the TMC particles) will be helpful. In-situ small angle X-ray scattering (SAXS) could monitor and clarify the structural evolution of the PDC-NCs during the polymer-to-ceramic conversion as reported in Ref. [129].

The incorporation of boron on a molecular level is a well-known method to achieve high-temperature stability and increased oxidation/corrosion resistance [57,108,133,145]. However, the detection of such low boron contents (in this work ~ 0.44 at-% B in the sintered $\text{SiBC}/(\text{Hf}_{0.75}\text{Ta}_{0.25})\text{C}$, cf. Table 13) is difficult. A suitable method to detect boron would be the use of EELS instrumentations, which are nowadays incorporated into modern TEMs. In general, the TEM sample preparation is a major obstacle, especially for powdered ceramic nanocomposites containing several different phases like different carbides (with hardness of $H = 37$ GPa for SiC) and for example some residual amorphous regions with completely different properties. Therefore, it is of particular interest to prepare the ceramic particles appropriately for TEM and further characterization methods. Here, the preparation with FIB-SEM is particularly suitable, whereas standard methods like grinding using a clean agate pestle mortar give inappropriate results since it destroys the initial microstructure of the powder particles.

To synthesize novel non-oxide PDC-NCs, a proper storage of chemicals, particularly organometallic complexes such as TDMAH or PDMAT is important preventing against oxygen contamination. In particular, the whole PDC production chain should be carried out in a glovebox to avoid contamination with unwanted oxygen and thereby unfavoured grain coarsening of TMCs. This also includes mortaring of the as-pyrolyzed precursor either in a clean agate mortar or a ball mill inside the glovebox. The compaction of the as-pyrolyzed PDC powders via FAST-sintering derived dense monolithic UHTC-NCs and thus, helped to determine the constituting phases, the mechanical properties and the oxidation behaviour.

Nevertheless, it should be noted that when comparing several composites sintered with different dwell times, the same starting material with the same grain size distribution should be used to ensure comparability. For this purpose, the comminution of the as-pyrolyzed amorphous ceramics can be standardized and a recipe with a fixed grinding time and the same grinding tools can be used. Literature states that the powder particle size has a significant influence on the compaction during sintering [286]. When a series of FAST-sintered nanocomposites is compared with each other, it is advantageous to prepare a series of nanocomposites in which only one parameter changes for the time being in order to determine the exact effects on the microstructure development (either change the dwell time or the initial powder particle size).

However, since the ultimate goal is to develop novel top-coats for TBC systems, it is important to move from novel ceramic powder nanocomposites and bulk ceramics towards the anticipated coatings at some point. Although, it was shown that the microstructural changes in the ceramic powder samples upon several different heat treatments are transferable to the dense sintered bulk samples, however, it can be

assumed that the microstructure of the ceramic thin films, when deposited via inexpensive dip/spray or spin-coating techniques in the liquid unpyrolyzed state, will show fundamental differences regarding the emerging microstructures in bulk ceramics upon high temperature annealing or sintering. Still, early crystallization of TMCs in the temperature range of 1000 °C will play a major role in the microstructure of the coating and should definitely be considered, otherwise it will induce severe failure of the coatings. Since currently used benchmark TBC materials (7YSZ) contain porosity levels of 10 - 20% [20], the reduction of the porosity in novel bulk PDC-NCs is not necessary. The aim could be to keep the thermal conductivity of the material as low as possible. Indeed, a certain amount of porosity in combination with microstructural defects helps to reduce the thermal conductivity [28,32]. Ceramic nanocomposites with some micro or nano-porous microstructure will cause phonon scattering which lowers the thermal conductivity. In addition, pores help to prevent heat from passing unhindered through the material. Thus, when the thermal conductivity of the material is in general not low enough, the thickness of the coating should be increased [32].

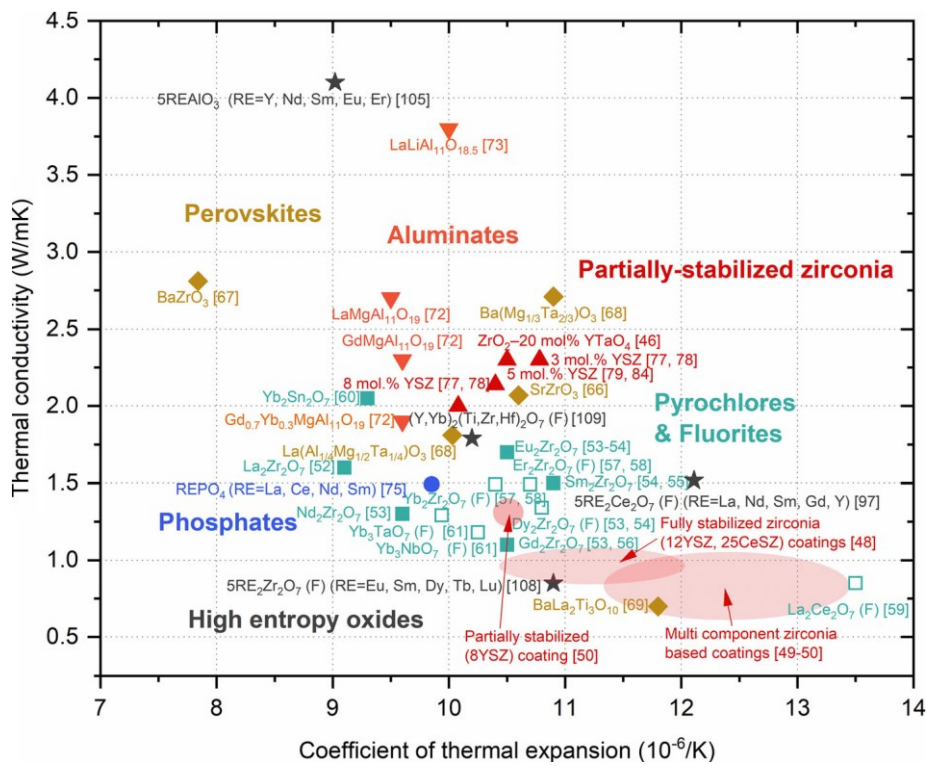


Figure 91 Possible TBC top coat materials with low thermal conductivity. Pyrochlores and Fluorites are depicted in green. Reprinted from Ref. [32] under Creative Common CC BY license.

Phases like the here studied SiC and TMCs generally have relatively high thermal conductivities. An alternative approach would be to consider materials with lower thermal conductivities. Figure 91 shows the currently, most discussed materials for TBC top coats. These are pyrochlores and fluorites such as Yb_3NbO_7 or $La_2Ce_2O_7$ described in Refs. [32,287,288]. In Figure 90, the thermal conductivity is plotted against the CTE. Even though the thermal conductivity of pyrochlores and fluorites is very low, there are many other aspects to consider when developing novel ceramic topcoat materials, such as oxidation resistance or phase stability under thermal cycling processes.

References

- [1] United Nations Framework Convention on Climate Change, The Paris Agreement, 2015. https://unfccc.int/sites/default/files/resource/parisagreement_publication.pdf?download (accessed 25 June 2023).
- [2] H. Kobayashi, A. Hayakawa, K.K.A. Somarathne, E.C. Okafor, Science and technology of ammonia combustion, *Proc. Combust. Inst.* 37 (2019) 109–133. <https://doi.org/10.1016/j.proci.2018.09.029>.
- [3] M. Hulme, 1.5 °C and climate research after the Paris Agreement, *Nat. Clim. Chang.* 6 (2016) 222–224. <https://doi.org/10.1038/nclimate2939>.
- [4] T. Konegger, J. Torrey, O. Flores, T. Fey, B. Ceron-Nicolat, G. Motz, F. Scheffler, M. Scheffler, P. Greil, R.K. Bordia, Ceramics for Sustainable Energy Technologies with a Focus on Polymer-Derived Ceramics, in: A.K. Agarwal, A. Pandey, A.K. Gupta, S.K. Aggarwal, A. Kushari (Eds.), *Novel Combustion Concepts for Sustainable Energy Development*, Springer India, New Delhi, 2014, pp. 501–533.
- [5] B. Zakeri, K. Paulavets, L. Barreto-Gomez, L.G. Echeverri, S. Pachauri, B. Boza-Kiss, C. Zimm, J. Rogelj, F. Creutzig, D. Ürge-Vorsatz, D.G. Victor, M.D. Bazilian, S. Fritz, D. Gielen, D.L. McCollum, L. Srivastava, J.D. Hunt, S. Pouya, Pandemic, War, and Global Energy Transitions, *Energies* 15 (2022) 6114. <https://doi.org/10.3390/en15176114>.
- [6] U.S. Energy Information Administration, Annual Energy Outlook 2020. <https://www.eia.gov/todayinenergy/detail.php?id=42655> (accessed 23 July 2023).
- [7] M. Heilmaier, R. Riedel, K. Albe, Y. Eggeler, M. Galetz, H.-J. Kleebe, M. Lepple, M. Oechsner, A. Pundt, R. Schwaiger, H.J. Seifert, B.-X. Xu, RTG 2561 Proposal: MatCom-ComMat: Materials Compounds from Composite Materials for Applications in Extreme Conditions 2020.
- [8] U.S. Energy Information Administration, Annual Energy Outlook 2022. https://www.eia.gov/outlooks/aeo/pdf/AEO2022_Narrative.pdf (accessed 13 September 2023).
- [9] E. Ionescu, S. Bernard, R. Lucas, P. Kroll, S. Ushakov, A. Navrotsky, R. Riedel, Polymer-Derived Ultra-High Temperature Ceramics (UHTCs) and Related Materials, *Adv. Eng. Mater.* 21 (2019) 1900269. <https://doi.org/10.1002/adem.201900269>.
- [10] G. Barroso, Q. Li, R.K. Bordia, G. Motz, Polymeric and ceramic silicon-based coatings – a review, *J. Mater. Chem. A* 7 (2019) 1936–1963. <https://doi.org/10.1039/C8TA09054H>.
- [11] Nageswara Rao Muktinutalapati, Materials for Gas Turbines - An Overview, in: Ernesto Benini (Ed.), *Advances in Gas Turbine Technology*, firstst Edition, Intech, Croatia, 2011.
- [12] W.G. Fahrenholtz, G.E. Hilmas, Ultra-high temperature ceramics: Materials for extreme environments, *Scr. Mater.* 129 (2017) 94–99. <https://doi.org/10.1016/j.scriptamat.2016.10.018>.
- [13] E. Wuchina, E. Opila, M. Opeka, B. Fahrenholtz, I. Talmy, UHTCs: Ultra-High Temperature Ceramic Materials for Extreme Environment Applications, *Electrochem. Soc. Interface* 16 (2007) 30–36. <https://doi.org/10.1149/2.f04074if>.
- [14] D.R. Clarke, M. Oechsner, N.P. Padture, Thermal-barrier coatings for more efficient gas-turbine engines, *MRS Bull.* 37 (2012) 891–898. <https://doi.org/10.1557/mrs.2012.232>.
- [15] J.H. Perepezko, Materials science. The hotter the engine, the better, *Science* 326 (2009) 1068–1069. <https://doi.org/10.1126/science.1179327>.
- [16] M.L. Grilli, D. Valerini, A.E. Slobozeanu, B.O. Postolnyi, S. Balos, A. Rizzo, R.R. Piticescu, Critical Raw Materials Saving by Protective Coatings under Extreme Conditions: A Review of Last Trends in Alloys and Coatings for Aerospace Engine Applications, *Mater.* 14 (2021). <https://doi.org/10.3390/ma14071656>.

- [17] J.G. Thakare, C. Pandey, M.M. Mahapatra, R.S. Mulik, Thermal Barrier Coatings—A State of the Art Review, *Met. Mater. Int.* 27 (2021) 1947–1968. <https://doi.org/10.1007/s12540-020-00705-w>.
- [18] D. Tejero-Martin, C. Bennett, T. Hussain, A review on environmental barrier coatings: History, current state of the art and future developments, *J. Eur. Ceram. Soc.* 41 (2021) 1747–1768. <https://doi.org/10.1016/j.jeurceramsoc.2020.10.057>.
- [19] G. Gottstein, *Materialwissenschaft und Werkstofftechnik: Physikalische Grundlagen*, fourth. Aufl. twentiethfourteenth, Springer Berlin Heidelberg, Berlin, Heidelberg, 2014.
- [20] R.S. Lima, Perspectives on Thermal Gradients in Porous ZrO₂-7–8 wt.% Y₂O₃ (YSZ) Thermal Barrier Coatings (TBCs) Manufactured by Air Plasma Spray (APS), *Coat.* 10 (2020) 812. <https://doi.org/10.3390/coatings10090812>.
- [21] Z.-Y. Wei, G.-H. Meng, L. Chen, G.-R. Li, M.-J. Liu, W.-X. Zhang, L.-N. Zhao, Q. Zhang, X.-D. Zhang, C.-L. Wan, Z.-X. Qu, J. Feng, L. Liu, H. Dong, Z.-B. Bao, X.-F. Zhao, X.-F. Zhang, L. Guo, L. Wang, B. Cheng, W.-W. Zhang, P.-Y. Xu, G.-J. Yang, H.-N. Cai, H. Cui, Y. Wang, F.-X. Ye, Z. Ma, W. Pan, M. Liu, K.-S. Zhou, C.-J. Li, Progress in ceramic materials and structure design toward advanced thermal barrier coatings, *J. Adv. Ceram.* 11 (2022) 985–1068. <https://doi.org/10.1007/s40145-022-0581-7>.
- [22] M. Krüger, S. Franz, H. Saage, M. Heilmaier, J.H. Schneibel, P. Jéhanno, M. Böning, H. Kestler, Mechanically alloyed Mo–Si–B alloys with a continuous α -Mo matrix and improved mechanical properties, *Intermetallics* 16 (2008) 933–941. <https://doi.org/10.1016/j.intermet.2008.04.015>.
- [23] S. Obert, A. Kauffmann, S. Seils, S. Schellert, M. Weber, B. Gorr, H.-J. Christ, M. Heilmaier, On the chemical and microstructural requirements for the pesting-resistance of Mo–Si–Ti alloys, *J. Mater. Res. Technol.* 9 (2020) 8556–8567. <https://doi.org/10.1016/j.jmrt.2020.06.002>.
- [24] M.A. Azim, D. Schliephake, C. Hochmuth, B. Gorr, H.-J. Christ, U. Glatzel, M. Heilmaier, Creep Resistance and Oxidation Behavior of Novel Mo-Si-B-Ti Alloys, *JOM* 67 (2015) 2621–2628. <https://doi.org/10.1007/s11837-015-1560-z>.
- [25] M. Azimovna Azim, S. Burk, B. Gorr, H.-J. Christ, D. Schliephake, M. Heilmaier, R. Bornemann, P.H. Bolívar, Effect of Ti (Macro-) Alloying on the High-Temperature Oxidation Behavior of Ternary Mo–Si–B Alloys at 820–1,300 °C, *Oxid. Met.* 80 (2013) 231–242. <https://doi.org/10.1007/s11085-013-9375-1>.
- [26] D. Schliephake, A. Kauffmann, X. Cong, C. Gombola, M. Azim, B. Gorr, H.-J. Christ, M. Heilmaier, Constitution, oxidation and creep of eutectic and eutectoid Mo-Si-Ti alloys (2019). <https://doi.org/10.5445/IR/1000087430>.
- [27] F. Hinrichs, A. Kauffmann, A.S. Tirunilai, D. Schliephake, B. Beichert, G. Winkens, K. Beck, A.S. Ulrich, M.C. Galetz, Z. Long, H. Thota, Y. Eggeler, A. Pundt, M. Heilmaier, A novel nitridation- and pesting-resistant Cr-Si-Mo alloy, *Corros. Sci.* 207 (2022) 110566. <https://doi.org/10.1016/j.corsci.2022.110566>.
- [28] N.P. Padture, Advanced structural ceramics in aerospace propulsion, *Nat. Mater.* 15 (2016) 804–809. <https://doi.org/10.1038/nmat4687>.
- [29] M. Lenz Leite, U. Degenhardt, W. Krenkel, S. Schafföner, G. Motz, In Situ Generated Yb₂Si₂O₇ Environmental Barrier Coatings for Protection of Ceramic Components in the Next Generation of Gas Turbines, *Adv. Mater. Interfaces* 9 (2022) 2102255. <https://doi.org/10.1002/admi.202102255>.
- [30] E. Bakan, R. Vaßen, Ceramic Top Coats of Plasma-Sprayed Thermal Barrier Coatings: Materials, Processes, and Properties, *J. Therm. Spray. Tech.* 26 (2017) 992–1010. <https://doi.org/10.1007/s11666-017-0597-7>.

- [31] N.P. Padture, M. Gell, E.H. Jordan, Thermal barrier coatings for gas-turbine engine applications, *Science* 296 (2002) 280–284. <https://doi.org/10.1126/science.1068609>.
- [32] R. Vaßen, E. Bakan, D.E. Mack, O. Guillon, A Perspective on Thermally Sprayed Thermal Barrier Coatings: Current Status and Trends, *J. Therm. Spray. Tech.* 31 (2022) 685–698. <https://doi.org/10.1007/s11666-022-01330-2>.
- [33] R.C. Reed, *The superalloys: Fundamentals and applications*, first. publ, Cambridge Univ. Press, Cambridge, 2006.
- [34] D.R. Clarke, S.R. Phillpot, Thermal barrier coating materials, *Materials Today* 8 (2005) 22–29. [https://doi.org/10.1016/S1369-7021\(05\)70934-2](https://doi.org/10.1016/S1369-7021(05)70934-2).
- [35] D. Hasselman, L.F. Johnson, L.D. Bentsen, S. Rahmatullah, L.L. Hong, M.V. Swain, Thermal diffusivity and conductivity of dense polycrystalline ZrO₂ Ceramics: A Survey, *Am. Ceram. Soc. Bull.* (1987) 799–806.
- [36] L. Pawlowski, D. Lombard, P. Fauchais, Structure-thermal properties—relationship in plasma sprayed zirconia coatings, *J. Vac. Sci. Technol.* 3 (1985) 2494–2500. <https://doi.org/10.1116/1.572865>.
- [37] T.M. Pollock, S. Tin, Nickel-Based Superalloys for Advanced Turbine Engines: Chemistry, Microstructure and Properties, *J. Propuls. Power* 22 (2006) 361–374. <https://doi.org/10.2514/1.18239>.
- [38] S. Cruchley, H. Evans, M. Taylor, An overview of the oxidation of Ni-based superalloys for turbine disc applications: surface condition, applied load and mechanical performance, *Mater.* 33 (2016) 465–475. <https://doi.org/10.1080/09603409.2016.1171952>.
- [39] M. Li, Q. Xu, L. Wang, High-Temperature Chemical Stability of Hf₆Ta₂O₁₇ Ceramic for Thermal Barrier Coatings, *KEM* 512-515 (2012) 635–638. <https://doi.org/10.4028/www.scientific.net/KEM.512-515.635>.
- [40] R.A. Andrievskii, N.S. Strel'nikova, N.I. Poltoratskii, E.D. Kharkhardin, V.S. Smirnov, Melting point in systems ZrC-HfC, TaC-ZrC, TaC-HfC, *Powder Metall. Met.* 6 (1967) 65–67. <https://doi.org/10.1007/BF00773385>.
- [41] Q. Wen, Z. Yu, Y. Xu, Y. Lu, C. Fasel, K. Morita, O. Guillon, G. Buntkowsky, E. Ionescu, R. Riedel, SiC/Hf_yTa_{1-y}C_xN_{1-x}/C ceramic nanocomposites with Hf_yTa_{1-y}C_xN_{1-x} -carbon core-shell nanostructure and the influence of the carbon-shell thickness on electrical properties, *J. Mater. Chem. C* 6 (2018) 855–864. <https://doi.org/10.1039/C7TC05023B>.
- [42] H.O. Pierson, *Handbook of refractory carbides and nitrides: Properties, characteristics, processing, and applications*, Noyes Publ, Westwood, NJ, 1996.
- [43] S.Z. Nazarova, E.Z. Kurmaev, N.I. Medvedeva, A. Mowes, Physical properties and electronic structure of TaC-HfC solid solutions, *Russ. J. Inorg. Chem.* 52 (2007) 233–237. <https://doi.org/10.1134/S0036023607020155>.
- [44] O. Gaballa, B.A. Cook, A.M. Russell, Reduced-temperature processing and consolidation of ultra-refractory Ta₄HfC₅, *IJRMHM* 41 (2013) 293–299. <https://doi.org/10.1016/j.ijrmhm.2013.04.018>.
- [45] S.A. Ghaffari, M.A. Faghihi-Sani, F. Golestani-Fard, H. Mandal, Spark plasma sintering of TaC–HfC UHTC via disilicides sintering aids, *J. Eur. Ceram. Soc.* 33 (2013) 1479–1484. <https://doi.org/10.1016/j.jeurceramsoc.2013.01.017>.
- [46] S. Urbonaite, M. Johnsson, G. Svensson, Synthesis of TiC_{1-x}N_x and TaC_{1-x}N_x by spark plasma sintering, *J. Mater. Sci.* 39 (2004) 1907–1911. <https://doi.org/10.1023/B:JMSS.0000016216.61410.4e>.
- [47] Q. Wen, R. Riedel, E. Ionescu, Solid-Solution Effects on the High-Temperature Oxidation Behavior of Polymer-Derived (Hf,Ta)C/SiC and (Hf,Ti)C/SiC Ceramic Nanocomposites, *Adv. Eng. Mater.* 21 (2019) 1800879. <https://doi.org/10.1002/adem.201800879>.

- [48] Z. Li, Y. Wang, X. Xiong, X. Li, Z. Chen, W. Sun, Microstructure and growth behavior of Hf(Ta)C ceramic coating synthesized by low pressure chemical vapor deposition, *J. Alloys Compd.* 705 (2017) 79–88. <https://doi.org/10.1016/j.jallcom.2017.02.101>.
- [49] E. Wuchina, M. Opeka, S. Causey, K. Buesking, J. Spain, A. Cull, J. Routbort, F. Guitierrez-Mora, Designing for ultrahigh-temperature applications: The mechanical and thermal properties of HfB₂ HfC_x HfN_x and Hf(N), *J. Mater. Sci.* 39 (2004) 5939–5949. <https://doi.org/10.1023/B:JMSC.0000041690.06117.34>.
- [50] A. Bellosi, F. Monteverde, D. Sciti, Fast Densification of Ultra-High-Temperature Ceramics by Spark Plasma Sintering, *Int. J. Appl. Ceram. Technol.* 3 (2006) 32–40. <https://doi.org/10.1111/j.1744-7402.2006.02060.x>.
- [51] M.M. Opeka, I.G. Talmy, E.J. Wuchina, J.A. Zaykoski, S.J. Causey, Mechanical, Thermal, and Oxidation Properties of Refractory Hafnium and zirconium Compounds, *J. Eur. Ceram. Soc.* 19 (1999) 2405–2414. [https://doi.org/10.1016/s0955-2219\(99\)00129-6](https://doi.org/10.1016/s0955-2219(99)00129-6).
- [52] D. Sciti, L. Silvestroni, S. Guicciardi, D.D. Fabbriche, A. Bellosi, Processing, mechanical properties and oxidation behavior of TaC and HfC composites containing 15 vol% TaSi₂ or MoSi₂, *J. Mater. Res.* 24 (2009) 2056–2065. <https://doi.org/10.1557/jmr.2009.0232>.
- [53] W.C. Tripp, H.H. Davis, H.C. Graham, Effect of an SiC addition on the oxidation of ZrB₂, *Amer. Ceram. Soc. Bull.* 52 (1973) 612–616.
- [54] P. Colombo, G. Mera, R. Riedel, G.D. Sorarù, Polymer-Derived Ceramics: 40 Years of Research and Innovation in Advanced Ceramics, *J. Am. Ceram. Soc.* (2010) 1805–1837. <https://doi.org/10.1111/j.1551-2916.2010.03876.x>.
- [55] J. Bill, F. Aldinger, Precursor-derived Covalent Ceramics, *Adv. Mater.* 7 (1995) 775–787. <https://doi.org/10.1002/adma.19950070903>.
- [56] Z. Ren, S.B. Mujib, G. Singh, High-Temperature Properties and Applications of Si-Based Polymer-Derived Ceramics: A Review, *Materials* 14 (2021). <https://doi.org/10.3390/ma14030614>.
- [57] E. Kroke, Y.-L. Li, C. Konetschny, E. Lecomte, C. Fasel, R. Riedel, Silazane derived ceramics and related materials, *Mater. Sci. Eng. R Rep.* 26 (2000) 97–199. [https://doi.org/10.1016/S0927-796X\(00\)00008-5](https://doi.org/10.1016/S0927-796X(00)00008-5).
- [58] Y. Lu, F. Chen, P. An, L. Ye, W. Qiu, T. Zhao, Polymer precursor synthesis of TaC–SiC ultrahigh temperature ceramic nanocomposites, *RSC Adv.* 6 (2016) 88770–88776. <https://doi.org/10.1039/C6RA17723A>.
- [59] E. Ionescu, H.-J. Kleebe, R. Riedel, Silicon-containing polymer-derived ceramic nanocomposites (PDC-NCs): preparative approaches and properties, *Chem. Soc. Re.* 41 (2012) 5032–5052. <https://doi.org/10.1039/c2cs15319j>.
- [60] B. Feng, J. Peter, C. Fasel, Q. Wen, Y. Zhang, H.-J. Kleebe, E. Ionescu, High-temperature phase and microstructure evolution of polymer-derived SiZrCN and SiZrBCN ceramic nanocomposites, *J. Am. Ceram. Soc.* 103 (2020) 7001–7013. <https://doi.org/10.1111/jace.17149>.
- [61] C. Zhou, X. Gao, Y. Xu, G. Buntkowsky, Y. Ikuhara, R. Riedel, E. Ionescu, Synthesis and high-temperature evolution of single-phase amorphous Si–Hf–N ceramics, *J. Eur. Ceram. Soc.* 35 (2015) 2007–2015. <https://doi.org/10.1016/j.jeurceramsoc.2015.01.026>.
- [62] J. Yuan, M. Galetz, X.G. Luan, C. Fasel, R. Riedel, E. Ionescu, High-temperature oxidation behavior of polymer-derived SiHfBCN ceramic nanocomposites, *J. Eur. Ceram. Soc.* 36 (2016) 3021–3028. <https://doi.org/10.1016/j.jeurceramsoc.2015.12.006>.
- [63] B. Papendorf, E. Ionescu, H.-J. Kleebe, C. Linck, O. Guillon, K. Nonnenmacher, R. Riedel, High-Temperature Creep Behavior of Dense SiOC-Based Ceramic Nanocomposites: Microstructural and Phase Composition Effects, *J. Am. Ceram. Soc.* 96 (2013) 272–280. <https://doi.org/10.1111/jace.12067>.

- [64] Q. Wen, Y. Xu, B. Xu, C. Fasel, O. Guillon, G. Buntkowsky, Z. Yu, R. Riedel, E. Ionescu, Single-source-precursor synthesis of dense SiC/HfC_(x)N_(1-x)-based ultrahigh-temperature ceramic nanocomposites, *Nanoscale* 6 (2014) 13678–13689. <https://doi.org/10.1039/C4NR03376K>.
- [65] J. Yuan, D. Li, K.E. Johanns, C. Fasel, K. Durst, H.-J. Kleebe, Z. Shen, R. Riedel, E. Ionescu, Preparation of dense SiHf(B)CN-based ceramic nanocomposites via rapid spark plasma sintering, *J. Eur. Ceram. Soc.* 37 (2017) 5157–5165. <https://doi.org/10.1016/j.jeurceramsoc.2017.04.066>.
- [66] J. Yuan, S. Hapis, H. Breitzke, Y. Xu, C. Fasel, H.-J. Kleebe, G. Buntkowsky, R. Riedel, E. Ionescu, Single-source-precursor synthesis of hafnium-containing ultrahigh-temperature ceramic nanocomposites (UHTC-NCs), *Inorg. Chem.* 53 (2014) 10443–10455. <https://doi.org/10.1021/ic501512p>.
- [67] R. Sujith, A.B. Kousaalya, R. Kumar, Coarsening Induced Phase Transformation of Hafnia in Polymer-Derived Si-Hf-C-N-O Ceramics, *J. Am. Ceram. Soc.* 94 (2011) 2788–2791. <https://doi.org/10.1111/j.1551-2916.2011.04719.x>.
- [68] R. Riedel, G. Mera, R. Hauser, A. Kloneczynski, Silicon-Based Polymer-Derived Ceramics: Synthesis Properties and Applications-A Review, *Nippon Seramikkusu Kyokai gakujutsu ronbunshi* 114 (2006) 425–444. <https://doi.org/10.2109/jcersj.114.425>.
- [69] T. Konegger, C.C. Tsai, R.K. Bordia, Preparation of Polymer-Derived Ceramic Coatings by Dip-Coating, *MSF* 825-826 (2015) 645–652. <https://doi.org/10.4028/www.scientific.net/MSF.825-826.645>.
- [70] J.D. Torrey, R.K. Bordia, C.H. Henager, Y. Blum, Y. Shin, W.D. Samuels, Composite polymer derived ceramic system for oxidizing environments, *J. Mater. Sci* 41 (2006) 4617–4622. <https://doi.org/10.1007/s10853-006-0242-1>.
- [71] M. Günthner, T. Kraus, W. Krenkel, G. Motz, A. Dierdorf, D. Decker, Particle-Filled PHPS Silazane-Based Coatings on Steel, *Int. J. Appl. Ceram. Technol.* 6 (2009) 373–380. <https://doi.org/10.1111/j.1744-7402.2008.02346.x>.
- [72] K. Wang, M. Günthner, G. Motz, R.K. Bordia, High performance environmental barrier coatings, Part II: Active filler loaded SiOC system for superalloys, *J. Eur. Ceram. Soc.* 31 (2011) 3011–3020. <https://doi.org/10.1016/j.jeurceramsoc.2011.05.047>.
- [73] M. Günthner, A. Schütz, U. Glatzel, K. Wang, R.K. Bordia, O. Greißl, W. Krenkel, G. Motz, High performance environmental barrier coatings, Part I: Passive filler loaded SiCN system for steel, *J. Eur. Ceram. Soc.* 31 (2011) 3003–3010. <https://doi.org/10.1016/j.jeurceramsoc.2011.05.027>.
- [74] R. Anand, B.B. Nayak, S.K. Behera, Coarsening kinetics of nanostructured ZrO₂ in Zr-doped SiCN ceramic hybrids, *J. Alloys Compd.* 811 (2019) 151939. <https://doi.org/10.1016/j.jallcom.2019.151939>.
- [75] M. Zaheer, T. Schmalz, G. Motz, R. Kempe, Polymer derived non-oxide ceramics modified with late transition metals, *Chem. Soc. Rev.* 41 (2012) 5102–5116. <https://doi.org/10.1039/C2CS15326B>.
- [76] G. Mera, M. Gallei, S. Bernard, E. Ionescu, Ceramic Nanocomposites from Tailor-Made Pre-ceramic Polymers, *Nanomater.* 5 (2015) 468–540. <https://doi.org/10.3390/nano5020468>.
- [77] B. Papendorf, K. Nonnenmacher, E. Ionescu, H.-J. Kleebe, R. Riedel, Strong influence of polymer architecture on the microstructural evolution of hafnium-alkoxide-modified silazanes upon ceramization, *Small* 7 (2011) 970–978. <https://doi.org/10.1002/sml.201001938>.
- [78] D. Sciti, L. Silvestroni, V. Medri, F. Monteverde, Sintering and Densification Mechanisms of Ultra-High Temperature Ceramics, in: W.G. Fahrenholtz, E.J. Wuchina, W.E. Lee, Y. Zhou

- (Eds.), *Ultra-High Temperature Ceramics*, John Wiley & Sons, Inc, Hoboken, NJ, 2014, pp. 112–143.
- [79] R. Orrù, G. Cao, Comparison of Reactive and Non-Reactive Spark Plasma Sintering Routes for the Fabrication of Monolithic and Composite Ultra High Temperature Ceramics (UHTC) Materials, *Mater.* 6 (2013) 1566–1583. <https://doi.org/10.3390/ma6051566>.
- [80] F. Monteverde, Ultra-high temperature HfB₂-SiC ceramics consolidated by hot-pressing and spark plasma sintering, *J. Alloys Compd.* 428 (2007) 197–205. <https://doi.org/10.1016/j.jallcom.2006.01.107>.
- [81] R. Licheri, R. Orrù, C. Musa, A.M. Locci, G. Cao, Spark plasma sintering of ZrB₂- and HfB₂-based Ultra High Temperature Ceramics prepared by SHS, *Int. J Self-Propag. High-Temp. Synth.* 18 (2009) 15–24. <https://doi.org/10.3103/S106138620901004X>.
- [82] R. Licheri, R. Orrù, A.M. Locci, G. Cao, Efficient Synthesis/Sintering Routes To Obtain Fully Dense Ultra-High-Temperature Ceramics (UHTCs), *Ind. Eng. Chem. Res.* 46 (2007) 9087–9096. <https://doi.org/10.1021/ie0701423>.
- [83] A. Balbo, D. Sciti, Spark plasma sintering and hot pressing of ZrB₂-MoSi₂ ultra-high-temperature ceramics, *Mater. Sci. Eng.* 475 (2008) 108–112. <https://doi.org/10.1016/j.msea.2007.01.164>.
- [84] N. Thor, J. Bernauer, N.-C. Petry, E. Ionescu, R. Riedel, A. Puntdt, H.-J. Kleebe, Microstructural evolution of Si(Hf_xTa_{1-x})(C)N polymer-derived ceramics upon high-temperature anneal, *J. Eur. Ceram. Soc.* 43 (2023) 1417–1431. <https://doi.org/10.1016/j.jeurceramsoc.2022.11.060>.
- [85] N. Thor, G. Winkens, J. Bernauer, N.-C. Petry, K. Beck, J. Wang, R. Schwaiger, R. Riedel, U. Kolb, M. Lepple, A. Puntdt, Microstructure characterization and mechanical properties of polymer-derived (Hf_{0.7}Ta_{0.3})C/SiC ceramic prepared upon field-assisted sintering technique (FAST/SPS): in preparation.
- [86] D. Ni, Y. Cheng, J. Zhang, J.-X. Liu, J. Zou, B. Chen, H. Wu, H. Li, S. Dong, J. Han, X. Zhang, Q. Fu, G.-J. Zhang, *Advances in ultra-high temperature ceramics, composites, and coatings*, *J. Adv. Ceram.* 11 (2022) 1–56. <https://doi.org/10.1007/s40145-021-0550-6>.
- [87] W.G. Fahrenholtz, G.E. Hilmas, I.G. Talmy, J.A. Zaykoski, Refractory Diborides of Zirconium and Hafnium, *J. Am. Ceram. Soc.* 90 (2007) 1347–1364. <https://doi.org/10.1111/j.1551-2916.2007.01583.x>.
- [88] V. Medri, F. Monteverde, A. Balbo, A. Bellosi, Comparison of ZrB₂-ZrC-SiC Composites Fabricated by Spark Plasma Sintering and Hot-Pressing, *Adv. Eng. Mater.* 7 (2005) 159–163. <https://doi.org/10.1002/adem.200400184>.
- [89] I.G. Talmy, J.A. Zaykoski, C.A. Martin, Flexural Creep Deformation of ZrB₂/SiC Ceramics in Oxidizing Atmosphere, *J. Am. Ceram. Soc.* 91 (2008) 1441–1447. <https://doi.org/10.1111/j.1551-2916.2008.02370.x>.
- [90] E. Opila, S. Levine, J. Lorincz, Oxidation of ZrB₂- and HfB₂-based ultra-high temperature ceramics: Effect of Ta additions, *J. Mater. Sci* 39 (2004) 5969–5977. <https://doi.org/10.1023/B:JMSC.0000041693.32531.d1>.
- [91] A. Paul, J. Binner, B. Vaidhyanathan, UHTC Composites for Hypersonic Applications, in: W.G. Fahrenholtz, E.J. Wuchina, W.E. Lee, Y. Zhou (Eds.), *Ultra-High Temperature Ceramics*, John Wiley & Sons, Inc, Hoboken, NJ, 2014, pp. 144–166.
- [92] A.L. Chamberlain, W.G. Fahrenholtz, G.E. Hilmas, D.T. Ellerby, High-Strength Zirconium Diboride-Based Ceramics, *J. Am. Ceram. Soc.* 87 (2004) 1170–1172. <https://doi.org/10.1111/j.1551-2916.2004.01170.x>.
- [93] F. Monteverde, A. Bellosi, Microstructure and Properties of an HfB₂-SiC Composite for Ultra High Temperature Applications, *Adv. Eng. Mater.* 6 (2004) 331–336. <https://doi.org/10.1002/adem.200400016>.

- [94] F. Monteverde, A. Bellosi, Effect of the addition of silicon nitride on sintering behaviour and microstructure of zirconium diboride, *Scr. Mater.* 46 (2002) 223–228. [https://doi.org/10.1016/S1359-6462\(01\)01229-5](https://doi.org/10.1016/S1359-6462(01)01229-5).
- [95] L. Silvestroni, D. Sciti, J. Kling, S. Lauterbach, H.-J. Kleebe, Sintering Mechanisms of Zirconium and Hafnium Carbides Doped with MoSi₂, *J. Am. Ceram. Soc.* 92 (2009) 1574–1579. <https://doi.org/10.1111/j.1551-2916.2009.03049.x>.
- [96] D. Sciti, L. Silvestroni, A. Bellosi, Fabrication and properties of HfB₂–MoSi₂ composites produced by hot pressing and spark plasma sintering, *J. Mater. Res.* 21 (2006) 1460–1466. <https://doi.org/10.1557/jmr.2006.0180>.
- [97] D. Sciti, L. Silvestroni, G. Celotti, C. Melandri, S. Guicciardi, Sintering and Mechanical Properties of ZrB₂-TaSi₂ and HfB₂-TaSi₂ Ceramic Composites, *J. Am. Ceram. Soc.* 91 (2008) 3285–3291. <https://doi.org/10.1111/j.1551-2916.2008.02593.x>.
- [98] T. Mizuguchi, S. Guo, Y. Kagawa, Transmission electron microscopy characterization of spark plasma sintered ZrB₂ ceramic, *Ceram. Int.* 36 (2010) 943–946. <https://doi.org/10.1016/j.ceramint.2009.10.025>.
- [99] H. Liu, L. Liu, F. Ye, Z. Zhang, Y. Zhou, Microstructure and mechanical properties of the spark plasma sintered TaC/SiC composites: Effects of sintering temperatures, *J. Eur. Ceram. Soc.* 32 (2012) 3617–3625. <https://doi.org/10.1016/j.jeurceramsoc.2012.04.042>.
- [100] W. Lengauer, Transition Metal Carbides, Nitrides, and Carbonitrides, in: R. Riedel (Ed.), *Handbook of Ceramic Hard Materials*, Wiley-VCH Verlag GmbH, Weinheim, Germany, 2000, pp. 202–252.
- [101] S.T. Oyama, Preparation and catalytic properties of transition metal carbides and nitrides, *Catal. Today* 15 (1992) 179–200. [https://doi.org/10.1016/0920-5861\(92\)80175-M](https://doi.org/10.1016/0920-5861(92)80175-M).
- [102] R. Davis (Ed.), *Advances in Ceramics: Nonstoichiometric Compounds*, The American Ceramic Society, 1987.
- [103] K. Momma, F. Izumi, VESTA: a three-dimensional visualization system for electronic and structural analysis, *J. Appl. Crystallogr.* 41 (2008) 653–658. <https://doi.org/10.1107/S0021889808012016>.
- [104] D.K. Deardorff, M.I. Copeland, R.P. Adams, *The Hafnium-carbon Phase Diagram*, U.S. Department of the Interior, Bureau of Mines, 1967.
- [105] V.I. Razumovskiy, A.V. Ruban, J. Odqvist, D. Dilner, P.A. Korzhavyi, Effect of carbon vacancies on thermodynamic properties of TiC–ZrC mixed carbides, *Calphad* 46 (2014) 87–91. <https://doi.org/10.1016/j.calphad.2014.02.005>.
- [106] A.I. Gusev, Phase Diagrams of the Pseudo-Binary TiC–NbC, TiC–TaC, ZrC–NbC, ZrC–TaC, and HfC–TaC Carbide Systems (in English), *Russ. J. Phys. Chem.* (1985) 336–340.
- [107] S. Fu, M. Zhu, Y. Zhu, Organosilicon polymer-derived ceramics: An overview, *J. Adv. Ceram.* 8 (2019) 457–478. <https://doi.org/10.1007/s40145-019-0335-3>.
- [108] R. Sujith, S. Jothi, A. Zimmermann, F. Aldinger, R. Kumar, Mechanical behaviour of polymer derived ceramics – a review, *Int. Mater. Rev.* 66 (2021) 426–449. <https://doi.org/10.1080/09506608.2020.1784616>.
- [109] A. Morlier, S. Cros, J.-P. Garandet, N. Alberola, Thin gas-barrier silica layers from perhydropolysilazane obtained through low temperature curings: A comparative study, *Thin Solid Films* 524 (2012) 62–66. <https://doi.org/10.1016/j.tsf.2012.09.065>.
- [110] R.G. Jones, *Silicon-Containing Polymers: The Science and Technology of Their Synthesis and Applications*, Springer Netherlands, Dordrecht, 2000.
- [111] P. Colombo (Ed.), *Polymer derived ceramics: From nano-structure to applications*, DEStech Publications, Lancaster, Pa., 2010.

-
- [112] M. Zeldin (Ed.), *Inorganic and organometallic polymers: Macromolecules containing silicon, phosphorus, and other inorganic elements*; Denver, Colorado, April 5-10, 1987, 2nd ed., American Chemical Soc, Washington, DC, 1989.
- [113] J.M. Zeigler, J.M. Zeigler, F.W.G. Fearon (Eds.), *Silicon-based polymer science: A comprehensive resource; developed from the International Topical Workshop Advances in Silicon-Based Polymer Science ... Makaha, Oahu, Hawaii, November 21 - 24, 1987*, 2nd ed., ACS, Washington, D.C., 1991.
- [114] S.-D. Kim, P.-S. Ko, K.-S. Park, Perhydropolysilazane spin-on dielectrics for inter-layer-dielectric applications of sub-30 nm silicon technology, *Semicond. Sci. Technol.* 28 (2013) 35008. <https://doi.org/10.1088/0268-1242/28/3/035008>.
- [115] Y.-L. Li, E. Kroke, R. Riedel, C. Fasel, C. Gervais, F. Babonneau, Thermal cross-linking and pyrolytic conversion of poly(ureamethylvinyl)silazanes to silicon-based ceramics, *Appl. Organometal. Chem.* 15 (2001) 820–832. <https://doi.org/10.1002/aoc.236>.
- [116] Choong Kwet Yive, N. S., R.J.P. Corriu, D. Leclercq, P.H. Mutin, A. Vioux, Silicon carbonitride from polymeric precursors: thermal cross-linking and pyrolysis of oligosilazane model compounds, *Chem. Mater.* 4 (1992) 141–146. <https://doi.org/10.1021/cm00019a029>.
- [117] S. Müller, Y. de Hazan, D. Penner, Effect of temperature, humidity and aminoalkoxysilane additive on the low temperature curing of polyorganosilazane coatings studied by IR spectroscopy, gravimetric and evolved gas analysis, *Prog. Org. Coat.* 97 (2016) 133–145. <https://doi.org/10.1016/j.porgcoat.2016.03.021>.
- [118] A. Lukacs, G.J. Knasiak, A. Lukacs III (KION CORP [US]) US2003083453 (A1), 2002.
- [119] A. Morlier, S. Cros, J.-P. Garandet, N. Alberola, Structural properties of ultraviolet cured polysilazane gas barrier layers on polymer substrates, *Thin Solid Films* 550 (2014) 85–89. <https://doi.org/10.1016/j.tsf.2013.10.140>.
- [120] L. Prager, A. Dierdorf, H. Liebe, S. Naumov, S. Stojanović, R. Heller, L. Wennrich, M.R. Buchmeiser, Conversion of perhydropolysilazane into a SiO_x network triggered by vacuum ultraviolet irradiation: access to flexible, transparent barrier coatings, *Chemistry* 13 (2007) 8522–8529. <https://doi.org/10.1002/chem.200700351>.
- [121] T. Taki, S. Maeda, K. Okamura, M. Sato, T. Matsuzawa, Oxidation curing mechanism of polycarbosilane fibres by solid-state ²⁹Si high-resolution NMR, *J. Mater. Sci. Lett.* 6 (1987) 826–828. <https://doi.org/10.1007/BF01729026>.
- [122] H.Q. Ly, R. Taylor, R.J. Day, F. Heatley, Conversion of polycarbosilane (PCS) to SiC-based ceramic Part 1. Characterisation of PCS and curing products, *J. Mater. Sci.* 36 (2001) 4037–4043. <https://doi.org/10.1023/A:1017942826657>.
- [123] Y. Urabe, T. Sameshima, Polysilazane Precursor Used for Formation of Oxidized Insulator, *MRS Proc.* 1066 (2008). <https://doi.org/10.1557/PROC-1066-A05-02>.
- [124] R.M. Laine, F. Babonneau, Preceramic polymer routes to silicon carbide, *Chem. Mater.* 5 (1993) 260–279. <https://doi.org/10.1021/cm00027a007>.
- [125] Y.D. Blum, K.B. Schwartz, R.M. Laine, Preceramic polymer pyrolysis, *J. Mater. Sci.* 24 (1989) 1707–1718. <https://doi.org/10.1007/BF01105695>.
- [126] H. Ichikawa, H. Teranishi, T. Ishikawa, Effect of curing conditions on mechanical properties of SiC fibre (Nicalon), *J. Mater. Sci. Lett.* 6 (1987) 420–422. <https://doi.org/10.1007/BF01756783>.
- [127] G.D. Soraru, F. Babonneau, J.D. Mackenzie, Structural concepts on new amorphous covalent solids, *J. Non-Cryst. Solids* 106 (1988) 256–261. [https://doi.org/10.1016/0022-3093\(88\)90270-0](https://doi.org/10.1016/0022-3093(88)90270-0).
- [128] P. Greil, Polymer Derived Engineering Ceramics, *Adv. Eng. Mater.* 2 (2000) 339–348. [https://doi.org/10.1002/1527-2648\(200006\)2:6<339:AID-ADEM339>3.0.CO;2-K](https://doi.org/10.1002/1527-2648(200006)2:6<339:AID-ADEM339>3.0.CO;2-K).

- [129] T. Konegger, C. Drechsel, H. Peterlik, In-situ small angle X-ray scattering (SAXS) – A versatile tool for clarifying the evolution of microporosity in polymer-derived ceramics, *Microporous Mesoporous Mater.* 324 (2021) 111268. <https://doi.org/10.1016/j.micromeso.2021.111268>.
- [130] R. Riedel (Ed.), *Handbook of ceramic hard materials*, Wiley-VCH, Weinheim, 2000.
- [131] E. Bernardo, P. Colombo, E. Dainese, G. Lucchetta, P.F. Bariani, Novel 3D Wollastonite-Based Scaffolds from Pre-ceramic Polymers Containing Micro- and Nano-Sized Reactive Particles, *Adv. Eng. Mater.* 14 (2012) 269–274. <https://doi.org/10.1002/adem.201100241>.
- [132] S. Yajima, K. Okamura, J. Hayashi, Structural Analysis In Continuous Silicon Carbide Fiber Of High Tensile Strength, *Chem. Lett.* 4 (1975) 1209–1212. <https://doi.org/10.1246/cl.1975.1209>.
- [133] R. Riedel, A. Kienzle, W. Dressler, L. Ruwisch, J. Bill, F. Aldinger, A silicoboron carbonitride ceramic stable to 2,000°C, *Nature* 382 (1996) 796–798. <https://doi.org/10.1038/382796a0>.
- [134] J. Bill, T.W. Kamphowe, A. Müller, T. Wichmann, A. Zern, A. Jalowieki, J. Mayer, M. Weinmann, J. Schuhmacher, K. Müller, J. Peng, H.J. Seifert, F. Aldinger, Precursor-derived Si-(B)-C-N ceramics: thermolysis, amorphous state and crystallization, *Appl. Organometal. Chem.* 15 (2001) 777–793. <https://doi.org/10.1002/aoc.242>.
- [135] F. Berger, M. Weinmann, F. Aldinger, K. Müller, Solid-State NMR Studies of the Preparation of Si–Al–C–N Ceramics from Aluminum-Modified Polysilazanes and Polysilylcarbodiimides, *Chem. Mater.* 16 (2004) 919–929. <https://doi.org/10.1021/cm0351700>.
- [136] Y. Mori, T. Ueda, S. Kitaoka, Y. Sugahara, Preparation of Si-Al-N-C ceramic composites by pyrolysis of blended precursors, *J. Ceram. Soc. Japan* 114 (2006) 497–501. <https://doi.org/10.2109/jcersj.114.497>.
- [137] G.D. Soraru, A. Ravagni, R. Camprostrini, F. Babonneau, Synthesis and Characterization of β -SiAlON Ceramics from Organosilicon Polymers, *J. Am. Ceram. Soc.* 74 (1991) 2220–2223. <https://doi.org/10.1111/j.1151-2916.1991.tb08288.x>.
- [138] S. Yajima, T. Iwai, T. Yamamura, K. Okamura, Y. Hasegawa, Synthesis of a polytitanocarbosilane and its conversion into inorganic compounds, *J. Mater. Sci* 16 (1981) 1349–1355. <https://doi.org/10.1007/BF01033851>.
- [139] T. Yamamura, T. Ishikawa, M. Shibuya, T. Hisayuki, K. Okamura, Development of a new continuous Si-Ti-C-O fibre using an organometallic polymer precursor, *J. Mater. Sci.* 23 (1988) 2589–2594. <https://doi.org/10.1007/BF01111919>.
- [140] F. Babonneau, G.D. Sorarù, Synthesis and characterization of SiZrCO ceramics from polymer precursors, *J. Eur. Ceram. Soc.* 8 (1991) 29–34. [https://doi.org/10.1016/0955-2219\(91\)90089-I](https://doi.org/10.1016/0955-2219(91)90089-I).
- [141] A. Saha, S.R. Shah, R. Raj, Amorphous Silicon Carbonitride Fibers Drawn from Alkoxide Modified Ceraset™, *J. Am. Ceram. Soc.* 86 (2003) 1443–1445. <https://doi.org/10.1111/j.1151-2916.2003.tb03493.x>.
- [142] M. Zaheer, G. Motz, R. Kempe, The generation of palladium silicide nanoalloy particles in a SiCN matrix and their catalytic applications, *J. Mater. Chem.* 21 (2011) 18825. <https://doi.org/10.1039/C1JM13665H>.
- [143] C. Zhou, C. Fasel, R. Ishikawa, M. Gallei, Y. Ikuhara, S. Lauterbach, H.-J. Kleebe, R. Riedel, E. Ionescu, One-pot synthesis of a C/SiFeN(O)-based ceramic paper with in-situ generated hierarchical micro/nano-morphology, *J. Eur. Ceram. Soc.* 37 (2017) 5193–5203. <https://doi.org/10.1016/j.jeurceramsoc.2017.03.007>.

- [144] G.J. Chen, C. Tamborski, Synthesis and reactions of some perfluoroalkyl ether substituted silanes, *J. Organomet. Chem.* 293 (1985) 313–321. [https://doi.org/10.1016/0022-328x\(85\)80301-6](https://doi.org/10.1016/0022-328x(85)80301-6).
- [145] R. Riedel, J. Bill, A. Kienzle, Boron-modified Inorganic Polymers Precursors for the Synthesis of Multicomponent Ceramics, *Appl. Organometal. Chem.* 10 (1996) 241–256. [https://doi.org/10.1002/\(SICI\)1099-0739\(199604\)10:3/4<241:AID-AOC471>3.0.CO;2-W](https://doi.org/10.1002/(SICI)1099-0739(199604)10:3/4<241:AID-AOC471>3.0.CO;2-W).
- [146] S.D. Oguntuyi, O.T. Johnson, M.B. Shongwe, Spark Plasma Sintering of Ceramic Matrix Composite of ZrB₂ and TiB₂: Microstructure, Densification, and Mechanical Properties—A Review, *Met. Mater. Int.* 27 (2021) 2146–2159. <https://doi.org/10.1007/s12540-020-00874-8>.
- [147] A. Nisar, C. Zhang, B. Boesl, A. Agarwal, Unconventional Materials Processing Using Spark Plasma Sintering, *Ceram.* 4 (2021) 20–39. <https://doi.org/10.3390/ceramics4010003>.
- [148] S.-J.L. Kang, *Sintering: Densification, Grain Growth, and Microstructure*, first ed., Elsevier Science & Technology, Oxford, 2005.
- [149] J. Hojo (Ed.), *Materials Chemistry of Ceramics*, 1st ed., Springer, Singapore, 2019.
- [150] E. Macherauch, H.-W. Zoch, Sintern, in: E. Macherauch, H.-W. Zoch (Eds.), *Praktikum in Werkstoffkunde*, Springer Fachmedien Wiesbaden, Wiesbaden, 2019, pp. 779–786.
- [151] M.N. Rahaman, *Ceramic processing and sintering*, Second edition, Taylor & Francis, Boca Raton, London, New York, 2003.
- [152] J. Frenkel, Viscous Flow of Crystalline Bodies under the Action of Surface Tension, *J. Phys. (U. S. S. R)* 9 (1945) 385.
- [153] G.C. Kuczynski, The geometry and mechanism of sintering, 1949.
- [154] G.C. Kuczynski, Self-Diffusion in Sintering of Metallic Particles, in: S. Sōmiya, Y. Moriyoshi (Eds.), *Sintering Key Papers*, Springer Netherlands, Dordrecht, 1990, pp. 509–527.
- [155] F. Lenel, Sintering in the Presence of a Liquid Phase, 1948.
- [156] R.L. Coble, Initial Sintering of Alumina and Hematite, *J. Am. Ceram. Soc.* 41 (1958) 55–62. <https://doi.org/10.1111/j.1151-2916.1958.tb13519.x>.
- [157] R.L. Coble, Sintering Crystalline Solids. I. Intermediate and Final State Diffusion Models, *J. Appl. Phys.* 32 (1961) 787–792. <https://doi.org/10.1063/1.1736107>.
- [158] W. Kingery, Sintering from Prehistoric Times to the Present, *SSP 25-26* (1992) 1–10. <https://doi.org/10.4028/www.scientific.net/ssp.25-26.1>.
- [159] W.D. Kingery, M. Berg, Study of the Initial Stages of Sintering Solids by Viscous Flow, Evaporation-Condensation, and Self-Diffusion, *J. Appl. Phys.* 26 (1955) 1205–1212. <https://doi.org/10.1063/1.1721874>.
- [160] R.M. German, Z.A. Munir, Morphology relations during bulk-transport sintering, *Metall Mater. Trans. A: Phys.* 6 (1975). <https://doi.org/10.1007/BF02818648>.
- [161] Z.A. Munir, U. Anselmi-Tamburini, M. Ohyanagi, The effect of electric field and pressure on the synthesis and consolidation of materials: A review of the spark plasma sintering method, *J. Mater. Sci.* 41 (2006) 763–777. <https://doi.org/10.1007/s10853-006-6555-2>.
- [162] C. Zhang, A. Gupta, S. Seal, B. Boesl, A. Agarwal, Solid solution synthesis of tantalum carbide-hafnium carbide by spark plasma sintering, *J. Am. Ceram. Soc.* 100 (2017) 1853–1862. <https://doi.org/10.1111/jace.14778>.
- [163] M.S. Jensen, M.-A. Einarsrud, T. Grande, The Effect of Surface Oxides During Hot Pressing of TiB₂, *J. Am. Ceram. Soc.* 92 (2009) 623–630. <https://doi.org/10.1111/j.1551-2916.2009.02923.x>.

- [164] P. Dong, Z. Wang, W. Wang, S. Chen, J. Zhou, Understanding the spark plasma sintering from the view of materials joining, *Scr. Mater.* 123 (2016) 118–121. <https://doi.org/10.1016/j.scriptamat.2016.06.014>.
- [165] M. Suarez, A. Fernandez, J.L. Menendez, R. Torrecillas, H. U., J. Hennicke, R. Kirchner, T. Kessel, Challenges and Opportunities for Spark Plasma Sintering: A Key Technology for a New Generation of Materials, in: B. Ertug (Ed.), *Sintering Applications*, Intech, 2013.
- [166] Z.A. Munir, D.V. Quach, M. Ohyanagi, Electric Current Activation of Sintering: A Review of the Pulsed Electric Current Sintering Process, *J. Am. Ceram. Soc.* 94 (2011) 1–19. <https://doi.org/10.1111/j.1551-2916.2010.04210.x>.
- [167] D. Schwesig, G. Schierning, R. Theissmann, N. Stein, N. Petermann, H. Wiggers, R. Schmechel, D.E. Wolf, From nanoparticles to nanocrystalline bulk: percolation effects in field assisted sintering of silicon nanoparticles, *Nanotechnology* 22 (2011) 135601. <https://doi.org/10.1088/0957-4484/22/13/135601>.
- [168] O. Guillon, J. Gonzalez-Julian, B. Dargatz, T. Kessel, G. Schierning, J. Räthel, M. Herrmann, Field-Assisted Sintering Technology/Spark Plasma Sintering: Mechanisms, Materials, and Technology Developments, *Adv. Eng. Mater.* 16 (2014) 830–849. <https://doi.org/10.1002/adem.201300409>.
- [169] O. Guillon, W. Rheinheimer, M. Bram, A Perspective on Emerging and Future Sintering Technologies of Ceramic Materials, *Adv. Eng. Mater.* (2023) 2201870. <https://doi.org/10.1002/adem.202201870>.
- [170] P. Cavaliere (Ed.), *Spark plasma sintering of materials: Advances in processing and applications*, Springer Nature Switzerland, Cham, 2019.
- [171] M. Suganuma, Y. Kitagawa, S. Wada, N. Murayama, Pulsed Electric Current Sintering of Silicon Nitride, *J. Am. Ceram. Soc.* 86 (2003) 387–394. <https://doi.org/10.1111/j.1151-2916.2003.tb03310.x>.
- [172] F. Kaiser, P. Simon, U. Burkhardt, B. Kieback, Y. Grin, I. Veremchuk, Spark Plasma Sintering of Tungsten Oxides WO_x ($2.50 \leq x \leq 3$): Phase Analysis and Thermoelectric Properties, *Cryst.* 7 (2017) 271. <https://doi.org/10.3390/cryst7090271>.
- [173] J.R. Groza, M. Garcia, J.A. Schneider, Surface effects in field-assisted sintering, *J. Mater. Res.* 16 (2001) 286–292. <https://doi.org/10.1557/JMR.2001.0043>.
- [174] B. Ertug (Ed.), *Sintering Applications*, Intech, 2013.
- [175] R. Marder, C. Estournès, G. Chevallier, R. Chaim, Plasma in spark plasma sintering of ceramic particle compacts, *Scr. Mater.* 82 (2014) 57–60. <https://doi.org/10.1016/j.scriptamat.2014.03.023>.
- [176] E. Ionescu, B. Papendorf, H.-J. Kleebe, F. Poli, K. Müller, R. Riedel, Polymer-Derived Silicon Oxycarbide/Hafnia Ceramic Nanocomposites. Part I: Phase and Microstructure Evolution During the Ceramization Process, *J. Am. Ceram. Soc.* (2010). <https://doi.org/10.1111/j.1551-2916.2010.03765.x>.
- [177] E. Ionescu, G. Mera, R. Riedel, Polymer-Derived Ceramics (PDCs), in: I.M. Low, Y. Sakka, C.F. Hu (Eds.), *MAX Phases and Ultra-High Temperature Ceramics for Extreme Environments*, IGI Global, 2013, pp. 203–245.
- [178] E. Ionescu, B. Papendorf, H.-J. Kleebe, H. Breitzke, K. Nonnenmacher, G. Buntkowsky, R. Riedel, Phase separation of a hafnium alkoxide-modified polysilazane upon polymer-to-ceramic transformation—A case study, *J. Eur. Ceram. Soc.* 32 (2012) 1873–1881. <https://doi.org/10.1016/j.jeurceramsoc.2011.09.003>.
- [179] E. Ionescu, B. Papendorf, H.-J. Kleebe, R. Riedel, Polymer-Derived Silicon Oxycarbide/Hafnia Ceramic Nanocomposites. Part II: Stability Toward Decomposition and Microstructure Evolution at $T \gg 1000^\circ\text{C}$, *J. Am. Ceram. Soc.* (2010). <https://doi.org/10.1111/j.1551-2916.2009.03527.x>.

-
- [180] K. Nonnenmacher, H.-J. Kleebe, J. Rohrer, E. Ionescu, R. Riedel, Carbon Mobility in SiOC/HfO₂ Ceramic Nanocomposites, *J. Am. Ceram. Soc.* 96 (2013) 2058–2060. <https://doi.org/10.1111/jace.12440>.
- [181] H.-J. Kleebe, K. Nonnenmacher, E. Ionescu, R. Riedel, Decomposition-Coarsening Model of SiOC/HfO₂ Ceramic Nanocomposites Upon Isothermal Anneal at 1300°C, *J. Am. Ceram. Soc.* 95 (2012) 2290–2297. <https://doi.org/10.1111/j.1551-2916.2012.05227.x>.
- [182] W. Yi, X. Yongdong, W. Yiguang, C. Laifei, Z. Litong, Effects of TaC addition on the ablation resistance of C/SiC, *Mater. Lett.* 64 (2010) 2068–2071. <https://doi.org/10.1016/j.matlet.2010.04.051>.
- [183] Q. Wen, Z. Yu, R. Riedel, E. Ionescu, Single-source-precursor synthesis and high-temperature evolution of a boron-containing SiC/HfC ceramic nano/micro composite, *J. Eur. Ceram. Soc.* 41 (2021) 3002–3012. <https://doi.org/10.1016/j.jeurceramsoc.2020.05.031>.
- [184] K. Thorne, E. Liimatta, J.D. Mackenzie, Synthesis of SiC/TaC ceramics from tantalum alkoxide modified polycarbosilane, *J. Mater. Res.* 6 (1991) 2199–2207. <https://doi.org/10.1557/JMR.1991.2199>.
- [185] E. Hornbogen, B. Skrotzki, *Mikro- und Nanoskopie der Werkstoffe*, third. Aufl., Springer, Berlin, Heidelberg, 2009.
- [186] R. Telle (Ed.), *Keramik: Mit 132 Tabellen*, 7th ed., Springer, Berlin, Heidelberg, 2007.
- [187] H. Insley, V. Frechette, *Microscopy of Ceramics and Cements*, Academic Press, New York, 1955.
- [188] H. Freund, *Handbuch der Mikroskopie in der Technik: Mikroskopie der Silikate*, *Geol. fören. Stockh. förh.* 79 (1957) 816–817. <https://doi.org/10.1080/11035895709454880>.
- [189] E. Hornbogen, B. Skrotzki, *Werkstoffmikroskopie: Direkte Durchstrahlung mit Elektronen zur Analyse der Mikrostruktur*, second. überarbeitete und erweiterte Auflage, Springer, Berlin, Heidelberg, 1993.
- [190] R.W. Cahn, P. Haasen, E.J. Kramer (Eds.), *Materials science and technology: A comprehensive treatment*, VCH, Weinheim, 1992.
- [191] B.J. Inkson, Scanning electron microscopy (SEM) and transmission electron microscopy (TEM) for materials characterization, in: *Materials Characterization Using Nondestructive Evaluation (NDE) Methods*, Elsevier, 2016, pp. 17–43.
- [192] H.-J. Bargel, G. Schulze (Eds.), *Werkstoffkunde*, 12th ed., Springer Vieweg, Berlin, Heidelberg, 2018.
- [193] R. Fischer, E.-D. Franz, R. Telle, *Gefügeuntersuchungen an Spritzgusskeramiken mit der Methode der Durchlichtpolarisationsmikroskopie* (1992) 797–804.
- [194] G. Petzow, *Metallographisches, keramographisches, plastographisches Ätzen*, seventh. leicht korrigierte Auflage, Gebrüder Borntraeger, Stuttgart, 2015.
- [195] J. Goldstein, D.E. Newbury, J.R. Michael, N.W.M. Ritchie, J.H.J. Scott, D.C. Joy, *Scanning electron microscopy and X-ray microanalysis*, Fourth edition, Springer, New York, NY, U.S.A., 2018.
- [196] S.J.B. Reed, *Electron Microprobe Analysis and Scanning Electron Microscopy in Geology*, Cambridge University Press, 2005.
- [197] D.B. Williams, *Practical analytical electron microscopy in materials science*, (No Title) (1987).
- [198] D.B. Williams, C.B. Carter, *Transmission electron microscopy: A textbook for materials science*, Springer; Plenum Press anfangs, New York, New York, NY, 1996.
- [199] R.F. Egerton, *Physical Principles of Electron Microscopy*, Springer International Publishing, Cham, 2016.

- [200] P. Echlin, Handbook of sample preparation for scanning electron microscopy and x-ray microanalysis, Springer, New York, NY, 2009.
- [201] S. Deshpande, A. Kulkarni, S. Sampath, H. Herman, Application of image analysis for characterization of porosity in thermal spray coatings and correlation with small angle neutron scattering, *Surf. Coat. Technol.* 187 (2004) 6–16. <https://doi.org/10.1016/j.surfcoat.2004.01.032>.
- [202] M. Lau, F. Morgenstern, R. Hübscher, A. Knospe, M. Herrmann, M. Döring, W. Lippmann, Image Segmentation Variants for Semi-Automated Quantitative Microstructural Analysis with ImageJ, *Prakt. Metallogr.* 57 (2020) 752–775. <https://doi.org/10.3139/147.110626>.
- [203] K.L. Scrivener, The Use Of Backscattered Electron Microscopy And Image Analysis To Study The Porosity Of Cement Paste, *MRS Proc.* 137 (1988). <https://doi.org/10.1557/PROC-137-129>.
- [204] R. Telle, V. Carle, F. Predel, U. Schäfer, U. Täffner, G. Petzow, Keramographie von Hochleistungskeramiken Teil IX: Poren und Ausbrüche / Ceramography of High Performance Ceramics Part IX: Pores and Chips, *Pract. Metallogr.* 32 (1995) 440–466. <https://doi.org/10.1515/pm-1995-320902>.
- [205] C.A. Schneider, W.S. Rasband, K.W. Eliceiri, NIH Image to ImageJ: 25 years of image analysis, *Nat. Methods* 9 (2012) 671–675. <https://doi.org/10.1038/nmeth.2089>.
- [206] J. Melngailis, Focused ion beam technology and applications, *J. Vac. Sci.* 5 (1987) 469. <https://doi.org/10.1116/1.583937>.
- [207] R.M. Langford, Focused ion beams techniques for nanomaterials characterization, *MRT* 69 (2006) 538–549. <https://doi.org/10.1002/jemt.20324>.
- [208] S. Reyntjens, R. Puers, A review of focused ion beam applications in microsystem technology, *J. Micromech. Microeng.* 11 (2001) 287–300. <https://doi.org/10.1088/0960-1317/11/4/301>.
- [209] L.-H. Lee, C.-H. Yu, Y.-T. Hong, C.-Y. Wen, A Plan-view TEM Specimen Preparation Method Using Focused Ion Beam, *Microsc. Microanal.* 23 (2017) 266–267. <https://doi.org/10.1017/S143192761700201X>.
- [210] C.R. Perrey, C.B. Carter, J.R. Michael, P.G. Kotula, E.A. Stach, V.R. Radmilovic, Using the FIB to characterize nanoparticle materials, *J. Microsc.* 214 (2004) 222–236. <https://doi.org/10.1111/j.0022-2720.2004.01325.x>.
- [211] R. Haswell, D.W. McComb, W. Smith, Preparation of site-specific cross-sections of heterogeneous catalysts prepared by focused ion beam milling, *J. Microsc.* 211 (2003) 161–166. <https://doi.org/10.1046/j.1365-2818.2003.01216.x>.
- [212] B.I. Prenitzer, L.A. Giannuzzi, K. Newman, S.R. Brown, R.B. Irwin, F.A. Stevie, T.L. Shofner, Transmission electron microscope specimen preparation of Zn powders using the focused ion beam lift-out technique, *Metall. Mater. Trans. A. Phys.* 29 (1998) 2399–2406. <https://doi.org/10.1007/s11661-998-0116-z>.
- [213] A. Ernst, M. Wei, M. Aindow, FIB Milling strategies for TEM Sample Preparation of Spheroidal Powder Particles, *Microsc. Microanal.* 24 (2018) 826–827. <https://doi.org/10.1017/S1431927618004622>.
- [214] R. Theisen, Quantitative Electron Microprobe Analysis, Springer Berlin Heidelberg, Berlin, Heidelberg, s.l., 1965.
- [215] B. Fultz, J. Howe, Transmission Electron Microscopy and Diffractometry of Materials, third, thirdrd ed. twentieth0eighth, Springer Berlin Heidelberg, Berlin, Heidelberg, 2007.
- [216] J. Thomas, T. Gemming, Analytische Transmissionselektronenmikroskopie: Eine Einführung für den Praktiker, Springer, Wien, Heidelberg, 2013.
- [217] O. Scherzer, The Theoretical Resolution Limit of the Electron Microscope, *J. Appl. Phys.* 20 (1949) 20–29. <https://doi.org/10.1063/1.1698233>.

- [218] C. Kisielowski, B. Freitag, M. Bischoff, H. van Lin, S. Lazar, G. Knippels, P. Tiemeijer, M. van der Stam, S. von Harrach, M. Stekelenburg, M. Haider, S. Uhlemann, H. Müller, P. Hartel, B. Kabius, D. Miller, I. Petrov, E.A. Olson, T. Donchev, E.A. Kenik, A.R. Lupini, J. Bentley, S.J. Pennycook, I.M. Anderson, A.M. Minor, A.K. Schmid, T. Duden, V. Radmilovic, Q.M. Ramasse, M. Watanabe, R. Erni, E.A. Stach, P. Denes, U. Dahmen, Detection of single atoms and buried defects in three dimensions by aberration-corrected electron microscope with 0.5-Å information limit, *Microsc Microanal* 14 (2008) 469–477. <https://doi.org/10.1017/S1431927608080902>.
- [219] M. Lentzen, Contrast transfer and resolution limits for sub-angstrom high-resolution transmission electron microscopy, *Microsc Microanal* 14 (2008) 16–26. <https://doi.org/10.1017/S1431927608080045>.
- [220] L. Reimer, *Transmission Electron Microscopy: Physics of Image Formation and Microanalysis*, Springer Berlin / Heidelberg, Berlin, Heidelberg, 1984.
- [221] M. Czank, *Beugungsmethoden, Spektroskopie, Physiko-chemische Untersuchungsmethoden: Mit 15 Tabellen*, Schweizerbart, Stuttgart, 2001.
- [222] S. Gates-Rector, T. Blanton, The Powder Diffraction File: a quality materials characterization database, *Powder Diffr.* 34 (2019) 352–360. <https://doi.org/10.1017/S0885715619000812>.
- [223] W. Kleber, *Einführung in die Kristallographie*, seventeenth., stark bearb. Aufl., Verl. Technik, Berlin, 1990.
- [224] A.-K. Fetzer, M. Trapp, S. Lauterbach, H.-J. Kleebe, Introduction to Transmission Electron Microscopy; The Basics, in: *Encyclopedia of Materials: Technical Ceramics and Glasses*, Elsevier, 2021, pp. 578–599.
- [225] E. Hornbogen, G. Eggeler, E. Werner, *Werkstoffe: Aufbau und Eigenschaften von Keramik-, Metall-, Polymer- und Verbundwerkstoffen*, ninth. Aufl., Springer, Berlin, Heidelberg, 2008.
- [226] Y.I. Golovin, Nanoindentation and mechanical properties of solids in submicrovolumes, thin near-surface layers, and films: A Review, *Phys. Solid State* 50 (2008) 2205–2236. <https://doi.org/10.1134/S1063783408120019>.
- [227] F.-J. Ulm, M. Vandamme, H.M. Jennings, J. Vanzo, M. Bentivegna, K.J. Krakowiak, G. Constantinides, C.P. Bobko, K.J. van Vliet, Does microstructure matter for statistical nanoindentation techniques?, *Cem. Concr. Compos.* 32 (2010) 92–99. <https://doi.org/10.1016/j.cemconcomp.2009.08.007>.
- [228] N.X. Randall, M. Vandamme, F.-J. Ulm, Nanoindentation analysis as a two-dimensional tool for mapping the mechanical properties of complex surfaces, *J. Mater. Res.* 24 (2009) 679–690. <https://doi.org/10.1557/JMR.2009.0149>.
- [229] E.D. Hintsala, U. Hangen, D.D. Stauffer, High-Throughput Nanoindentation for Statistical and Spatial Property Determination, *JOM* 70 (2018) 494–503. <https://doi.org/10.1007/s11837-018-2752-0>.
- [230] A.C. Fischer-Cripps, Critical review of analysis and interpretation of nanoindentation test data, *Surf. Coat. Technol.* 200 (2006) 4153–4165. <https://doi.org/10.1016/j.surfcoat.2005.03.018>.
- [231] G. Constantinides, K.S. Ravi Chandran, F.-J. Ulm, K.J. van Vliet, Grid indentation analysis of composite microstructure and mechanics: Principles and validation, *Mater. Sci. Eng.* 430 (2006) 189–202. <https://doi.org/10.1016/j.msea.2006.05.125>.
- [232] A.C. Fischer-Cripps, *Nanoindentation*, Springer Science+Business Media LLC, New York, NY, 2011.
- [233] I.G. Gogotšī, V. Domnich (Eds.), *High pressure surface science and engineering*, [CRC Press], Boca Raton, 2019.

- [234] W.C. Oliver, G.M. Pharr, Measurement of hardness and elastic modulus by instrumented indentation: Advances in understanding and refinements to methodology, *J. Mater. Res.* 19 (2004) 3–20. <https://doi.org/10.1557/jmr.2004.19.1.3>.
- [235] J.L. Hay, G.M. Pharr, *ASM handbook: Materials Testing and Evaluation*, 2000.
- [236] S. Guicciardi, A. Balbo, D. Sciti, C. Melandri, G. Pezzotti, Nanoindentation characterization of SiC-based ceramics, *J. Eur. Ceram. Soc.* 27 (2007) 1399–1404. <https://doi.org/10.1016/j.jeurceramsoc.2006.05.057>.
- [237] A.M. Borys, An Illustrated Guide to Schlenk Line Techniques, *Organometallics* 42 (2023) 182–196. <https://doi.org/10.1021/acs.organomet.2c00535>.
- [238] O. Cedillos-Barraza, S. Grasso, N.A. Nasiri, D.D. Jayaseelan, M.J. Reece, W.E. Lee, Sintering behaviour, solid solution formation and characterisation of TaC, HfC and TaC–HfC fabricated by spark plasma sintering, *J. Eur. Ceram. Soc.* 36 (2016) 1539–1548. <https://doi.org/10.1016/j.jeurceramsoc.2016.02.009>.
- [239] Y.D. Blum, H.-J. Kleebe, Chemical reactivities of hafnium and its derived boride, carbide and nitride compounds at relatively mild temperature, *J. Mater. Sci.* 39 (2004) 6023–6042. <https://doi.org/10.1023/B:JMSSC.0000041699.31019.03>.
- [240] H. Wada, M.-J. Wang, T.-Y. Tien, Stability of Phases in the Si-C-N-O System, *J. Am. Ceram. Soc.* 71 (1988) 837–840. <https://doi.org/10.1111/j.1151-2916.1988.tb07532.x>.
- [241] H.D. Batha, E.D. Whitney, Kinetics and Mechanism of the Thermal Decomposition of Si₃N₄, *J. Am. Ceram. Soc.* 56 (1973) 365–369. <https://doi.org/10.1111/j.1151-2916.1973.tb12687.x>.
- [242] M. Hnatko, D. Galusek, P. Šajgalík, Low-cost preparation of Si₃N₄–SiC micro/nano composites by in-situ carbothermal reduction of silica in silicon nitride matrix, *J. Eur. Ceram. Soc.* 24 (2004) 189–195. [https://doi.org/10.1016/S0955-2219\(03\)00604-6](https://doi.org/10.1016/S0955-2219(03)00604-6).
- [243] J. Suri, L.L. Shaw, M.F. Zawrah, Tailoring the Relative Si₃N₄ and SiC Contents in Si₃N₄/SiC Nanopowders through Carbothermic Reduction and Nitridation of Silica Fume, *Int. J. Appl. Ceram. Technol.* 9 (2012) 291–303. <https://doi.org/10.1111/j.1744-7402.2011.02710.x>.
- [244] C. Vakifahmetoglu, E. Pippel, J. Woltersdorf, P. Colombo, Growth of One-Dimensional Nanostructures in Porous Polymer-Derived Ceramics by Catalyst-Assisted Pyrolysis. Part I: Iron Catalyst, *J. Am. Ceram. Soc.* 93 (2010) 959–968. <https://doi.org/10.1111/j.1551-2916.2009.03448.x>.
- [245] G. Gregori, H.-J. Kleebe, D.W. Readey, G.D. Soraru, Energy-Filtered TEM Study of Ostwald Ripening of Si Nanocrystals in a SiOC Glass, *J. Am. Ceram. Soc.* 89 (2006) 1699–1703. <https://doi.org/10.1111/j.1551-2916.2006.00971.x>.
- [246] H.-J. Kleebe, D. Suttor, H. Müller, G. Ziegler, Decomposition-Crystallization of Polymer-Derived Si-C-N Ceramics, *J. Am. Ceram. Soc.* 81 (1998) 2971–2977. <https://doi.org/10.1111/j.1151-2916.1998.tb02722.x>.
- [247] H. Schmidt, W. Gruber, G. Borchardt, P. Gerstel, A. Müller, N. Bunjes, Coarsening of nano-crystalline SiC in amorphous Si–B–C–N, *J. Eur. Ceram. Soc.* 25 (2005) 227–231. <https://doi.org/10.1016/j.jeurceramsoc.2004.08.004>.
- [248] N.-C. Petry, Oxidationsverhalten von polymerabgeleiteten keramischen Nanokompositen: in preparation, Dissertation 2023.
- [249] B.N. Taylor, C.E. Kuyatt, Guidelines for evaluating and expressing the uncertainty of NIST measurement results, National Institute of Standards and Technology, Gaithersburg, MD, 2018.
- [250] S. Grasso, E.-Y. Kim, T. Saunders, M. Yu, A. Tudball, S.-H. Choi, M. Reece, Ultra-Rapid Crystal Growth of Textured SiC Using Flash Spark Plasma Sintering Route, *Cryst. Growth. Des.* 16 (2016) 2317–2321. <https://doi.org/10.1021/acs.cgd.6b00099>.

- [251] P. Raj, G.S. Gupta, V. Rudolph, Silicon carbide formation by carbothermal reduction in the Acheson process: A hot model study, *Thermochimi.Acta* 687 (2020) 178577. <https://doi.org/10.1016/j.tca.2020.178577>.
- [252] A. Saha, R. Raj, Crystallization Maps for SiCO Amorphous Ceramics, *J. Am. Ceram. Soc.* 90 (2007) 578–583. <https://doi.org/10.1111/j.1551-2916.2006.01423.x>.
- [253] J.-X. Liu, X. Huang, G.-J. Zhang, Pressureless Sintering of Hafnium Carbide-Silicon Carbide Ceramics, *J. Am. Ceram. Soc.* 96 (2013) 1751–1756. <https://doi.org/10.1111/jace.12339>.
- [254] B.-K. Yoon, E.-Y. Chin, S.-J.L. Kang, Dedensification During Sintering of BaTiO₃ Caused by the Decomposition of Residual BaCO₃, *J. Am. Ceram. Soc.* 91 (2008) 4121–4124. <https://doi.org/10.1111/j.1551-2916.2008.02772.x>.
- [255] A. Maître, A.V. Put, J.P. Laval, S. Valette, G. Trolliard, Role of boron on the Spark Plasma Sintering of an α -SiC powder, *J. Eur. Ceram. Soc.* 28 (2008) 1881–1890. <https://doi.org/10.1016/j.jeurceramsoc.2008.01.002>.
- [256] M. Omori, H. Takei, Preparation of pressureless-sintered SiC-Y₂O₃-Al₂O₃, *J. Mater. Sci.* 23 (1988) 3744–3749. <https://doi.org/10.1007/BF00540522>.
- [257] T. Sakai, H. Watanabe, T. Aikawa, Effects of carbon on phase transformation of β -SiC with Al₂O₃, *J. Mater. Sci. Lett.* 6 (1987) 865–866. <https://doi.org/10.1007/BF01729040>.
- [258] L. Stobierski, A. Gubernat, Sintering of silicon carbide II. Effect of boron, *Ceram. Int.* 29 (2003) 355–361. [https://doi.org/10.1016/S0272-8842\(02\)00144-X](https://doi.org/10.1016/S0272-8842(02)00144-X).
- [259] L. Stobierski, A. Gubernat, Sintering of silicon carbide I. Effect of carbon, *Ceram. Int.* 29 (2003) 287–292. [https://doi.org/10.1016/S0272-8842\(02\)00117-7](https://doi.org/10.1016/S0272-8842(02)00117-7).
- [260] A.V. Rau, K. Knott, K. Lu, Porous SiOC/SiC ceramics via an active-filler-catalyzed polymer-derived method, *Mater. Chem. Front.* 5 (2021) 6530–6545. <https://doi.org/10.1039/d1qm00705j>.
- [261] D. Pandey, P. Krishna, The origin of polytype structures, *Prog. Cryst. Growth Charact. Mater.* 7 (1983) 213–258. [https://doi.org/10.1016/0146-3535\(83\)90033-3](https://doi.org/10.1016/0146-3535(83)90033-3).
- [262] U. Kaiser, A. Chuvilin, W. Richter, On the peculiarities of bright/dark contrast in HRTEM images of SiC polytypes, *Ultramicroscopy* 76 (1999) 21–37. [https://doi.org/10.1016/S0304-3991\(98\)00069-2](https://doi.org/10.1016/S0304-3991(98)00069-2).
- [263] Verma, Ajit Ram, Krishna, P., Polymorphism and polytypism in crystals, (No Title).
- [264] R. Dong, W. Yang, P. Wu, M. Hussain, Z. Xiu, G. Wu, P. Wang, Microstructure characterization of SiC nanowires as reinforcements in composites, *Mater. Charact.* 103 (2015) 37–41. <https://doi.org/10.1016/j.matchar.2015.03.013>.
- [265] F. Li, G. Wen, A novel method for massive fabrication of β -SiC nanowires, *J. Mater. Sci.* 42 (2007) 4125–4130. <https://doi.org/10.1007/s10853-007-1682-y>.
- [266] Y. Ryu, Y. Tak, K. Yong, Direct growth of core-shell SiC-SiO₍₂₎ nanowires and field emission characteristics, *Nanotechnology* 16 (2005) S370-4. <https://doi.org/10.1088/0957-4484/16/7/009>.
- [267] K. Vanmeensel, A. Laptev, J. Hennicke, J. Vleugels, O. VANDERBIEST, Modelling of the temperature distribution during field assisted sintering, *Acta Mater.* 53 (2005) 4379–4388. <https://doi.org/10.1016/j.actamat.2005.05.042>.
- [268] A. Nino, T. Hirabara, S. Sugiyama, H. Taimatsu, Preparation and characterization of tantalum carbide (TaC) ceramics, *IJRMHM* 52 (2015) 203–208. <https://doi.org/10.1016/j.ijrmhm.2015.06.015>.
- [269] L.G. Radosevich, W.S. Williams, Thermal Conductivity of Transition Metal Carbides, *J. Am. Ceram. Soc.* 53 (1970) 30–33. <https://doi.org/10.1111/j.1151-2916.1970.tb11994.x>.

- [270] S.K. Sharma, M. Fides, P. Hvizdoš, M.J. Reece, S. Grasso, Flash Spark Plasma Sintering of SiC: Impact of Additives, *Silicon* 14 (2022) 7377–7382. <https://doi.org/10.1007/s12633-021-01407-7>.
- [271] T.B. Holland, J.F. Löffler, Z.A. Munir, Crystallization of metallic glasses under the influence of high density dc currents, *J. Appl. Phys.* 95 (2004) 2896–2899. <https://doi.org/10.1063/1.1642280>.
- [272] R. Marder, R. Chaim, C. Estournès, Grain growth stagnation in fully dense nanocrystalline Y2O3 by spark plasma sintering, *Mater. Sci. Eng. A.* 527 (2010) 1577–1585. <https://doi.org/10.1016/j.msea.2009.11.009>.
- [273] S.G. Huang, K. Vanmeensel, O. Malek, O. van der Biest, J. Vleugels, Microstructure and mechanical properties of pulsed electric current sintered B4C–TiB2 composites, *Mater. Sci. Eng. A.* 528 (2011) 1302–1309. <https://doi.org/10.1016/j.msea.2010.10.022>.
- [274] S.L. Dole, S. Prochazka, R.H. Doremus, Microstructural Coarsening During Sintering of Boron Carbide, *J. Am. Ceram. Soc.* 72 (1989) 958–966. <https://doi.org/10.1111/j.1151-2916.1989.tb06252.x>.
- [275] J. Rösler, H. Harders, M. Bäker, *Mechanisches Verhalten der Werkstoffe*, fifth., aktualisierte und erweiterte Auflage, Springer Vieweg, Wiesbaden, 2016.
- [276] D. Sciti, S. Guicciardi, M. Nygren, Densification and Mechanical Behavior of HfC and HfB₂ Fabricated by Spark Plasma Sintering, *J. Am. Ceram. Soc.* 91 (2008) 1433–1440. <https://doi.org/10.1111/j.1551-2916.2007.02248.x>.
- [277] Q. Wen, Z. Yu, X. Liu, S. Bruns, X. Yin, M. Eriksson, Z.J. Shen, R. Riedel, Mechanical properties and electromagnetic shielding performance of single-source-precursor synthesized dense monolithic SiC/HfC x N 1–x /C ceramic nanocomposites, *J. Mater. Chem. C* 7 (2019) 10683–10693. <https://doi.org/10.1039/C9TC02369K>.
- [278] S. Hayun, V. Paris, R. Mitrani, S. Kalabukhov, M.P. Dariel, E. Zaretsky, N. Frage, Microstructure and mechanical properties of silicon carbide processed by Spark Plasma Sintering (SPS), *Ceram. Int.* 38 (2012) 6335–6340. <https://doi.org/10.1016/j.ceramint.2012.05.003>.
- [279] A. Datye, L. Li, W. Zhang, Y. Wei, Y. Gao, G.M. Pharr, 2016. Extraction of Anisotropic Mechanical Properties From Nanoindentation of SiC-6H Single Crystals. *J. Appl. Mech.* 83, 091003. <https://doi.org/10.1115/1.4033790>.
- [280] A. Nisar, C. Zhang, B. Boesl, A. Agarwal, Synthesis of Hf₆Ta₂O₁₇ superstructure via spark plasma sintering for improved oxidation resistance of multi-component ultra-high temperature ceramics, *Ceram. Int.* 49 (2023) 783–791. <https://doi.org/10.1016/j.ceramint.2022.09.050>.
- [281] M. Li, Q. Xu, L. Wang, Preparation and Thermal Conductivity of Hf₆Ta₂O₁₇ Ceramic, *KEM* 434-435 (2010) 459–461. <https://doi.org/10.4028/www.scientific.net/KEM.434-435.459>.
- [282] S.J. McCormack, W.M. Kriven, Crystal structure solution for the A₆B₂O₁₇ (A = Zr, Hf; B = Nb, Ta) superstructure, *Acta Crystallogr. B: Struct. Sci. Cryst. Eng. Mater* 75 (2019) 227–234. <https://doi.org/10.1107/S2052520619001963>.
- [283] J. Bernauer, N.-C. Petry, N. Thor, S. Kredel, D. Teppala Teja, M. Lepple, A. Pundt, R. Riedel, E. Ionescu, Exceptional Hardness and thermal properties of SiC/(Hf,Ta)C(N)/C composites unlocked through boron doping: in preparation.
- [284] J.S. Burgess, C.K. Acharya, J. Lizarazo, N. Yancey, B. Flowers, G. Kwon, T. Klein, M. Weaver, A.M. Lane, C. Heath Turner, S. Street, Boron-doped carbon powders formed at 1000°C and one atmosphere, *Carbon* 46 (2008) 1711–1717. <https://doi.org/10.1016/j.carbon.2008.07.022>.
- [285] Q. Wen, Z. Yu, R. Riedel, E. Ionescu, Significant improvement of high-temperature oxidation resistance of HfC/SiC ceramic nanocomposites with the incorporation of a small

-
- amount of boron, *Journal of the European Ceramic Society* 40 (2020) 3499–3508. <https://doi.org/10.1016/j.jeurceramsoc.2020.03.067>.
- [286] Z.Z. Fang, H. Wang, Densification and grain growth during sintering of nanosized particles, *International Materials Reviews* 53 (2008) 326–352. <https://doi.org/10.1179/174328008X353538>.
- [287] L. Chen, M. Hu, F. Wu, P. Song, J. Feng, Thermo-mechanical properties of fluorite Yb₃TaO₇ and Yb₃NbO₇ ceramics with glass-like thermal conductivity, *Journal of Alloys and Compounds* 788 (2019) 1231–1239. <https://doi.org/10.1016/j.jallcom.2019.02.317>.
- [288] X. Cao, R. Vassen, W. Fischer, F. Tietz, W. Jungen, D. Stöver, Lanthanum–Cerium Oxide as a Thermal Barrier-Coating Material for High-Temperature Applications, *Advanced Materials* 15 (2003) 1438–1442. <https://doi.org/10.1002/adma.200304132>.
- [289] W.D. Verbeek (BAYER AG) US3853567 (A), 1973.
- [290] J. Lipowitz, J. Rabe, NMR Characterization of Polymethyldisilylazine Polymer--a Precursor to Si--C--N--O Ceramics, 1987.
- [291] D. Seyferth, H. Plenio, Borasilazane Polymeric Precursors for Borosilicon Nitride, *J. Am. Ceram. Soc.* 73 (1990) 2131–2133. <https://doi.org/10.1111/j.1151-2916.1990.tb05286.x>.
- [292] Y. Li, W. Han, H. Li, J. Zhao, T. Zhao, Synthesis of nano-crystalline ZrB₂/ZrC/SiC ceramics by liquid precursors, *Mater. Lett.* 68 (2012) 101–103. <https://doi.org/10.1016/j.matlet.2011.10.060>.
- [293] D. Pizon, L. Charpentier, R. Lucas, S. Foucaud, A. Maître, M. Balat-Pichelin, Oxidation behavior of spark plasma sintered ZrC–SiC composites obtained from the polymer-derived ceramics route, *Ceram. Int.* 40 (2014) 5025–5031. <https://doi.org/10.1016/j.ceramint.2013.08.105>.
- [294] S. Kaur, R. Riedel, E. Ionescu, Pressureless fabrication of dense monolithic SiC ceramics from a polycarbosilane, *J. Eur. Ceram. Soc.* 34 (2014) 3571–3578. <https://doi.org/10.1016/j.jeurceramsoc.2014.05.002>.
- [295] C. Zhou, A. Ott, R. Ishikawa, Y. Ikuhara, R. Riedel, E. Ionescu, Single-source-precursor synthesis and high-temperature evolution of novel mesoporous SiVN(O)-based ceramic nanocomposites, *J. Eur. Ceram. Soc.* 40 (2020) 6280–6287. <https://doi.org/10.1016/j.jeurceramsoc.2019.11.021>.

Appendix

Table A 1 A selection of polymeric precursors modified with organometallic complexes used for the preparation of PDCs, ascending by publishing year. The table shows selected compositions and is not complete.

Precursors with modified organometallic complexes	Final ceramics	Year of Publication	Ref.
Polycarbosilazane	Si/C/N fibres	1974	[289]
Polycarbosilazane	Si ₃ N ₄ -SiC fibres	1975	[132]
Polysilazane	Si/C/N fibres	1987	[290]
Polydimethylsilane + Polyborodiphenylsiloxane + Titanium-tetraisopropoxide	SiTiCO fibres	1988	[139]
Polyborosilazane	Si/B/C/N	1990	[291]
Polycarbosilane + aluminium alkoxide	SiAlON	1991	[137]
Polycarbosilane + zirconium alkoxide	SiZrCO	1991	[140]
Polyborosilazane	Si/B/C/N bulk	1996	[133]
Poly(ureamethylvi-nyl)silazane + zirconia-alkoxide	SiCN/ZrO ₂ fibres	2004	[141]
aluminum-modified poly(vinylsilazanes)	SiAlCN	2004	[135]
Perhydropolysilazane + cage-type poly(ethyliminoalane)	SiAlNC	2006	[136]
Polysilsesquioxane + hafnium tetra(n-butoxide)	SiOC/HfO ₂	2010	[176]
Polyzirconoxanesal + boric acid + poly(methylsilylene)ethynylene	ZrB ₂ /ZrC/SiC	2012	[292]
Polycarbomethylsilane + ZrC powder	ZrC-SiC	2014	[293]
Polysilane	SiC monoliths	2014	[294]
Polysilazane + tetrakis(diethylamido)hafnium + borane dimethyl sulfide complex	SiHfBCN UHTC-NC	2014	[66]
allylhydrido polycarbosilane + tetrakis(dimethylamido) hafnium(IV)	SiHfC _x N _{1-x} UHTC-NC	2014	[64]
Perhydropolysilazane + tetrakis(dimethylamido) hafnium(IV)	SiHfN	2015	[61]
Polycarbosilane + polytantalozone	TaC-SiC nanomaterials	2016	[58]
Perhydropolysilazane + iron(II) acetylacetonate	C/SiFeN(O)	2017	[143]
Polysilane + tetrakis(diethylamino)hafnium(IV) + pentakis(dimethylamino) tantalum(V)	SiHfTaCN	2018	[41]
Perhydropolysilazane + vanadium(IV)oxide acetylacetonate	SiVNO	2020	[295]
Perhydropolysilazane + tetrakis(diethylamino)hafnium(IV) + pentakis(dimethylamino) tantalum(V)	Si(Hf,Ta)(C)N	2023	[84]
Polycarbosilane + tetrakis(diethylamino)hafnium(IV) + pentakis(dimethylamino) tantalum(V) + borane dimethyl sulfide complex	Si(Hf,Ta)BC	in preparation	[283]

```

terminal Help spectrumanalysisneu.py - Visual Studio Code
spectrumanalysisneu.py X
C:\Users\Nathalie Thor\Desktop> spectrumanalysisneu.py > ...
1 # Import necessary libraries
2 import matplotlib.pyplot as plt
3 import os
4 import numpy as np
5 from matplotlib import rc, rcParams
6 from matplotlib.font_manager import FontProperties
7 #rc('font', **{'family': 'serif', 'serif': ['Times']})
8 #rc('font', **{'family': 'Arial', 'style': 'normal'})
9 #rc('text', usetex = True)
10
11 #font = {'size' : 16}
12 #matplotlib.rc('font', **font)
13
14
15 #params = {'mathtext.default': 'regular'}
16 #plt.rcParams.update(params)
17
18 # Set the file path
19 # copy the file path and add one \ for each directory
20 path = "C:\Users\Nathalie Thor\HESSENBOX-DA\Promotion\GRK\samples\ceramics\Si(HfTax)(BC)N\SiHfTa\ITEMS
21
22 file_name = "soil Spectrum 4.txt"
23 FILE_PATH = os.path.join(path, file_name)
24
25 # Create lists for the data
26 data_list = []
27 x_list = []
28 y_list = []
29
30
31 # Read the file and split the x and y values
32 with open(FILE_PATH, "r") as file:
33     for line in file:
34         splitted = line.strip().rstrip().split('\n')
35         if splitted[0] != '':
36             if not '#' in splitted[0]:
37                 data_list.append(''.join(splitted).split(','))
38
39 # Convert the strings into float data
40 x_list = [float(i[0]) for i in data_list]
41 y_list = [float(i[1]) for i in data_list]
42
43 # Plot the x and y values
44 #rc('font', **{'family': 'serif', 'serif': ['Computer Modern']})
45 #rc('text', usetex=True)
46 fig, ax = plt.subplots()
47 plt.plot(x_list, y_list, color = 'black', linewidth = 1.5)
48 plt.xlim((0,1,3))
49 plt.ylim((0,4050))
50
51
52 #plt.title("Si(Hf0.2Ta0.8)N-1000°C", fontsize=15)
53 plt.title("", fontsize=20, fontname="Times New Roman")
54
55 plt.grid(alpha=0.3)
56 plt.xlabel('E in keV', fontsize=20, fontname="Times New Roman")
57 plt.ylabel('counts in a.u.', fontsize=20, fontname="Times New Roman")
58 lw=0.3
59 ax.spines["top"].set_linewidth(lw)
60 ax.spines["bottom"].set_linewidth(lw)
61 ax.spines["left"].set_linewidth(lw)
62 ax.spines["right"].set_linewidth(lw)
63 ax.tick_params(length=1)
64 ax.tick_params(axis='both', which='major', labelsize=13)
65 plt.xticks(fontname="Times New Roman")
66 plt.yticks(fontname="Times New Roman")
67 plt.show()

```

terminal Help spectrumanalysisneu.py - Visual Studio Code

PROBLEMS OUTPUT DEBUG CONSOLE TERMINAL

PS C:\Users\Nathalie Thor>

Ln 15, Col 42 Spaces: 4 UTF-8 CRLF

Figure A 1 Python script to plot the EDS spectra.

Table A 2 showing the exact calculations of the Hf:Ta ratios within the amorphous matrix phase of the Si(Hf_{0.2}Ta_{0.8})(C)N PDCs described in chapter 6.2.

SiHf _{0.2} Ta _{0.8} (C)N-1000	matrix phase					
measurement date	spectrum no.	Hf (in at-%)	Ta in (at-%)	sum	Hf ratio	Ta ratio
07.03.2021	1	0.37	1.58	1.95	0.19	0.81
07.03.2021	2	0.42	1.71	2.13	0.20	0.80
07.03.2021	11	0.74	3	3.74	0.20	0.80
07.03.2021	12	0.35	1.49	1.84	0.19	0.81
				mean	0.19	0.81
				σ	0.00	0.00
				2σ	0.01	0.01

Table A 3 showing the exact calculations of the Hf:Ta ratios within the crystalline precipitates of the Si(Hf_{0.2}Ta_{0.8})(C)N PDCs described in chapter 6.2.

SiHf _{0.2} Ta _{0.8} (C)N-1000	precipitates					
measurement date	spectrum no.	Hf (in at-%)	Ta in (at-%)	sum	Hf ratio	Ta ratio
07.03.2021	7	8.52	36.15	44.67	0.19	0.81
07.03.2021	8	5.71	28.34	34.05	0.17	0.83
07.03.2021	5	13.99	57.89	71.88	0.19	0.81
07.03.2021	16	18.74	69.07	87.81	0.21	0.79
				mean	0.19	0.81
				σ	0.02	0.02
				2σ	0.03	0.03

Table A 4 showing the exact calculations of the Hf:Ta ratios within the TMC of the Si(Hf_{0.7}Ta_{0.3})(C)N PDCs described in chapter 6.3.

SiHf _{0.7} Ta _{0.3} (C)N-1600	TMC					
measurement date	spectrum no.	Hf (in at-%)	Ta in (at-%)	sum	Hf ratio	Ta ratio
21.05.2021	2	12.48	3.63	16.11	0.77	0.23
19.08.2021	3	1.9	0.99	2.89	0.66	0.34
19.08.2021	4	1.21	0.71	1.92	0.63	0.37
08.04.2021	1	68.22	24.81	93.03	0.73	0.27
08.04.2021	5	72.02	16.3	88.32	0.82	0.18
				mean	0.72	0.28
				σ	0.07	0.07
				2σ	0.14	0.14

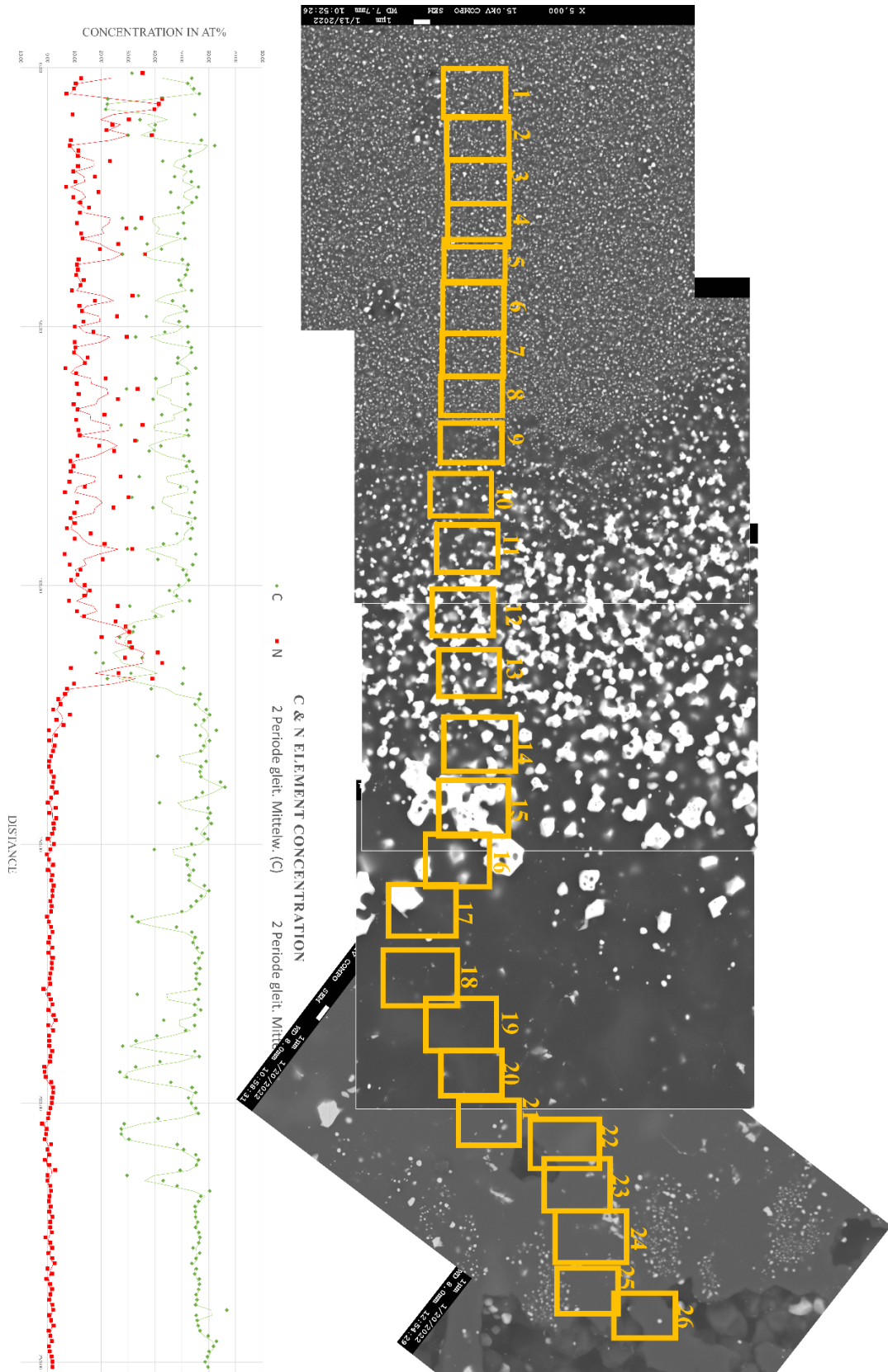


Figure A2 Element concentration profiles of Nitrogen (red) and Carbon (green) for 251 individual EDS measurements. Individual EDS measurements were taken in each of the small yellow boxes. In total, 26 frames and 251 single EDS measurements were measured and plotted.

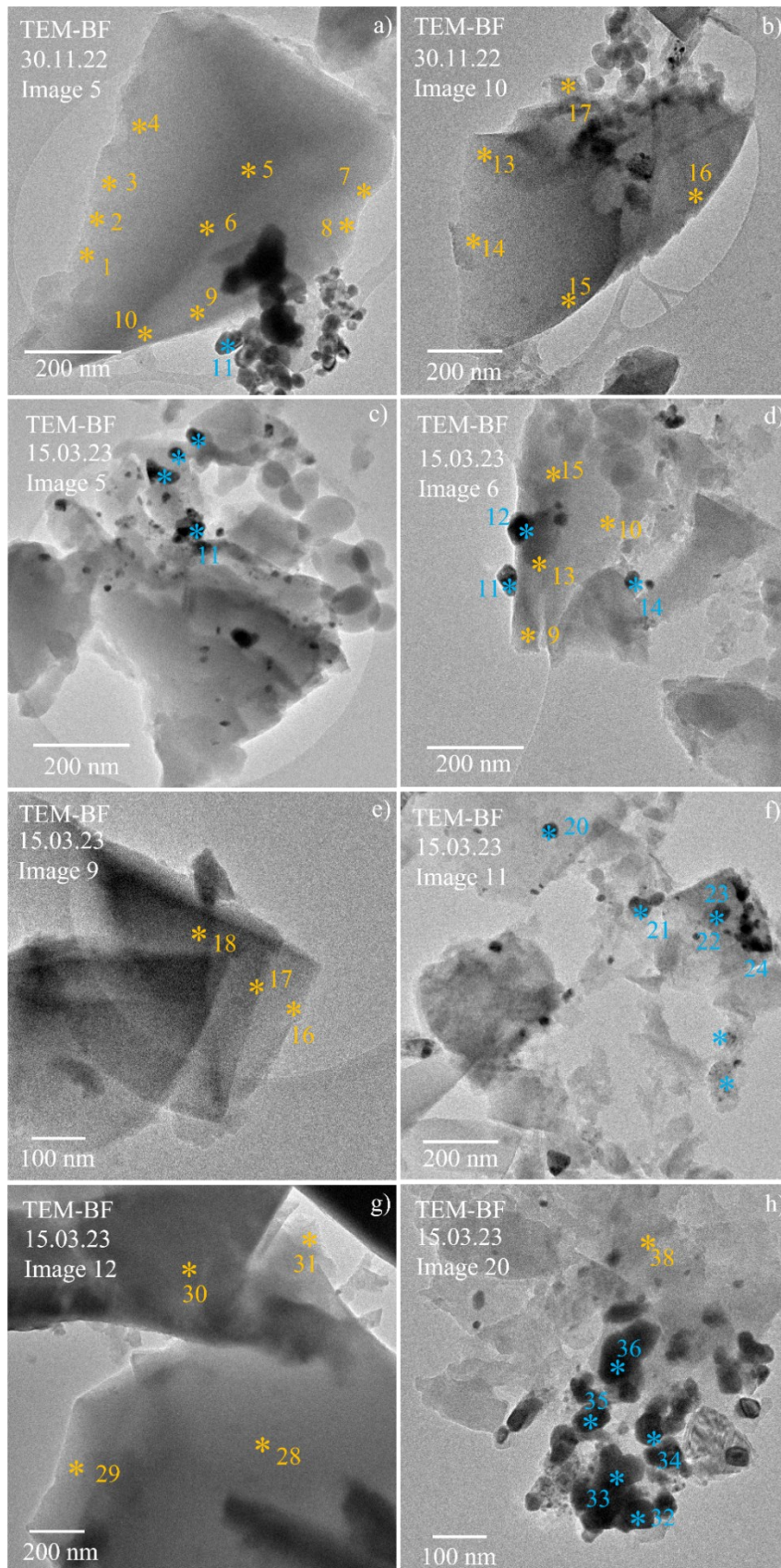


Figure A3 TEM-BF images of the exact locations of each individual EDS point measurement utilized for the calculation of the Hf:Ta ratio in the amorphous matrix (depicted with orange asterisks) and the nanocrystalline precipitates (depicted with blue asterisks).

Table A 5 showing the exact calculations of the Hf:Ta ratios within the amorphous matrix phase and the nano-precipitates of the Si(Hf_{0.7}Ta_{0.3})C(N,O) PDCs described in chapter 7.2. Each individual EDS measurement own a spectrum number which corresponds to the image in Figure A3.

Si(HfTa)C(NO)		matrix							
date	Image No.	Spectrum No.	Hf (in at%)	Ta (in at%)	Sum	Hf ratio	Ta ratio		
30.11.2022	Image 5	1	2.62	1.06	3.68	0.712	0.288		
		2	2.96	1.23	4.19	0.706	0.294		
		3	3.11	1.25	4.36	0.713	0.287		
		4	2.96	1.2	4.16	0.712	0.288		
		5	2.52	1.05	3.57	0.706	0.294		
		6	2.32	0.95	3.27	0.709	0.291		
		7	0.98	0.37	1.35	0.726	0.274		
		8	1.08	0.44	1.52	0.711	0.289		
		9	1.27	0.55	1.82	0.698	0.302		
			10	1.83	0.73	2.56	0.715	0.285	
		Image 10	13	3.54	1.91	5.45	0.650	0.350	
			14	3.79	2.51	6.3	0.602	0.398	
			15	1.54	0.67	2.21	0.697	0.303	
			16	1.42	0.64	2.06	0.689	0.311	
			17	3.41	1.82	5.23	0.652	0.348	
	15.03.2023	Image 6	9	1.29	0.49	1.78	0.725	0.275	
			10	1.15	0.45	1.6	0.719	0.281	
13			1.44	0.53	1.97	0.731	0.269		
			15	1.32	0.5	1.82	0.725	0.275	
		Image 9	16	1.2	0.5	1.7	0.706	0.294	
			17	1.43	0.57	2	0.715	0.285	
			18	1.77	0.67	2.44	0.725	0.275	
		Image 12	28	3.43	1.28	4.71	0.728	0.272	
			29	2.25	0.84	3.09	0.728	0.272	
			30	1.98	0.79	2.77	0.715	0.285	
			31	1.99	0.79	2.78	0.716	0.284	
		Image 20	38	0.29	0.15	0.44	0.659	0.341	
					mean	0.703	0.297		
					σ	0.029	0.029		
					2 σ	0.059	0.059		
HfTaC(O)		precipitates							
date	Image No	Spectrum No	Hf (in at%)	Ta (in at%)	Sum	Hf ratio	Ta ratio		
30.11.2022	Image 5	11	12.76	43.87	56.63	0.225	0.775		
15.03.2022		5	4.17	16.39	20.56	0.203	0.797		
		6	6.7	21.63	28.33	0.236	0.764		
		7	4.14	13.8	17.94	0.231	0.769		
		8	5.04	16.92	21.96	0.230	0.770		
	Image 6	11	12.79	42.69	55.48	0.231	0.769		
		12	15.69	42.02	57.71	0.272	0.728		
		14	6.57	21.55	28.12	0.234	0.766		
	Image 11	20	4.19	12.52	16.71	0.251	0.749		
		21	3.56	11.54	15.1	0.236	0.764		
		22	4.04	16.3	20.34	0.199	0.801		
		23	5.97	18.53	24.5	0.244	0.756		
		24	5.43	19.52	24.95	0.218	0.782		
	Image 20	32	5.62	18.63	24.25	0.232	0.768		
		33	6.35	17.15	23.5	0.270	0.730		
		34	6.45	20.29	26.74	0.241	0.759		
		35	7.38	25.05	32.43	0.228	0.772		
		36	6.9	20.75	27.65	0.250	0.750		
					mean	0.235	0.765		
					σ	0.018	0.018		
					2 σ	0.037	0.037		

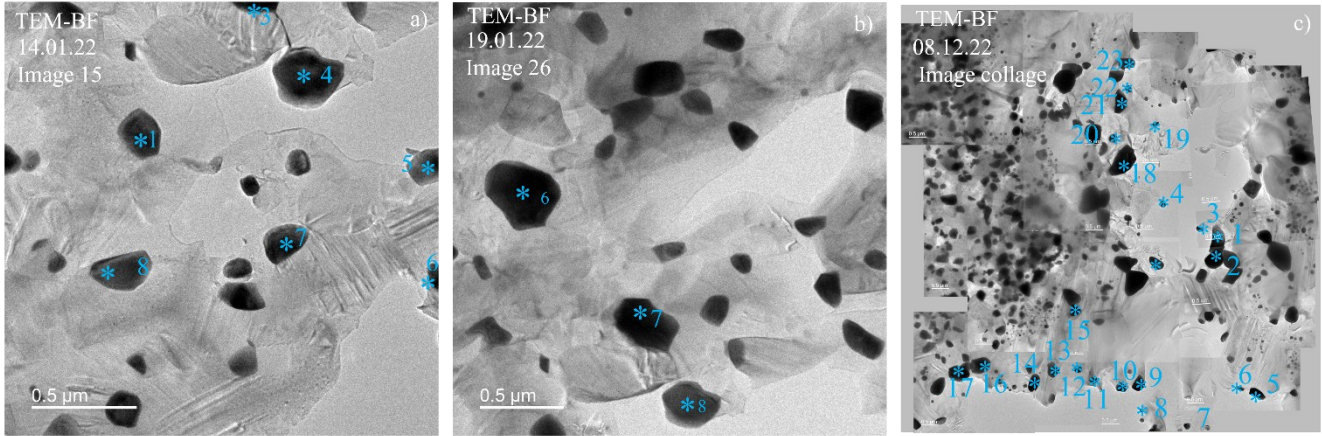


Figure A4 TEM-BF images of the exact locations of each individual EDS point measurement utilized for the calculation of the Hf:Ta ratio in the $(\text{Hf}_{0.7}\text{Ta}_{0.3})\text{C}$ in the sintered $\text{SiC}/(\text{Hf}_{0.7}\text{Ta}_{0.3})\text{C}$ depicted with blue asterisks.

Table A6 showing the calculations of the Hf:Ta ratios within the $(\text{Hf}_{0.7}\text{Ta}_{0.3})\text{C}$ in the sintered $\text{SiC}/(\text{Hf}_{0.7}\text{Ta}_{0.3})\text{C}$ PDCs described in chapter 7.3. Each individual EDS measurement own a spectrum number which corresponds to the image in Figure A4.

$(\text{Hf}_{0.7}\text{Ta}_{0.3})\text{C}$							
date	Image no	Spectrum No	Hf	Ta	Sum	Hf ratio	Ta ratio
14.01.2022	Image 15	1	47.41	17.15	64.56	0.734	0.266
		3	58.33	20.3	78.63	0.742	0.258
		4	49.19	16.78	65.97	0.746	0.254
		5	41.93	16.01	57.94	0.724	0.276
		6	49.18	18.23	67.41	0.730	0.270
		7	21.61	8.06	29.67	0.728	0.272
		8	50.17	17.67	67.84	0.740	0.260
		19.01.2022	Image 26	6	58.17	20.53	78.7
		7	51.1	18.33	69.43	0.736	0.264
		8	48.67	17.45	66.12	0.736	0.264
		08.12.2022	collage	1	46.78	11.91	58.69
		2	72.88	22.77	95.65	0.762	0.238
		3	62.99	21.61	84.6	0.745	0.255
		4	42.11	14.3	56.41	0.746	0.254
		5	49.15	16.91	66.06	0.744	0.256
		6	30.15	11.51	41.66	0.724	0.276
		7	64.27	23.56	87.83	0.732	0.268
		8	36.74	14.66	51.4	0.715	0.285
		9	44.68	16.07	60.75	0.735	0.265
		10	48.03	16.81	64.84	0.741	0.259
		11	72.47	24.27	96.74	0.749	0.251
		12	44.7	12.55	57.25	0.781	0.219
		13	35.81	13.24	49.05	0.730	0.270
		14	62.61	22.15	84.76	0.739	0.261
		15	48.58	17.47	66.05	0.736	0.264
		16	53.36	18.78	72.14	0.740	0.260
		17	48.6	16.73	65.33	0.744	0.256
		18	29.99	9.7	39.69	0.756	0.244
		19	18.74	6.7	25.44	0.737	0.263
		20	42.47	16.6	59.07	0.719	0.281
		21	38.83	11.26	50.09	0.775	0.225
		22	67.19	23.13	90.32	0.744	0.256
		23	71.1	22.24	93.34	0.762	0.238
							mean
					σ	0.017	0.017
					2σ	0.034	0.034

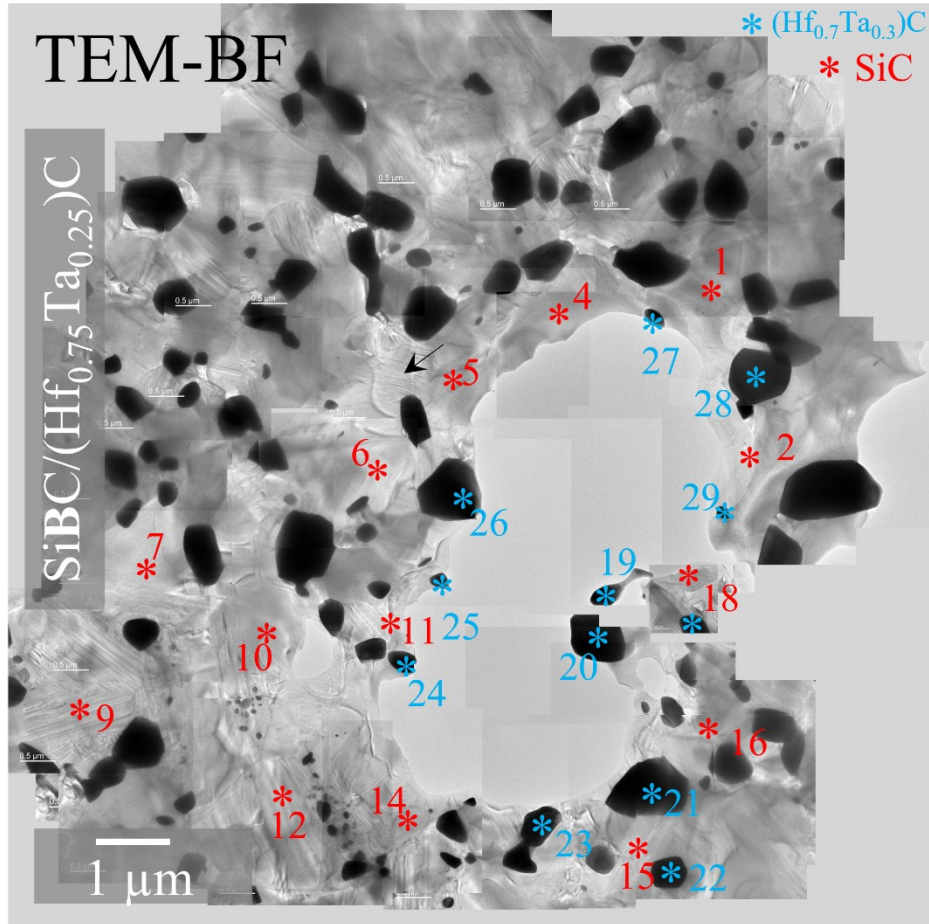


Figure A5 Collage of several TEM-BF images showing the exact locations of each individual EDS point measurement of the SiC (red) and (Hf_{0.7}Ta_{0.3})C (blue) in the sintered SiC/(Hf_{0.7}Ta_{0.3})C.

Table A7 give information of the oxygen contents of the EDS point measurements in the SiC (red) and (Hf_{0.7}Ta_{0.3})C (blue) phases. Each location of the point measurement is indicated with an asterisk in Figure A5.

SiC				(Hf _{0.7} Ta _{0.3})C					
Spectrum No	Si	C	O	Spectrum No	Hf	Ta	C	O	
1	77.54	21.15	1.31	19	51.67	19.42	26.27	2.65	
2	86.99	12.56	0.45	20	59.22	21.45	16.78	2.55	
4	75.1	24.34	0.56	21	50.31	18.21	29.08	2.4	
5	80.5	18.31	1.19	22	51.11	19.39	24.82	4.68	
6	79.6	19.46	0.93	23	32.96	12.71	49.6	4.74	
7	67.89	29.6	2.52	24	57.01	22.47	16.31	4.21	
9	77.43	22.14	0.43	25	48.63	18.3	25.26	7.81	
10	78.54	21.03	0.42	26	52.63	19.9	24.84	2.62	
11	65.74	33.27	0.99	27	53.7	20.17	21.29	4.84	
12	66.73	31.02	2.26	28	62.82	23.3	11.82	2.06	
14	72.58	26.64	0.77	29	62.32	23.88	12.36	1.44	
15	60.6	37.99	1.41	mean	52.944	19.927	23.494	3.636	
16	71.76	26.45	1.79	σ	7.816	2.924	9.949	1.746	
18	58.27	39.49	2.24	2σ	15.631	5.849	19.899	3.492	
mean	72.805	25.961	1.234						
σ	7.842	7.396	0.698						
2σ	15.684	14.792	1.395						

List of Figures

Figure 1 Long-term projections showing the energy consumption by fuel. Figure taken from Ref. [8].	1
Figure 2 The specific core powder as function of the turbine rotor inlet temperature. Figure adapted from Ref. [15].	2
Figure 3 Yield strength versus temperature for different Ni-base superalloys for turbine engines employed in the hot-sections of gas turbine engines. Figure adapted from Ref. [20].	3
Figure 4 Temperature limit of superalloys for the aircraft turbine and recent developments of thermal barrier coatings and the deposition methods in the last 60 years. Figure adapted from Refs. [16,28].	4
Figure 5 Common crystal structure of the TMC of HfC (NaCl type, Fm3m, space group no. 225). Large atoms refer to the metal atom (Hf), the small atom depict carbon atom. Structure created with VESTA [103].	9
Figure 6 The phase equilibrium diagrams for the Hf-C and Ta-C systems. Figure adapted from Refs. [13,104].	10
Figure 7 Phase diagram of HfC and TaC showing a complete solid solution at temperatures exceeding 887 °C and a miscibility gap below 887 °C. Figure redrawn after Ref. [106].	11
Figure 8 Oversimplified formula of the molecular structure of an organosilicon polymer. R ¹ and R ² corresponds to the mainly organic side groups, which are connected to the backbone. Redrawn after [54].	13
Figure 9 Silicon-based polymers and their fundamental chemical units. Figure redrawn after Ref. [54].	14
Figure 10 Simplified chemical formulas of organopolysilazanes (OPSZ) (left) and perhydropolysilazane (PHPS) (right). For this work PHPS was used (right formula).	15
Figure 11 Simplified chemical formula of polycarbosilane. For this work SMP-10 was used (right diagram).	16
Figure 12 Graphical illustration of the PDC processing, correlating the temperature with the processing phases and mass changes of a polycarbosilane under inert gas atmosphere. Figure adapted from Ref. [10].	17
Figure 13 Various preparation methods of PDCs via precursor processing. Figure adapted from Ref. [55].	19
Figure 14 Different material transport mechanisms happening during the sintering of crystalline particles: (1) Surface diffusion from the surface, (2) volume diffusion from the surface, (3) Gas phase transport including evaporation/condensation, (4) grain boundary diffusion from the grain boundary, (5) volume diffusion from the grain boundary, and (6) plastic flow by dislocation motion. Figure adapted from. Ref. [151].	20
Figure 15 Relative density as a function of the sintering time. Schematic showing the three sintering stages (initial, intermediate and final stage) and the densification curve. Figure adapted from Ref. [148].	22
Figure 16 The three stages during sintering, starting with the initial stage, where powder particles are in tangential contact. At the end of the initial stage, the particles begin to coalesce, initiating neck growth. The intermediate stage consists of a metastable continuous pore phase and in the final stage isolated pores are present.	22
Figure 17 Schematic of a FAST apparatus. Figure adapted from Refs. [165,166,172]	24
Figure 18 Schematic illustration of the set-up of a typical SEM microscope, encompassing the electron gun, electromagnetic lenses to focus the electrons into an electron beam, a vacuum chamber including the specimen stage and several different electron detectors to collect the emitted signals from the sample. Figure adapted from Ref. [191].	28

Figure 19	Fluorescence yield ω (also named backscattering coefficient η) for the K-shell X-rays as function of the atomic number (Z). Figure adapted from Refs. [186,196,198].	29
Figure 20	a) High resolution SEM microscope JSM-76000F from JEOL Ltd., Tokyo, Japan situated at the Materials Science Institute of the Technical University of Darmstadt, b) Sample box and aluminium Stub with sticky carbon pad and mounted cross-sectioned bulk ceramic sample for inspection under the SEM. c) The base part of the 12.5 mm sample holder (left) and the adapter part with a mounted aluminium stub ready to insert into the base part of sample holder (right).	30
Figure 21	The dual beam FEI Strata 400 STEM system with a FEG (Schottky) at the Institute of Nanotechnology (INT) at the Karlsruhe Institute of Technology (KIT), Germany.	33
Figure 22	A schematic illustration of a typical TEM set-up, dividing the TEM into three main parts: the illumination system, the objective lens and stage, and the Imaging system. Figure adapted from Ref. [191].	35
Figure 23	Simplified representation of the two main modes of the TEM imaging system: Diffraction mode (left) and imaging mode (right). In diffraction mode, through the relay lens the back focal plane and in imaging mode the image plane of the objective lens Object selected and magnified on screen. Figure taken from [198].	36
Figure 24	a) SAED pattern of a solid solution of a TMC (Hf,Ta)C crystal displaying discrete diffraction spots. b) Micrograph of the florescent viewing screen, showing the corresponding Kikuchi bands under convergent illumination settings in diffraction mode. The Kikuchi bands cross at the centre, indicating a precise orientation along the zone axis.	39
Figure 25	a) Schematic drawing of the Ewald sphere in a hypothetical reciprocal lattice. $1/\lambda_e$ is the radius of the Ewald sphere. I_i is the incident beam, I_d the diffracted beam, θ is the Bragg angle, g the reciprocal lattice vector, which represents the lattice planes. Please note the reciprocal lattice rods, also known as rel-rods. b) corresponding schematic diffraction pattern. The star (*) symbol represents the incident electron beam; the size of the diffraction spots correlates to the differences in the intensity. Figure adapted from Ref. [221].	40
Figure 26	Schematic drawing, showing that the intensity of the diffracted beam beams depends on the excitation error, s . There also will be intensity in a diffraction spot, even when the reciprocal lattice point does not lie exactly on the Ewald sphere and Bragg's condition is not exactly fulfilled. Redrawn after Ref. [224].	40
Figure 27	a) Transmission Electron Microscope JEM-2100F (JEOL Ltd., Tokyo, Japan) used for investigations in this study, b, c) Photomicrographs showing the double-tilt holder (JEOL Ltd., Tokyo, Japan).	42
Figure 28	Signals generated by electron-matter interaction in thin (electron transparent) specimen in a), and bulk samples in b). Figure adapted from Ref. [191].	43
Figure 29	Schematic illustration of the ionization process including the generation of characteristic X-rays. An inner (K) shell electron is ejected from the atom by an incoming high-energy electron. The hole in the K shell is filled with another higher-shell electron (electron from the L3 shell), thereby generating characteristic (K_α) X-rays. Figure adapted from Refs. [191,198].	44
Figure 30	Photographs of the sintered SiHfCN bulk pellets (SiHfCN_01 and SiHfCN_02) after sintering (Mirva Eriksson, Stockholm University) and after sawing.	48
Figure 31	a) Possible reaction pathways during the synthesis of the perhydropolysilazan (PHPS). b) The organo-metallic complexes of $M(NMe_2)_x$ with $M = Hf, Ta$ and $Me = CH_3$ (TDMAH & PDMAT).	49

Figure 32 Various photographs of the synthesis steps showing a Schlenk flask, the transparent liquid precursor, the metal-modified brown liquid and the obtained brown ceramic powder. All photographs are taken by J. Bernauer.	49
Figure 33 Photomicrographs of the polymer-derived ceramic powders in the $\text{Si}(\text{Hf}_x\text{Ta}_{1-x})\text{(C)N}$ system. The as-pyrolyzed and annealed Hf-rich $\text{Si}(\text{Hf}_{0.7}\text{Ta}_{0.3})\text{(C)N}$ ceramic powders are shown in b) and c), the as-pyrolyzed and annealed Ta-rich $\text{Si}(\text{Ta}_{0.8}\text{Hf}_{0.2})\text{(C)N}$ ceramic powders in d) and e).	50
Figure 34 Photograph showing the $\text{Si}(\text{Hf}_x\text{Ta}_{1-x})\text{C(N,O)}$ polymer-derived ceramic powders (left) and cut sample pieces of the sintered $\text{SiC}/(\text{Hf}_x\text{Ta}_{1-x})\text{C}$ bulk ceramics (right), with pen for scale. FAST was performed by Prof. Bram and his team, Institute of Energy and Climate (IEK), at the Forschungszentrum Jülich GmbH.	52
Figure 35 Various sample preparation steps for ceramic powder samples. a) molds filled with small amounts of ceramic powder and resin, b) Low-magnified SEM-BSE image showing ceramic powder particles on a sticky carbon pad for inspection in SEM, c) powder samples for inspection under optical light microscope, d) ceramic powder particles embedded in resin, cured and subsequently polished, e) photomicrograph of embedded powder particles.	54
Figure 36 TEM specimen preparation for ceramic powder particles using TEM support grids with carbon film; a) TEM lacy gold grid with freshly pipetted ethanol and pulverized ceramic powder solution, b) photomicrograph of the fluorescent TEM viewing screen showing individual powder particles sitting on the carbon film, c) TEM-BF image showing the carbon film, the hole in the carbon film and the ceramic powder particle located over a hole.	56
Figure 37 CLEM of the embedded and polished cross-section of the $\text{Si}(\text{Hf}_{0.7}\text{Ta}_{0.3})\text{(C)N}$ ceramic powder particles. a) optical light micrograph of the cold-embedded and subsequently cross-sectioned and polished powder particles, b) correlated sample position in the SEM-BSE image, c, d) SEM-BSE image of the magnified region of interest (ROI) before and after FIB milling.	57
Figure 38 Several SEM images showing the FIB lift-out technique, applied to a single powder particle of the annealed $\text{Si}(\text{Hf}_{0.7}\text{Ta}_{0.3})\text{(C)N}$ PDC, shown in a); b) SEM image, displaying the region of interest (ROI); c) Pt deposition to protect the underlying material; d) extracted lamella (white arrow) transferred and pinned to a Mo lift-out grid; e) pre-thinned FIB lamella with the intact Pt deposition at the top; f) thinned FIB lamella with thinning marks (in vertical direction) from the thinning process. All images in this figure are taken by Dr. S. Schlabach.	58
Figure 39 Various tools used for sample preparation in the ultra-high temperature laboratory at the Institute for Applied Geosciences at the Technical University Darmstadt; a) ceramic bulk sample glued onto glass slide for sawing; b) handling with heating plate; c) cross-sectioned and polished ceramic bulk sample; d) Tripod polisher; e) final polished TEM specimen, ready to be glued onto TEM grid; f) TEM specimen glued onto TEM grid; g) TEM specimen onto TEM grid, mounted onto sample holder for final Ion-thinning process; h) Gatan Duomill for Ar^+ -ion thinning; i) View onto the fluorescent viewing screen of the TEM.	59
Figure 40 Correlation between OLM and SEM-BSE micrograph. The SEM-BSE image on the right consists of 25 individually mounted SEM-BSE images of the sintered SiHfCN_01 ceramic bulk sample.	60
Figure 41 a, b) SEM-BSE images and c) SEM-SE micrograph of the sintered, cross-sectioned and polished SiHfCN_01 ceramic bulk sample show four different microstructural regions: former powder particles, crystallization fronts, sinter necks and porosity.	61

- Figure 42** Microstructural characterization of the three different microstructure regions: former powder particle, crystallization front and sinter neck; SEM-BSE images and EDS element concentration profile of carbon and nitrogen of the consolidated SiHfCN_01 bulk ceramic. 251 individual point measurements starting from the inside of a former powder particle (left side), continue over to the crystallization front (middle) into the sinter neck (right side) of the cross-sectioned and polished SiHfCN_01. TEM-BF and corresponding SAED pattern in addition to EDS spectra of the constituting phases: Si₃N₄, TMC and SiC. 63
- Figure 43** a, b) TEM-BF images, c) HR-TEM image and SAED patterns of the SiC-twin as insets in c). 64
- Figure 44** EPMA analysis giving a SEM-BSE image as overview and quantitative element distribution maps of Si, Hf, C, and N for the cross-sectioned and polished SiHfCN_01 bulk ceramic. 65
- Figure 45** TEM-BF, SAED patterns and EDS spectra of the SiHfCN_02 ceramic. 66
- Figure 46** Microstructure comparison between SiHfCN_01 in a) and SiHfCN_02 in b). The difference between the sinter parameters of both ceramics lies in the dwell time. The microstructure and densification state of SiHfCN_01 are assigned to the intermediate sinter stage, whereas SiHfCN_02 is assigned to the final sinter stage with grain coarsening and isolated pores. 67
- Figure 47** XRD patterns of the as-pyrolyzed and annealed Hf-rich and Ta-rich Si(Hf_xTa_{1-x})(C)N polymer-derived ceramic powders. X-ray powder diffraction diffractogram of a) both as-pyrolyzed ceramic samples. and b) the annealed ceramic samples. The Ta-rich compositions are shown in black color, the Hf-rich compositions are presented in red. Figure adapted from Ref. [84]. 69
- Figure 48** SEM-BSE image of the as-pyrolyzed Si(Hf_{0.7}Ta_{0.3})(C)N ceramic powder. Figure taken from Ref. [84]. 70
- Figure 49** SEM-BSE images showing a fracture surface of a the as-pyrolyzed Si(Hf_xTa_{1-x})(C)N polymer-derived ceramic powder particle with two microstructurally different regions present: the surface region and the bulk region; a) Overview of the whole particle; b) on the surface, nano-sized precipitates are marked with black arrows. 70
- Figure 50** SEM-BSE (a, d) and SEM-SE (b) images of the as-pyrolyzed Si(Hf_{0.7}Ta_{0.3})(C)N polymer-derived ceramic powder sample, showing the powder particle surface with nano-sized precipitates; c) EDS spectra showing the difference between the two microstructural regions. The Hf-rich precipitate is marked with the blue star symbol in d), the corresponding spectrum is shown in blue in c), whereas the red triangle in d) represents the SiCN phase; the respective spectrum is shown in red in c). The indexed elements correspond to the characteristic X-ray energies: C (K_α), N (K_α), Si (K_α), Hf (M_α, L_α). Figure adapted from Ref. [84]. 72
- Figure 51** TEM-BF and HR-TEM images representing the amorphous microstructure of the bulk region within the as-pyrolyzed Si(Hf_{0.2}Ta_{0.8})(C)N polymer-derived ceramic powder. The inset in a) shows a distinct diffuse SAED pattern; the HR-TEM image in b) depicts the amorphous nature of the bulk regions, where the star symbol marks the location of the EDS point measurement; c) the corresponding EDS spectrum of the amorphous bulk region is shown exemplarily with the containing elements correlated as follows: C (K_α), N (K_α), O(K_α), Si(K_α), Hf (M_α, L_α), and Ta (M_α, L_α). The Hf:Ta ratio is Hf:Ta = 0.19:0.81 (±0.01). 73
- Figure 52** TEM micrographs of the Si(Hf_{0.2}Ta_{0.8})(C)N polymer-derived ceramic powder sample pyrolyzed at 1000 °C in NH₃ atmosphere; a) TEM-BF image of the particle surface with nano-sized TMCN precipitates, b) HR-TEM image with inset of IFFT image, giving information of the lattice spacings of the TMCN, c) two EDS spectra of the mostly

- amorphous bulk region (shown in red) and the nano-sized TMCN phase (shown in blue). The elements in the EDS spectra are indexed via their characteristic X-ray energies as follows: C (K_{α}), N (K_{α}), Si (K_{α}), Hf (M_{α} , L_{α}), Ta (M_{α} , L_{α}). The Hf:Ta ratio of the precipitates (blue EDS spectrum) is Hf:Ta = 0.19:0.81 (± 0.03).....75
- Figure 53** SEM-BSE image of the surface topography of the annealed $\text{Si}(\text{Hf}_x\text{Ta}_{1-x})(\text{C})\text{N}$ ceramic powders. Figure published in Ref. [84].....76
- Figure 54** SEM-SE, SEM-BSE micrographs of an individual powder particle of the annealed $\text{Si}(\text{Hf}_{0.2}\text{Ta}_{0.8})\text{CN}$ polymer-derived ceramic. In addition, g) and h) show two EDS spectra giving information on the chemistry of the constituent phases present at the surface region. For the spectrum in g) the constituting elements are: C (K_{α}) and Si (K_{α}). For the spectrum in h) the elements are: C (K_{α}), Hf (M_{α} , L_{α}) and Ta (M_{α} , L_{α}). Figure adapted from Ref. [84].77
- Figure 55** a, d) TEM-BF, b, e) HR-TEM images, c, f) SAED patterns and g, h) EDS spectra showing the phase assemblage of the surface region within the annealed $\text{Si}(\text{Hf}_{0.2}\text{Ta}_{0.8})(\text{C})\text{N}$ PDC. The surface regions constitutes SiC and $(\text{Hf}_{0.2}\text{Ta}_{0.8})\text{C}$ with a Hf:Ta ratio = 0.22:0.78. Each carbide is encapsulated by a thin residual carbon layer/shell. For the EDS spectrum in g) the characteristic X-ray energies are correlated as follows: C (K_{α}) and Si (K_{α}). For the spectrum in h) the elements are: C (K_{α}), Hf (M_{α} , L_{α}) and Ta (M_{α} , L_{α}). Figure adapted from Ref. [84].78
- Figure 56** SEM and TEM images showing pronounced crystal growth at surface regions of the annealed $\text{Si}(\text{Hf}_{0.7}\text{Ta}_{0.3})(\text{C})\text{N}$. a, b, c, g, h, i) SEM-BSE images, d, e,) SEM-SE images and f) TEM-BF micrograph of idiomorphic silicon nitride (Si_3N_4) next to silicon carbide (SiC) whiskers.....80
- Figure 57** a, b) TEM-BF and d) HR-TEM images, e) SAED pattern and c, f) EDS spectra showing the microstructure and chemistry of the annealed $\text{Si}(\text{Hf}_{0.7}\text{Ta}_{0.3})(\text{C})\text{N}$ polymer-derived ceramic powder samples. The phase assemblage constitutes of $\beta\text{-Si}_3\text{N}_4$ and embedded nano-sized Hf-rich TMCNs ($\text{Hf}_{0.7}\text{Ta}_{0.3})\text{CN}$ with a Hf:Ta ratio of Hf:Ta=0.72:0.28 (± 0.14). The SAED pattern of the oriented Si_3N_4 phase in e) corresponds to the HR-TEM image in d). The exact EDS point measurement positions are indicated in the TEM-BF image with an asterisk in b). The corresponding EDS spectrum in c) represent the TMCN phase, with the elements indexed as follows: C (K_{α}), N (K_{α}), Hf (M_{α} , L_{α}) and Ta (M_{α} , L_{α}). The EDS spectrum in f) represents the Si_3N_4 phase with the following elements indexed: N (K_{α}) and Si (K_{α}). Figure adapted from Ref. [84].81
- Figure 58** a, c) TEM-BF and b, d) HR-TEM micrographs of the Hf-rich $\text{Si}(\text{Hf}_{0.7}\text{Ta}_{0.3})(\text{C})\text{N}$ (a, b) and Ta-rich $\text{Si}(\text{Hf}_{0.2}\text{Ta}_{0.8})(\text{C})\text{N}$ (c, d) annealed polymer-derived ceramics. Amorphous carbon was detected around TMCs in both Hf-rich and Ta-rich ceramic powder samples. c, d) Besides solid solutions of TMCs, also pure TaC was found within the Ta-rich PDC. The insets in b, d) show the EDS spectra of $(\text{Hf}_{0.7}\text{Ta}_{0.3})\text{C}$ in b) and TaC in d) where the peaks are correlated as follows: C (K_{α}), Au (M_{α}), Hf (M_{α} , L_{α}), and Ta (M_{α} , L_{α}).....82
- Figure 59** Various SEM-BSE images of the embedded $\text{Si}(\text{Hf}_x\text{Ta}_{1-x})(\text{C})\text{N}$ polymer-derived ceramic powder particles after annealing at 1600°C . Images in a), b), c), g), h) and i) show an overview of the whole powder particle, whereas the micrographs in d), e), f), j), k), and l) depict enlarged areas of the surface and bulk regions. Surface regions are characterized by an enrichment of TMCs (appearing bright in SEM-BSE images). The thickness of the surface regions is marked with yellow arrows in each magnified BSE image and the thickness of the surface region differs in each powder particle. An increase in the TMC grain sizes is visible from bulk to surface, in particular in e), f), j) and k). Internal surfaces are detected within an individual powder particle (Figure 55a, and d).....84

- Figure 60** a, b) SEM-BSE micrographs showing a cross-section of an individual annealed polymer-derived ceramic powder particle in the $\text{Si}(\text{Hf}_{0.7}\text{Ta}_{0.3})\text{(C)N}$ system. TMC(N)s grains increase in size from inner bulk (TMCN) to outer surface regions (TMC); c) Relative elemental concentrations of C, N, O, Si, Hf, and Ta based on EDS point profiles in the red and green marked regions. The TMC(N) particle size increases in the surface-near region, coinciding with an elevated C and O content. The Si and N elemental concentrations are depleted, in the near-surface region. Figure published in Ref. [84]. 86
- Figure 61** a) SEM-SE image of the TEM lamella prepared from the annealed $\text{Si}(\text{Hf}_{0.7}\text{Ta}_{0.3})\text{CN}$ polymer-derived ceramic powder particle via FIB-SEM. b) Collage of TEM-BF images showing the cross-section through the bulk-to-surface transition zone of an individual powder particle. Slight contrast variations enhance the edges of the frame and do not contribute to the microstructure. TEM lamella preparation was carried out by Dr. S. Schlabach, KIT. 87
- Figure 62** a) TEM-BF image, b-d) SAED patterns and e-h) O, N, Si, C element concentration profiles in at-% from bulk and transition zone into the surface region, as marked by the line. 88
- Figure 63** Structural formula of the organo-metallic complexes PDMAT and TDMAH used to modify the polymeric precursors. 89
- Figure 64** Ellingham diagram showing the temperature as a function of the Gibbs free energy. The temperature dependence of the change in the Gibbs free energy of the possible reactions of HfN plus free C decomposing into HfC plus gaseous N_2 at high temperatures. The temperature range between 1000 °C and 1600 °C represents the pyrolysis temperature and annealing temperatures of the here studied $\text{Si}(\text{Hf}_x\text{Ta}_{1-x})\text{(C)N}$ PDCs (redrawn after Ref. [66], data taken from Ref. [239]). 90
- Figure 65** Schematic illustration of the microstructural evolution of the polymer-derived ceramic $\text{Si}(\text{Hf}_x\text{Ta}_{1-x})\text{(C)N}$ upon pyrolysis at 1000 °C and subsequent heat treatment at 1600 °C. 93
- Figure 66** XRD pattern of the as-pyrolyzed $\text{Si}(\text{Hf}_{0.7}\text{Ta}_{0.3})\text{C(N,O)}$ ceramic powder pyrolyzed at 1000 °C in Ar (bottom) and XRD pattern of the bulk $\text{SiC}/(\text{Hf}_{0.7}\text{Ta}_{0.3})\text{C}$ ceramic sintered at 2200 °C (top). 95
- Figure 67** a) SEM-BSE micrograph and b) EDS spectrum of the as-pyrolyzed $\text{Si}(\text{Hf}_{0.7}\text{Ta}_{0.3})\text{C(N,O)}$ polymer-derived ceramic. The containing elements in b) are indexed following the characteristic X-ray energies with: C (K_α), N (K_α), O (K_α), Si (K_α), Hf (M_α , L_α) and Ta (M_α , L_α). 96
- Figure 68** a) TEM-BF image, b) HR-TEM image, c) SAED pattern and d) EDS spectrum of the amorphous as-pyrolyzed $\text{Si}(\text{Hf}_{0.7}\text{Ta}_{0.3})\text{C(N,O)}$ polymer-derived ceramic with a Hf:Ta ratio of Hf:Ta = 0.70:0.30 (± 0.06). The EDS spectrum in d) represent the amorphous $\text{Si}(\text{Hf}_{0.7}\text{Ta}_{0.3})\text{C(N,O)}$ phase, with the elements indexed as follows: C (K_α), N (K_α), O (K_α), Si (K_α), Hf (M_α , L_α) and Ta (M_α , L_α). 97
- Figure 69** $\text{Si}(\text{Hf}_{0.7}\text{Ta}_{0.3})\text{C(N,O)}$ polymer-derived ceramic microstructure and elemental distribution after pyrolysis at 1000 °C, a) TEM-BF image, b) HR-TEM micrograph, c) SAED pattern, d) EDS spectrum and f) IFFT images. A amorphous $\text{Si}(\text{Hf}_{0.7}\text{Ta}_{0.3})\text{C(N,O)}$ glass network is visible by the homogeneous amplitude contrast in a), and Ta-rich nanoparticles via higher mass contrast in a). The EDS spectrum in d) at the position “*” b) shows a Ta-rich nanoparticle with a Hf:Ta ratio of Hf:Ta = 0.24:0.76 (± 0.04) with the elements indexed as follows: C (K_α), N (K_α), O (K_α), Hf (M_α , L_α) and Ta (M_α , L_α); e) FFT image with discrete diffraction spots (pink) showing the presence of graphite around the Ta-rich particle, exact position of FFT is indicated as small rectangle in b); IFFT images in f) give

- information about the lattice spacings of $(\text{Ta}_x\text{Ha}_{1-x})\text{C}(\text{O})$ in blue and the graphitic carbon in pink. 98
- Figure 70** Correlative light and electron microscopy (CLEM) showing the three distinct microstructural regions of the consolidated $\text{SiC}/(\text{Hf}_{0.7}\text{Ta}_{0.3})\text{C}$ PDC: former powder particles, sinter necks and porosity; a, b) optical light micrographs with three different colored arrows depicting the different appearance of pores within the sintered ceramic; the white arrow depicts the macropores in the sinter neck, the black arrows depict the pores within the former powder particle and the yellow arrows depict the pores, present c, d) SEM-BSE images showing the exact the same area of interest as in the optical light micrographs in a, b). 100
- Figure 71** SEM-BSE images showing the constituting microstructural regions of the sintered bulk ceramic. a) magnified SEM-BSE image showing the sinter neck in the middle of the image and two former powder particles on the left and right. The three different appearances of pores within the microstructure of the sintered $\text{SiC}/(\text{Hf}_{0.7}\text{Ta}_{0.3})\text{C}$ PDC are depicted with yellow, white and black arrows. SEM-BSE images in b, c, d and e) show TMCs very well aligned at or near the internal surface of the former powder particles. 101
- Figure 72** Low-magnified (LM) SEM-BSE image giving an overview where the total of 22 pictures were taken for the evaluation of the quantitative image analysis enabling for the determination of the porosity values. Yellow marked image frames were taken at a magnification of 500x, image frames depicted in green were taken at a magnification of 1000x. 102
- Figure 73** SEM-BSE images and further processed images used for the determination of the porosity in the $\text{SiC}/(\text{Hf}_{0.7}\text{Ta}_{0.3})\text{C}$ bulk sample. a, b) original SEM-BSE images with magnifications of 500x and 1000x. c, d) Thresholding of the darkest contrast in a, b) leads to the blue-marked pores. e, f) Final image after thresholding gives the indexed pores in black. 104
- Figure 74** SEM-BSE image (a) and correlative EPMA element distribution maps of Si, C, Hf, Ta, O and N in b-g) of a cross-sectioned and polished sintered $\text{SiC}/(\text{Hf}_{0.7}\text{Ta}_{0.3})\text{C}$ bulk ceramic. Dark blue equals low element concentrations, red equals high element concentrations. 105
- Figure 75** TEM-BF collage composing 253 individual TEM-BF images giving a high magnification with a large field of view of the microstructure of the consolidated PDC. Two microstructural regions are shown: the former powder particles and the sinter neck. The dashed green line separates the former powder particle from the sinter neck. 106
- Figure 76** a-d) TEM-BF images showing the transition zone between the former powder particles and the sinter neck; d) EDS point measurement of the TMC is marked with blue asterisk and EDS point measurement of SiC is marked with a green asterisk; e) the EDS spectra from the corresponding asterisks in d). Elements are indexed as follows: for $(\text{Hf}_{0.7}\text{Ta}_{0.3})\text{C}$ in blue: C ($K\alpha$), Mo ($L\alpha$), Hf ($M\alpha$, $L\alpha$), Ta ($M\alpha$, $L\alpha$) and for SiC in green: C ($K\alpha$), Si ($K\alpha$), Mo ($L\alpha$); f, g) SAED patterns of $(\text{Hf}_{0.7}\text{Ta}_{0.3})\text{C}$ TMC and SiC , both aligned to a specific zone axis. 107
- Figure 77** a, b) TEM-BF images of the sintered $\text{SiC}/(\text{Hf}_{0.7}\text{Ta}_{0.3})\text{C}$ PDC, focusing on a SiC grain with regions, enriched in stacking faults. c, d) HR-TEM images showing a region where no SFs are present, and a region where SFs are depicted as bright/dark contrast. d, f) FFT images of the corresponding regions marked in d). 108
- Figure 78** a) Optical light micrograph showing the probed 50 x 50 indentation grid. b) Hardness and Modulus maps of the corresponding area indented in a). Each indent was attributed to one of the three microstructural components: yellow for the former powder particle constituting small-scaled and homogeneous distributed $(\text{Hf}_{0.7}\text{Ta}_{0.3})\text{Cs}$ in a SiC matrix, red

for the sinter necks, mainly constituting SiC and enlarged (Hf _{0.7} Ta _{0.3})Cs and blue for porous regions.....	110
Figure 79 The thermal conductivity of (Ta _{0.8} Hf _{0.2})C (sintered at 5 different temperatures) plotted against the temperature. Measured from room temperature to 1400 °C. Figure redrawn after Ref. [238].....	115
Figure 80 Influence of the electric current on the microstructural evolution within the SiC/(Hf _{0.7} Ta _{0.3})C PDC. Schematic drawing showing the microstructure of the initial amorphous Si(Hf _{0.7} Ta _{0.3})C(N,O) powder during FAST, and the microstructure of the consolidated SiC/(Hf _{0.7} Ta _{0.3})C bulk ceramic after FAST. The current pathways along the internal surfaces of adjacent powder particles (red lines and arrows) and the increase grain size of TMCs (in blue) on internal particles, as well as increased SiC crystals (in green) in the sinter necks are shown. Further, the different pore sizes (black) are shown: In the former powder particles, the pores are small, in the sinter necks, pores are bigger in size.	116
Figure 81 Microstructure of the former powder particle region; a) schematically drawn microstructure with twinned SiC as the matrix phase depicted in green, the TMCs as secondary phase depicted in blue and micro-/nano pores represented in black color. b) SEM-BSE image with blue-marked pores (thresholding via ImageJ). The triangles show schematically the cross-sections of the nano indenter.	118
Figure 82 Micrographs showing the cut sintered pellets of SiC/(Hf _{0.75} Ta _{0.25})C (left) and SiBC/(Hf _{0.75} Ta _{0.25})C (right) for further sample SEM and TEM preparation steps	123
Figure 83 XRD patterns of the as-pyrolyzed Si(B)(Hf _{0.75} Ta _{0.25})C(N,O) ceramic powder pyrolyzed at 1000 °C in Ar (bottom) and XRD pattern of the bulk Si(B)C/(Hf _{0.75} Ta _{0.25})C ceramic sintered at 2200 °C (top). Diffraction analysis was performed by J. Bernauer. .	124
Figure 84 Comparison of the SEM-BSE images of SiC/(Hf _{0.75} Ta _{0.25}) and SiBC/(Hf _{0.75} Ta _{0.25})C.	125
Figure 85 a, b) TEM-BF images, c, d) HR-TEM images with SAED pattern as insets and e, f) EDS spectra of the constituting phases SiC and (Hf _{0.75} Ta _{0.25})C in the sintered SiBC/(Hf _{0.75} Ta _{0.25})C ceramic.....	126
Figure 86 Low-magnified (LM) SME-BSE image highlighting the 40 BSE image positions for evaluating the sample porosity. Green marked image frames were taken at a magnification of 1000x, image frames depicted in blue were taken at a magnification of 3000x.	127
Figure 87 SEM-BSE images and further processed images used for the determination of the porosity in the SiBC/(Hf _{0.75} Ta _{0.25})C bulk sample. a, b) original SEM-BSE images with magnifications of 1000x and 3000x. c, d) Thresholding of the darkest contrast in a, b) leads to the blue-marked pores. e, f) Final image after thresholding gives the indexed pores in black as sum of the porosity in area%.	129
Figure 88 a) SEM-BSE image taken from Figure 87 d) and further processed images in b) and c) used for the determination of the area% and numbers of TMC particles in the SiBC/(Hf _{0.75} Ta _{0.25})C bulk sample.	130
Figure 89 Different polymeric precursor systems plotted against temperature in °C. Figure redrawn after Ref. [128].....	135
Figure 90 Schematic drawing and comparison between the final microstructures of pyrolyzed and annealed ceramic powders in a), and FAST-sintered bulk ceramics prepared upon different polymers and sintered at different temperatures and dwell times in b). The first and last frames of the top row are shown as dashed lined because the model drawings for these temperatures are hypothetical and have not been supported by experimental data.	136

Figure 91 Possible TBC top coat materials with low thermal conductivity. Pyrochlores and Fluorites are depicted in green. Reprinted from Ref. [32] under Creative Common CC BY license..... 139

List of Tables

Table 1 Selected physical and structural properties at room temperature of stoichiometric group IV and V TMCs and TMNs. Data taken from Ref. [9,43,45,100].	11
Table 2 Six material transport mechanisms during sintering. Table taken from Ref. [148]....	21
Table 3 The FAST sinter parameter of the two prepared SiHfCN bulk ceramics.....	47
Table 4 Processing parameter of the Si(M)(C)N, (M = metal) polymer-derived ceramics. Table adapted from [84].	50
Table 5 Summary of sample names, processing parameters, chemicals used for synthesis and exemplarily elemental analysis in at-%.	53
Table 6 Characteristic X-ray energies of C, N, O, Si, Cu, Hf, Ta and Au. Cu and Au are the elements that make up the TEM grids, whereas the other elements listed are those expected chemicals in the prepared ceramics.	56
Table 7 Chemical composition of the as-pyrolyzed Si(Hf _{0.7} Ta _{0.3})C(N,O) and sintered SiC/(Hf _{0.7} Ta _{0.3})C ceramics. Table taken from Ref. [85].	94
Table 8 Resulting porosity values for eleven BSE images at magnifications of 500x and 1000x.	103
Table 9 Mechanical properties of the three microstructural regions in the monolithic SiC/(Hf _{0.7} Ta _{0.3})C ceramic.	111
Table 10 Literature review giving an idea about the oxygen impurities promoting grain coarsening in actual oxygen-free Si-based ceramic systems.	117
Table 11 Mechanical Properties of the three microstructural regions detected within the SiC/(Hf _{0.7} Ta _{0.3})C ceramic composite, listed alongside to chemically similar SiC-based ceramics published in literature.	119
Table 12 Molar ratios and quantities of the used chemicals in addition to the FAST parameter used for the preparation of SiC/(Hf _{0.75} Ta _{0.25}) and SiBC/(Hf _{0.75} Ta _{0.25})C.	123
Table 13 Chemical composition of the as-pyrolyzed SiB(Hf _{0.75} Ta _{0.25})C(N,O), sintered SiBC/(Hf _{0.75} Ta _{0.25})C ceramic samples in wt-% and at-% and the empirical formula of each sample.	124
Table 14 Resulting porosity values for eleven SEM-BSE images at magnifications of 500x and 1000x.	128

Acknowledgements

I would like to appreciate those who have supported, accompanied and helped me during my PhD work; I would never have been able to finish my dissertation without the guidelines from my colleagues at the Technical University Darmstadt, the Karlsruhe Institute of Technology and the DECHEMA Forschungsinstitut, as well as support from my family and friends.

Firstly, I would like to give many thanks to Prof. Astrid Pundt and Prof. Hans-Joachim Kleebe, who provided me the opportunity being part of the Research Training Group. I would like to thank Prof. Hans-Joachim Kleebe for providing me access to the electron microscopes and the preparation lab. I also appreciate his expertise in electron microscopy and his deep knowledge regarding the polymer-derived ceramics. I like to express my deepest gratitude and appreciation to Prof. Astrid Pundt. I am very grateful for her exceptional guidance and unwavering support through the challenging journey of completing this dissertation. As my supervisor, she provided invaluable insights, constructive feedback and expert knowledge that significantly contributed to the quality of my research.

I am very grateful for Prof. Ute Kolb. Thanks a lot for agreeing to supervise my doctorate and for taking the role as my main supervisor. I would also like to thank her for the insightful discussions and the constructive feedback on my scientific work. In particular, I want to thank her for immediately including me into her research group. Likewise, I would like to thank the committee members Prof. Karsten Albe and Prof. Christoph Schüth for their time and interest.

I would like to thank the two spokespersons of our research training program Prof. Ralf Riedel and Prof. Martin Heilmaier. In addition, I would like to thank Prof. Riedel giving me the opportunity to work in close collaboration with Jan, Samuel and Laura. Many thanks to Jan for kindly supporting my work, especially in the preparation of the PDCs and the XRD experiments. Moreover, he has shared his plentiful experience with me on material synthesis. I would like to thank Nils for his constructive feedback on my work and for our very pleasant collaboration during the whole time. I want to thank Georg Winkens for his great support through my whole PhD and the fruitful collaboration regarding the nanoindentation experiments. I like to thank Katharina Beck for her contributions in our joint research paper, especially for the measurement, data evaluation and her knowledge regarding the XRD.

Many thanks also to Prof. Ruth Schwaiger for allowing us to carry out experiments in the laboratories at FZ Jülich and for helping us with her expertise, especially in the field of nanoindentation. I would like to thank Dr. Jin Wang for conducting the nanoindentation tests and for helping us in the paper writing process. Special thanks to Dr. Emanuel Ionescu and Prof. Maren Lepple for constructive feedback and kind suggestions during the writing process, for encouraging me and supporting me during my PhD work. I would especially like to thank Dr. Ann Katrin Fetzer, who explained and showed me the entire sample preparation and always had an open ear for me. I am very grateful that you were my colleague during this time.

Thanks to Dr. Stefan Lauterbach and Prof. Yolita Eggeler for the practical hands-on instruction at the TEM labs at TU Darmstadt and KIT. Thanks to Ulrike Kunz for the practical hands-on instruction at the SEM. I would like to thank Angelika Willführ, Natali Vakalopoulou and Astrid Kern for their administrative support. Thanks to Nadine, Alina, Mozhdeh, Frauke, Laura and Julian for proofreading. A deep thank you to my parents and my sister.

Thanks to all the PhD candidates and associates within the RTG: Mozhdeh, Samuel, Laura, Frauke, Juri, Andreas and Hemanth for being such a great company at the Graduate Schools.

Thanks to all my colleagues in the different groups: Kerstin, Emilia, Johannes, Max, Tobias, Hui, Lisa, Jane, Ying, Dario, Isabell.

Special thanks to Carolin König, Martina Merk and Ute Henning for their great support during these years.

I also would like to acknowledge the financial support from the Deutsche Forschungsgemeinschaft (DFG).

Finally, the most important person in my life Julian, whom I would like to express my special thanks for the ongoing and everytime support, all those constructive conversations and that you believe in me all the time.

Curriculum Vitae

Zur Person

Name Nathalie Thor
Geburtsdatum 29. Januar 1994

Bildungsweg

2013 Allgemeines Abitur, Städtisches Gymnasium Kreuztal

2013 – 2016 **Universität zu Köln**
Bachelorstudium am Institut für Geologie und Mineralogie an der mathematisch-naturwissenschaftlichen Fakultät

09/2016 Bachelor of Science Geowissenschaften (Gesamtnote: 2.2)

2016 – 2019 **Universität zu Köln**
Masterstudium am Institut für Geologie und Mineralogie an der mathematisch-naturwissenschaftlichen Fakultät

10/2019 Master of Science Geowissenschaften (Gesamtnote: 1.9)

2020 – 2024 **Technische Universität Darmstadt**
Promotionsstudium am Institut Angewandte Geowissenschaften im Fachbereich für Material- und Geowissenschaften

Publications & Conference Contributions

- [1] **Thor, N.**, Bernauer, J., Petry, N.-C., Ionescu, E., Riedel, R., Pundt, A., Kleebe, H.-J. (2023). Microstructural evolution of Si (Hf_xTa_{1-x})C/N polymer-derived ceramics upon high-temperature anneal. *Journal of the European Ceramic Society*, 43(4), 1417-1431.
- [2] **Thor, N.**, Winkens, G., Bernauer, J., Petry, N.-C., Beck, K., Wang, J., Schwaiger, R., Riedel, R., Kolb, U., Lepple, M., Pundt, A., Microstructure characterization and mechanical properties of polymer-derived (Hf_xTa_{1-x})C/SiC ceramic prepared upon field-assisted sintering technique (FAST/SPS). *In revision AEM 2024*
- [3] **Thor, N.**, Bernauer, J., Petry N.-C., Ionescu, E., Riedel, R. Pundt, A., Kleebe H.-J. (2023) Microstructural evolution of novel Si(M)(B,C)N polymer-derived ceramics upon different heat treatments, Microscopy Conference, Darmstadt, Germany 02/2023 (poster presentation)
- [4] Beck, K., Ulrich, A. S., **Thor, N.**, Oskay, C., Galetz, M. C., Chromium Diffusion Coatings for Improving the Oxidation Behaviour of Refractory Metals at Intermediate Temperatures. Submitted to *International Journal of Refractory Metals and Hard Metals*
- [5] Petry, N.-C., **Thor, N.**, Bernauer, J., Ulrich, A. S., Ionescu, E., Riedel, R., Kleebe, H.-J., Galetz, M. C., Lepple, M., Oxidation resistance and microstructural analysis of polymer-derived (Hf,Ta)C/SiC ceramic nanocomposite. *In revision AEM 2024*
- [6] Bernauer, J., Petry, N.-C., **Thor, N.**, Kredel, S.A., Teppala, D.T., Galetz, M., Lepple, M., Pundt, A., Ionescu, E., Riedel, R., Exceptional hardness and thermal properties of SiC/(Hf,Ta)C(N)/(B)C ceramic composites derived from single-source precursor. *Advanced Engineering Materials 2024*
- [7] Fathidoost, M., Yang, Y., **N. Thor**, Bernauer, J., Pundt, A., Riedel, R., Xu, B., working title: Thermal conductivity analysis of polymer-derived nano-composite via image-base structure reconstruction, computational homogenization and Machine Learning. *In revision AEM 2024*